NASA Contractor Report 4353

Nonequilibrium Phase Chemistry in High Temperature Structural Alloys

R. Wang

NASA

NASA Contractor Report 4353

Nonequilibrium Phase Chemistry in High Temperature Structural Alloys

R. Wang
Failure Analysis Associates, Inc.
Redmond, Washington

NASA

National Aeronautics and
Space Administration

Office of Management

Scientific and Technical
Information Division

1991

Page intentionally left blank

NONEQUILIBRIUM PHASE CHEMISTRY

IN

HIGH TEMPERATURE STRUCTURAL ALLOYS

PROJECT SUMMARY

This research project identified, characterized and produced Ti
and Ni aluminides of nonequilibrium microstructures and thin
gauge thickness for potential high temperature applications.
Phase I work demonstrated a high-rate sputter deposition
technique for rapid surveillance of the microstructures and
nonequilibrium phase chemistry obtained from a very high quench
rate. The sputter deposited alloy phases exhibited extension of
solid solubility limits, and grain size refinement not previously
found from rapid solidified alloys. Phase II initially
investigated a wider range of nonequilibrium alloy formation and
microstructures. Alloys with specific compositions were
synthesized with extended solid solutions, stable dispersoids and
specific phase boundaries associated with different heat
treatments. Phase stability and mechanical behavior of these
nonequilibrium alloys were extensively investigated and compared
with other alloys formed by rapid solidification and thermo-
mechanical processing.

Page intentionally left blank

CONTENTS

LIST OF ILLUSTRATIONS

LIST OF ILLUSTRATIONS (Continued)

LIST OF TABLES

1.   INTRODUCTION

Hypersonic vehicles require structural alloys that are able to withstand demanding operational conditions in their air-frames and engines. Advanced structural materials based on Al and Ti alloys and superalloys, would provide significant advantages if they could be utilized at temperatures from 100 to 150°C higher than current service temperatures. However, development of high-temperature alloys has taken a very long time. This slow improvement is due to the complex phase chemistry in nonequilibrium intermetallic alloys associated with major elemental additives needed for developing stable strengthening structures and microstructures.

This research utilized a high rate sputter deposition technique to explore nonequilibrium intermetallic alloys based on Ni_3Al, Ti-6Al-4V or Ti_3Al and containing excess elemental additives. These elemental additives were Hf, C, B, Nb and Cr, either for structure strengthening or ductility enhancement. Nonequilibrium phase formation and stability were investigated with alloys containing a graded composition of the elemental additives. The feasibility of forming high quality thin alpha2-Ti_3Al foils with the vapor-phase deposition technique was also investigated.

The program consisted of two phases. During the first phase, studies were conducted to demonstrate an efficient means to determine nonequilibrium phase chemistries and boundaries of sputtered alloy systems with potential spacecraft structural applications. Two baseline subsystems, sputter deposited Ti-6Al-4V and Ni_3Al systems were explored. The second phase investigated the Ni_3Al, Ti-6Al-4V and Ti_3Al material systems alloyed with HfC, Nb, Cr and B.

The potential of using sputter deposition as a means toward study of nonequilibrium phase chemistry in high temperature intermetallic alloys was demonstrated. The complex microstructure and phase stability characteristics of these systems were investigated including a discovery of a complex structure/chemistry relationship in the $(TiNb)_3Al$ orthorhombic phase. Several problems associated with high rate sputter deposition were also identified. Highly flexible and clean thin gauge foils were fabricated in this study. Additional refinement of the sputtering process would be needed to improve the quality of the thin foils.

The research was managed and conducted by R. Wang, at Failure Analysis Associates, Inc. Additional support was provided by M. D. Merz at Battelle Pacific Northwest Laboratories for high rate sputter deposition, V. K. Sikka and C.T. Liu at Oak Ridge National Laboratory for casting of sputtering targets and mechanical testing respectively, and M. Kaufman, University of Florida, and R. Ayer, STEM, Inc. for TEM work.

2. TECHNICAL APPROACH AND WORK OBJECTIVES

2a. Technical Approach

The technical approach to achieve higher temperature structural stabilities in Ti, Ni_3Al and Ti_3Al alloys was to obtain nonequilibrium microstructures with extended solubility limits, grain refinement, and stable dispersoids beyond those attainable from rapid solidification techniques. Our approach was to utilize a sputter deposition technique, providing the highest possible quench rate, on the order of 10^{11-12} K/s [1,2], to fabricate a series of new nonequilibrium alloys for rapid surveillance of the effects of high quench rate on nonequilibrium chemistry. Using alloys fabricated with gradient composition of the alloying additives, we could further demonstrate the ability to efficiently characterize a multi-element alloy system to determine solid solubility limits, and new metastable crystalline and amorphous phases achievable with the high quench rate. Our technique also provided a means for economically producing sufficient quantities of material for laboratory quantification of material metallurgical characteristics and physical properties.

During the program, we have characterized detailed nonequilibrium chemistry, especially with transmission electron microscopy, to establish key features associated with the alloy chemistry and sputtering effects. In addition to binary alloys, we have chosen several alloy additives to control the microstructure. The logic of choosing the alloying additives was based on high temperature stability of the dispersoids, grain size refinement and oxidation resistance. We selected ceramic dispersoids, such as TiB and HfC, because of their high melting temperatures. Our alloy development approach was to incorporate a sufficient amount of high temperature phases based on borides and carbides to improve the service temperature. We also incorporated a high concentration of high temperature metal, such as Nb, to improve the stability of ductile phase, such as the beta phase. Compositional gradient alloys in small quantity allowed preliminary quantification of the mechanical behavior, such as ductility, and microhardness as a function of alloy composition. Crystallographic and microstructural characterizations were conducted to determine phase stability at elevated temperatures and oxidation resistance.

Based on the determination of high temperature physical properties and microstructural stability, specific alloy compositions were identified as having potential for extended temperature service either as a structural material, or as a protective coating for existing structural materials. The selected alloys of single composition were fabricated as relatively thick sputter deposits of 6"-diameter size, allowing the preparation of sufficient numbers of specimens for high temperature mechanical properties determination.

2

The technical approach of this program is summarized as follows:

1.   Characterize extended solubility of Ni_3Al alloys using TEM.

2.   Fabricate and characterize 1 or 2 additional extended solubility gradient composition sputter deposits based on Ti-6Al-4V and Ni_3Al to assess the effects/potential of alternate alloy additions.

3.   Fabricate and characterize Ti_3Al based alloys with gradient Nb and Cr additions.

4.   Establish phase stability and phase boundaries for specific nonequilibrium alpha2-Ti_3Al alloys containing Nb or Cr additions.

5.   Investigate alloy microstructures and compositions as a function of sputtering parameters, and focus on variables to achieve high quality Ti_3Al thin foil formation.

6.   Evaluate room temperature and high temperature mechanical properties,

7.   Determine and demonstrate the fabrication of bulk quantities (i.e. Kg) of the most promising structural alloy identified in the previous tasks, utilizing a mechanical alloying technique to produce the materials' powder.

8.   Investigate oxidation behavior in Ti_3Al alloys containing different alloy additions.

2b. Work Objectives

The objectives of this program were to identify, characterize and produce both laboratory and pre-production quantities of new Ti based and/or Ni based structural alloys with extended service temperatures over the best currently available alloys. Specific objectives were:

1. to extend nonequilibrium compositions, structures and microstructures in alloys with potential aerospace application;

2. to determine extended solid solubility limits and related microstructure refinement;

3. to conduct alloy development for nonequilibrium Ni_3Al, and Ti alloys aimed at improved thermal stability;

4. to conduct high temperature mechanical tests to correlate development of thermally stable microstructures with achievement of necessary mechanical properties at service temperatures significantly over current Ti and Ni_3Al alloys;

5. to develop fabrication techniques that could produce bulk alloys replicating nonequilibrium chemistry of the sputter deposited alloys,

6. to apply the characterization and processing techniques to Ti_3Al related structural alloy systems,

7. to obtain high quality sputter deposited thin gauge foils for alpha2-Ti_3Al and determine processing variables to achieve the control of composition and microstructure of resultant alloys.

The program was conducted in seven Tasks to provide timely control of the research progress towards the technical objectives:

     Task 1. Nonequilibrium Alloy Characterization
     Task 2. New Alloy Additives
     Task 3. High Temperature Alloy Development
     Task 4. Test Specimen Fabrication
     Task 5. High Temperature Mechanical Testing
     Task 6. Bulk Alloy Fabrication
     Task 7. Optional Alloy Development

These tasks provided step-by-step check points for alloy development, starting from rapid surveillance of composition of additive elements then narrowing down to one or two key alloys for demonstrating improved high temperature mechanical properties. Consequently, attempts were made to produce optimized materials in large quantity to replicate the characteristics of sputter deposited alloys.

4

3. EXPERIMENTAL PROCEDURES

3a. Nonequilibrium Alloy Fabrication

A triode high-rate sputter deposition technique was used to fabricate nonequilibrium alloys and thin foils. Sputtering was performed with a triode sputter deposition system (Figure 3.1a) at Battelle Pacific Northwest Laboratory, using composite sputter targets designed and supplied by Failure Analysis Associates, Inc. Composite targets were constructed from 5" diameter and 0.25" thick host alloys such as cast Ni_3Al, Ti_3Al and commercial grade Ti-6Al-4V alloy. Elemental or compound additives were incorporated as two small subtargets comprised of high purity Nb (99.9%), Cr(99.5%), HfC, B and TiB_2. The size of the subtargets ranged from 1-1.5" diameter.

Sputter deposited alloy disks from the composite targets have metal or metalloid additives in a graded composition in order to compare structures and properties of materials formed under identical conditions. In order to cover a wide composition range for the additives, a relatively large 6-inch diameter sputter deposit was used to create the composition gradient over a surface distance. Depending on the sputtering yield of the specific element and the configuration of the sputtering target, the resultant as-deposited alloy disk had a continuous composition gradient of up to 30-40 at.% of the alloying additives in a region of nearly 8 cm (3-inch) diameter area. With two additive subtargets used in each sputter deposition, four zones of graded composition were produced, as illustrated in Figure 3.1b.

Each sputter deposited alloy disk was formed onto a polished copper substrate cooled with circulating water at 25°C. Sputtering was conducted in 10^{-3} Torr Kr gas at a sputtering rate of 20 μm/h. The resultant deposits typically had a nominal thickness ranging from 0.1-0.25 mm (4 to 10 mils). A thick alloy deposit was needed to eliminate surface induced phase transformation effects, and allowed for mechanical property testing. In the later part of the research, sputter fabrication of single composition high quality foils was investigated to provide for high temperature mechanical testing specimens. The sputter deposition runs made in this program are summarized in Table 3.1
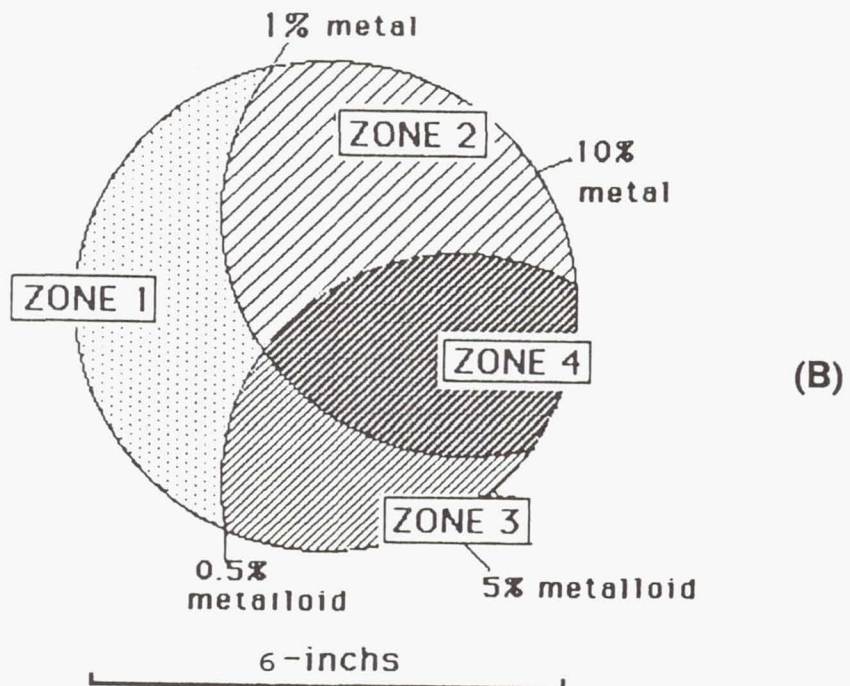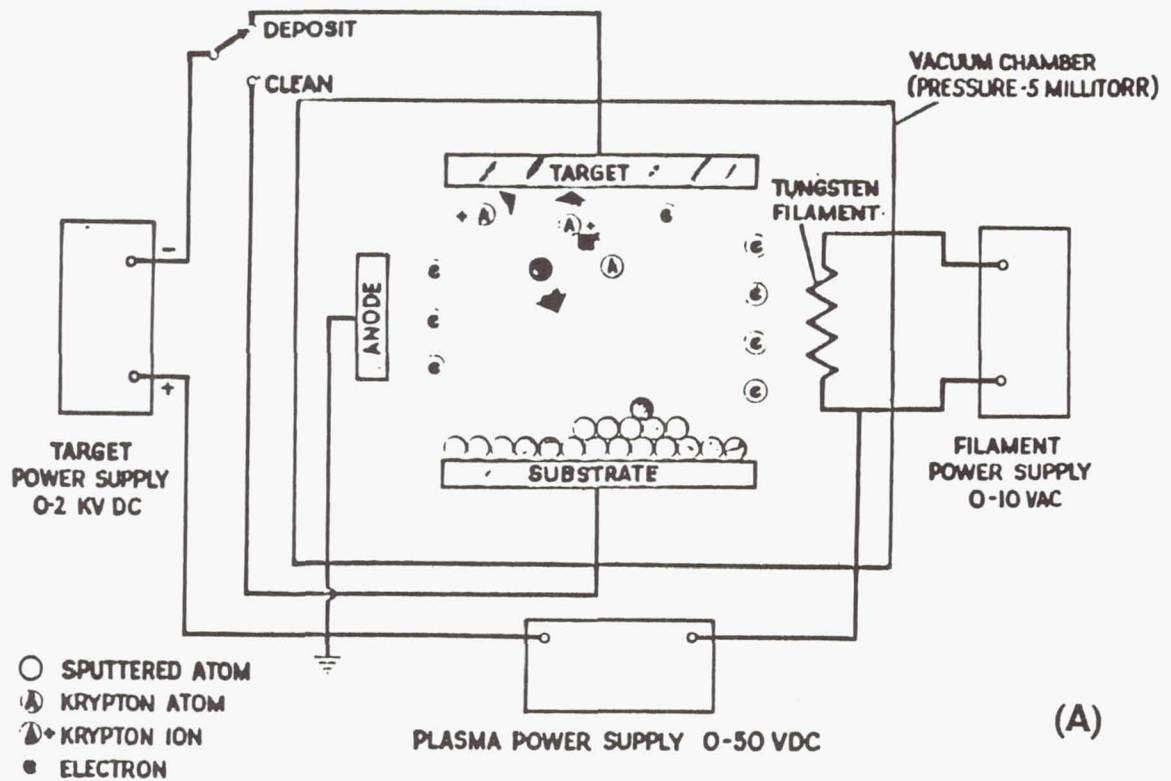
Figure 3.1 Fabrication of nonequilibrium structural alloys:
A) triode sputter deposition process, and B) design of sputter
deposited alloys containing zones of graded composition.

**Table 3.1.   Sputter-deposited alloy systems and thin foils
fabricated.**

	Sputter Host Deposit Target	Sub-target	Sub-strate	Thickness 10^{-3}"	Alloy System Formed (in at.%)
(1)	Ni_3Al	Hf, HfC	OFHC-Cu	9	Graded Ni_3Al-Hf, Ni_3Al-HfC
(2)	Ti-6Al-4V	B, TiB_2	OFHC-Cu	7	Graded (Ti-6Al-4V)-B
(3)	Ti-6Al-4V	Nb, B	OFHC-Cu	3	Graded (Ti-6Al-4V)-Nb, and Ti-6Al-4V-(Nb,B)
(4)	Ni_3Al	Nb, Cr	OFHC-Cu	10	Graded Ni_3Al-Nb, Ni_3Al-Cr and Ni_3Al-(Nb,Cr)
(5)	Ti_3Al	Nb, Cr	OFHC-Cu	8	Graded Ti_3Al-Nb, Ti_3Al-Cr and Ti_3Al-(Nb,Cr)
(6)	Ti_3Al	Nb, Cr	OFHC-Cu	4	HQ Ti_3Al-Nb foil
(7)	Ti_3Al+1Ru	–	OFHC-Cu	1	HQ Ti_3Al foil*
(8)	Ti_3Al+Nb	–	OFHC-Cu	7	HQ Ti-20Al-11Nb foil
(9)	Ti_3Al+Nb	–	6061-Al	8	HQ Ti-18Al-11Nb foil
(10)	Ti_3Al+Nb	–	6061-Al	10	HQ Ti-25Al-9Nb foil
(11)	WC-Alpha2[#]	–	6061-Al	4	HQ Ti-24Al-10Nb foil
(12)	WC-Alpha2	–	6061-Al	6	HQ Ti-24Al-10Nb foil

HQ =   High quality, used for microstructure and properties
evaluations

*   Magnetron Sputtering

Low oxygen content alpha2 alloy from Wah-Chang

3b. Specimen Preparation

Small alloy specimens over a selected composition range were prepared first by sectioning the as-sputter deposited alloy disk into several 5-mm wide strips. Sectioning was done with a high-pressure abrasive waterjet to prevent the loss of material and to minimize local plastic deformation. Alloy specimens of 5 x 5 mm size, were obtained by cutting the strip of deposit with a low speed SiC saw. The copper substrate backing was then removed by metallographic polishing. The final free-standing specimens were polished with 600 grit SiC paper to remove surface contaminates and cleaned with acetone and methanol before characterization and heat treatment. Thin TEM specimens were prepared by first dry polishing the specimen to 50-75 μm thickness with a 600 grit SiC paper, following by ion-milling. No electrolyte was used in preparation of the thin sections in order to avoid possible hydrogen effects.

Heat treatment was conducted in sealed Vycor brand tubing using a box furnace. Temperatures ranging from 800-950°C for 1 to 100 hours were studied. Each specimen was individually wrapped in a Ta foil. The tubing was evacuated with a mechanical vacuum pump and back flushed with high purity argon gas at least three times. The heat-treated specimens were analyzed for oxygen pickup by both wavelength dispersive spectroscopy (WDS) and auger electron spectroscopy methods. There was no detectable difference in oxygen content between the as-deposited and heat-treated specimens. Auger analysis detected no oxygen peak in the specimens after the surface oxide was removed.

For annealing of Ni_3Al and Ti-6Al-4V alloys, specimens were wrapped individually in a Ta foil and placed inside a Ta crucible. Annealing was conducted in a bell jar system with a 10^{-7} torr vacuum at either 900 or 1100°C for 4 hours. Annealing was also conducted in sealed Vycor brand tubes at a partial pressure of Ar of 10^{-3} torr.

3c. Material Characterization

The surface topography of the as-deposited alloys allowed visual identification of the phase boundary between the crystalline phases and the amorphous phase. Microstructure examinations for surface topography were conducted using optical microscopy and scanning electron microscopy.

The structure of the as-deposited and heat-treated alloys was investigated by x-ray diffraction at a scan rate of 0.2°/min with Cu-Kα radiation. Because of the small specimen size, the peak-to-background ratio was small, but sufficient for identification of

8

the structure as either amorphous or crystalline. Lattice parameters of the crystalline phases were determined from the (111) diffraction peak of the $L1_2$ and the beta phase, and (110) from the Ti_3Al phase.

Alloy composition in atomic percentage (at.%) was determined using a JEOL Model 733 SEM/electron microprobe equipped with a Tracor Northern-5500 minicomputer. Elemental analysis was made with a Tracor Northern lithium-drifted silicon detector for x-ray energy dispersive spectroscopy (EDS) analysis. Light elements such as O, C and B were determined by wavelength dispersive spectroscopy (WDS) using four spectrometers. Oxygen x-ray peak position, and quantitative oxygen counts were calibrated with oxygen spectra obtained from an alumina standard using a 15 KeV and 15 nA electron beam. The detection limit for oxygen was near 450 ppm. The composition of the alloy metalloid, such as B and C, was determined with an electron microprobe by comparison with a standard.

With a typical graded composition specimen size of 5 mm wide, the composition from one end to the other end would vary from 0.5 to 2 at.% of the alloying element. A wider spread of the composition, ranging from 5 to 10 at.%, resulted for specimens containing more than 20 at.% of the alloying element because these specimens were located directly above the subtarget of that alloying element. The composition of the alloying element was measured from a 200 μm square area (50 μm for microprobe) at the center of the specimen. The error in composition determination due to the instrumentation used was approximately 2 at.% or less, and the error due to locating the average composition (e.g. centering the analysis region) of the specimen should be less than 1 at.%.

Microstructure and phase chemistry were determined by analytical TEM analysis. Specimens for TEM analysis were mechanically polished to 0.003-0.005" thick and ion-milled with argon ions at 5 KV. The crystal structure was determined by Convergent Beam Electron Diffraction (CBED). The composition of each phase was established by quantitative x-ray microanalysis after necessary absorption correction based on the k factors of Ti_3Al and Ti-Nb binary alloy standards.

3d. Mechanical Testing

Mechanical testing was primarily performed with microhardness measurements, at both room temperature and high temperatures up to 900°C. Microhardness of the as-deposited alloys was measured on specimens equally separated by distance of 5 mm along the deposit composition gradient. Because of the nonlinear behavior of alloy composition gradient, microhardness measurements taken at a constant spacing resulted in more measurements of alloys with low dispersoid concentration levels than those of high concentration

9

levels.   For alloys containing a wide range of additive composition, the microhardness data were plotted versus the composition of the additive element when sufficient composition data points were available.   Similar hardness evaluations were performed for heat treated alloys.   The relationship between microhardness and alloy composition at the as-deposited alloys and the heat treated alloys was sensitive to different phase fields such as extended solid solubility regions and amorphous phases.

High temperature microhardness measurements were performed at Battelle Northwest Laboratory using a Nikon hot microhardness tester.   The specimen chamber was evacuated to 10^{-6} torr and pre-heated to the maximum test temperature, such as 900°C.   Once the specimens were introduced to the chamber, measurements were made from high temperature to the low temperature until room temperature was reached.   Measurements were made on the polished cross-section of the specimen (0.1 to 0.25 mm thick).   In most cases, three data points were collected for each temperature.

High temperature microhardness was used to evaluate and compare mechanical properties of sputter deposited alloys in the 600 to 900°C range.   Microhardness data for alloys of different compositions and varied processing were compared.   The capability of performing high temperature microhardness measurements was important for this research because sputter deposited foil specimens were too small and too thin for tensile testing. Specimens selected for high temperature microhardness measurement were typically annealed at 900°C for 2 to 4 hours in vacuum.   The Ni_3Al alloys were annealed at 1100°C for 4 hours.

10

4. NONEQUILIBRIUM Ni₃Al BASED ALLOYS

4a. Microstructures with HfC Dispersoids

The microstructures of nonequilibrium Ni_3Al containing excess HfC dispersoids were characterized by TEM to establish the formation of ultrafine and stable dispersoids. Possible occurrence of the antiphase domain (APD) in sputter deposited Ni_3Al alloys was investigated, because APD's are considered as the major contributing factor for ductility in Ni_3Al alloys [3].

HfC dispersoids were incorporated into the Ni_3Al matrix alloy by different approaches, Figure 4.1. The first approach was to incorporate elemental Hf and C separately resulting in a nearly equal composition Hf+C region between Hf- and C-rich regions. Another approach was by co-sputtering the HfC compound directly with the Ni_3Al matrix. Both resultant as-deposited alloys had similar microstructures consisting of a high density of defects and fine grain sizes less than 0.1 μm in size, Figure 4.2. The matrix alloys were the disordered $L1_2$ structure containing highly textured grains. No metastable phases other than the disordered $L1_2$ structures were found within the solid solution fields. Because the grains were extremely small, no APD was observed in as-deposited Ni_3Al alloys.

HfC dispersoids were formed by annealing the as-deposited nonequilibrium alloys between 900 and 1100°C. Heat treatment of alloys containing near equal atomic Hf and C contents resulted in very fine dispersoids in the Ni_3Al matrix grains. The micrograph of an Ni_3Al-6.5HfC annealed at 900°C for 4 hours is shown in Figure 4.3. The fine dispersoids were identified by electron diffraction as cubic HfC.

To establish the thermal stability of the microstructure and HfC dispersoids, Ni_3Al-5HfC alloy extracted from the HfC graded deposit was annealed at 1100°C for 4 hours. Compared with the 900°C annealed Ni_3Al-6.5HfC alloy, the 1100°C annealed alloy showed a slightly larger grain size, Figure 4.4. Thus the grain size increased from 0.5-1.5 μm of the 900°C alloy to about 1-5 μm size for the 1100°C alloy. Electron diffraction analysis of all the matrix grains showed the ordered $L1_2$ structure. No APD was observed in either microstructure.

Comparing with the 900°C annealed alloy, Figure 4.3, the size of the HfC dispersoids in the 1100°C annealed alloy remained small, averaging 37-50 nm, Figure 4.4. In both microstructures, the HfC dispersoids were uniformly distributed in the Ni_3Al matrix grains. In general, the 1100°C specimen showed varying degrees of depletion of the HfC particles in the regions near the grain boundaries of

the matrix. In some instances the depletion was obviously noticeable, while in other instances the depletion was mild. The grain boundary depletion zone was less predominant in the 900°C specimen.

The dispersoids in the 1100°C annealed alloy were more spherical in shape than those in the 900°C annealed alloy. Occasionally carbides with angular shapes were observed in the 1100°C annealed alloy. The angular shape is typical of MC carbides in superalloys which are usually exposed to temperatures below 1037°C (1900 F). The spherical morphology of the carbides in the present alloy is probably the result of spherodization during exposure to temperatures in excess of 1037°C (1900 F). The density of the carbide particles varied only slightly from region to region.

The high thermal stability of the fine grain size in sputter deposited $Ni_3Al-HfC$ alloys was probably due to the pinning of dislocations and grain boundaries by the fine HfC dispersoids. The carbide particles were observed to provide effective pinning of both dislocations and grain boundary motions, as shown in Figure 4.5. This was the result of small average interparticle spacing of the carbides in the alloy. Electron diffraction studies further indicated that the carbide particles did not show any obvious lattice correspondence with the matrix. Since both the aluminide matrix and the carbide particles have a cubic structure, a crystal structure correspondence similar to the austenite/$M_{23}C_6$ carbide system was expected. However, due to the large difference in the lattice parameters (approximately 3.57 Å for Ni_3Al and 4.4 Å HfC) and the exposure of the alloy to elevated temperature, any interfacial coherency and/or lattice correspondence that existed at room temperature would have been lost. The identification of fine HfC dispersoid phase in Ni_3Al was a significant finding in comparison with typical carbide phases, mostly $M_{23}C_6$ and/or M_6C phases, with shapes in plates or discontinuous irregular particles at the grain boundaries, since these asymmetric shapes usually can result in poor ductility and in increased cracking tendency.

4b. High Temperature Mechanical Behavior

Due to the small specimen size, high temperature mechanical behavior was investigated by the measurement of microhardness of these alloys as a function of temperature. A series of specimens with increasing HfC content, from approximately 0.2 to 8.5 at.% HfC, was used to determine the effects of HfC dispersoids in high temperature mechanical behavior. These specimens were annealed at 900°C for 4 hours before the measurement. The microhardness data are shown in Figure 4.6.

The hardness vs. HfC content plot indicated that increasing the concentration of HfC dispersoids resulted in higher microhardness

12

at both room temperature and 700°. However, the presence of HfC dispersoids did not result in any increase in the microhardness at 900°C, thus low temperature ductility was retained.

The hardness vs. temperature plot shows that 8.5 at.% HfC alloy had the highest microhardness values between room temperature and 700°C. Above 700°C the hardness of the 8.5 at.% HfC alloy dropped sharply, as the temperature increased, to a very low value at 900°C. In comparison, the specimen with approximately 5.8 at.% HfC had more balanced low and high temperature hardness values. Very low HfC content in the range of 0.2 to 0.5 at.% resulted in a lower room temperature hardness as well as lowered high temperature hardness.

Although ultrafine HfC dispersoids, on the order of 50 nm size are stable in the Ni_3Al matrix alloy up to 1100°C, they have not effectively increased the hardness at 900°C. Apparently, single-phase dispersoids in Ni_3Al were unable to suppress the high grain boundary activity (313 KJ/mol [4]) at temperatures above 700°C. Similar observation was also independently derived recently from liquid quenched Ni_3Al alloys containing HfC as the dispersoids. The mechanism for preventing grain boundary sliding at this temperature range is not adequately understood. In order to prevent grain boundary sliding, an additional strengthening phase at the grain boundary area would be needed. Mechanisms for strengthening of the grain boundary of Ni_3Al should be investigated.

4c. New Nonequilibrium Ni_3Al-(Nb,Cr) Alloys

This work expanded the study on Ni_3Al to additional alloy additives with potential high temperature stability, extended solid solution and high temperature oxidation resistance characteristics. Two additives, Nb and Cr, were of great interest for these applications, providing potential strengthening effects as well as improvement of oxidation resistant behavior. A single deposit containing graded compositions of Nb, Cr, and Nb+Cr was prepared, as shown in Figure 4.7. Specimens of Ni_3Al-Nb, Ni_3Al-Cr and Ni_3Al-(Nb,Cr) were extracted from this deposit and characterized.

4c.1. Nonequilibrium Ni_3Al-Nb Alloys

The nonequilibrium Ni_3Al-Nb alloys were deposited with Nb content ranging from 1 to 50 at.% (Figure 4.8a). The extended solid solubility limit for Nb in the disordered $L1_2$ structure was established by x-ray lattice parameter measurement as 12 at.%, Figure 4.8b. Alloys containing more than 15 at.% Nb, up to 50 at.% Nb, were amorphous.

Detailed microstructural investigation was conducted for Ni_3Al-Nb alloys formed at the region which had a mixture of disordered $L1_2$ and amorphous phases, Figure 4.9. The $L1_2$ phase had an average grain size of 45 nm and a lattice parameter of 3.65 Å. Both x-ray diffraction and TEM confirmed that the boundary of disordered $L1_2$ and amorphous phase would be at 15 at.% Nb. The disordered $L1_2$ phase contained 62-64 at.% Ni, 24-26 at.% Al, 10-11 at.% Nb and 1-2 at.% Cr. The amorphous phase had a composition of 56-59 at.% Ni, 16-19 at.% Al, 22-23 at.% Nb and 1-2 at.% Cr. The formation of the amorphous phase may be correlated to the occurrence of an eutectic composition at 16 at.% Nb, and a Ni_3Nb phase in the Ni-Nb binary alloys. This would explain why the amorphous phase had a composition similar to a $(NiAl)_3Nb$ alloy.

4c.2. Nonequilibrium Ni_3Al-Cr Alloys

Up to 60 at.% Cr was incorporated into the Ni_3Al matrix, as shown in Figure 4.10a. Chromium addition to Ni_3Al structure resulted in an extended solid solution to nearly 25 at.% Cr and a two phase region between 26 and 45 at.% Cr, Figure 4.10b. Alloys containing more than 45 at.% Cr were beta Cr-rich solid solution with a small lattice parameter of 2.9 Å. TEM analysis of a $Ni_3Al-25Cr$ alloy showed a dominant disordered $L1_2$ phase containing a beta phase, Figure 4.11. The average grain size of the $L1_2$ phase was 45 nm and the beta phase 100 nm. The $L1_2$ phase had a lattice parameter of 3.65 Å, and beta phase, 2.85 Å, consistent with the x-ray data. Elemental analysis of $L1_2$ grains showed a wide composition range 52-57 at.% Ni, 22-29 at.% Al and 13-24 at.% Cr. No amorphous phase was identified in nonequilibrium Ni_3Al-Cr alloys.

4c.3. Nonequilibrium $Ni_3Al-(Nb,Cr)$ Alloys

Nonequilibrium $Ni_3Al-(Nb,Cr)$ in a wide composition range of Nb and Cr were studied, Figure 4.12a. X-ray diffraction studies showed two groups of alloys, with a two-phase mixture between 2-5 at.% Nb and an amorphous phase containing more than 12 at.% Nb, Figure 4.12b. The two-phase mixture consisted of the Nb-rich and Cr-rich beta phases as observed in the Ni_3Al-Cr alloys. Formation of the two-phase alloy is primarily controlled by the Cr content between 20-40 at.% Cr. However, formation of an amorphous phase is consistent with the amorphous Ni_3Al which requires more than 12 at.% Nb. In this case, Nb content is essential for the stabilization of the amorphous phase even though the alloy also contained a nearly equal amount of Cr.

4c.4. Microhardness

Room temperature microhardness was measured on as-deposited nonequilibrium alloys described above to corroborate the effect of alloy addition to the formation of alloy phases and microstructures. Microhardness of the Ni_3Al-Nb was in the range of 700-880 Kg/mm^2, Figure 4.13a. Initially, increasing Nb content up to 8 at.% Nb resulted in an increase of the microhardness values from 700 to 860 Kg/mm^2. Alloys containing more than 10 at.% Nb had a slightly reduced hardness value, averaging 820 Kg/mm^2, due to the presence of the amorphous phase. Microhardness further reduced to 780 Kg/mm^2 at 40 at.% Nb, at which composition the amorphous phase may be terminated. Although microhardness values are confined in the 700-880 Kg/mm^2 range, they do reflect the changes of alloy phase and microstructure.

The microhardness of the Ni_3Al-Cr alloys with Cr content up to 59 at.% ranged between 620 and 910 Kg/mm^2, Figure 4.13b. Initial increase of the Cr to nearly 4 at.% Cr resulted in a rapid increase of the hardness values from 620 to 810 Kg/mm^2. This rapid increase of the hardness may be related to a possible solution hardening effect in the $L1_2$ structure. The microhardness values showed a constant 800 Kg/mm^2 between 8 and 18 at.% Cr and reduced to 780 Kg/mm^2 between 25-35 at.% Cr. Alloys with more than 40 at.% Cr showed a rapid increase of the hardness value to 910 Kg/mm^2 at 59 at.% Cr.

The combination of Cr and Nb in the Ni_3Al alloys showed a different microhardness trend, Figure 4.13c. A high hardness value, nearly 1050 Kg/mm^2, was observed for alloys containing approximately 1-2 at.% Nb and 65 at.% Cr. Rapid reduction of Cr from 65 to 40 at.% Cr, accompanied by a slight increase of the Nb content from 1-2 at.% Nb resulted in a rapid decrease of the hardness value to about 780 Kg/mm^2. A near constant hardness value of 790-910 was observed for alloys containing 5 to 48 at.% Nb. This result indicates that both Cr and Nb additions could strengthen the Ni_3Al matrix alloys. It is possible that Cr addition to the Ni_3Al matrix containing 7 at.% HfC would create an additional strengthening mechanism to reduce high temperature grain boundary sliding.
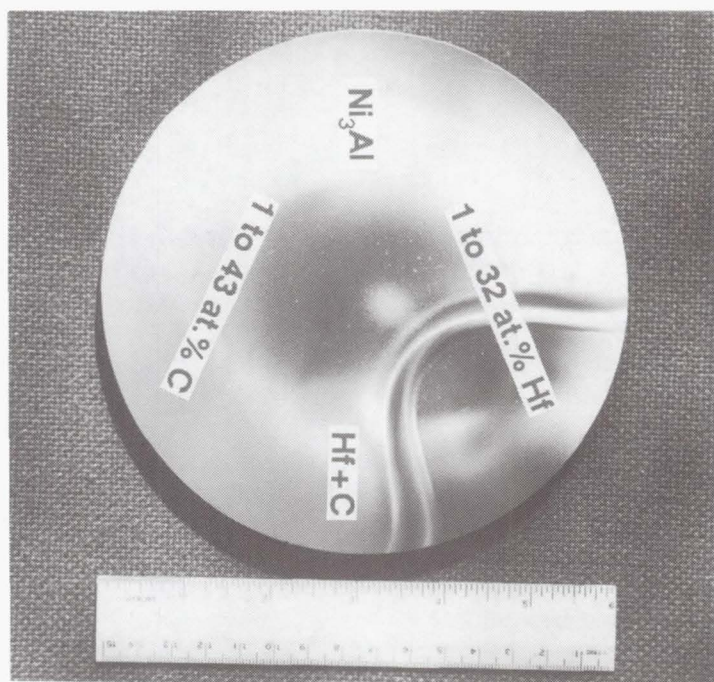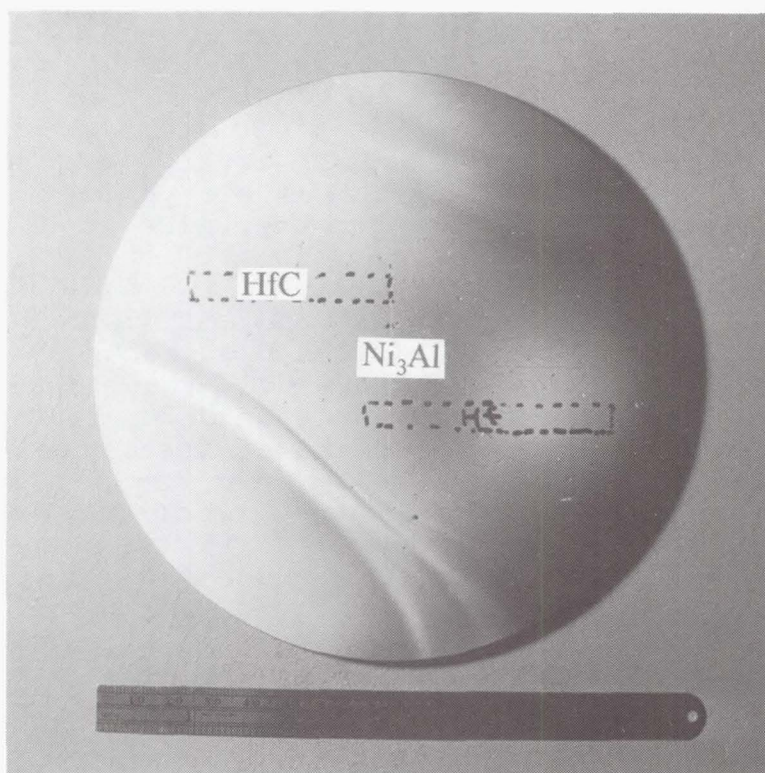
Figure 4.1. Sputter deposited Ni₃Al alloy disks containing graded HfC dispersoids, a) co-sputtering of elemental Hf and C to create the Hf+C zone, and b) co-sputtering of HfC compound.
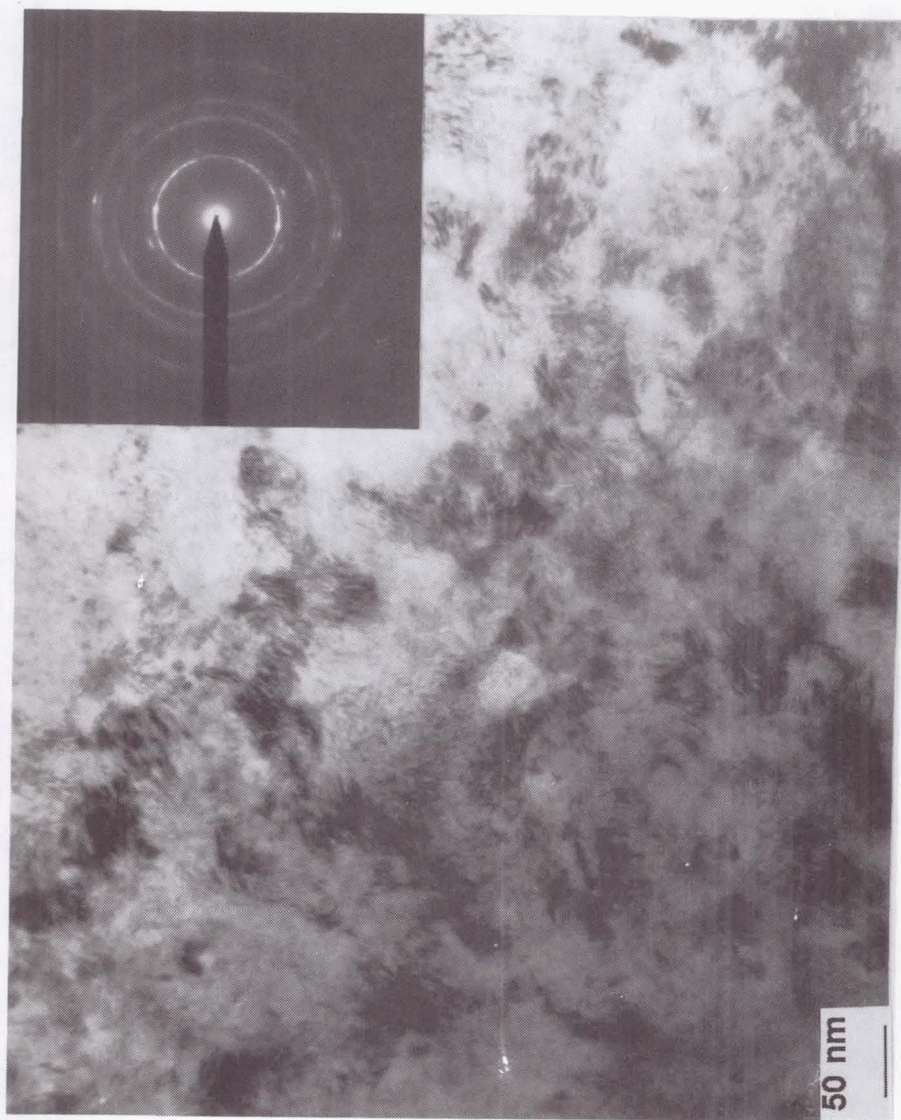
Figure 4.2. A typical microstructure of as-deposited Ni₃Al-(Hf,C) showing high density of defects and fine grain size.
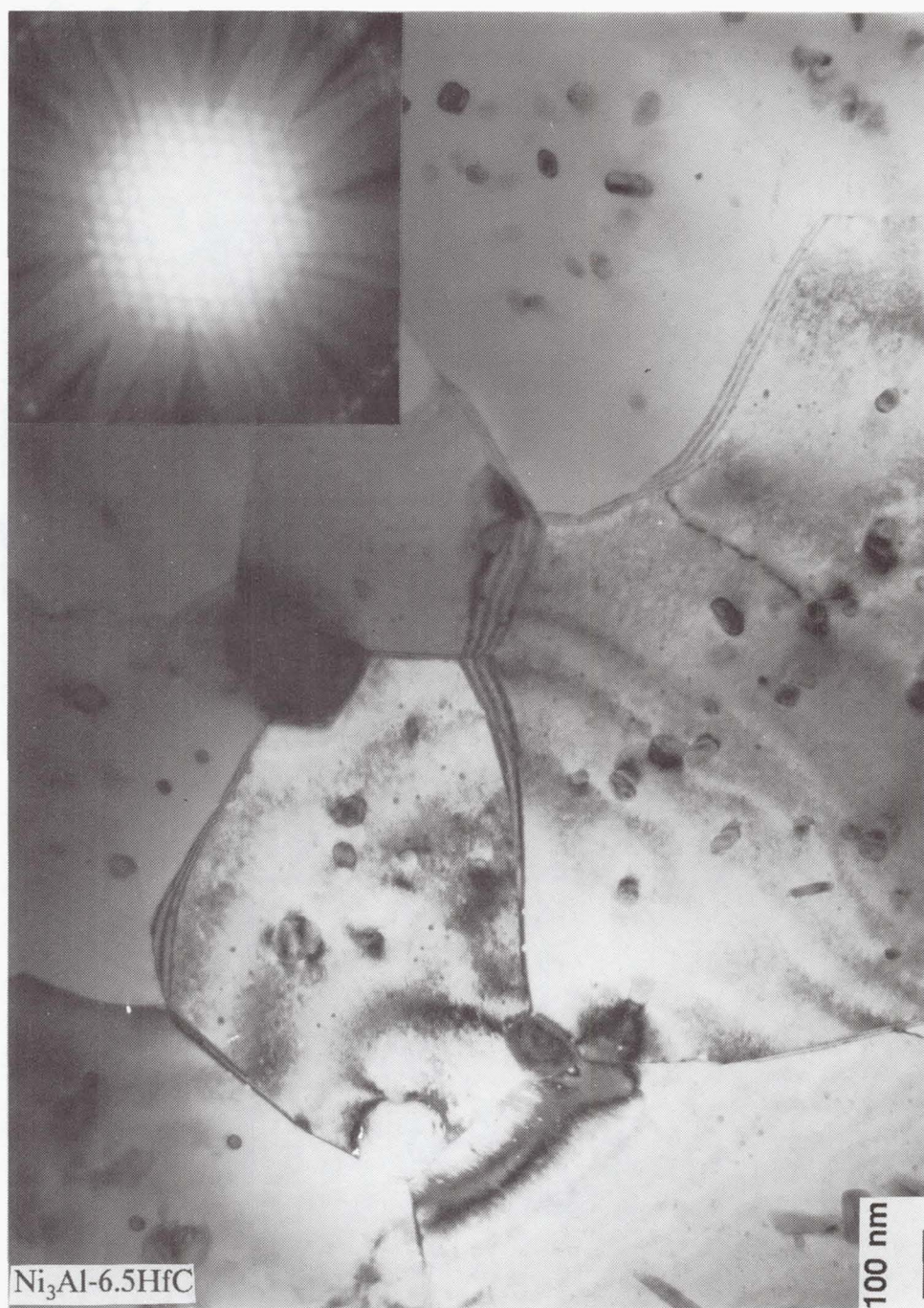
Figure 4.3. TEM micrograph of Ni₃Al-6.5Hf annealed at 900°C/4h showing grain size and HfC dispersoids.
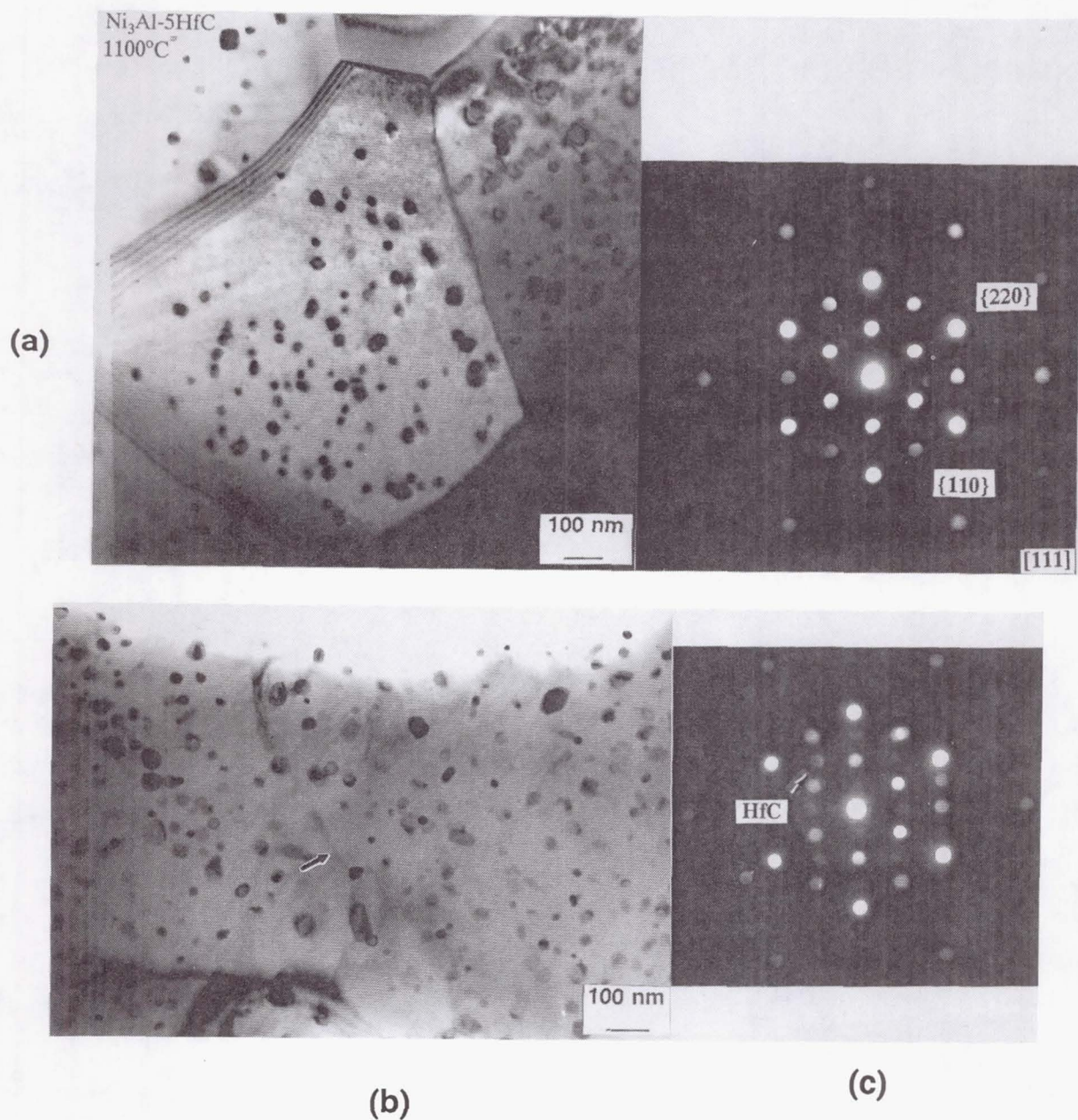
Figure 4.4.   TEM micrograph of Ni₃Al-5Hf annealed at 1100°C/4h showing distribution of HfC dispersoids, a) depleted near the grain boundary, b) no depletion near the grain boundary and c) electron diffraction patterns of the matrix superlattice and HfC dispersoid reflections.

19
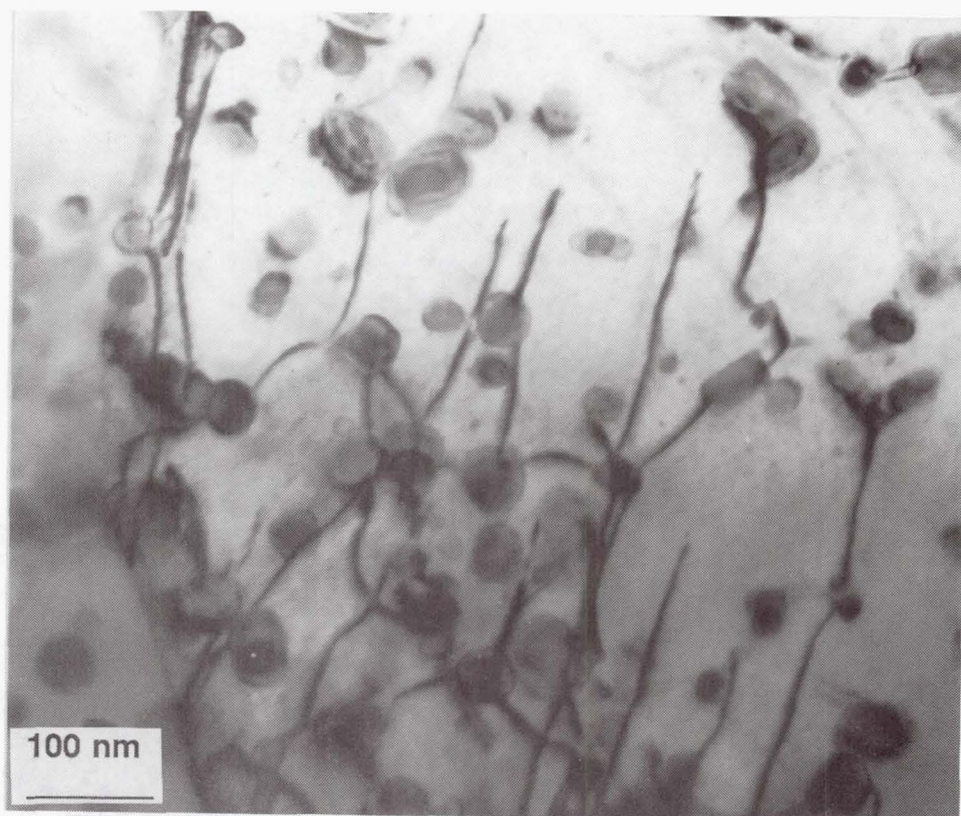
(a)
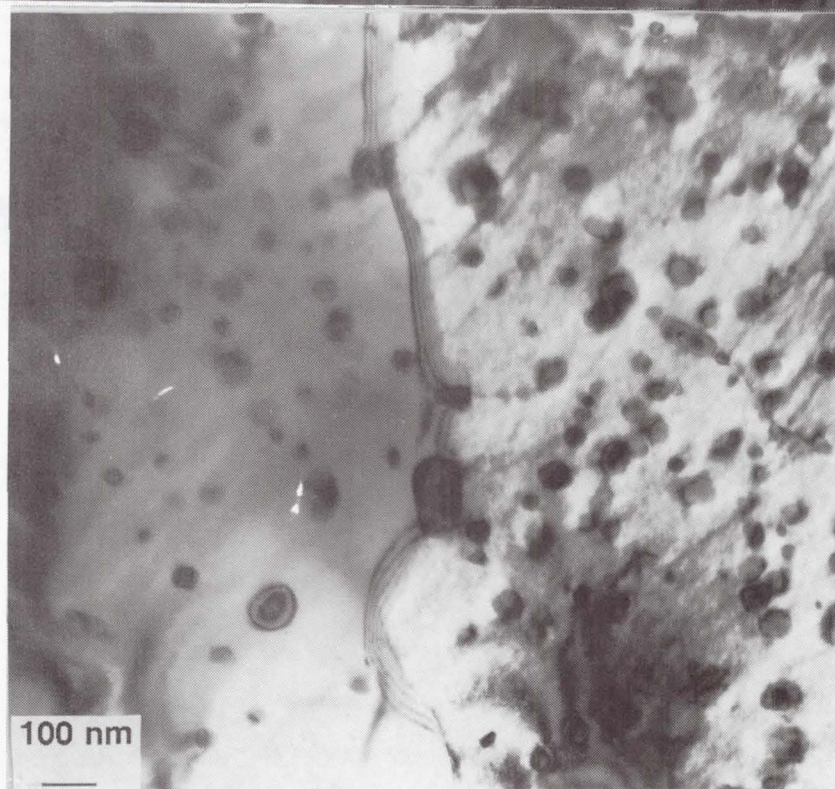
(b)

Figure 4.5. TEM micrograph of Ni$_3$Al-5Hf annealed at 1100°C/4h showing a) pinning of dislocations by the HfC particle, and b) pinning of the moving grain boundary.

20
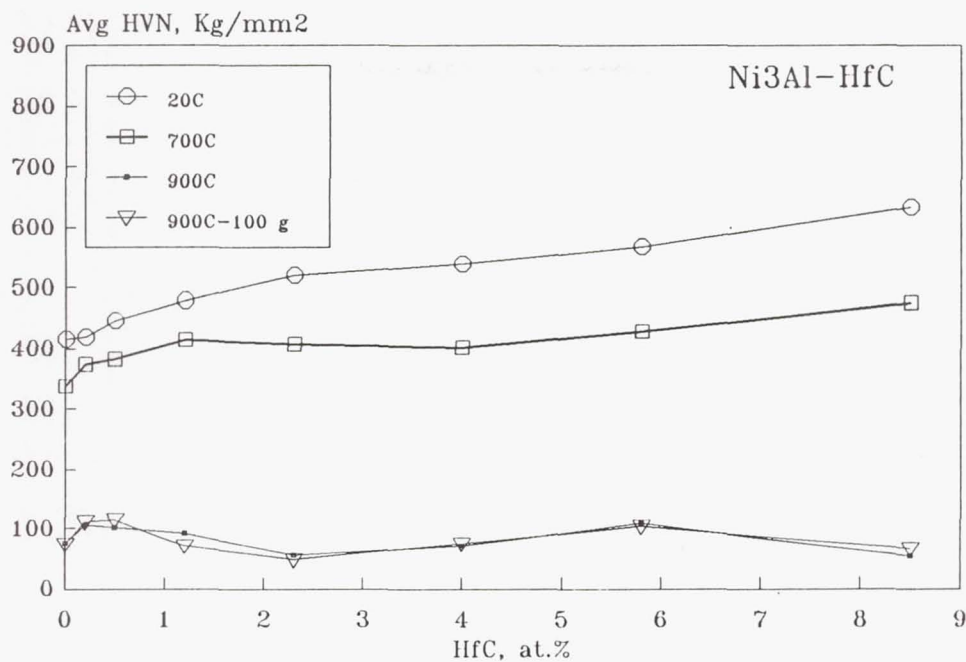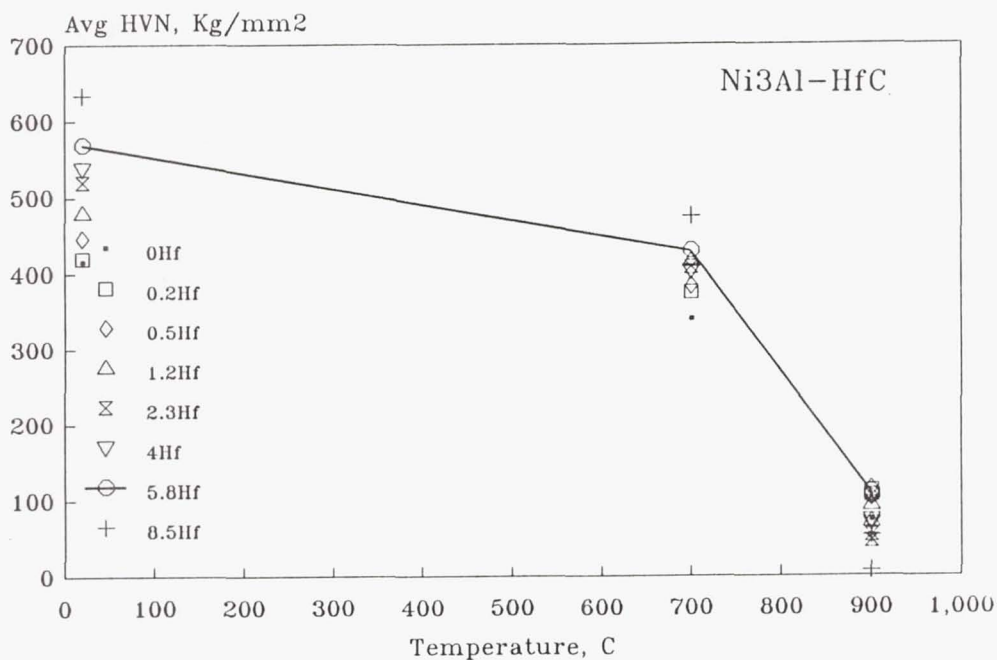
Figure 4.6. High temperature microhardness data of sputter deposited Ni₃Al-(Hf,C) alloys, a) as a function of HfC content, and b) as a function of temperature.

21
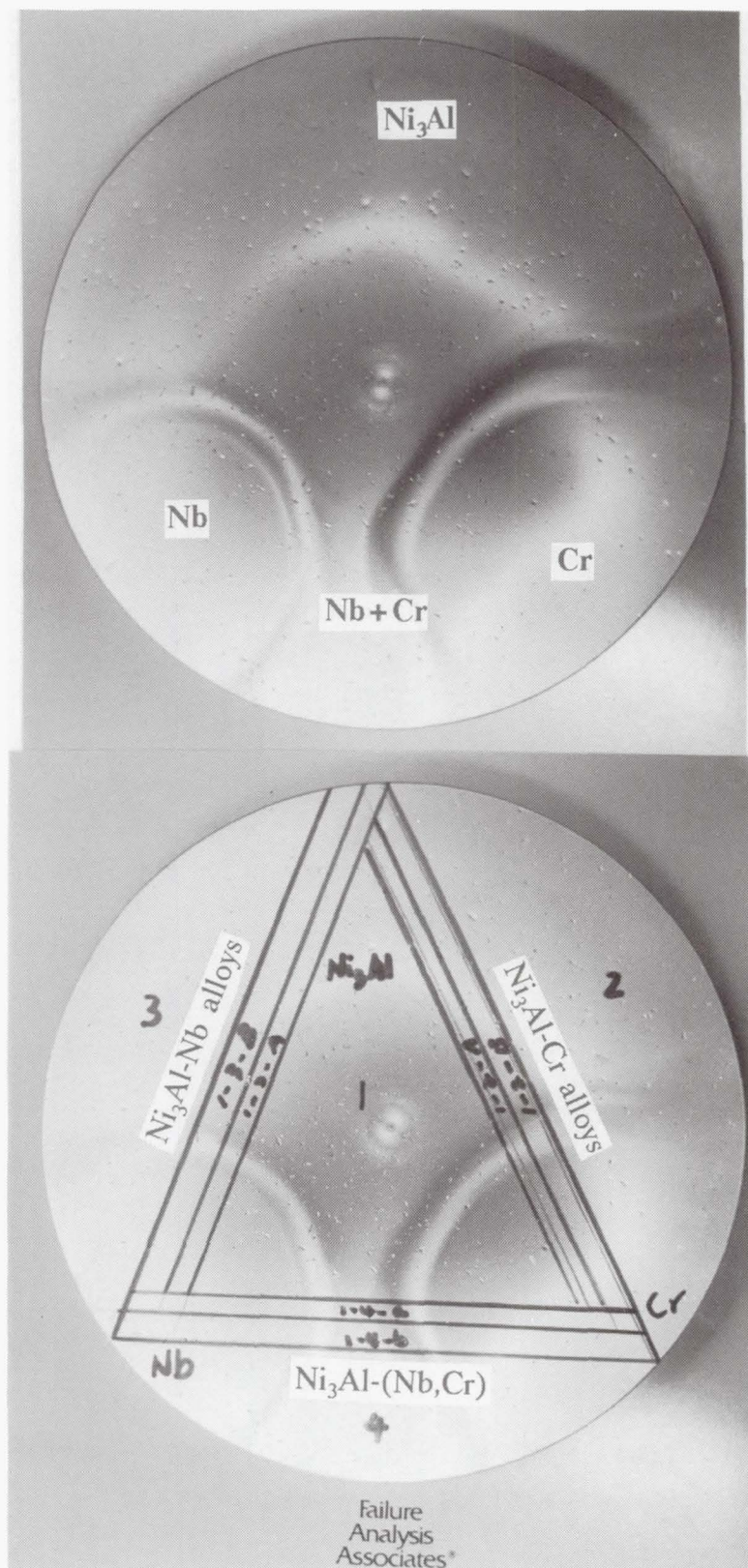
Figure 4.7. A single Ni_3Al deposit a) containing graded compositions of Nb and Cr, and b) specimens of Ni_3Al-Nb, Ni_3Al-Cr and Ni_3Al-(Nb,Cr) extracted from the deposit.

22
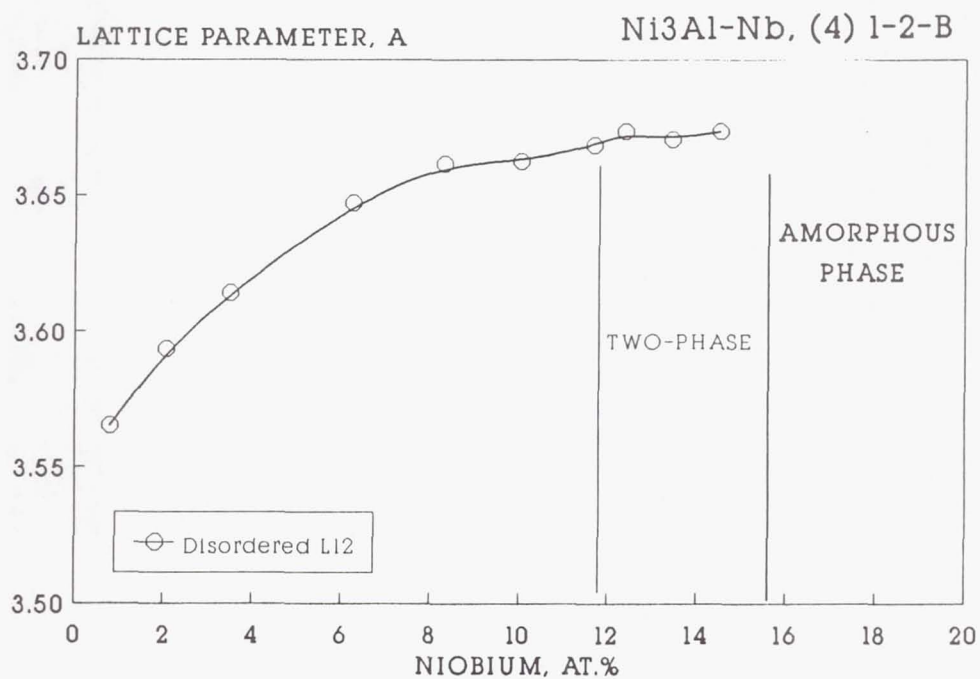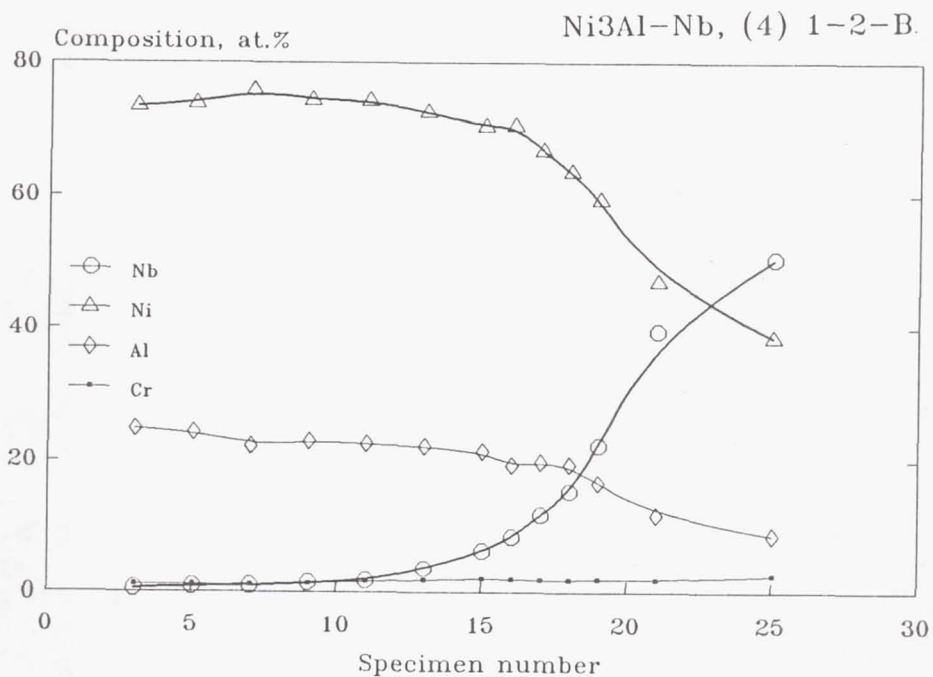
Figure 4.8. a) Composition analysis of nonequilibrium Ni_3Al-Nb alloys and b) lattice parameters and phase distribution as a function of Nb content.
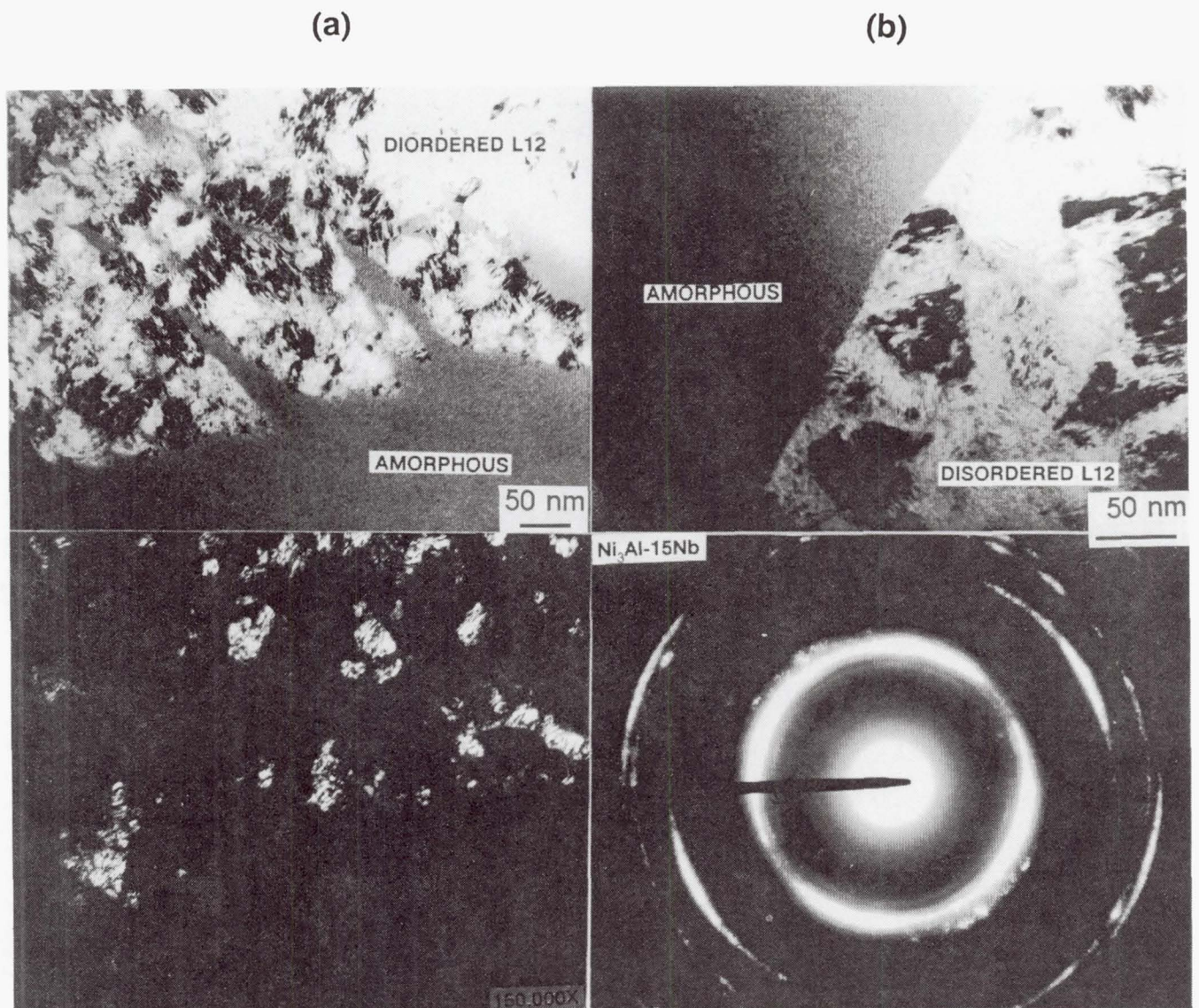
Figure 4.9. TEM micrographs and diffraction pattern of a Ni_3Al-15Nb alloy showing a) mixture of disordered L_{12} and an amorphous phase, and b) a linear L_{12}/amorphous boundary
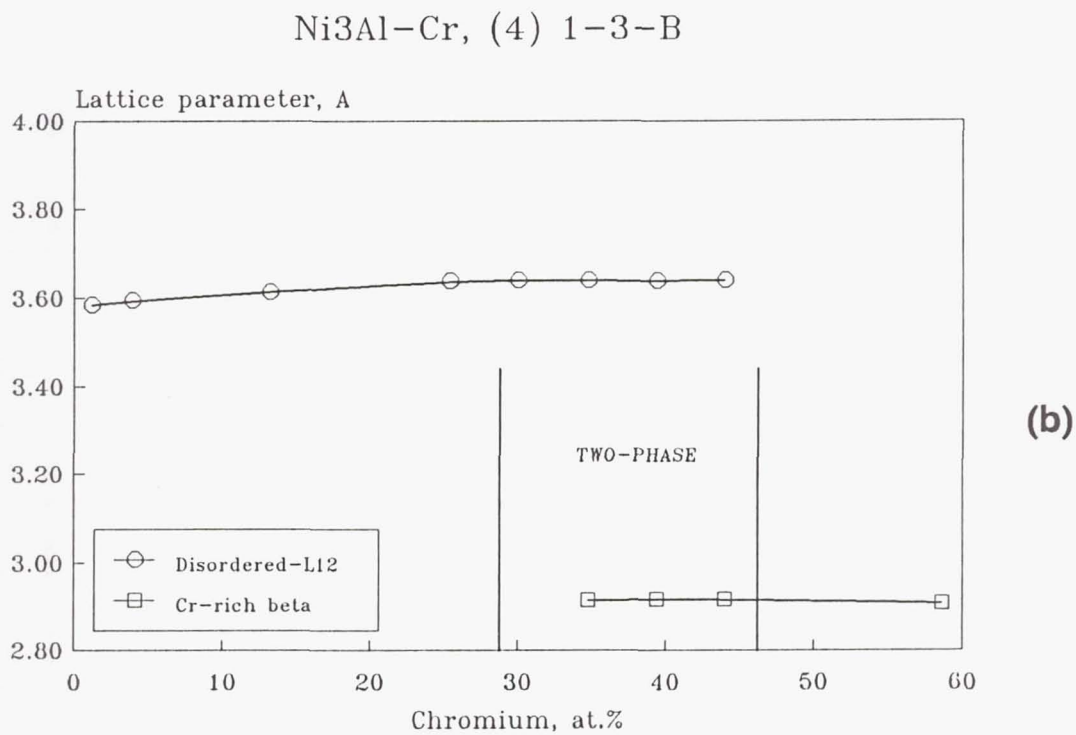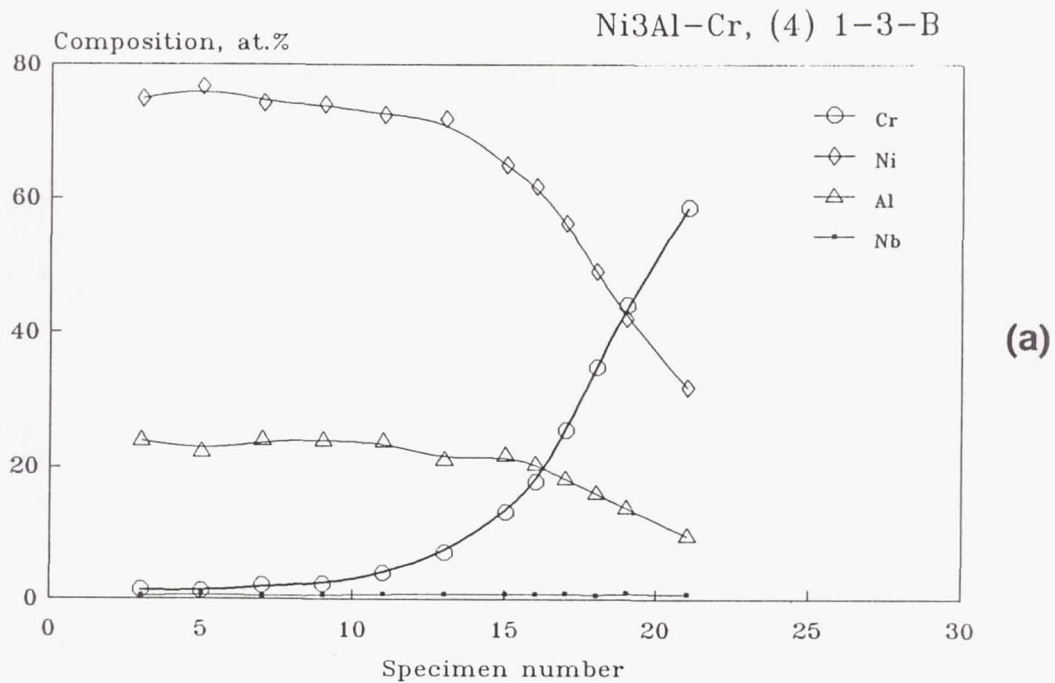
Figure 4.10. a) Composition analysis of nonequilibrium Ni₃Al-Cr alloys and b) lattice parameters and phase distribution as a function of Cr content.
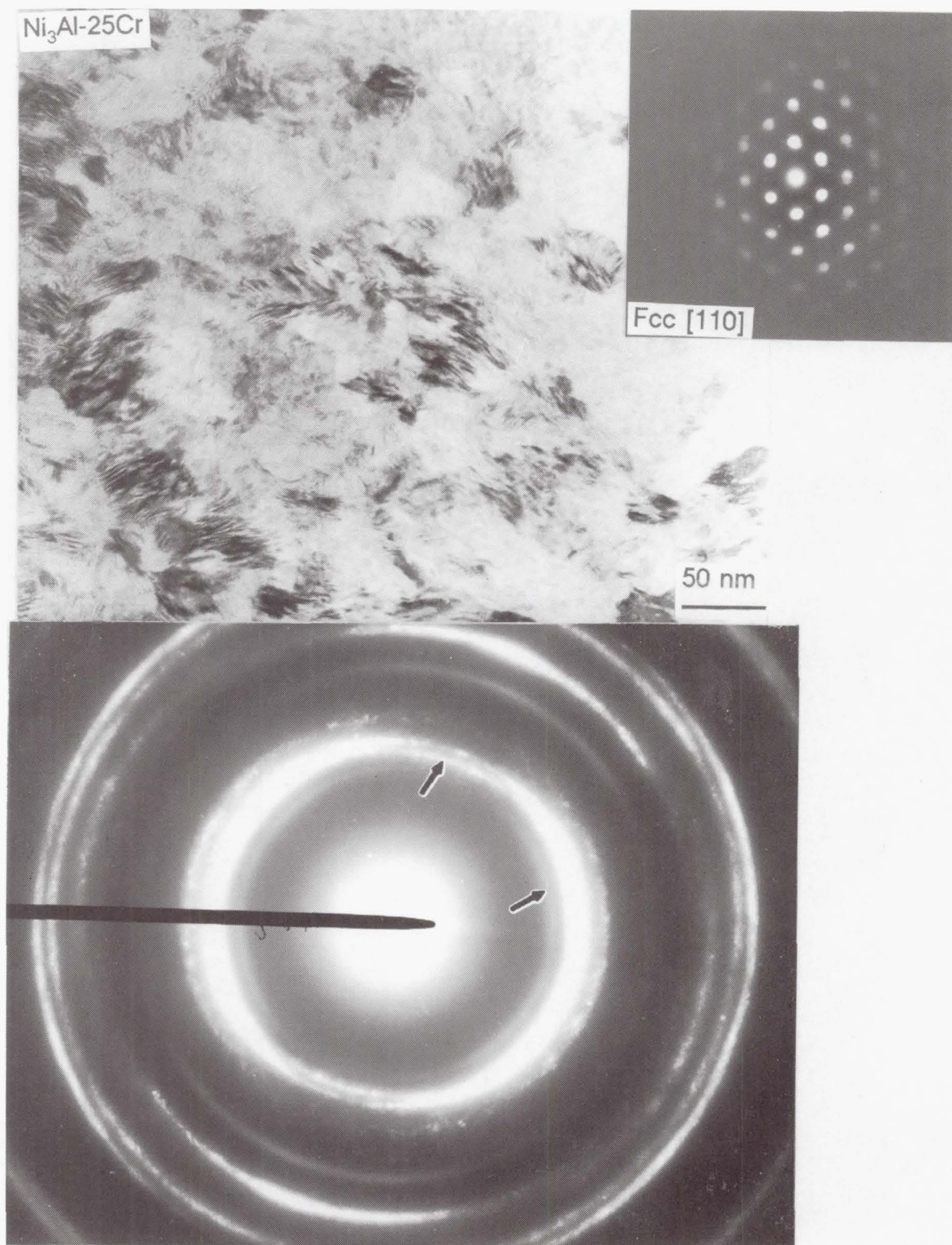
Figure 4.11. TEM micrographs and diffraction patterns of a Ni₃Al–25Cr alloy showing fine grained disordered L$_{12}$ phase.
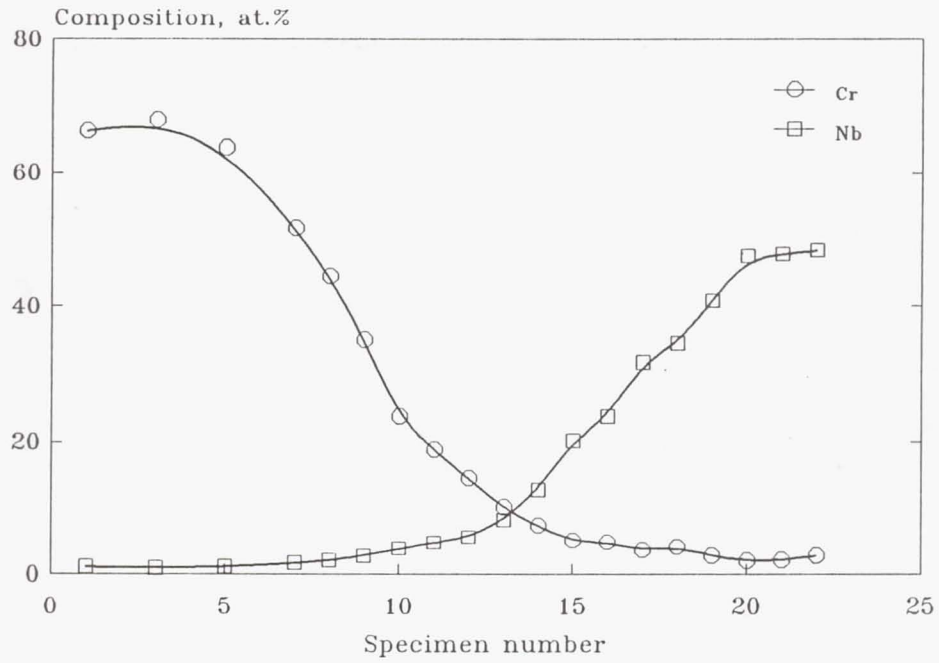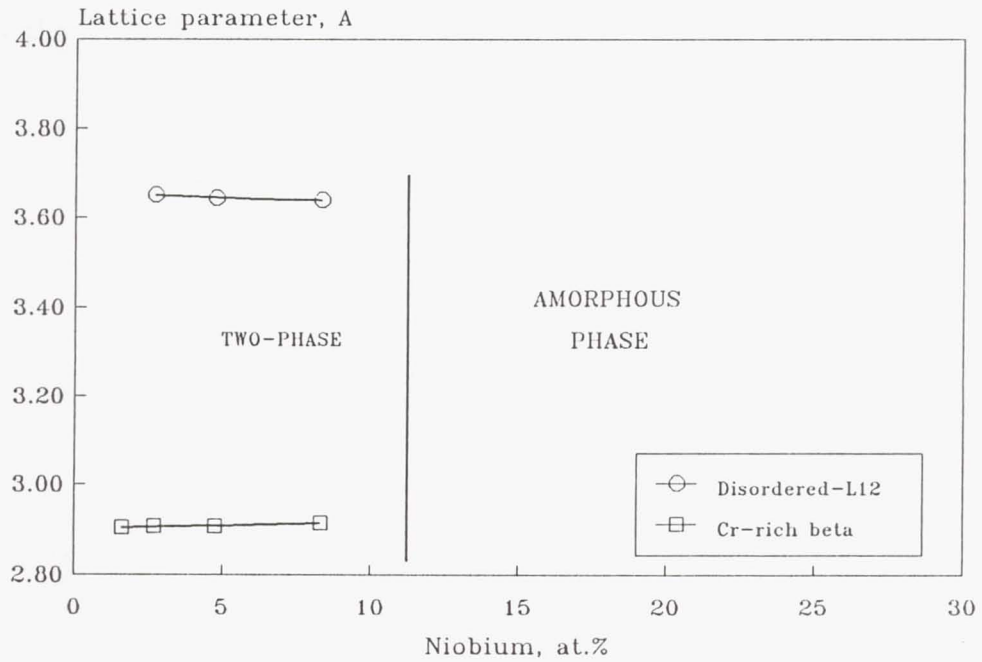
Ni3Al–(Nb,Cr) (4) 1–4–B

Figure 4.12.   a) Composition analysis of nonequilibrium Ni_3Al–(Nb,Cr) alloys and b) lattice parameters and phase distribution as a function of Nb content.

MICROHARDNESS OF SPUTTER DEPOSITED
Ni3Al−Nb, (4) 1−2−B ALLOYS

HVN, Kg/mm2

(a)

Avg. HVN−1 Kg
HVN1
HVN2
HVN3

Niobium, at.%
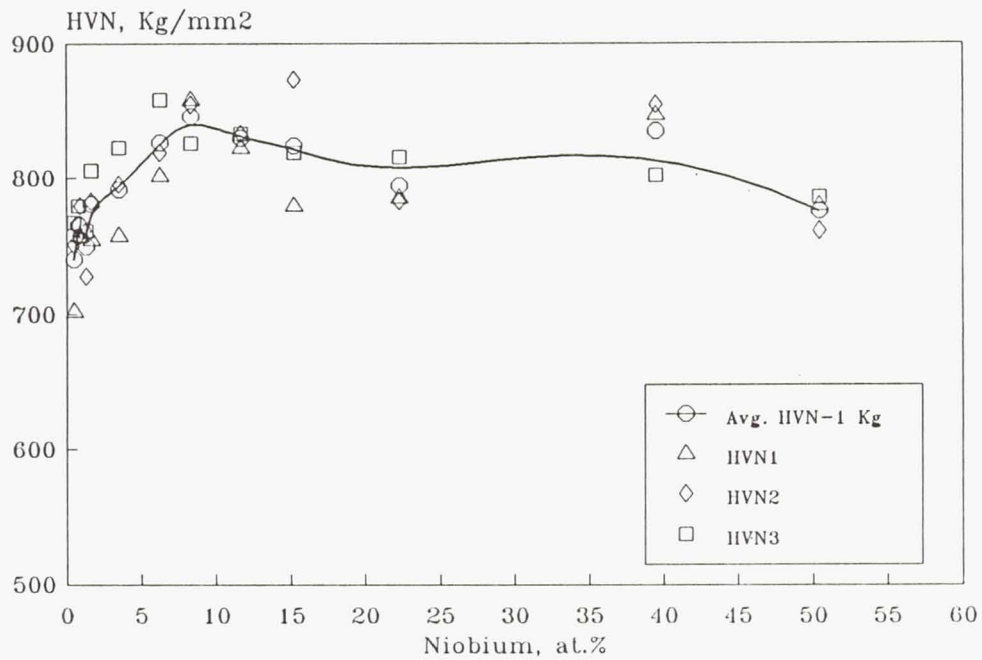
SPUTTER DEPOSITED Ni3Al−Cr, (4) 1−3−B

HVN, Kg/mm2

(b)

Avg HVN−1 Kg
HNV1
HVN2
HVN3

Chromium, at.%
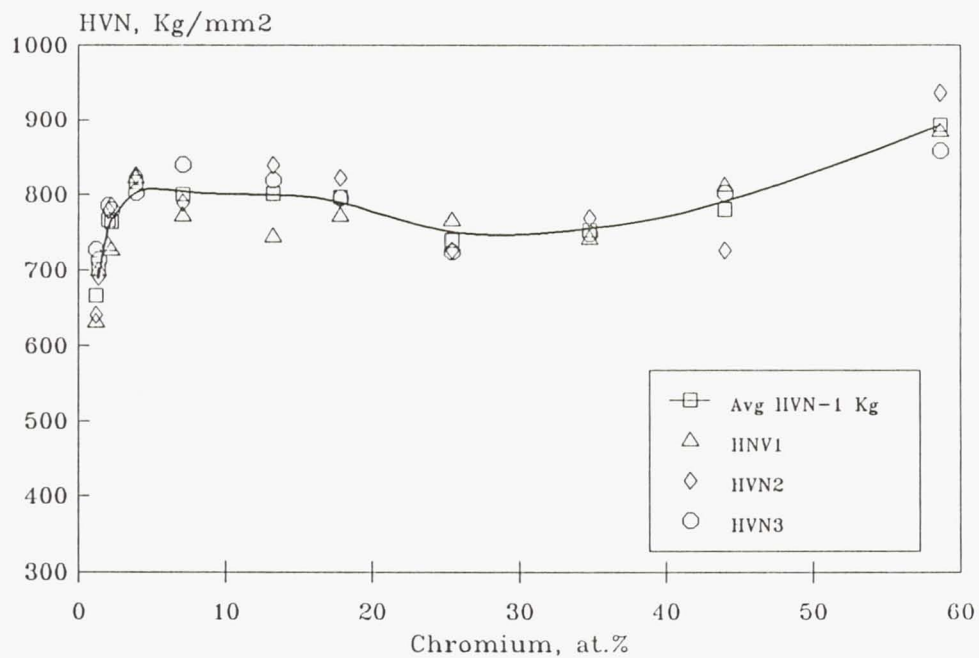
Figure 4.13. Microhardness of as-deposited a) Ni₃Al-Nb alloys; b) Ni₃Al-Cr alloys,

28

Ni3Al-(Nb,Cr) ALLOYS, (4) 1-4-B
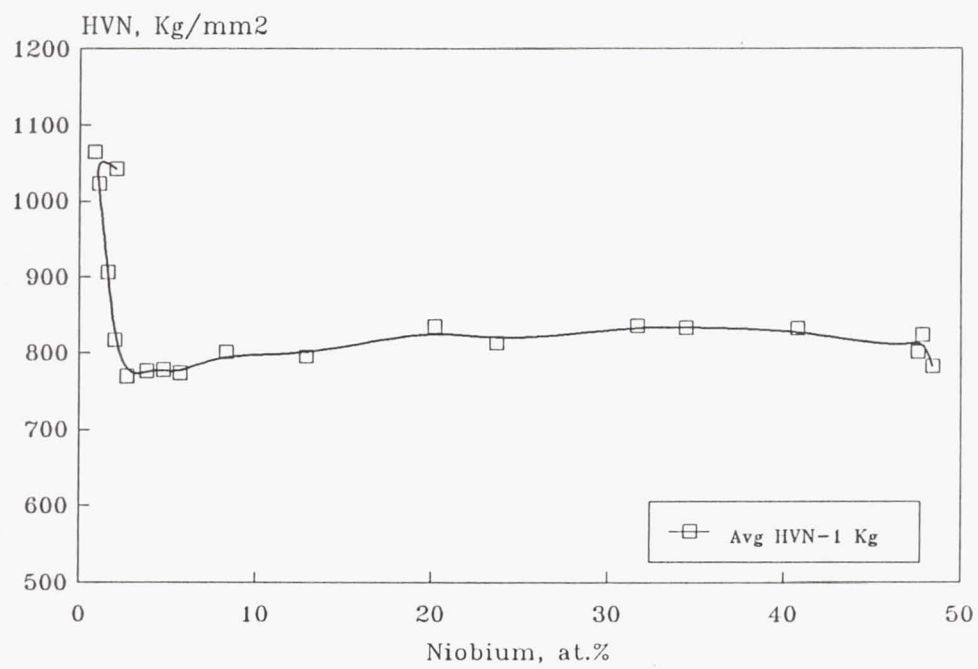
(c)

Figure 4.13. Microhardness of as-deposited , c) Ni$_3$Al-(Nb,Cr) alloys.

5. NONEQUILIBRIUM Ti-6Al-4V BASED ALLOYS

5a. Microstructure of (Ti-6Al-4V)-B Alloys

The presence of boron in sputter-deposited nonequilibrium (Ti-6Al-4V)-B alloys has resulted in grain refinement of low B content alloys, extended solid solubility in alpha Ti to near 10 at.% B, and amorphous phase formation in high B content alloys [3]. Sputter deposited alloys containing approximately 10 at.% B were investigated for the stability of microstructure and formation of TiB dispersoids. The size and distribution of the TiB dispersoids are important for structural stability and mechanical properties.

The as-deposited (Ti-6Al-4V)-B alloys had very fine grains containing a high density of defects, Figure 5.1. Heat treatment was done in vacuum at 900°C for 4 hours. After the heat treatments, specimens were quenched into water to retain the high temperature microstructure. Ion-milling was used to obtain adequate thin sections for TEM examination.

Initially, two TEM specimens, (2)-13 and (2)-16, containing nearly 8 and 3 at.% B, respectively, were prepared. The annealed microstructures, Figure 5.2, consisted of primary alpha (1-2 μm) and transformed beta grains (0.1-0.5 μm). Large needle-like dispersoids (35 x 5 nm) were found in alpha grains and outside transformed beta grains. In addition to the needle-like dispersoids, fine dispersoids (20-30 nm) were observed in primary alpha grains ((2)-13) and formed in a "cellular" fashion, i.e., along prior cell/grain boundaries. The dispersoids in the transformed beta grains are larger (30-40 nm) probably due to the high coarsening rates associated with the transformation of the beta phase. EDS data taken from one of the larger dispersoids indicated the presence of yttrium. According to the square diffraction patterns with d_1=5.2 Å and d_2=d_3=4.2 Å, larger dispersoids have a consistent match with Y_2O_3 (cubic-Ia3, a=10.6 Å), i.e., the two poles are [001] and [012] of the cubic lattice. The Y dispersoids detected in (Ti-6Al-4V)-B alloys were due to co-sputtering the Y subtarget with the B subtarget.

In order to investigate effects of B without interference of the Y dispersoids, a new Ti-6Al-4V deposit incorporating B and TiB_2 was prepared. The resultant deposit contained a high concentration of B and TiB_2 in the center with a smooth surface texture, as shown in Figure 5.3. X-ray diffraction indicated that this was a region of amorphous alloys. Crystalline alloys were formed outside the amorphous region. Two specimens, containing approximately 5 at.% B, were extracted: one each from crystalline regions formed by boron and TiB_2 additions. The specimens were annealed at 900°C for 4 hours before TEM examination.

Microstructures of the two specimens were similar, containing relatively large grains (2-4 μm) and smaller grains (0.1 μm). The microstructure is consistent with the hexagonal alpha phase. The titanium boride dispersoids were formed in thin laths approximately 0.5-1.0 μm long and 0.1 μm wide, Figure 5.4a. Both large and small grain regions contained similar distribution and size of laths, Figure 5.4b. A selected area diffraction pattern (SADP) taken from one of the laths showed the d spacing as d_1=6.0 Å and d_2=4.6 Å. These do not correspond to TiB_2, rather they appeared to be consistent with TiB or Ti_2B phase.

The formation of the titanium boride phase in thin lath forms indicated that excess boron addition would result in second phase segregation from fine Ti-6Al-4V grains. Excess boron, over 10 at.% B, also contributed to embrittlement of the Ti-6Al-4V matrix alloy. It is possible that beneficial addition of B in Ti alloys should be limited to the microalloying range.

5b. New Nonequilibrium Ti-6Al-4V Alloys Containing Nb and B

Nonequilibrium Ti-6Al-4V alloys containing a new additive, Nb, and Nb+B, were prepared. The resultant deposit had a thickness of 13 mils and was designated as deposit (3), shown in Figure 5.5. The boron-rich region of the deposit was shattered after the plasma was switched off at the end of the sputtering run. Evidently, the boron-rich alloys were brittle in comparison with the Nb-rich and Ti-6Al-4V alloys. Twenty five specimens of (Ti-6Al-4V)-Nb, about 4 mm x 5 mm x 0.1 mm thick each, were extracted from the deposit. Twelve specimens of Ti-6Al-4V-(Nb,B) were also extracted.

Nonequilibrium (Ti-6Al-4V)-Nb alloys were obtained between 1 and 60 at.% Nb, Figure 5.6. At low Nb concentration, fine grain and textured hexagonal alpha was obtained, as shown by x-ray diffraction. Increasing Nb concentration first led to a rapid increase of lattice parameter in the region of 3 to 9 at.% Nb, followed by a phase transition from the alpha to a Nb-stabilized beta at 10-15 at.% Nb, Figure 5.6. The phase fields and stability of as-deposited alpha and beta would be closely related to the binary Ti-Nb alloys.

Nonequilibrium Ti-6Al-4V-(Nb,B) alloys were formed between 5 and 55 at.% Nb, Figure 5.7. The concentration of B in these alloys was not analyzed, but would be similar to the B content in (Ti-6Al-4V)-B ranging from 5 to 40 at.% B. Alloy structures were identified as the beta phase by x-ray diffraction. At low Nb concentration, below 10 at.% Nb, fine grain and textured beta phase had a lattice parameter near 3.3 Å, Figure 5.7. Increasing Nb content resulted in a slight reduction of the lattice parameter to approximately 3.28 Å.

5b.1. Microstructures

A nonequilibrium (Ti-6Al-4V)-17.5Nb alloy was characterized for phase distribution and extended solid solubilities. As shown in Figure 5.8 the as-deposited microstructure consisted of grain sizes ranging from 25-100 nm, with an average of 60 nm. Electron diffraction showed the alloy to be nearly 60% alpha phase, with the balance beta phase. Quantitative analysis of the extended solubility for the alpha phase resulted in 71-74 at.% Ti, 10-11 at.% Al, 2-3 at.% V and 12-15 at.% Nb, comparing to a mere 2 at.% Nb solubility in equilibrium alpha-Ti. The beta phase with a composition of 62-64 at.% Ti, 7-8 at.% Al, 2-3 at.% V and 24-26 at.% Nb indicated a wide alpha/beta two-phase field between 15 and 24 at.% Nb. The data obtained from microstructural analyses were consistent with the phase analyses by x-ray diffraction.

5b.2. Mechanical behavior

Room temperature microhardness was measured on 600 grit polished as-deposited alloys using a diamond pyramid indentor along the specimen strip with increasing Nb content, Figure 5.9. An independent room temperature microhardness measurement was conducted by Prof. R. Lin at University of Cincinnati to verify the in-house measured hardness data. Both measurements confirmed that Nb addition to nonequilibrium Ti-6Al-4V alloys rapidly reduced the microhardness from an initial 580 Kg/mm^2 to near 400 Kg/mm^2 when a 10 at.% Nb concentration was reached.

The microhardness in Ti-6Al-4V-(Nb,B) alloys was initially high, close to 700 Kg/mm^2, due to the presence of a large quantity of boron in alloys containing 3 at.% Nb. The high hardness values of boron-rich alloys should explain the shattering of the boron-rich region during cooling of the deposit. Further addition of Nb (with a decrease of B accordingly) rapidly reduced the microhardness value to nearly 450 Kg/mm^2 approaching 8 at.% Nb. Alloys containing more than 10 at.% Nb up to 50 at.% Nb exhibited microhardness values between 450 and 500 Kg/mm^2. At this composition range, the microhardness was comparable with the (Ti-6Al-4V)-Nb alloys, independent of the boron content, which was probably below 5 at.% in the high Nb alloys.
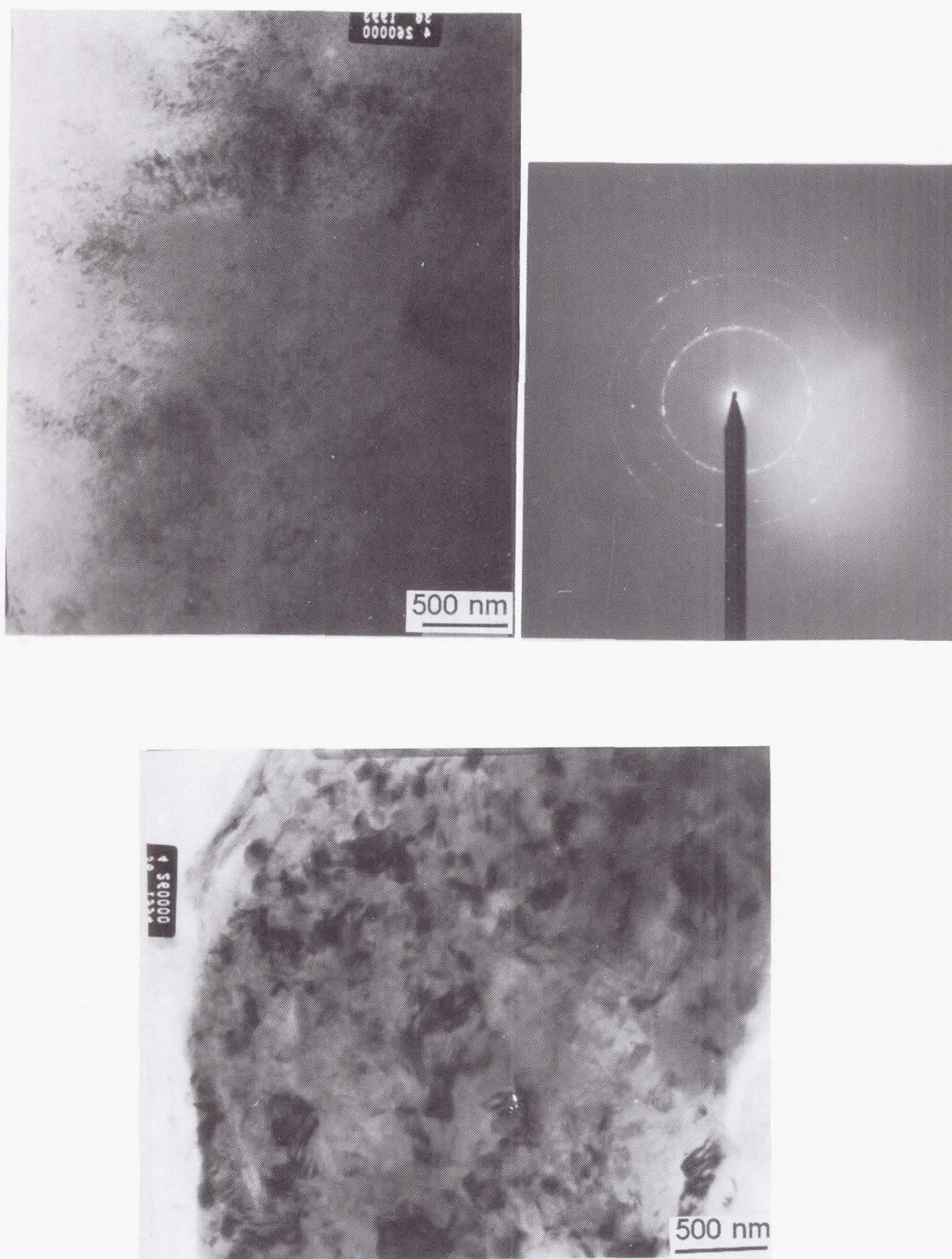
Figure 5.1. Typical TEM micrograph of as-deposited Ti-6Al-4V-B alloys containing fine grained alpha structure and high density of defects.

(a)

500 nm

(b)

100 nm
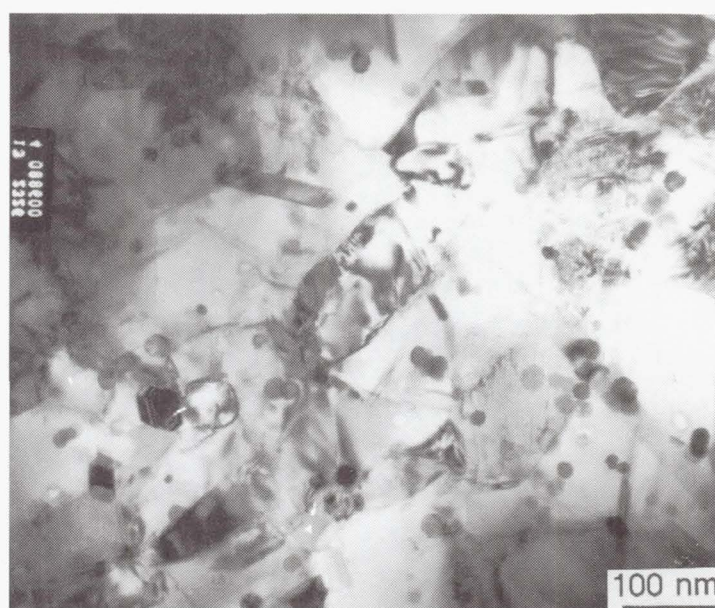
Figure 5.2. Typical TEM micrograph of 900°C/4h annealed Ti-6Al-4V-xB alloys, a) specimen (2)-16, with 3 at.%B, and b) specimen (2)-13, with 8 at.%B, containing fine grained alpha structure.
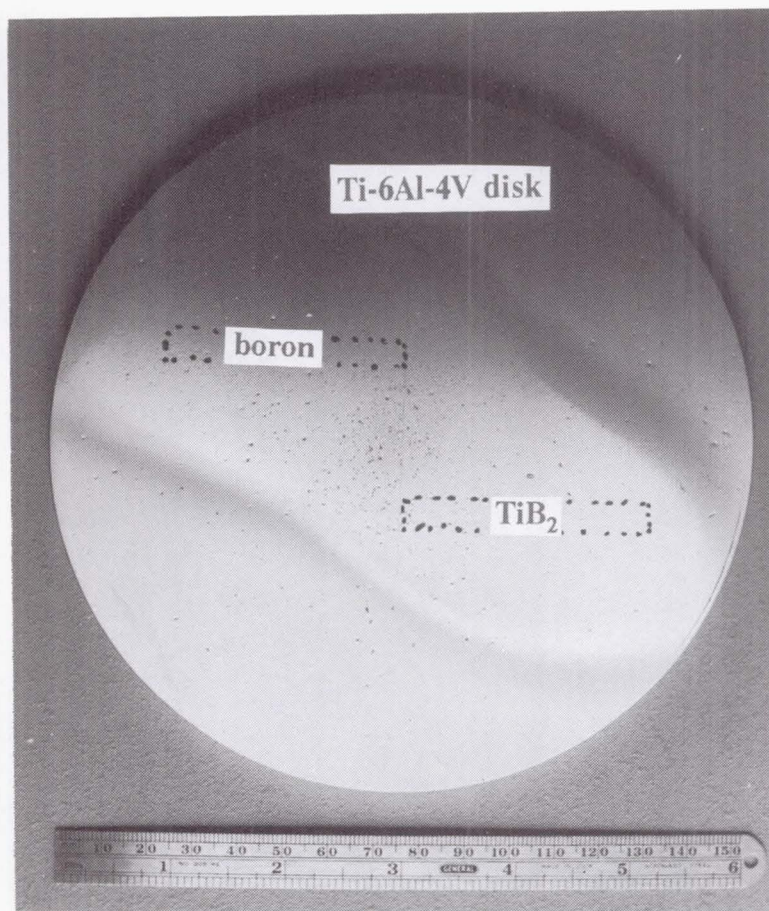
Figure 5.3. A sputter-deposited Ti-6Al-4V disk containing boron and TiB_2 additives.
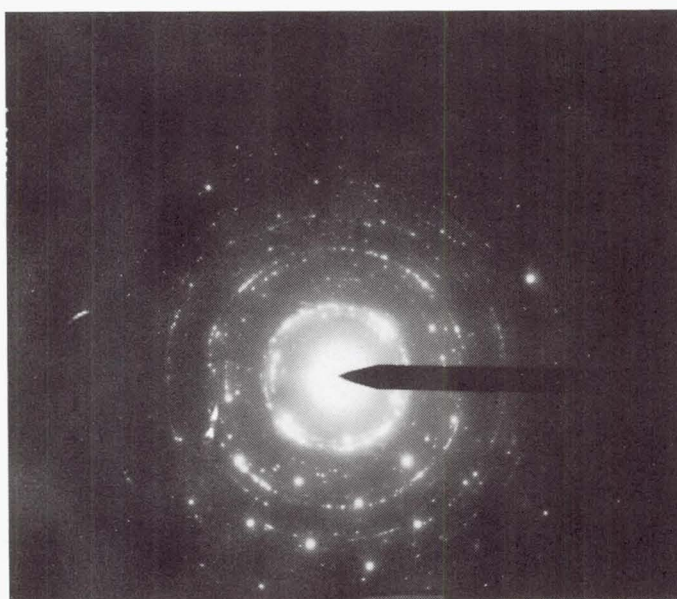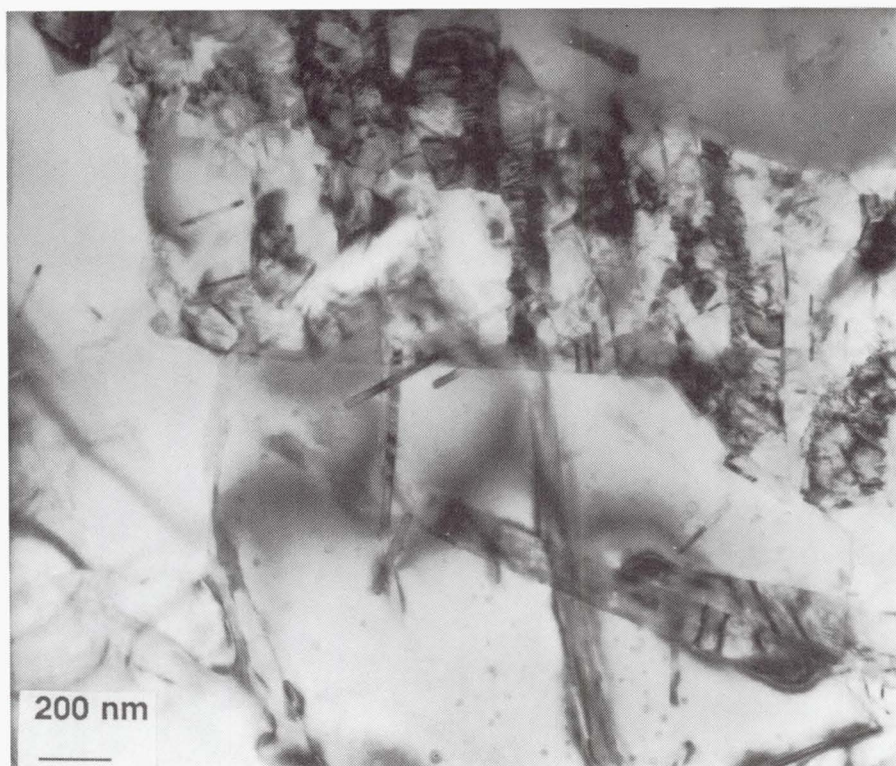
Figure 5.4a. TEM micrograph and diffraction pattern of an annealed (900°C/4h) Ti-6Al-4V-5B alloy showing relatively large (2-4 μm) grains and smaller polycrystalline grains (0.1 μm). Note the presence of very thin laths of TiB/Ti₂B in both larger grains and polycrystalline region.
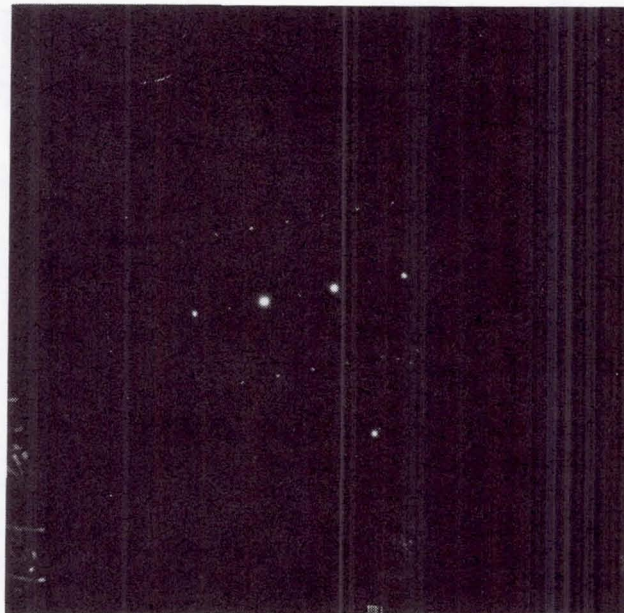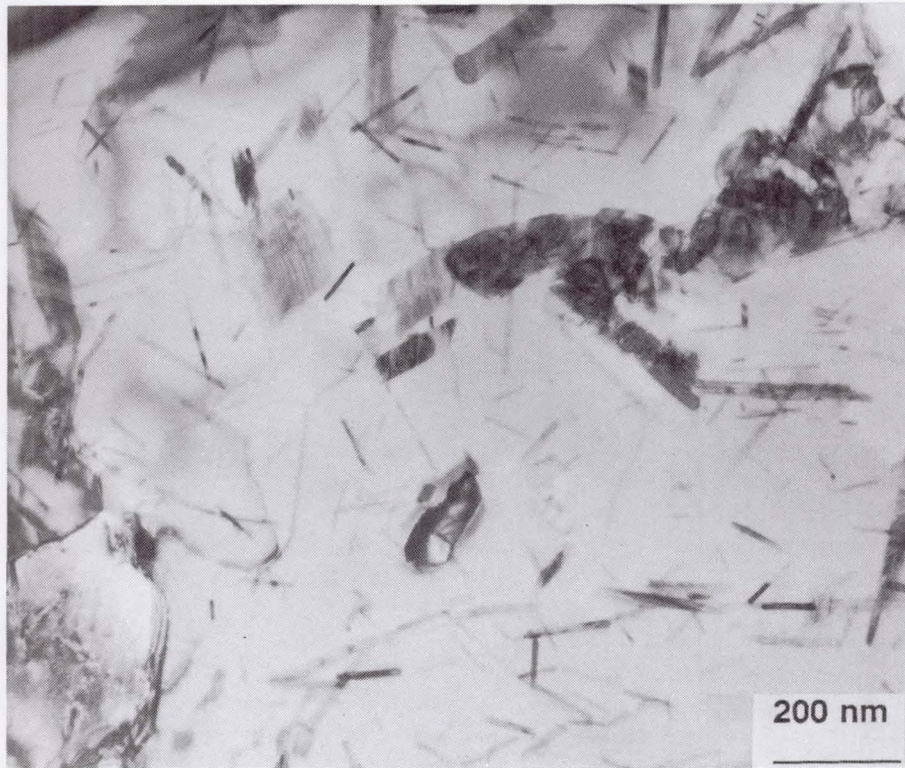
Figure 5.4b. TEM micrograph and diffraction pattern of an annealed (900°C/4h) Ti-6Al-4V-5B alloy showing the size and the faulted nature of the TiB/Ti$_2$B laths. The diffraction pattern showed either TiB or Ti$_2$B phase.
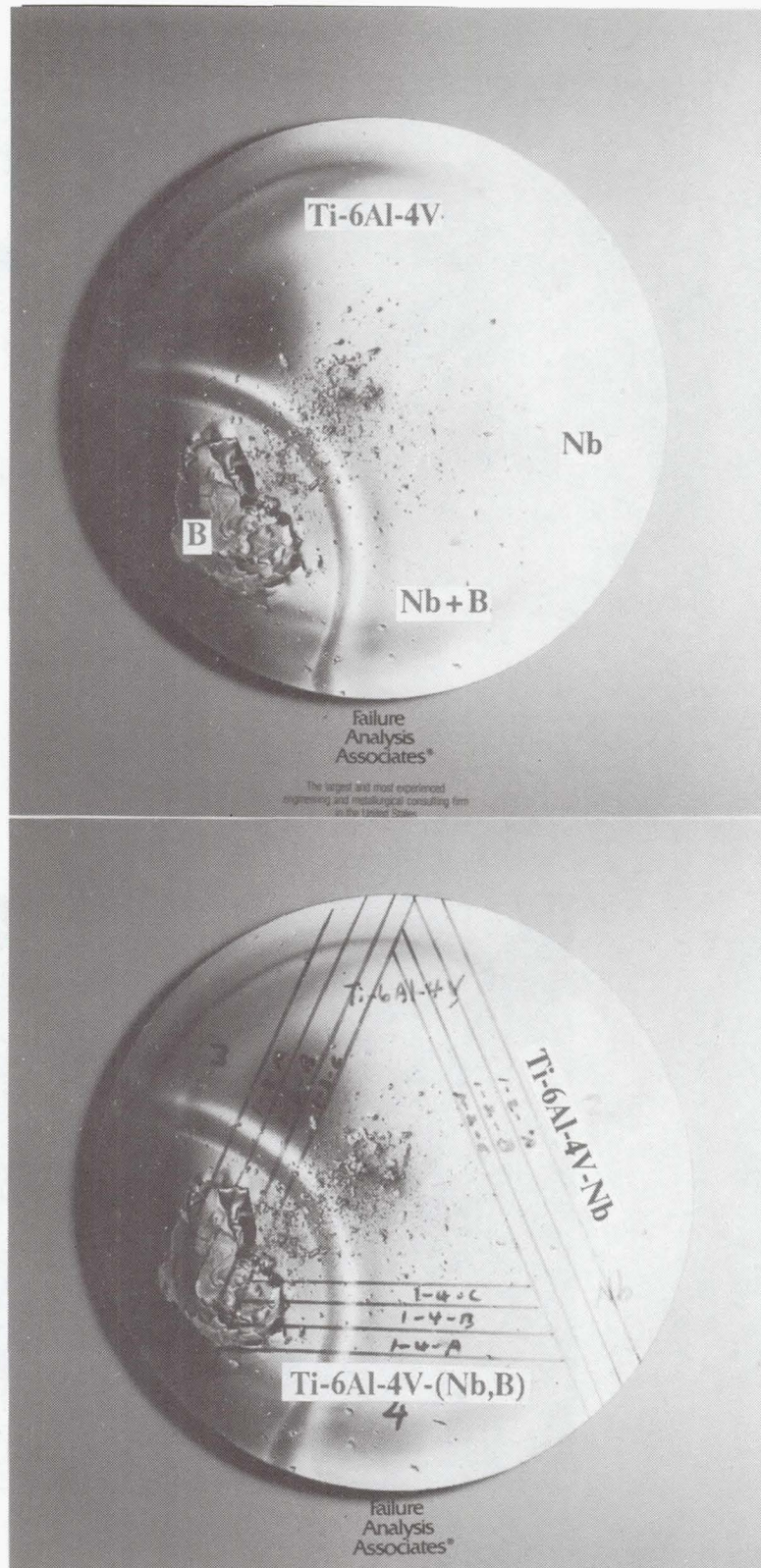
Figure 5.5. A single Ti-6Al-4V deposit containing three series of nonequilibrium alloys graded with Nb, B and Nb+B.

(Ti−6Al−4V)−Nb,(3) 1−2−C

Composition, at.%
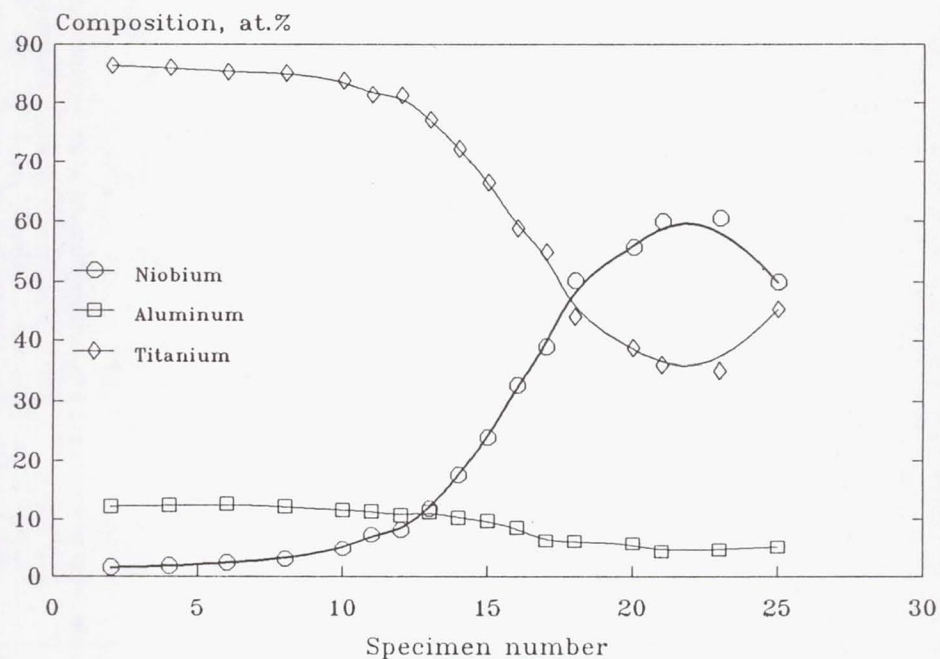
(a)

(Ti−6Al−4V)−Nb, (3) 1−2−C SPECIMENS

Lattice parameter, A
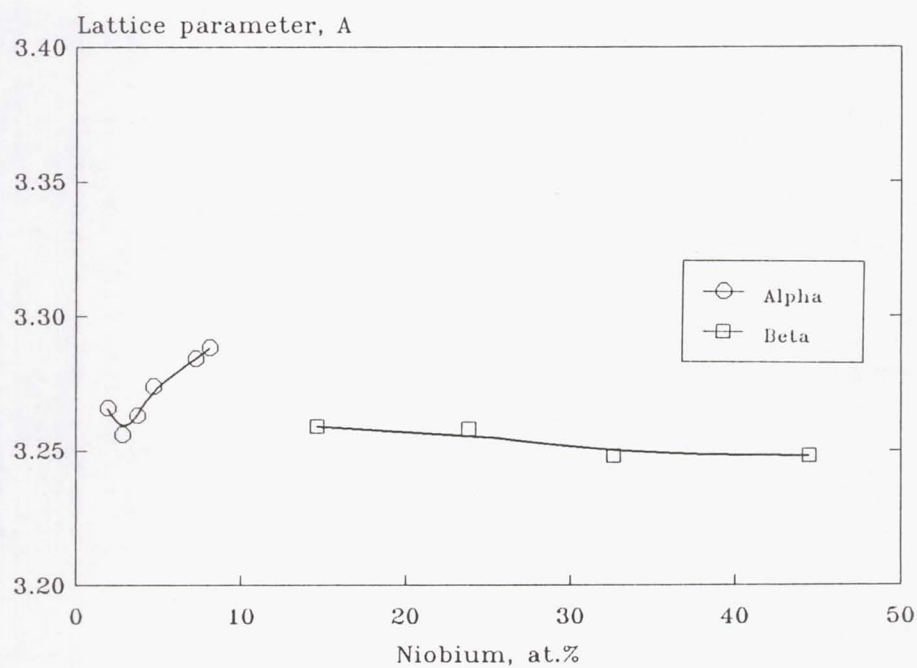
(b)

Figure 5.6. Nonequilibrium(Ti−6Al−4V)−Nb alloys showing a) Nb content in the specimens, and b) lattice parameter/phase distribution as a function of Nb content.

Ti-6Al-4V-(Nb,B), (3) 1-4-C
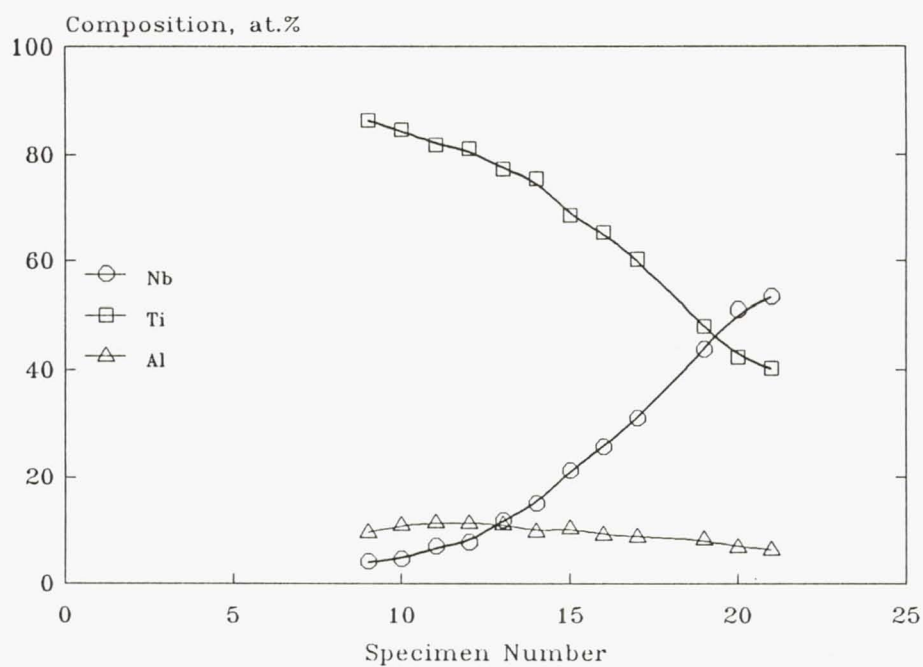
(a)

Ti-6Al-4V-(Nb,B), (3) 1-4-C
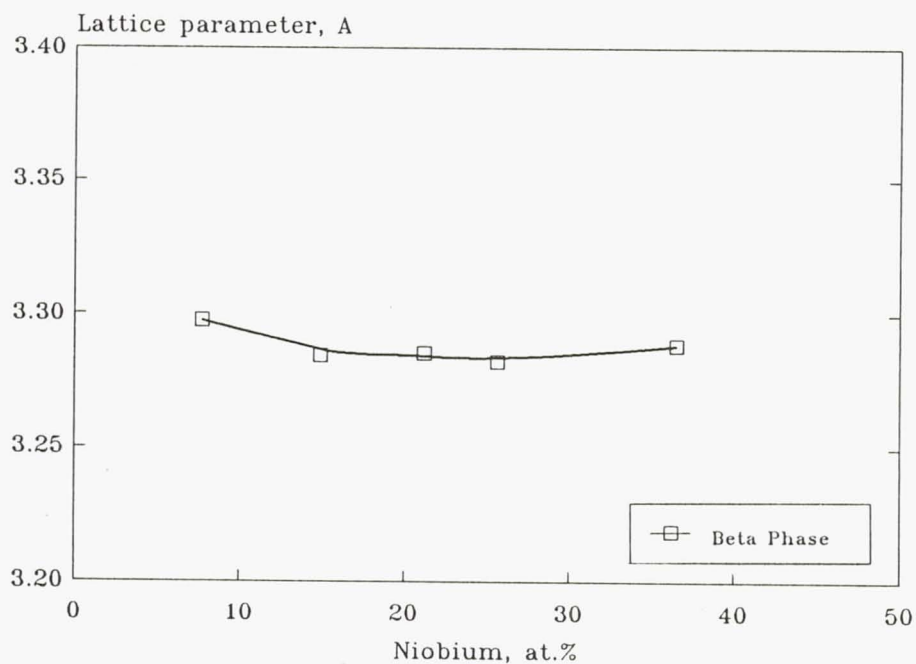
(b)

Figure 5.7. Nonequilibrium Ti-6Al-4V-(Nb,B) alloys showing a) Nb content in the specimens, and b) lattice parameter/phase distribution as a function of Nb content.
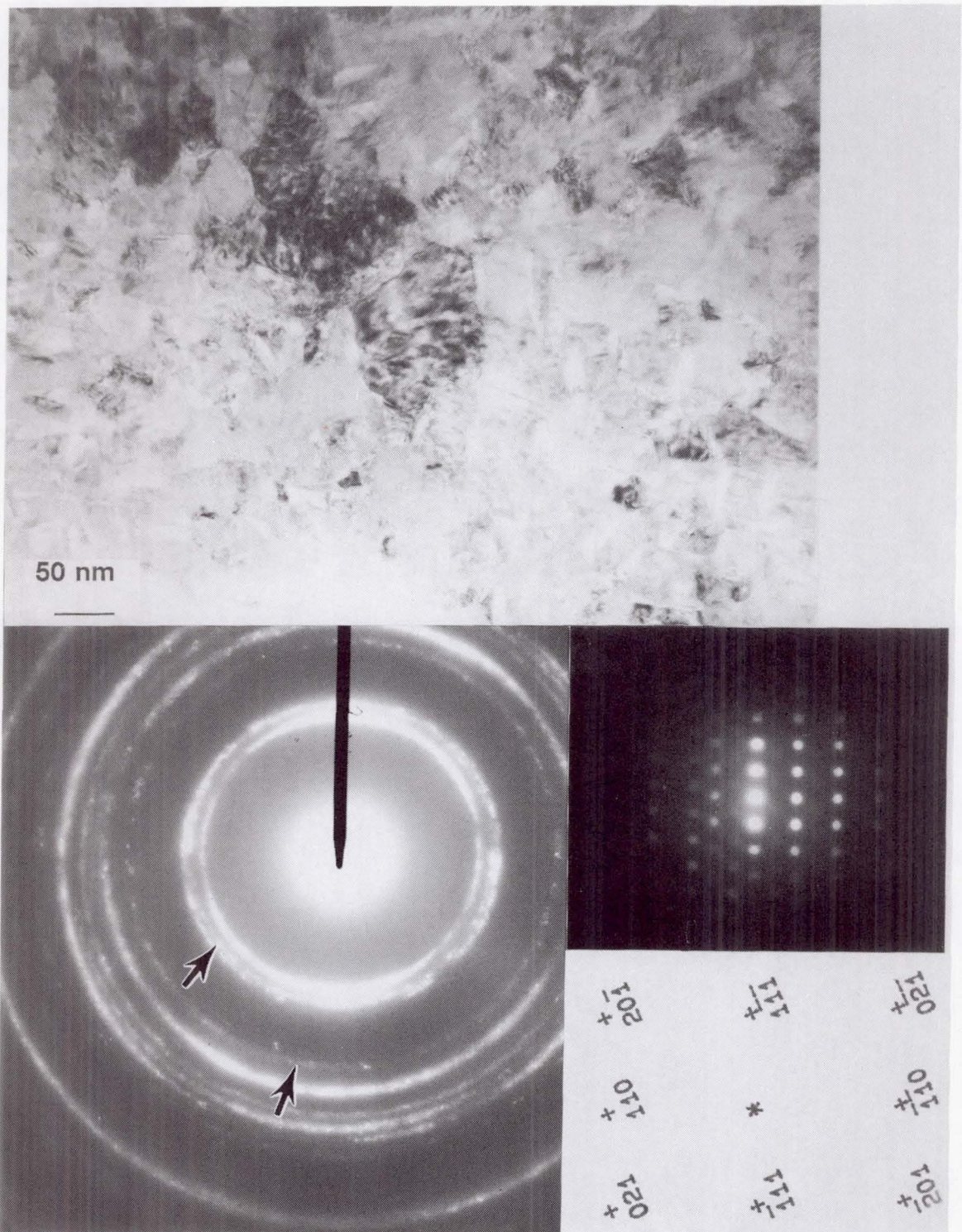
Figure 5.8. Typical TEM micrograph and diffraction patterns for a Ti-6Al-4V-17.5Nb alloy showing alpha grains of 25-100 nm. Arrows show the presence of small amount of beta.

(Ti−6Al−4V)−Nb, (3) 1−2−A

HVN, Kg/mm2

(a)

Legend:
- Avg HVN−500 g
- Avg HVN−1 Kg
- 1−2−C, 1 Kg

Niobium, at.%

Ti−6Al−4V−(Nb,Cr) (3) 1−4−0

HVN, Kg/mm2

(b)

Legend:
- Avg HVN−1 Kg
- HNV1
- HVN2
- HVN3

Niobium, at.%
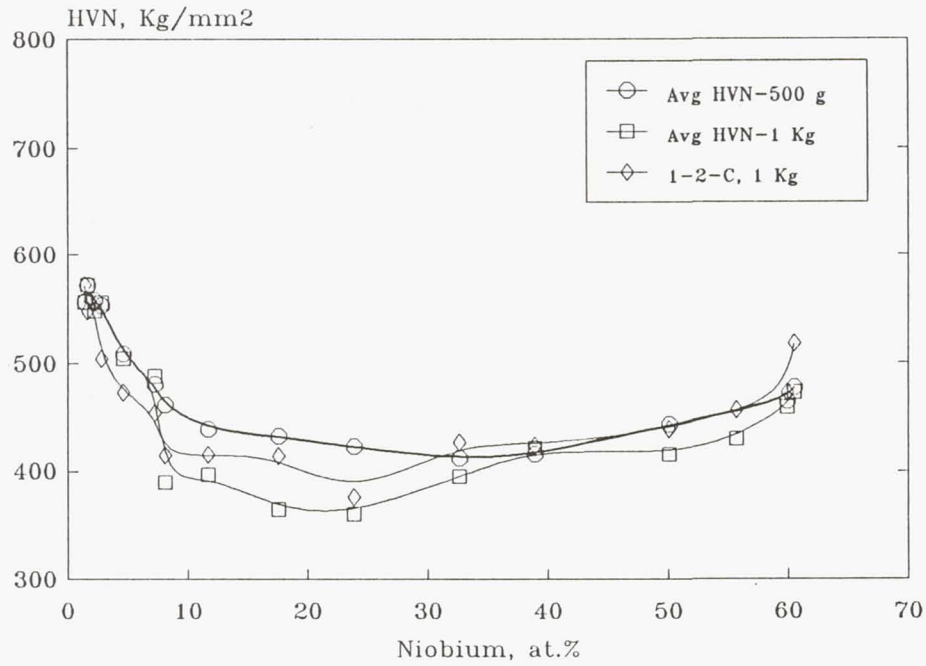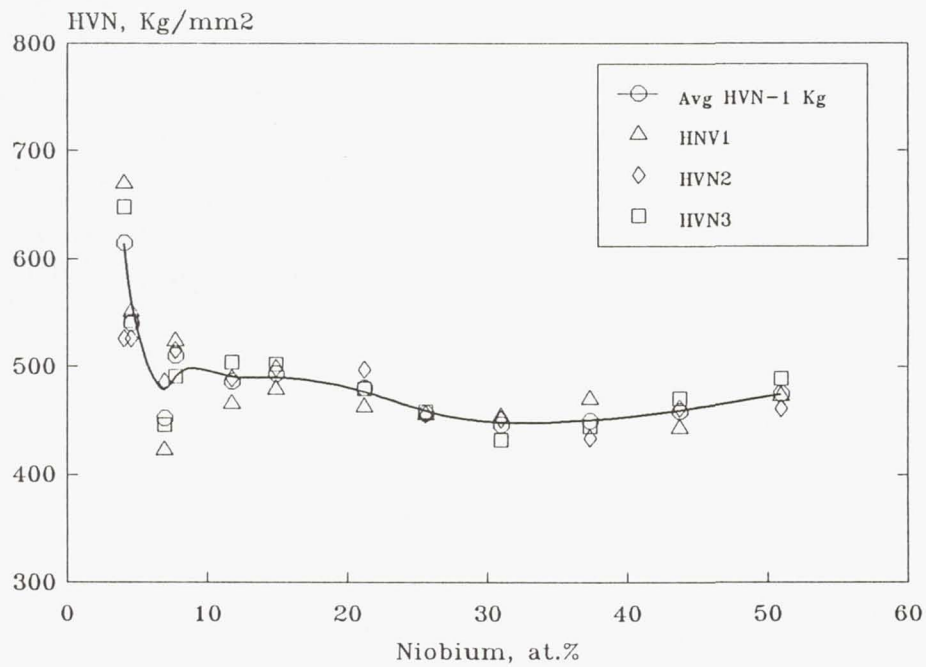
Figure 5.9. Microhardness of as-deposited a (Ti-6Al-4V)-Nb alloys;
b) Ti-6Al-4V-(Nb,B) alloys as a function of Nb content.

42

6.   NONEQUILIBRIUM Ti$_3$Al BASED ALLOYS

6a.   Alloy Phase and Microstructure

The nonequilibrium alloys formed by co-sputtering Ti$_3$Al, Cr and Nb were extensively investigated. The initial sputter deposited alloy disk, designated Deposit (5), is shown in Figure 6.1 consisted of four regions: Ti$_3$Al solid solutions, Ti$_3$Al-Nb alloys formed between Ti$_3$Al and Nb-rich alloys, Ti$_3$Al-Cr alloys between Ti$_3$Al and Cr-rich alloys, and Ti$_3$Al-(Nb,Cr) alloys formed between the Nb- and Cr-rich alloys.

Nonequilibrium phases and microstructures of as-deposited alloys were investigated by x-ray diffraction, electron microprobe and analytical TEM in order to determine their phase distribution, grain size/orientation and phase chemistry. Due to high defect density and extremely fine grain size in all as-deposited alloys, clear convergent beam diffraction patterns could not be readily obtained to reveal the crystal symmetry of each phase. Diffraction analysis had to be restricted to the zero layer patterns for interpretation. In this case, it was necessary to analyze many patterns and EDS spectra in order to derive a positive phase identification. For example, the as-deposited alloys showed primarily 200-500 nm size disordered beta and ultrafine grained alpha2 (10-50 nm). Amorphous phase was confirmed by both x-ray and TEM analyses as formed only in Ti$_3$Al-Cr alloys. Nonequilibrium phase distribution, microstructure and alloy chemistry data are summarized in Table 6.1.

6a.1. Ti$_3$Al

The as-deposited Ti$_3$Al alloy had a very fine microstructure with grain sizes on the order of 10-50 nm, Figure 6.2. The microstructure was highly disordered, containing numerous dislocations and stacking faults typical of sputter deposited intermetallic compounds. Bright field micrographs and diffraction patterns did not reveal presence of a second phase and/or dispersoids. Several electron diffraction patterns further confirmed the single alpha2 structure with some (0002) textured orientation.

Table 6.1: STEM CBED and elemental analysis studies of alloy phase, grain size and chemistry of sputter deposited Ti_3Al containing Nb, Cr and Nb+Cr.

Sputtered Alloy	Phase Vol%	Size (nm)	Composition (at.%)			
			Ti	Al	Cr	Nb
Ti_3Al	Alpha2	10-50				
Ti_3Al-7.5Nb	Alpha2	50	61-63	26-28	0	10-12
	Beta 5%	250	57	25	0	18
Ti_3Al-12Nb	Alpha2	30				
	Beta 35%	200				
Ti_3Al-21Nb	Alpha2	20				
	Beta 95%	500				
Ti_3Al-21Nb-11Cr	Alpha2	50	48	23	11	18
	Beta 80%	250	43-44	19-20	14-15	21-23
Ti_3Al-30Cr	Beta	65	45-51	24-26	21-29	1-2
	Amo.70%	30-37	30-37	16-20	45-51	1·2

6a.2. Ti_3Al-Nb Alloys

The sputter deposited nonequilibrium Ti_3Al-Nb system was formed between 1 and 64 at.% Nb (Figure 6.3a). At low Nb concentration, the as-deposited Ti_3Al had a textured microstructure which consisted primarily of the hexagonal alpha2 phase. Directly formed ultrafine alpha2 phase in sputter-deposited nonequilibrium Ti_3Al-Nb alloys has significance when comparison is made with grain sizes obtained from other processes, including liquid quenched alloys of similar compositions. Ultrafine alpha2 microstructure was not obtainable by rapid quenching from the melt, since either large alpha2 grains resulted for Ti_3Al without Nb addition, or beta phase resulted with as little as 5% Nb addition [5].

Increasing Nb concentration first led to a rapid increase of lattice parameter, followed by a transition from the alpha2 phase to a Nb-stabilized beta phase at near 12-15 at.% Nb (Figure 6.3b). However, all the as-deposited alloys were highly textured, with (0002) and (110) textures for alpha2 and beta, respectively. The textures were related to the columnar nature typical of sputter-

deposited materials formed onto a room temperature substrate. In this case, phase stability of the as-deposited nonequilibrium Ti_3Al-Nb alloys would be similar to the nonequilibrium (Ti-6Al-4V)-Nb alloys, containing an alpha to beta transition with addition of Nb.

Three as-deposited Ti_3Al-Nb alloys, consisting of 7.5Nb ((5)1-2-B14), 12Nb ((5)-1-2-C13) and 21Nb ((5)1-2-C11), were examined by TEM. The Ti_3Al-7.5Nb alloy showed a mixture of two structures, a course structure region consisted of grains about 100-250 nm and a fine grained region of 50 nm grains, Figure 6.4. Microdiffraction and elemental analysis of the course grains indicated that they had alpha2 structure with compositions in the range of 61-63Ti, 26-28Al and 10-12Nb. The fine grain region consisted of a mixture of alpha2 and beta with similar chemistry to the course grain regions. The beta phase had a chemistry of 52Ti, 40Al and 8Nb. A comparison of the elemental analysis of alpha2 and beta phases is shown in Figure 6.5. The high Nb content associated with the beta phase will be discussed in following sections.

The microstructures of Ti_3Al-12Nb and -21Nb alloys were similar in general, Figures 6.6 and 6.7. Both alloys had a non-uniform fine grained (30-200 nm) structure representing the presence of both alpha2 and beta phases, Figure 6.6. The smaller grains were the alpha2 phase. The larger grains were beta phase with electron diffraction patterns very close to the expected beta reflections for randomly oriented grains (i.e.(110), (200), (112), (220) and (013) were all present). The beta phase had a lattice parameter of a=3.25(0.05) Å. This is similar to the lattice parameter for the beta phase observed in rapidly quenched $(TiNb)_3Al$ alloys reported by Kaufman et al [6]. The microstructure of Ti_3Al-21Nb alloy consisted of larger beta grains and only a few small alpha2 gains, Figure 6.7. Based on the grain size distribution, a comparison of grain sizes of sputter deposited Ti_3Al-Nb alloys with similar alloys processed by other processing methods is given in Figure 6.8.

6a.3. Ti_3Al-Cr Alloy

The Ti_3Al-Cr system was deposited with Cr concentration between 1 and 73 at.% Cr, Figure 6.9a. X-ray diffraction and lattice parameter studies indicated that Cr addition to the alpha2 structure resulted in an extended solid solution to nearly 30 at.% Cr with an alpha-to-beta transition at near 8-10 at.% Cr. An amorphous phase was found over a narrow range of composition of 30-45 at.% Cr (Figure 6.9b). Based on the Ti-Cr binary phase diagram, the formation of the amorphous phase would relate to presence of the intermetallic Ti_2Cr phase, with three allotropes as alpha, beta, and gamma phase. With complex crystal structure and allotropic phases of the Ti_2Cr, stability of the amorphous phase

has been increased in contrast to simple structures such as B2 and alpha2 [7]. For the same reason, amorphous phase would not be expected in Ti_3Al-Nb alloys since Ti and Nb form mutual solid solutions without the presence of any intermetallic phase. Alloys containing more than 45 at.% Cr formed Cr-rich beta solid solution.

The boundary of a possible amorphous phase in the Ti_3Al-Cr system was investigated with TEM. A specimen ((5)1-4-B18) containing - 30Cr was selected since it would consist of a mixture of beta and amorphous phase, as shown in Figure 6.9. The microstructure consisted of a mixture of crystalline and amorphous phases, Figure 6.10. The crystalline phase had fine and uniform grains averaging nearly 65 nm. The grains contained numerous defects which reflected in poor symmetry in the diffraction patterns. However, studying several electron diffraction patterns obtained from individual grains showed that they have a disordered beta structure since no ordered reflections were found. Elemental analysis of the beta phase grains exhibited a wide range of composition, 38-43Ti, 35-39Al, 16-23Cr and 0-1Nb. This composition indicated that the beta phase boundary would be approximately 25-30 Cr which is consistent with the x-ray lattice parameter data.

The amorphous phase in specimen (5)1-4-B18 was found to be dominant, estimated as approximately 70 vol.%. The crystalline/amorphous interfaces were mostly planar. In a few instances, the amorphous region had grown into the crystalline region. Inclusion of the amorphous phase within the crystalline regions was also observed. The elemental analysis defined a phase boundary for the amorphous region as 30-37Ti, 16-20Al, 45-51Cr, and 1-2Nb, which was also consistent with the x-ray diffraction data.

6a.4. Ti_3Al-(Nb,Cr) Alloy

The nonequilibrium Ti_3Al-(Nb,Cr) alloys were investigated to compare with Ti_3Al-Nb, and Ti_3Al-Cr systems. Only a section of the deposit consisting of 30-50 at.% (Nb,Cr) was investigated, Figure 6.11. Phase distribution and lattice parameters of the alloys were correlated to both Nb and Cr, respectively, Figure 6.12. The nonequilibrium alloys consisted of a Nb-rich beta phase and a Cr-rich beta phase separated by an amorphous phase. The formation of the amorphous phase is completely dominated by the presence of Cr. Amorphous phase was formed between 30 and 55 at.% Cr with only 3-6 at.% Nb. In this case, the nonequilibrium Ti_3Al-(Nb,Cr) system was more closely related to the Ti_3Al-Cr system than to the Ti_3Al-Nb system.

A specimen ((5)1-3-B12.5) of a Ti_3Al-20Nb-11Cr alloy composition was selected for TEM analysis because this composition could be the two-phase boundary of alpha2 and beta, indicated by x-ray

diffraction. The microstructure clearly showed a two-phase mixture and also two different grain sizes. Nearly 80% of the grains were larger beta phase (250 nm) balanced with smaller alpha2 phase (50 nm), Figure 6.13. Elemental analysis showed the chemistry of the beta phase as 43-44Ti, 19-20Al, 14-15Cr and 21-23Nb, and the alpha2 phase as 48Ti, 23Al, 11Cr and 18Nb. Even though the alloy contained more than 30 at.%(Nb,Cr), no amorphous phase was detected. This implies that Cr content is the key factor for formation of amorphous phase.

6b. Alloy chemistry and phase stability

Both nonequilibrium Ti_3Al-Nb and Ti_3Al-Cr alloys in the as-sputter deposited forms always consisted of a disordered alpha2, beta and/or amorphous phase. X-ray diffraction and TEM studies did not reveal the disordered alpha2 phase, an high temperature alpha-Ti phase [8] with the Jaffee-Margolin titanium-aluminum diagram [9-11] at near 40 at.% Al. Likewise, the orthorhombic phase observed by Banerjee et at [12] for Ti_3Al-Nb at 12.5 at.% Nb was also not observed in the as-deposited alloy.

Because of the potential aerospace applications of alpha2- and superalpha2-$(TiNb)_3Al$ alloys [13], phase stability and phase chemistry of nonequilibrium Ti_3Al-Nb alloys were extensively characterized to determine the effects of heat-treatment. Heat treatment was conducted in vacuum sealed Vycor brand tubes at 800 or 850°C from 0.5 to 100 hours. Since oxygen content in these alloys was a major concern, oxygen levels were quantitatively analyzed by AES and SIMS and compared with a rapidly solidified RibTech-alpha2 alloy (Ribbon Technology, Gahanna, Ohio). The oxygen contents were similar in sputter-deposited and liquid quenched alloys. Semiquantitative oxygen analyses were further conducted on a series of sputter deposited alloys by WDS analysis, as described in Section 7, "High Quality Sputter Deposited Foils". In most cases, oxygen level in heat-treated alloys was below 1500 ppm at the surface. Since TEM specimens were mechanically polished to remove 2-3 mils of material from both sides of the deposit after heat treatment, the microstructures of the internal region should contain very little oxygen.

6b.1. Annealing Effects

1. 850°C/0.5h annealing

Annealing studies were first conducted on a (5)1-2-B11.75 specimen which had a nominal composition of Ti_3Al-15Nb-2Cr. The presence of Cr was due to co-sputtering with a Cr subtarget. Heat treatment

was conducted at 800°C for 0.5 h. TEM micrographs and diffraction analysis of alloy phases are shown in Figure 6.14 and Figure 6.15 respectively. The composition of each individual phase is listed in Table 6.2. The microstructure consisted of equiaxial, recrystallized grains for the most part. Many of the grains contained some residual defects which contributed to diffused convergent beam electron diffraction (CBED) patterns. The grain size was fairly uniform ranging from 150 to 200 nm and averaging about 175 nm. Due to the similarities in the composition and grain size of the various phases present in the sample, phase identification was made exclusively by examining several diffraction patterns from individual grains. In most cases, extensive tilting of the specimen was required to obtain the desired orientation for identification. The elemental analysis data were results of at least 10 independent measurements from grains of each phase.

The annealed $Ti_3Al-15Nb-2Cr$ alloy consisted of three phases, a dominant orthorhombic phase with a Cmcm space group, a dominant bcc phase and the alpha2 phase. Orthorhombic and bcc phases were present in equal proportion. The orthorhombic phase had a high Nb content with a composition distribution of 51-52Ti, 22-24Al, 22-23Nb and 1-2Cr. The lattice parameters of the orthorhombic phase was a=9.15 Å, b=9.6 Å and c=4.6 Å. The bcc phase was an ordered B2 phase shown by the superlattice reflections. The composition of the B2 phase was 44-46Ti, 15-16Al, 32-34Nb and 4.5-6Cr. The alpha2 phase was observed only on a few occasions, and is estimated to be present only at a very small level, <5%. The chemical composition of the alpha2 phase (46Ti, 22Al, 29Nb and 2Cr) was not significantly different from the orthorhombic phase.

Table 6.2: Phase distribution, grain size and composition of an 800°C/0.5h annealed $Ti_3Al-15Nb-2Cr$ alloy.

SPUTTERED ALLOY	ALLOY PHASE	SIZE (nm)	COMPOSITION (at.%)			
			Ti	Al	Cr	Nb
$Ti_3Al-15Nb-2Cr$	Ortho.	200	51-52	22-24	1-2	22-23
800°C/0.5h	Alpha2	150	46	22	2	29
	Beta	200	44-46	15-16	4.5-6	32-34

48

2. 850°C/2h annealing

Initial TEM examination of the annealed $Ti_3Al-15Nb-2Cr$ alloy revealed complex phase distribution and different chemical constituents associated with each phase. We realized that analytical TEM would be a powerful tool for investigation of phase stability with respect to a specific heat treatment condition. For example, it was found that Cr was preferably incorporated in the B2 phase. Nearly the same amount of Nb was incorporated in the alpha2 and orthorhombic phases. Questions were raised as how the orthorhombic phase was formed relating to initial fine grained alpha2 and beta phases of as-deposited alloys, and what would be compositional and thermal stability boundaries of B2, alpha2 and orthorhombic phases. Understanding of the phase stability and microstructures is important for designing materials with optimized mechanical properties. Since as-sputter deposited nonequilibrium phases and microstructures were different than those obtained from liquid quenching, or bulk processing, the following studies focused on the nonequilibrium multiphase $Ti_3Al-xNb-2Cr$ system as a function of alloy composition and heat treatment.

Eight nonequilibrium alloys containing 10-25 at.% Nb, plus a rapidly solidified alpha2 alloy made previously by Ribbon Technology, Inc., were heat treated at 850°C in vacuum for 2 hours. Microstructural examination showed these alloys had similar grain size and phase distribution as the previously studied $Ti_3Al-15Nb$ specimen, Figure 6.14. The phase distribution and the chemistry of individual grains were analyzed and tabulated in Table 6.3. Beta phases characteristically showed a narrow range of composition, less Al and more Nb in comparison to the starting alloys which contained a wide range of Al and Nb content. Compared with beta phases, alpha2 phases were high in Al and low in Nb and Cr.

3. 850°C/100h annealing

Previous work on rapidly solidified Ti-25Al-Nb alloys with more than 12 at.% Nb showed the formation of a large portion of orthorhombic phase after heat treatment at above 800°C [6]. Since only a few orthorhombic phase grains were observed in our sputtered alloys, the annealing time might be too short to reach the equilibrium state in sputter deposited alloys. For this reason, four specimens, (5)B13, (5)B12, (5)B11.75, and (5)B11 containing 13 to 20 at.% Nb, were selected to be heat treated at 850°C for 100 hours; the results are tabulated in Table 6.4. The resultant microstructures consisted of four different phases, beta, alpha2, orthorhombic and twinned orthorhombic, as shown in Figure 6.16.

The amount of twinned orthorhombic phase increased with respect to a decrease of the Nb content in the as-deposited alloys. The nearly 80 % orthorhombic phases in B13 (12.6 at.% Nb) were twinned while B12 (16.2 at.% Nb) and B11.75 (15.5 at.% Nb) were nearly 30%

twinned and B11 (20.8 at.% Nb) about 20%. However, the amount of alpha2 phase also was reduced from B11 to B13. Chemical analysis of individual grains indicated that the composition of the twinned orthorhombic phase differed from the composition of the normal (un-twinned) orthorhombic phase, and was very close to the alpha2 composition observed. These differences in alloy chemistry are illustrated in Figure 6.17, the decrease of Nb content in alloys from B11 to B13 resulted primarily from the decrease of Nb contents in beta phases. More significantly, the Nb contents in orthorhombic and twinned orthorhombic phases were also decreased but to a lessor degree than the beta phase. In B13, atomic compositions of beta, orthorhombic and twinned orthorhombic phases had similar Nb contents with a difference of approximately 5 at.%.

6b.2. Phase Stability Boundaries

Due to the complexity of phase relationships observed in heat-treated alloys, phase stability was understood by mapping phase boundaries in terms of their unique compositions. In 850°C/2h annealed alloys, phase occurrence can be attributed to relative Cr, Nb and Al contents. In this case, plots of Cr/Al and Nb/Al were used to map different phase boundaries, as shown in Figure 6.18. In the Cr/Al plot, beta phases were all grouped in a small region between 3.5-5 at.% Cr and 11-14 at.% Al. On the other hand, alpha2 phases were grouped in a region of less than 2 at.% Cr and 17-23 at.% Al. In the Nb/Al plot, beta phases exhibited a wider spread of Nb content, from 16 to 30 at.% Nb, but form into two subgroups. One subgroup of beta phases, with 16 at.% Nb, was associated with the ordered B2 structure, while another subgroup of beta between 24 and 30 at.% Nb would be disordered. In the Nb/Al plot, alpha2 phases were found between 8 and 25 at.% Nb. The occurrence of the alpha2 phase was rapidly reduced and replaced with the orthorhombic phase at higher than 18 at.% Nb. The alpha2 phase boundary tends to incorporate more Nb as its Al content is reduced from 21 to 17 at.% Al.

For 850°C/100h alloys, plots of Cr/Al and Nb/Al to differentiate phase boundaries are shown in Figure 6.19. The stability region of beta phases was confined within 3-4 at.% Cr, but with a wide spread of Al content, between 14-18 at.% Al. In the Nb/Al plot, the spread of beta phases resulted in three subgroups, in terms of ordered and disordered beta phases. It was significant to show that twinned orthorhombic phase (11-16 at.% Nb) was compositionally well separated from the normal (un-twinned) orthorhombic phase (15-22 at.% Nb), and alpha2 phase located between the normal orthorhombic and twinned orthorhombic phases.

Based on the separated mapping of the phase boundaries of beta, alpha2, orthorhombic and twinned orthorhombic phases, it was possible to map the phase boundaries in the Ti-Al-Nb ternary

diagram, as shown in Figures 6.20 and 6.21 for 2 h and 100 h annealing respectively.

In Figure 6.20, phase boundaries of beta, alpha2, and orthorhombic phases resulting from 850°C/2h annealing are illustrated in comparison to the preliminary 1000°C partial section Ti-Al-Nb [14] derived from liquid quenched Ti_3Al-Nb alloys. All three phase boundaries, beta, alpha2 and orthorhombic, of the sputter deposited alloys are located in the beta phase field of the liquid quenched alloys.

In Figure 6.21, phase boundaries of beta and orthorhombic phases are basically similar to that of Figure 6.20. However, 100 h annealing resulted in moving the beta boundary in a more Al-rich direction. The orthorhombic phase boundaries in both maps stay nearly unchanged, except the tip of the alpha2 phase boundary of the 2 h annealed alloys now is occupied by the twinned orthorhombic phase of the 100 h annealed alloys. It is important to realize that after a 100 h annealing, all four different phases almost converged into a small region separated only by a narrow phase field. Comparing with the 100 h annealing data, it is possible that 2 h annealing was not long enough for the nonequilibrium alloys to reach the equilibrium condition.

6b.3. Discussion of the Results

Nonequilibrium Ti_3Al-Nb alloys formed by sputter deposition exhibited unique microstructure and alloy chemistry in comparison with liquid quenched Ti_3Al alloys of 15-30 at.% Nb. Although both nonequilibrium processes resulted in fine microstructure and disordered beta and ordered alpha2 phases, liquid quenched alloys had antiphase domains (APD) in as-quenched alloys. Sputtered alloys did not show the formation of APD. Since the formation of APD would require nucleation, the sputter deposited alloys may suppress the reaction because of highly disordered grains formed in as-deposited conditions.

In comparison with liquid quenched alloys, formation of the orthorhombic phases in sputter deposited alloys is unique in three aspects: 1) they required a longer term annealing, nearly 100 h, comparing with 0.5-2 h needed for the liquid quenched alloy, 2) exhibited a relatively low Al content, between 16-22 at.% Al comparing with the 25 at.% Al in liquid quenched alloys, and 3) formed twinned orthorhombic phase with a different composition than the normal orthorhombic phase.

Since the discovery of the $(TiNb)_3Al$ based orthorhombic phase [12], its formation and phase chemistry have been investigated primarily based on equilibrium alloys and liquid quenched nonequilibrium alloys with Al concentration between 23-25Al and 12-30Nb. Typical

formation of the orthorhombic phase was described by M. Kaufman, et al [6], Weykamp et al [15] and Banerjee, et at [12] as an equilibrium phase occurring at 15 to 30 at.% Nb. This is not surprising since similar orthorhombic phase structure was also found in Ti-Nb binary alloys [16]. However, until recently the formation of orthorhombic phase was considered as a simple phase transformation involving most of the metallic elements. It has been suspected that interstitial additions such as hydrogen and oxygen and internal stress fields might promote the orthorhombic phase [17].

The finding of two orthorhombic phases in sputter deposited alloys of different compositions and microstructures implies: 1) competing nucleation and growth of complex phases over narrow composition range, and 2) limited diffusion length resulting in stress induced phase segregation. The formation of orthorhombic phases is apparently favored as a result of long term heat treatment. The two different orthorhombic phases formed by 100 h annealing may be attributed to complex nucleation characteristics involving either beta or alpha2 grain boundaries. The untwinned orthorhombic phase may be formed at beta grain boundaries as well as from Nb-rich alpha2 grain boundaries. However, orthorhombic phase may also be formed at some alpha2 grain boundaries containing less Nb than the average alpha2 grains. In this case, the transformed orthorhombic phase would be highly stressed due to Nb deficiency and exhibit a high degree of twinning.

Formation of different orthorhombic phases may also be attributed to Al contents in these sputter deposited nonequilibrium alloys. Since Al content in the sputter deposited alloys was under 25 at.%, typically 18-22 at.%, the high quench rate would promote the formation of beta phase rather than the alpha2 phase. Annealing in short term could transform some of the nonequilibrium beta phase into alpha2 phase, as shown in the 850°C/2h annealing. Prolonged annealing further promotes transformation of alpha2 phase into orthorhombic phase, but the deficiency of Al possibly stressed the orthorhombic phase resulting in a highly twinned microstructure. In addition to Al content, the high mobility of Al in highly disordered as-sputter deposited alloys may also contribute to the competing nucleation processes. The nonequilibrium beta phases might continue to exchange Al composition with the disordered alpha2 phase. During the course of the Al exchange, free Al interacted with different nucleation sites may result in formation of orthorhombic and twinned orthorhombic phases.

In conclusion, we may have identified unique phase boundaries for orthorhombic phases formed in Ti-Al-Nb at the 17-22 at.% Al range in sputter deposited alloys. Starting with ultrafine grained beta+alpha2 phases with highly defected microstructures, the transformation processes may involve eight reactions affected by annealing time and temperature:

```
1)      beta-> ordered beta,
2)      beta-> alpha2,
3)      beta-> orthorhombic,
4)      ordered beta-> alpha2,
5)      ordered beta-> orthorhombic,
6)      alpha2-> orthorhombic,
7)      alpha2-> twinned orthorhombic,
8)      twinned orthorhombic-> orthorhombic
```

The relative Nb content in these phases would have the sequence of
beta>ordered beta=orthorhombic>alpha2>twinned orthorhombic. During
annealing, competition of phase formation and redistribution
results in complex intermediate microstructures. Based on these
observations, formation mechanism and kinetics of the orthorhombic
phases would require further investigation in terms of Al and Nb
content, and microstructures of the starting nonequilibrium alloys.
Furthermore, possible effects due to oxygen and stress fields
should also be considered in these investigations.

Table 6.3: Phase distribution and composition of 850°C/2h annealed Ti₃Al-xNb-2Cr alloys.

Specimen	Phase	File	Ti	Al	Nb	Cr (at.%)
RibTech*			64.6	25.0	10.3	0
	Alpha2	900410	66.2	20.5	12.5	0.8
	Alpha2	900413	66	20.4	13.2	0.7
	Alpha2	900416	65.0	22.5	12.5	0.7
	Ortho.	900375	70.9	15.2	13.8	0.1
(6)9Nb			65	24	10	1
	Beta	900133	67.4	11.8	16.4	4.4
	Beta	900134	67.4	12.2	17.0	3.5
	Beta	900136	66.8	12.6	16.4	4.2
	Alpha2	900119	68.0	21.9	9.0	1.0
	Alpha2	900125	68.4	20.7	9.6	1.3
	Alpha2	900135	69.8	20.3	8.8	1.1
(6)A115			64	20	15	1
	Alpha2	890397	67.3	20.1	11.8	0.8
	Alpha2	900397	67.6	19.9	11.7	0.8
	Alpha2	900398	66	22.4	10.6	0.9
	Alpha2	900435	67.0	22.5	10.4	?
(6)A125			60	19	20	1
	Beta	A12581	58.6	11.4	26	3.9
	Beta	A12584	59.4	11	24.9	4
	Beta	A12585	59	11.4	25.6	3.9
	Alpha2	900343	66.1	20.2	12.8	0.9
	Alpha2	900345	65.8	19.7	13.6	0.1
(5)12D11 890°C/4h			52	25	22	1
	Alpha2	900458	57.9	22.3	19.7	?
	Ortho.	12D11A	63	21.3	15.6	0.14
	Alpha2	900332	64.9	18.6	15.3	1.2

*Ribbon Technology Corporation, Gahanna, Ohio

54

Table 6.3 (Continue): Phase distribution and composition for 850°C/2h annealed alloys.

Specimen	Phase	File	Ti	Al	Nb	Cr (at.%)
(6)A135			58	16	25	1
	Beta	A13581	57.3	11.2	27.4	4.1
	Beta	A13582	56.8	11.4	27.7	4.2
	Alpha2	900340	62.8	21.0	15.3	1.0
FAA1						
	Beta	893373	60	12	25	4
	Beta	893390	59.5	12	24.9	3.8
	Beta	890403	60.5	12.4	23.6	3.5
	Alpha2	890406	65.7	20.6	12.9	0.7
	Alpha2	893380	64	21	14.6	0.8
	Alpha2	893385	65	21	14	0.7
	Alpha2	893395	65.5	21.3	12.3	0.8
	Alpha2	893399	66.3	19.7	13.3	0.8
FAAF						
	Beta	FAAFB1	53.5	14	27.4	5.1
	Beta	FAAFB2	52	13.4	29.6	5
	Alpha2	900473	62.6	18	18.5	1.1
	Alpha2	900475	56	17.6	24.9	1.3
	Alpha2	900476	54.6	18.5	25.5	1.4
	Alpha2	900487	57	19	22.6	1.3
	Alpha2	HEX1	54.3	18	25	1.8
	Ortho.	900472	58	17	22.5	1.8
	Ortho.	900485	55	20.6	22	1.3
	Ortho.	900496	53	19	26	0.9

Table 6.4: Phase distribution and composition of 850°C/100h annealed Ti₃Al-xNb-2Cr alloys.

Specimen	Phase	File ID	Ti	Al	Nb	Cr (at.%)
(5)B11			56.7	21.2	20.8	1.4
	Alpha2	900854	65.09	18.72	15.60	0.59
	Alpha2	900855	65.82	18.91	14.68	0.59
	Alpha2	900856	65.48	18.81	15.12	0.59
	Beta	B11B1	51.58	15.52	29.50	3.40
	Beta	B11B2	51.40	15.17	30.12	3.31
	Beta	B11B3	53.49	13.82	29.17	3.53
	Ortho.	900817	55.08	21.60	21.87	1.45
	Ortho.	900818	55.72	20.87	21.95	1.46
	Ortho.	B11O5	60.29	19.19	19.70	0.82
	Ortho.	B11BL1	59.58	18.13	21.25	1.05
	Ortho.	B11BL2	58.77	19.19	20.80	1.24
	Ortho T	B11TW1	65.61	18.14	15.36	0.89
	Ortho T	B11TW2	65.34	18.76	14.82	1.08
(5)B11.75			59.9	22.6	15.5	1.9
(5)B12			60.2	21.9	16.2	1.8
	Beta	B12B1	58.44	15.53	23.12	2.90
	Beta	B12B2	59.34	14.72	22.92	3.01
	Beta	B12B3	59.33	15.08	22.59	3.00
	Ortho.	900879	62.79	17.39	18.79	1.03
	Ortho.	B12BL1	64.79	17.19	17.41	0.61
	Ortho.	B12O1	60.93	18.49	19.96	0.62
	Ortho.	B12O22	62.31	18.31	18.77	0.61
	Ortho.	B12O3	61.72	18.85	18.72	0.71
	Ortho T	900878	67.82	17.53	13.67	0.98
	Ortho T	B12TW1	66.99	18.28	14.05	0.68
	O/A	900865	62.26	17.66	19.36	0.72
(5)B13			61.9	23.7	12.6	1.7
	Beta	B13B1	60.35	17.69	18.08	3.88
	Beta	B13B2	61.30	17.09	17.73	3.87
	Beta	B13B3	61.29	16.76	17.96	3.99
	Ortho.	900825	64.27	20.18	14.96	0.59
	Ortho.	B12BLA	64.98	18.18	15.55	1.29
	Ortho T	900828	68.92	18.92	11.68	0.48
	Ortho T	B12TW1	67.96	18.53	12.35	1.15
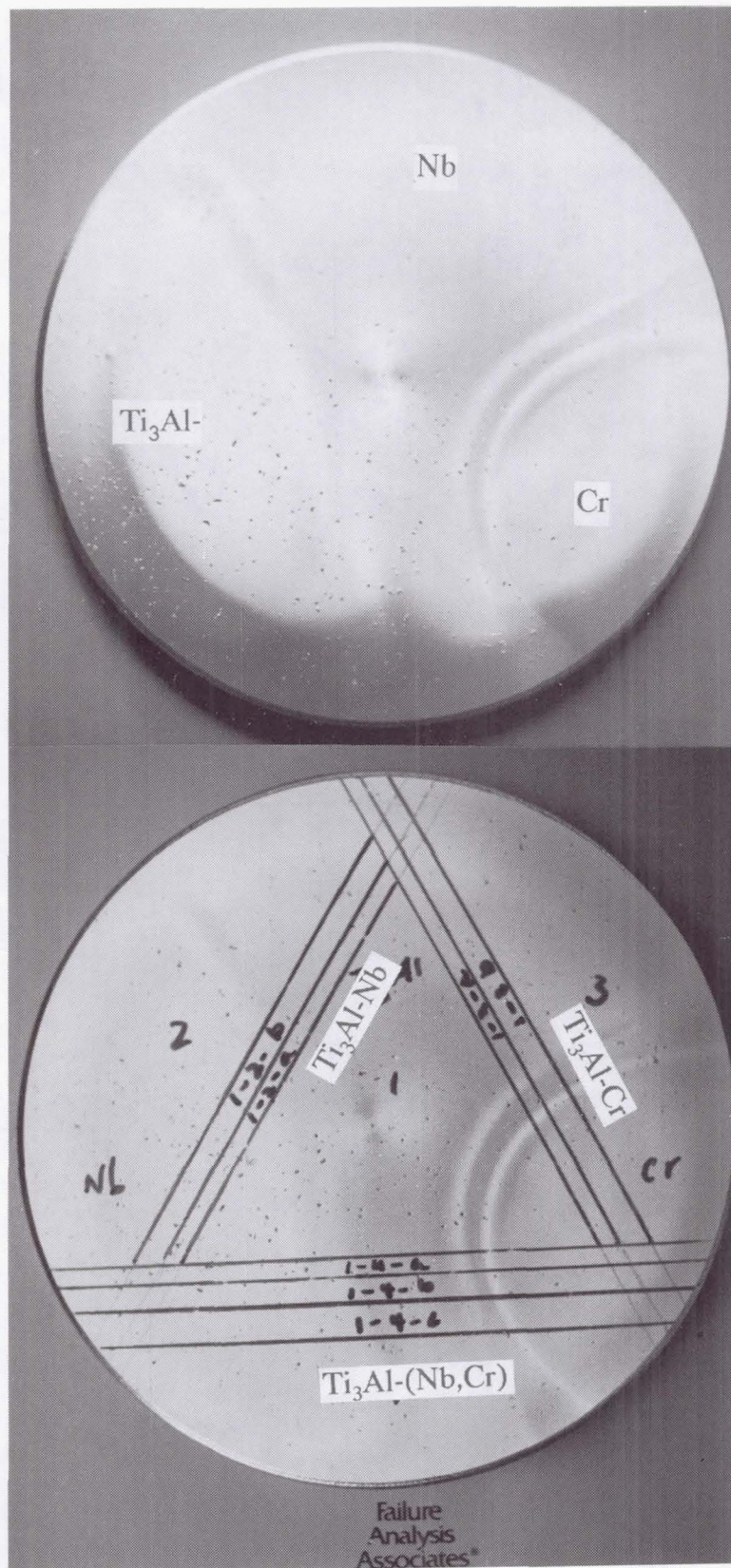
Figure 6.1. A single Ti$_3$Al deposit containing three series of nonequilibrium alloys graded with Nb, Cr and Nb+Cr.
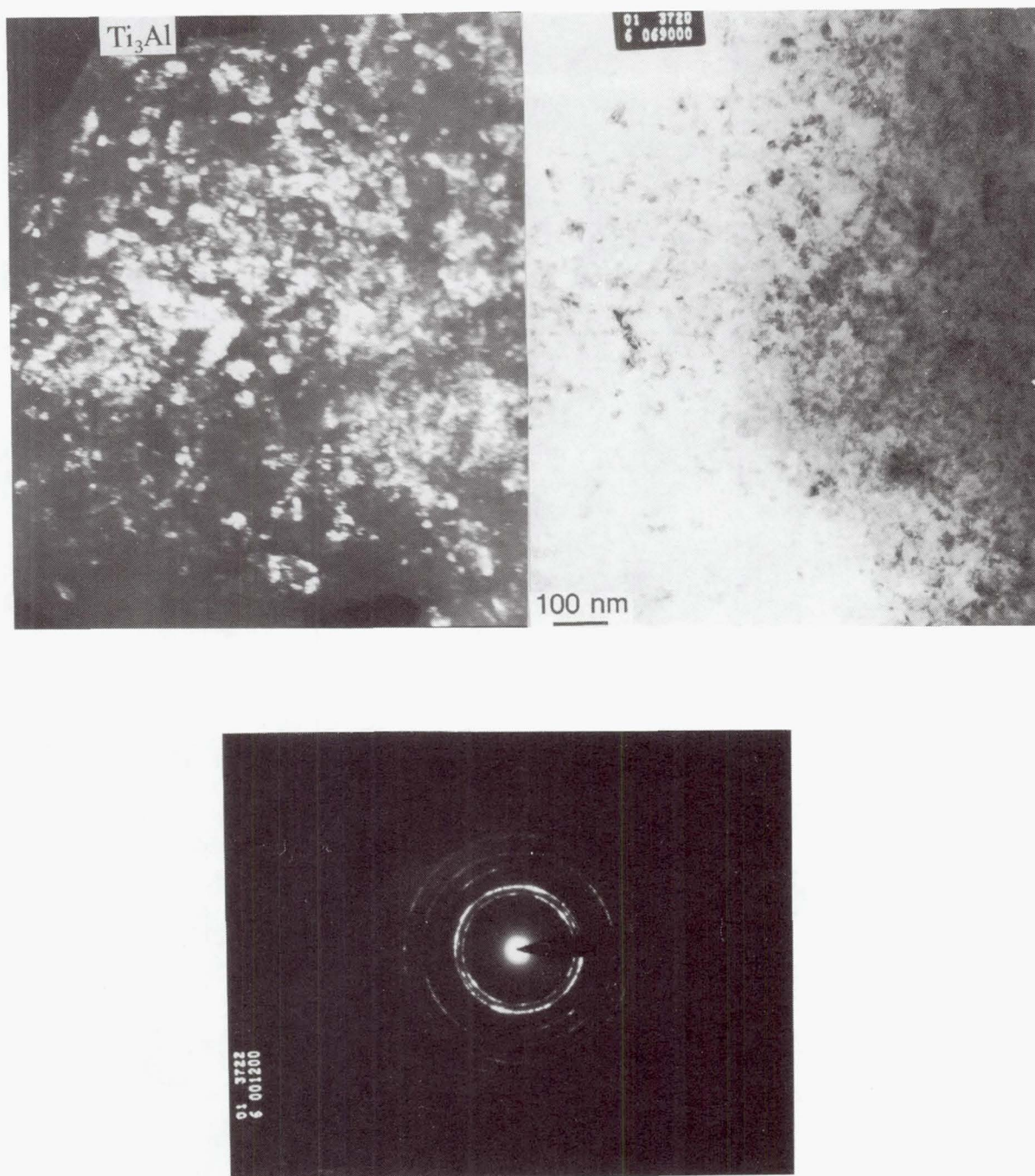
Figure 6.2. TEM micrographs and diffraction pattern of as-deposited Ti$_3$Al showing alpha2 phase and (0002) texture.

Ti3Al—Nb, (5) 1—2—B

Composition, at.%

(a)

Specimen number

Ti3Al—Nb, (5) 1—2—B

(b)

Niobium, at.%
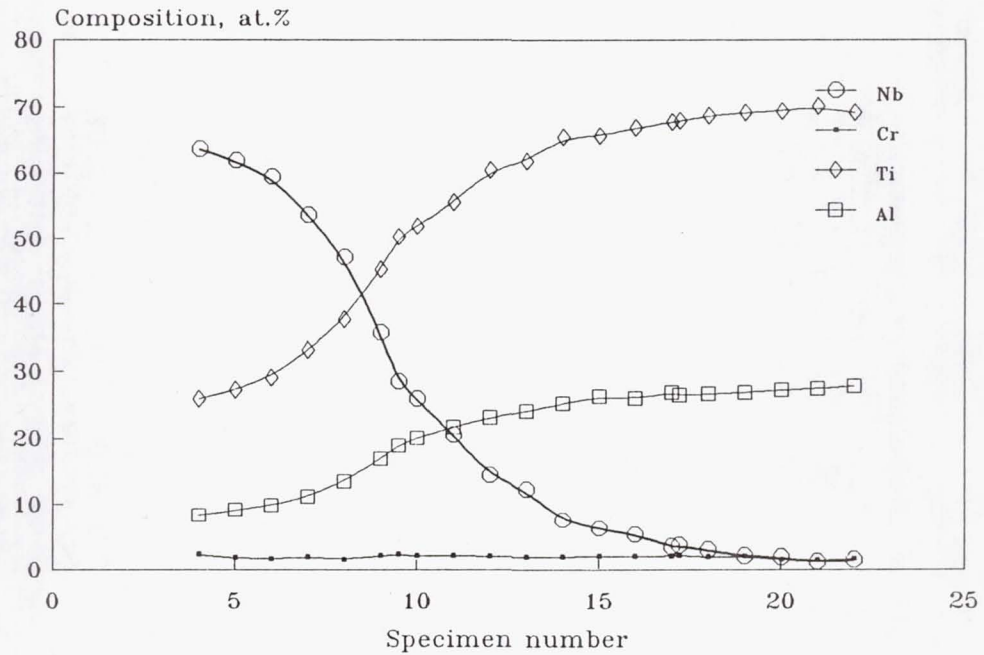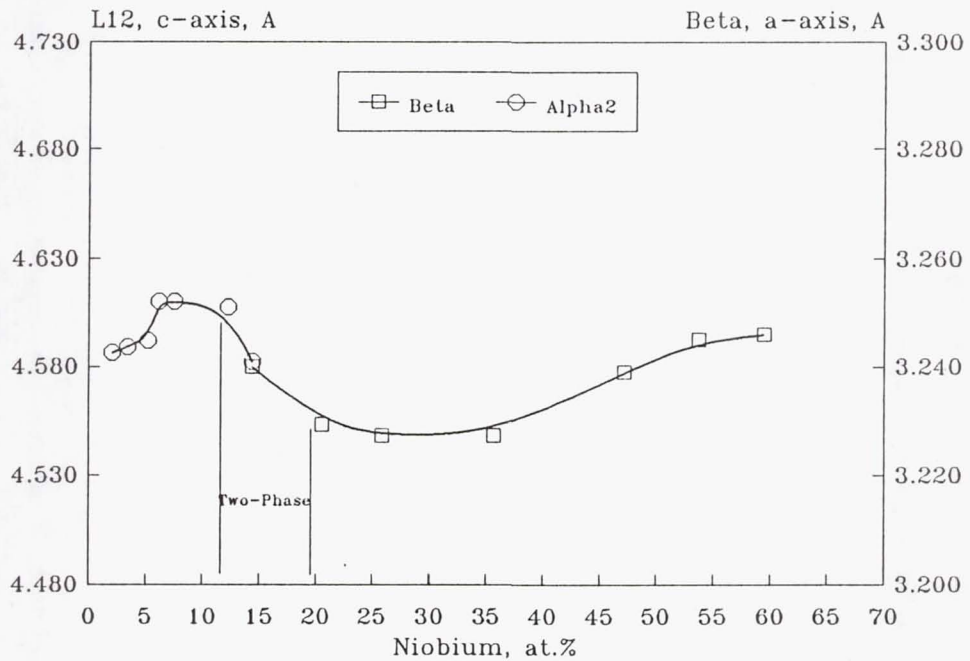
Figure 6.3. a) Composition analysis of nonequilibrium Ti$_3$Al—Nb alloys, and b) lattice parameters and phase distribution as a function of Nb content.
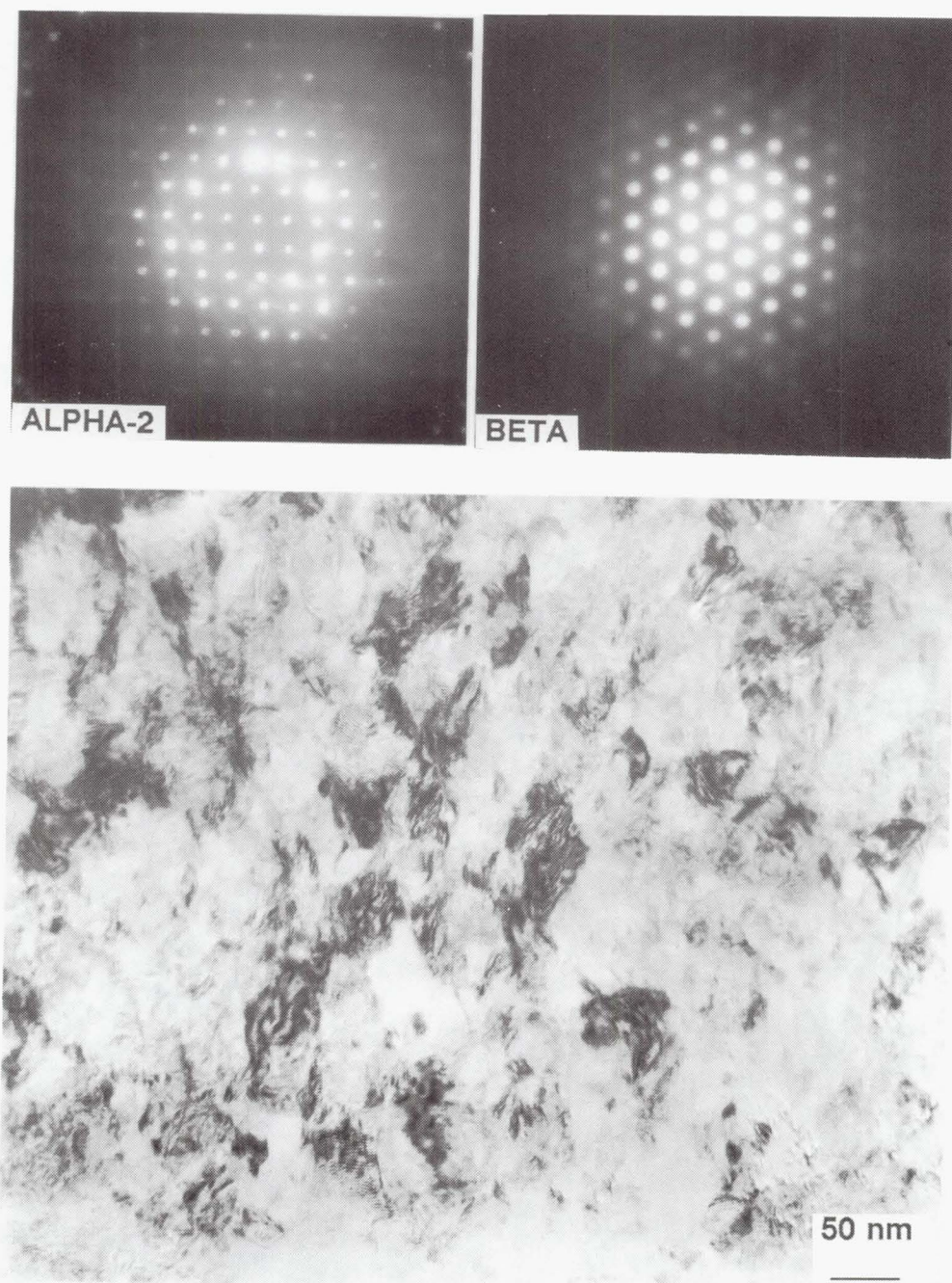
Figure 6.4. TEM micrographs and diffraction patterns of as-
deposited Ti₃Al-7.5Nb.
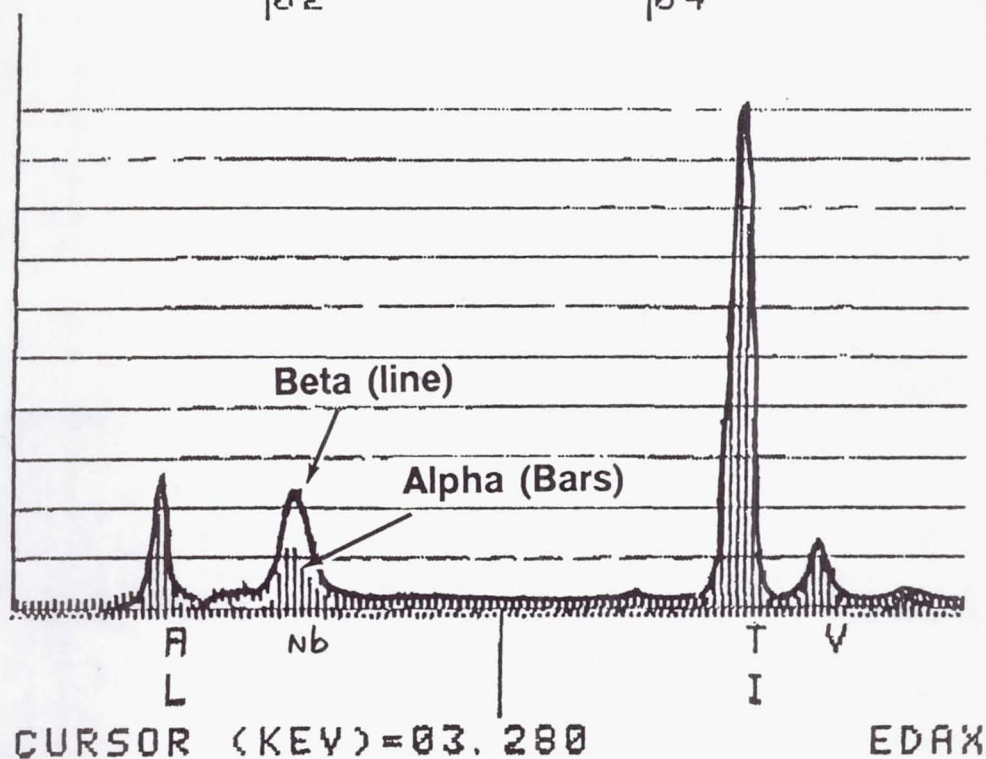
Figure 6.5. A comparison of the EDS spectra of alpha2 and beta phases. Higher Nb content was associated in the beta phase than the alpha2 phase.
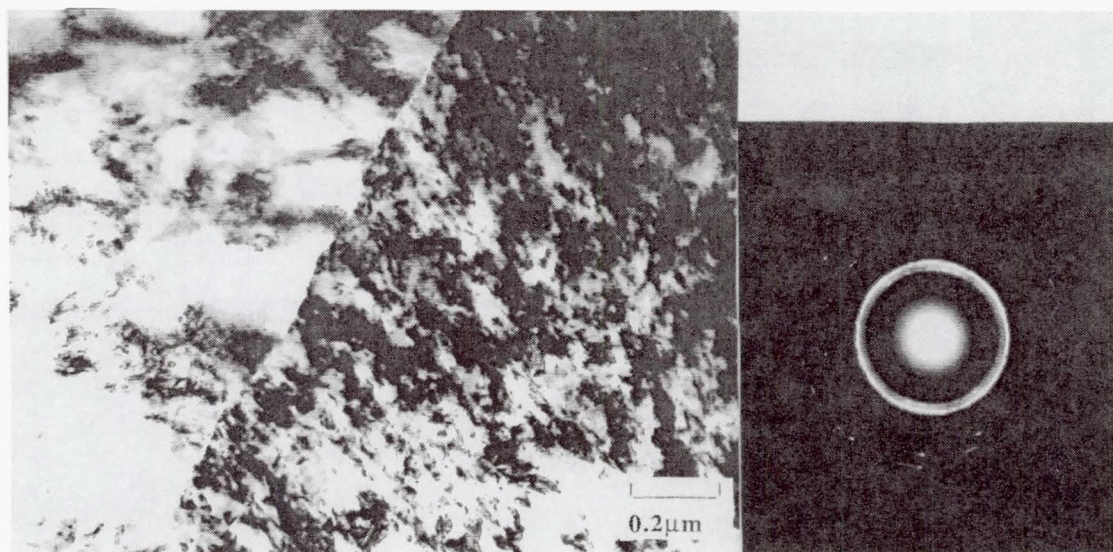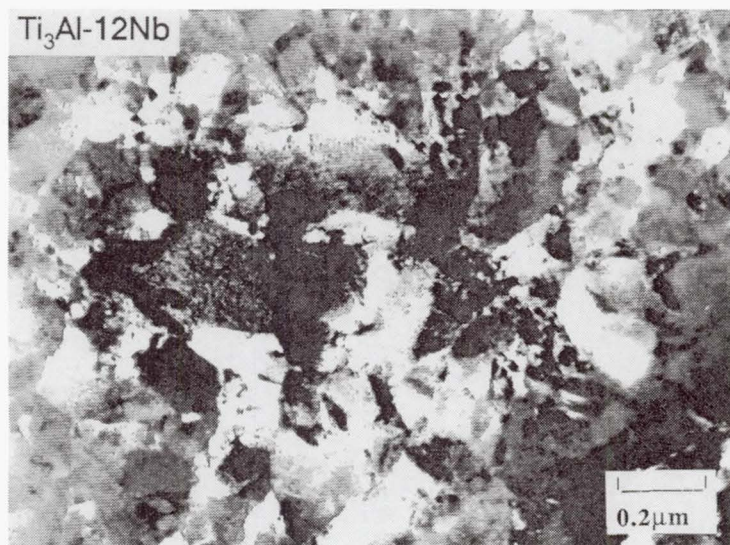
Figure 6.6. TEM micrographs and diffraction patterns of as-deposited Ti₃Al-12Nb.
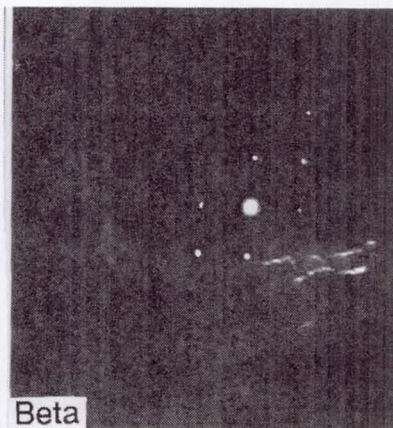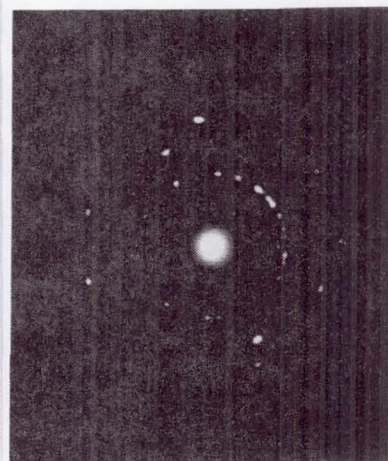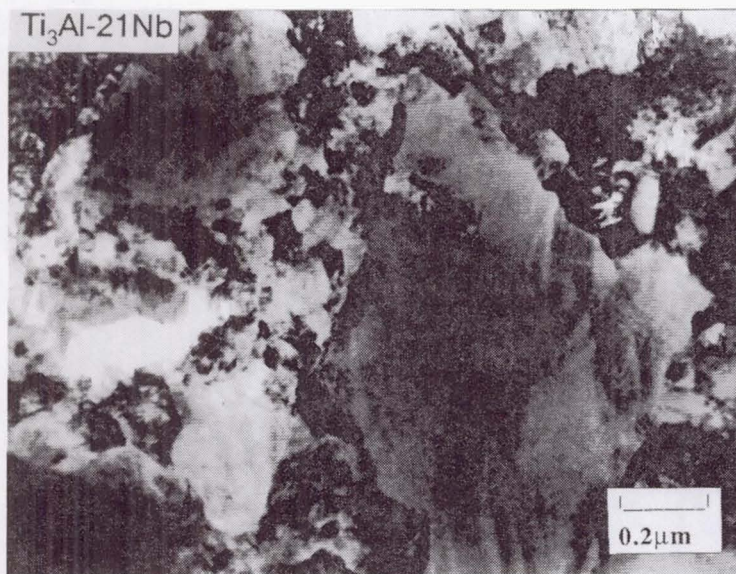
Figure 6.7. TEM micrographs and diffraction patterns of as-deposited Ti$_3$Al-21Nb.

GRAIN SIZE OF NONEQUILIBRIUM
Ti3Al–Nb ALLOYS
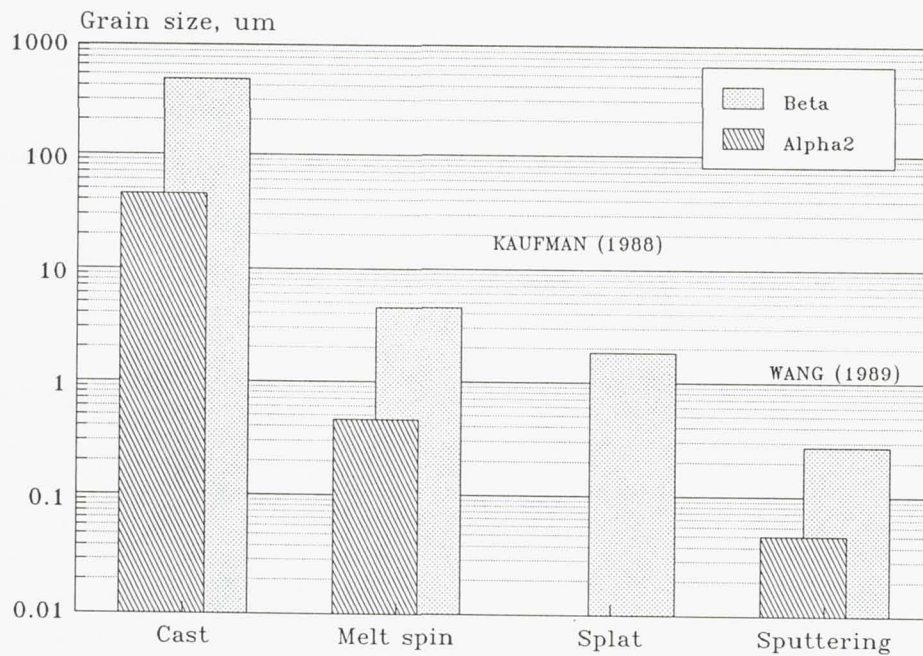
Figure 6.8. A comparison of grain sizes of sputter deposited Ti$_3$Al-Nb alloys with similar alloys processed by other processing methods.

Ti3Al–Cr, (5) 1–4–B

(a)
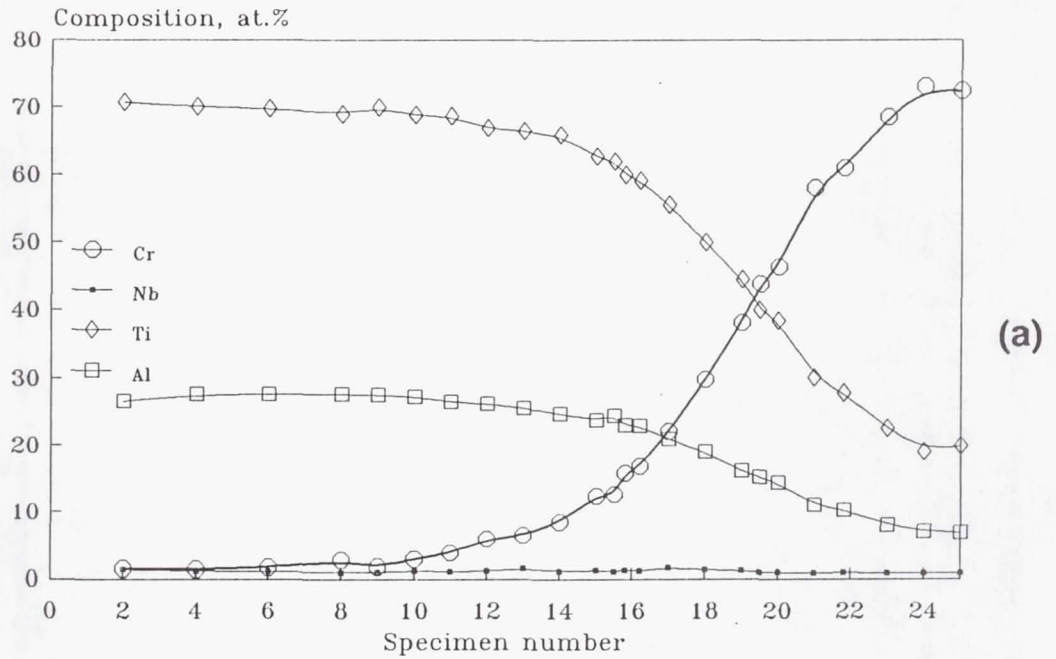
Ti3Al–Cr, (5) 1–4–B

(b)
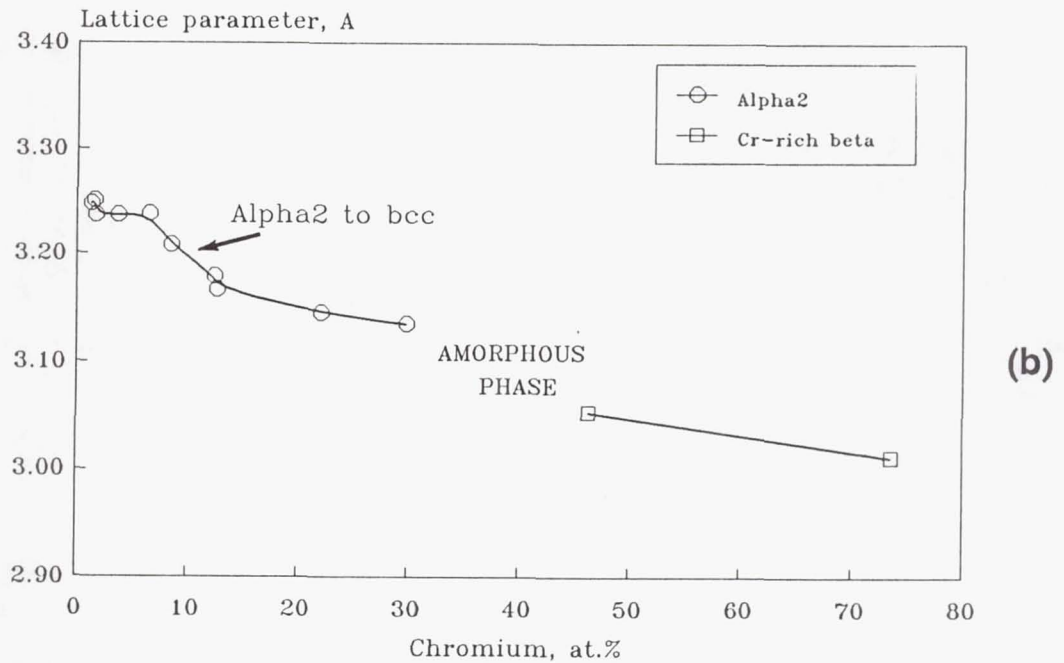
Figure 6.9. a) Composition analysis of nonequilibrium Ti$_3$Al-Cr alloys, and b) lattice parameters and phase distribution as a function of Cr content.
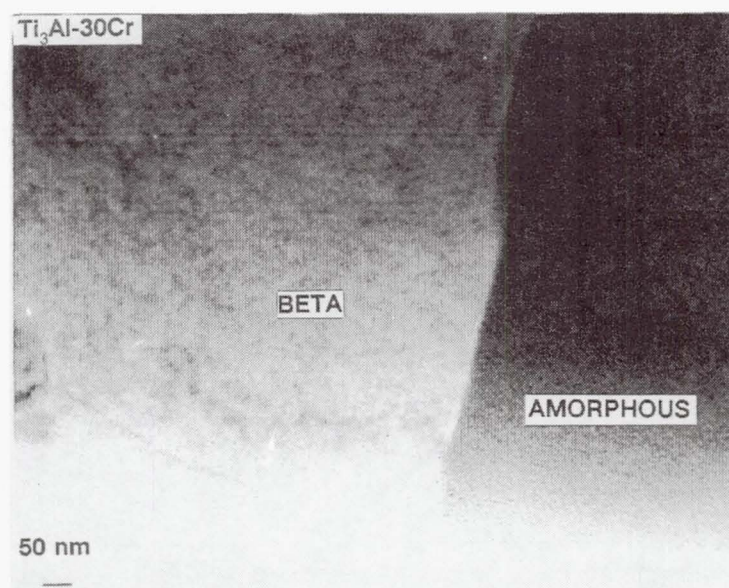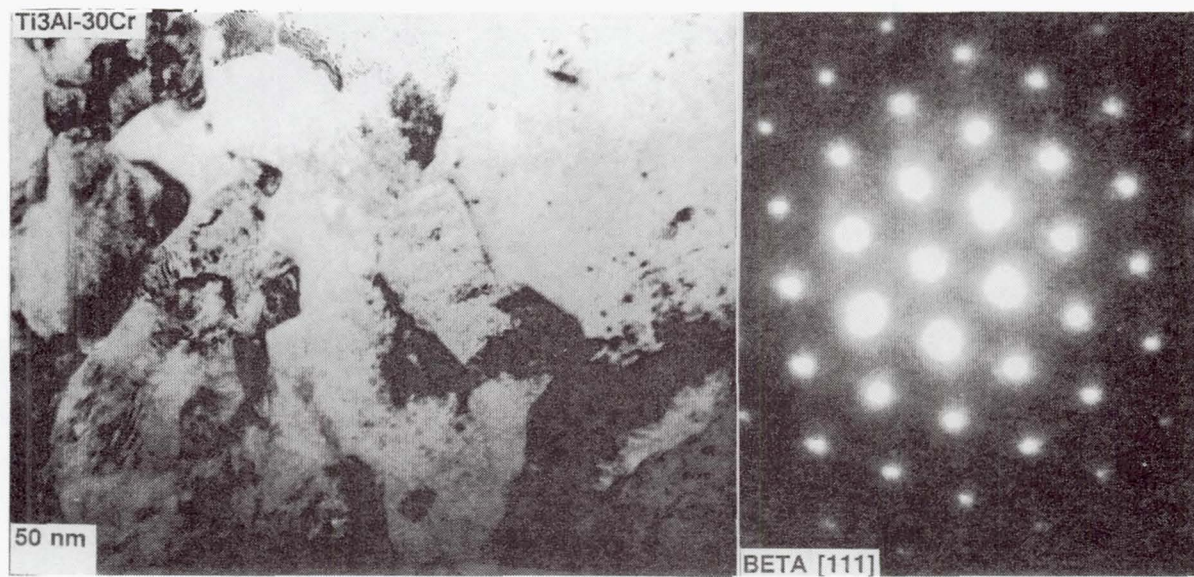
Figure 6.10. TEM micrographs and diffraction patterns of as-deposited Ti$_3$Al-30Cr.

66

ALLOY COMPOSITION OF SPUTTER DEPOSITED
Ti3Al-(Nb,Cr), (5) 1-3-B
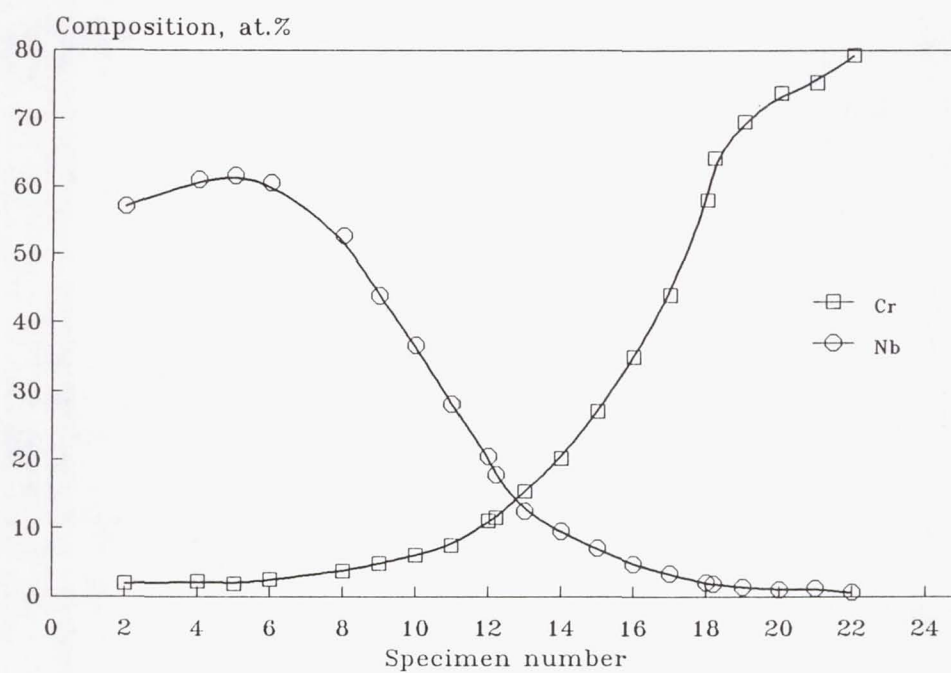
Figure 6.11. Composition analysis of nonequilibrium Ti$_3$Al-(Nb,Cr) alloys.

Ti3Al–(Nb,Cr), (5) 1–3–B
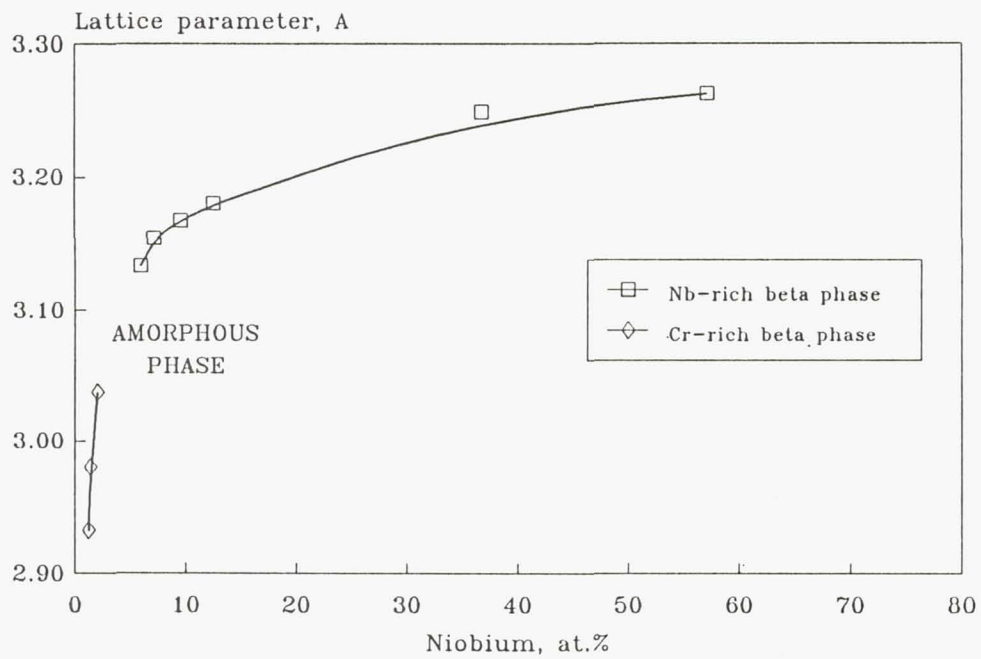
(a)

Ti3Al–(Nb,Cr), (5) 1–3–B
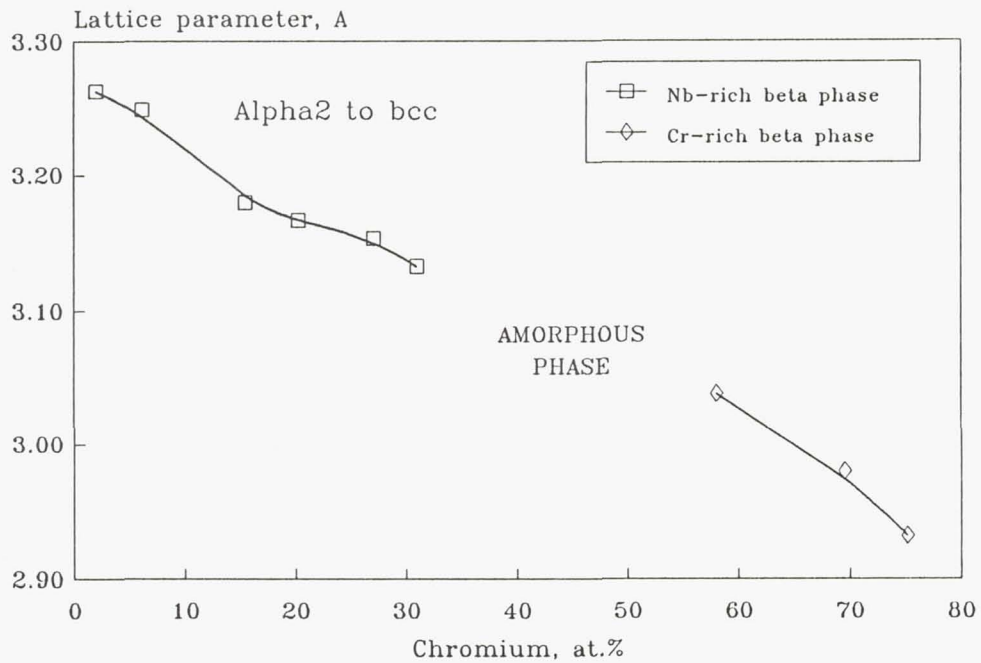
(b)

Figure 6.12. Lattice parameters and phase distribution as a function of a) Nb content and b) Cr content.
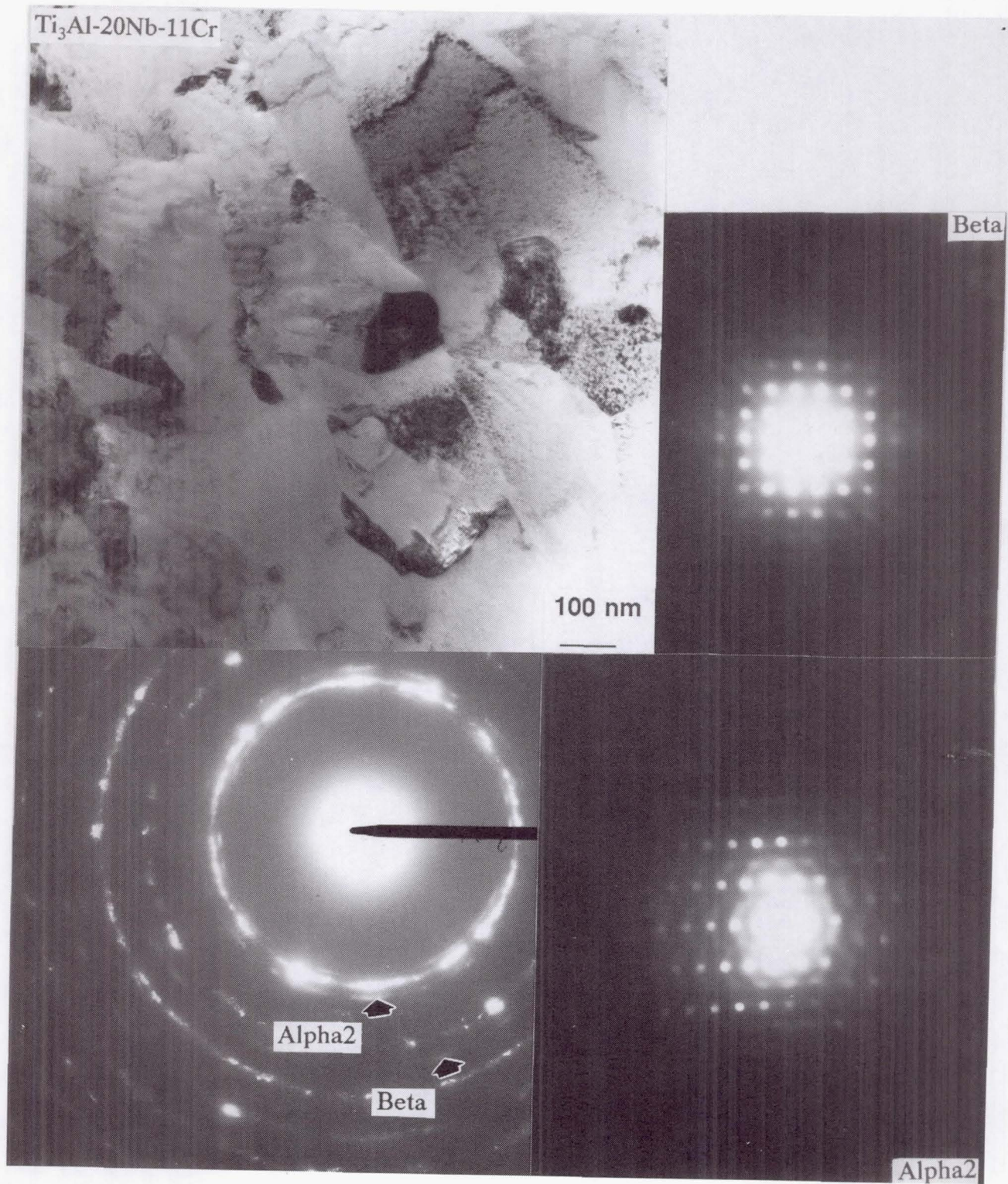
Figure 6.13.   TEM micrograph and diffraction patterns of as-deposited Ti₃Al-20Nb-11Cr showing alpha2 and beta phases.
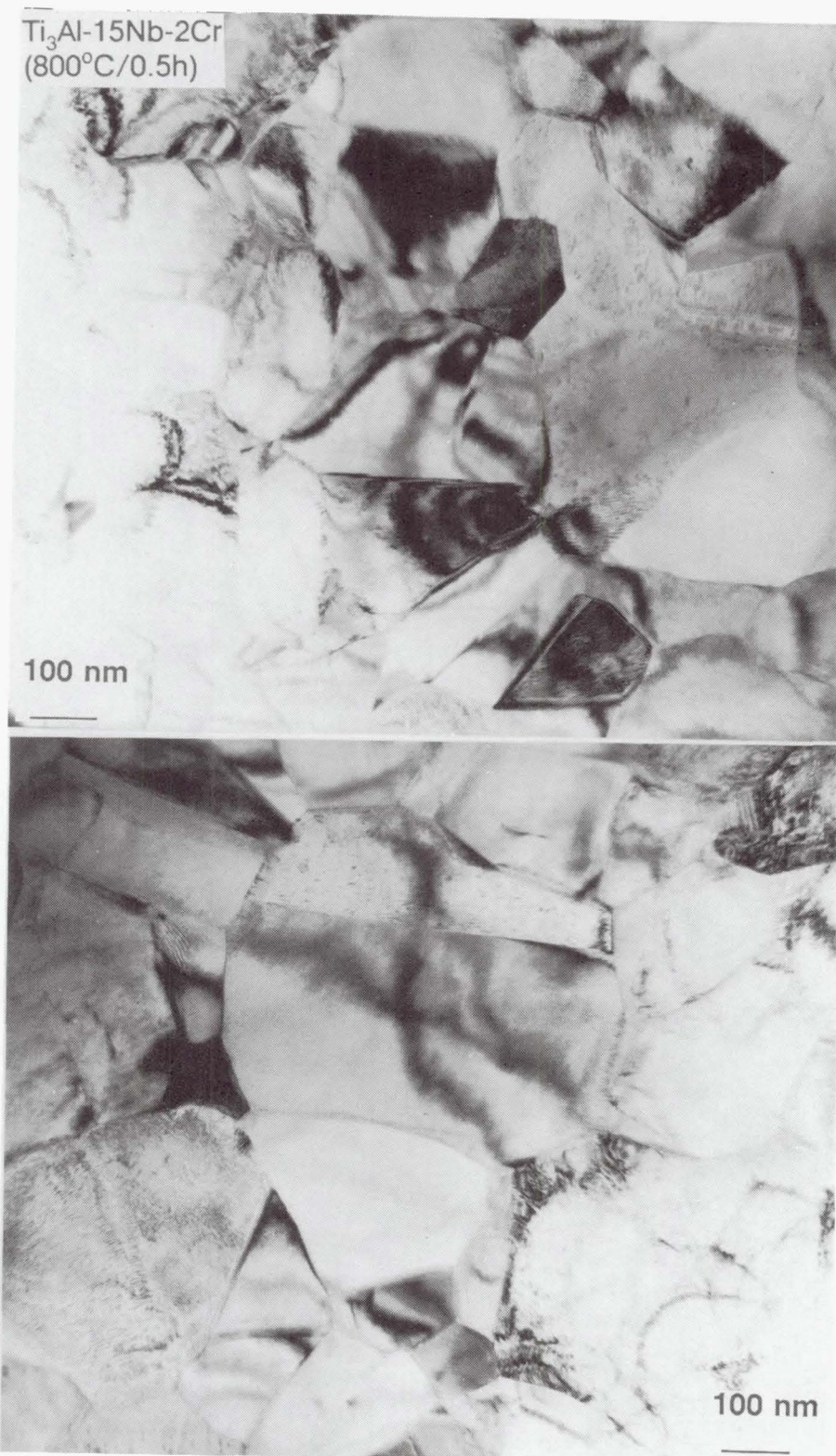
Figure 6.14. TEM micrographs of a 800°C/0.5h annealed Ti$_3$Al-15Nb-2Cr.

$\bar{2}00$ $\bar{1}10$ 020

$\quad\bar{1}00$ 010

$\bar{1}\underline{1}0$ $*$ 110

$\quad0\underline{1}0$ 100

$0\underline{2}0$ $1\underline{1}0$ 200

Ordered Beta [001]

Alpha2 [0001]

$\bar{2}20$ 020 220

$\quad\bar{1}10$ 110

$\bar{2}00$ $*$ 200

$\quad\bar{1}\underline{1}0$ $1\underline{1}0$

$\bar{2}\underline{2}0$ $0\underline{2}0$ $2\underline{2}0$

Ortho. [001]
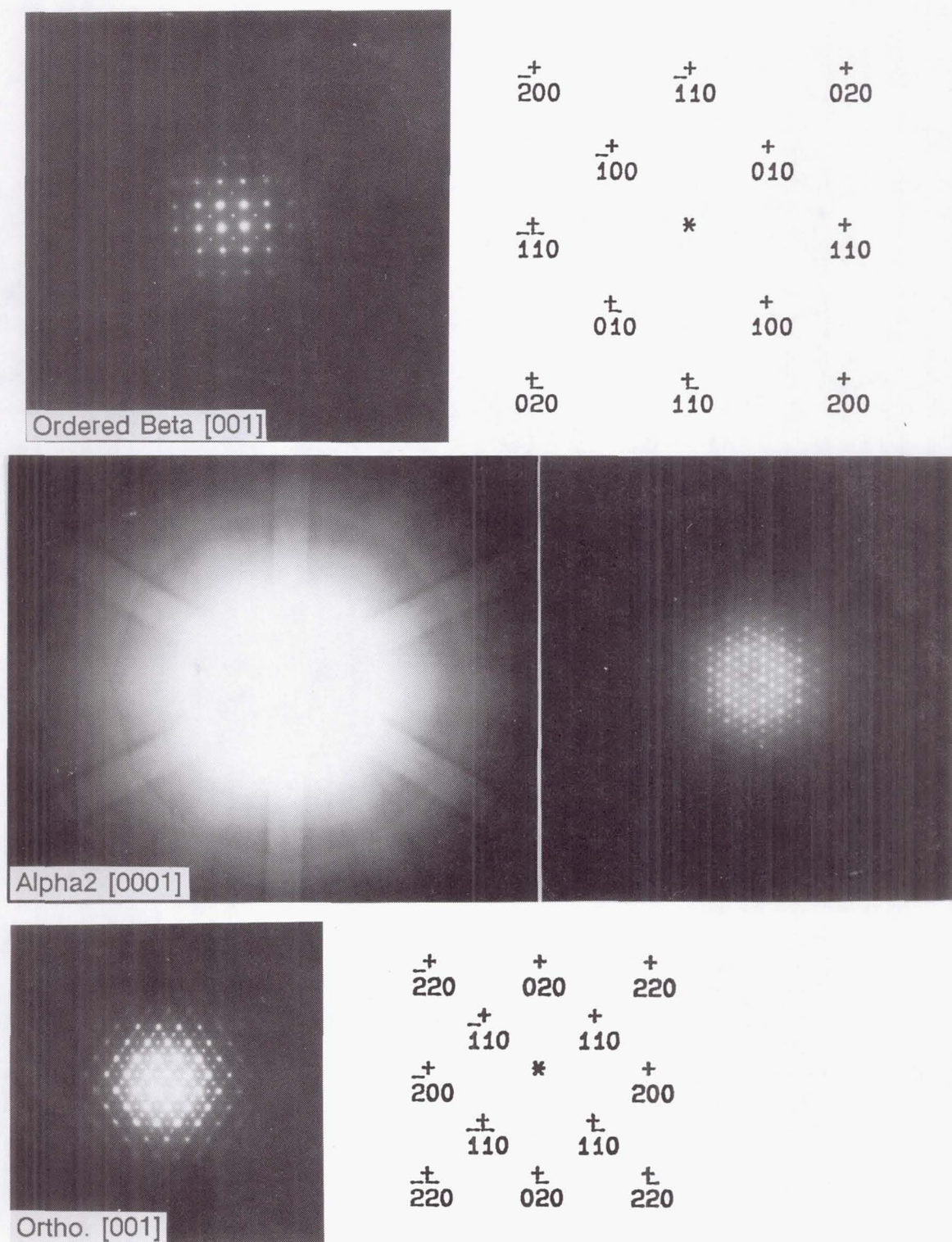
Figure 6.15. Electron diffraction patterns of a 850°C/2h annealed Ti$_3$Al-15Nb-2Cr showing alpha2, beta and orthorhombic phases.

71
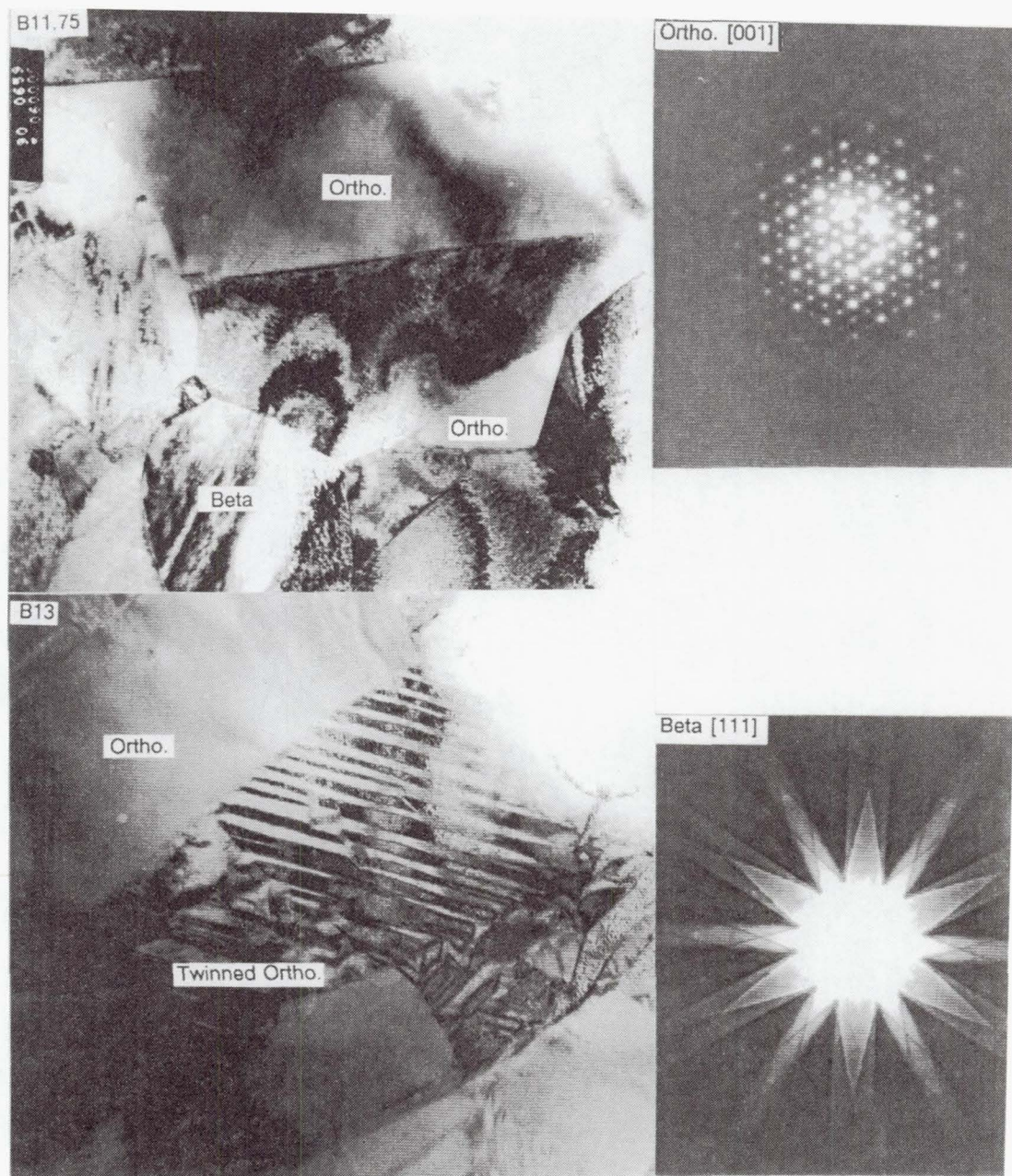
Figure 6.16. TEM micrographs and diffraction patterns of a 850°C/100h annealed B11.75 and B13 alloys showing twinned and untwinned orthorhombic phases with the beta phase.
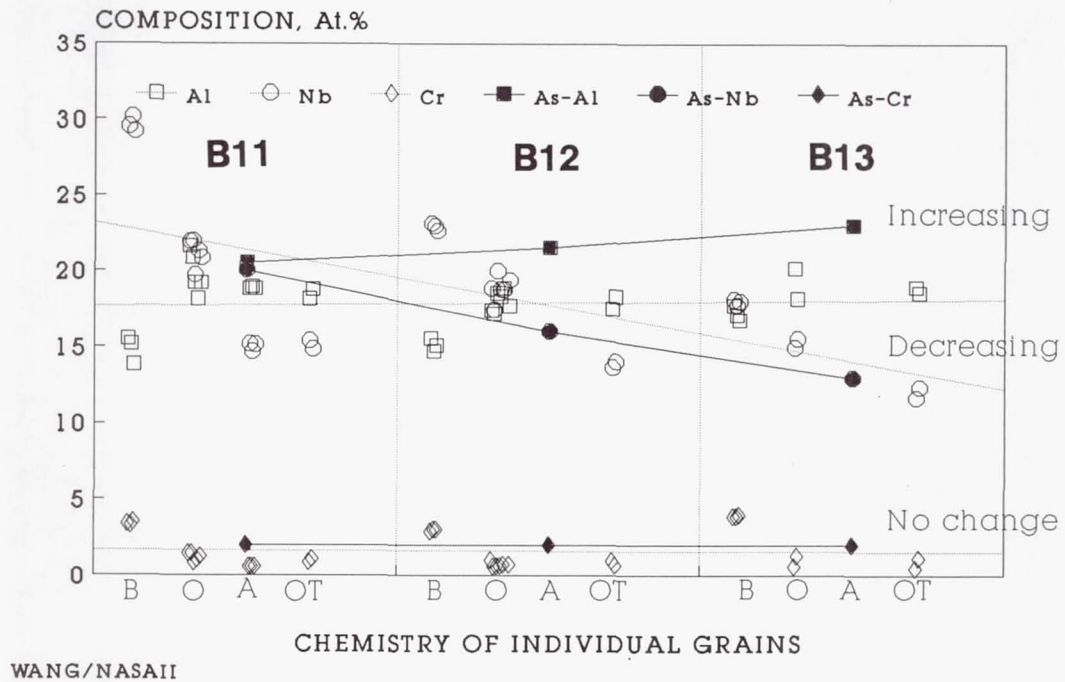
Figure 6.17. Differences in alloy composition associated with each individual phase showing decrease of Nb content in alloys from B11 to B13 resulting in the decrease of Nb content in their bcc phases, respectively. Similar trends are observed in orthorhombic and twinned orthorhombic phases.

Ti3Al–(Nb,Cr) ALLOYS
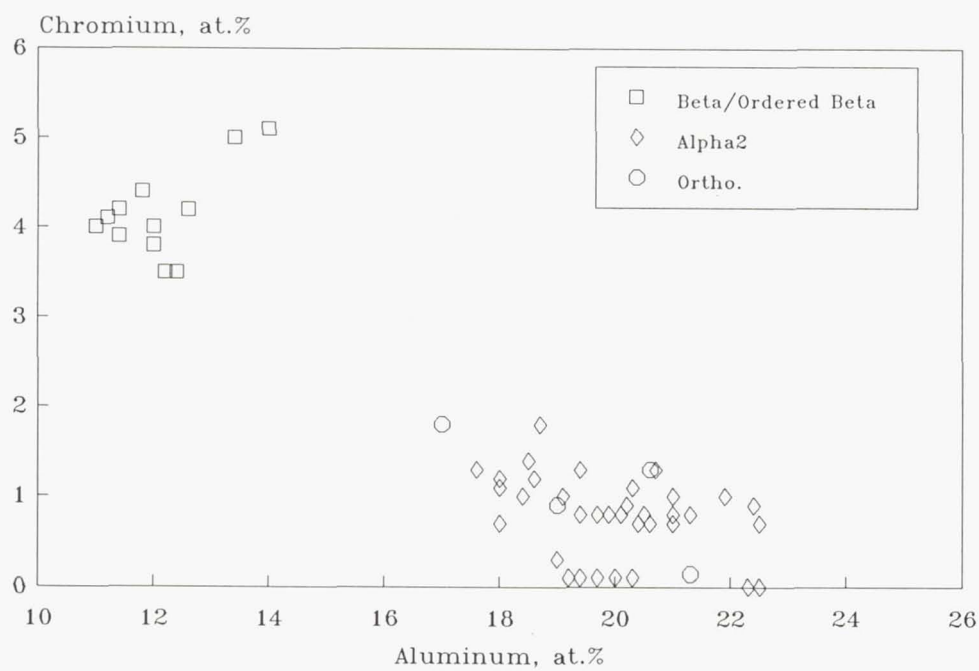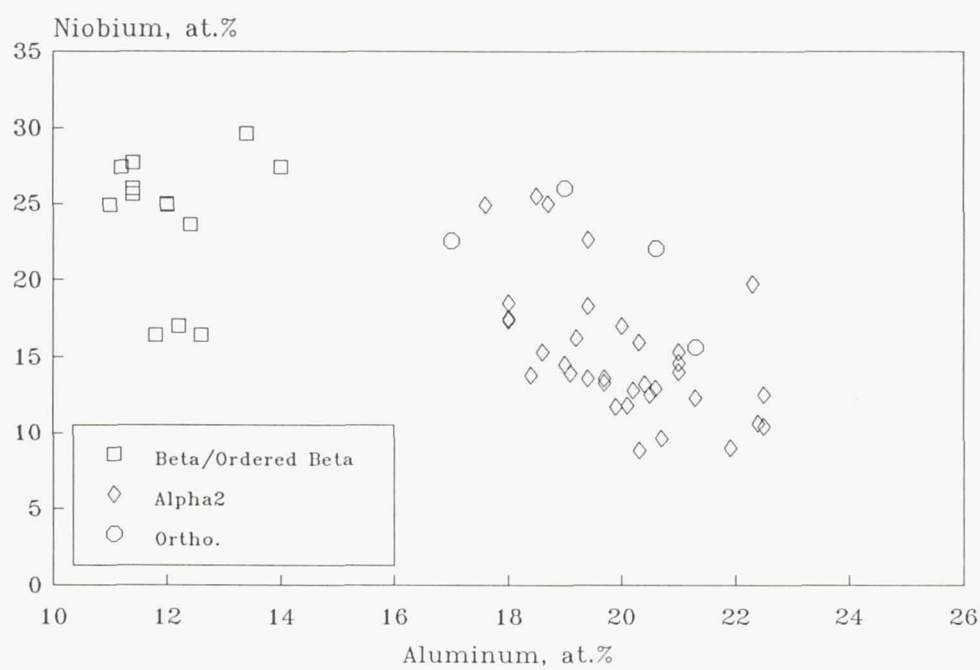
Figure 6.18. Mapping of phase boundaries in Ti-Al-Nb-Cr alloys resulting from 850°C/2h annealing.
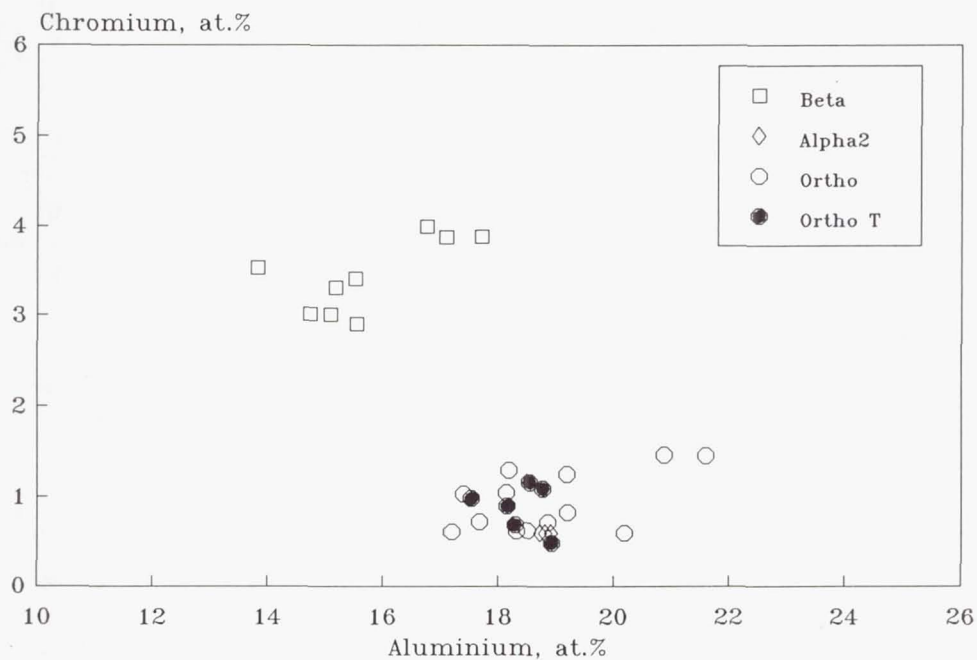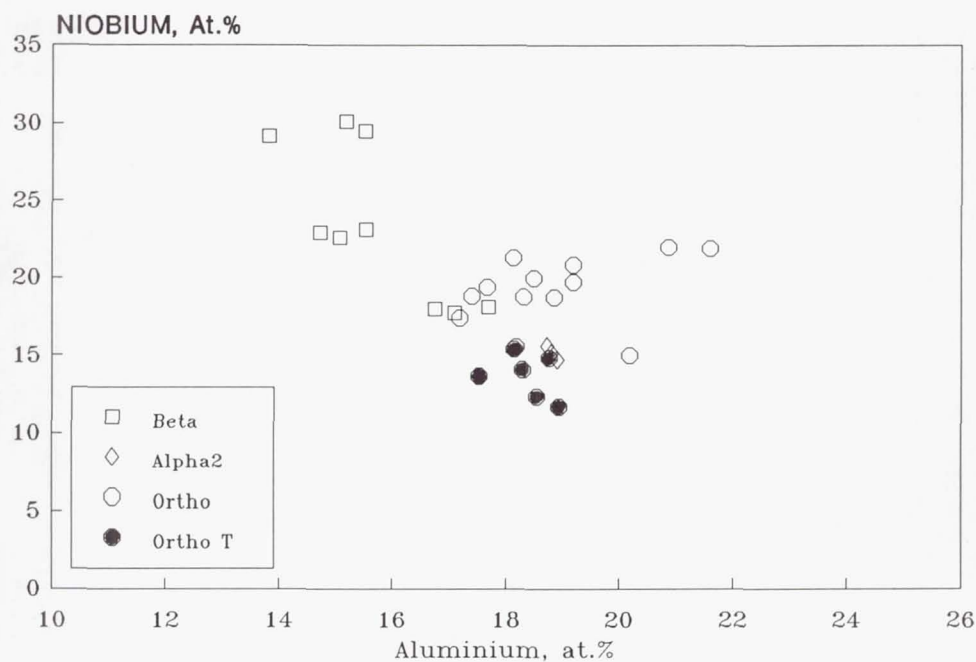
Figure 6.19.   Mapping of phase boundaries in Ti-Al-Nb-Cr alloys resulting from 850°C/100h annealing.

Figure 6.20. Phase boundaries of beta, alpha2, and orthorhombic phases in sputter deposited alloys resulting from 850°C/2h annealing (shaded areas) in comparison of the preliminary 1000°C partial section Ti-Al-Nb of liquid quenched alloys (dash lines) [Weykamp 1989].
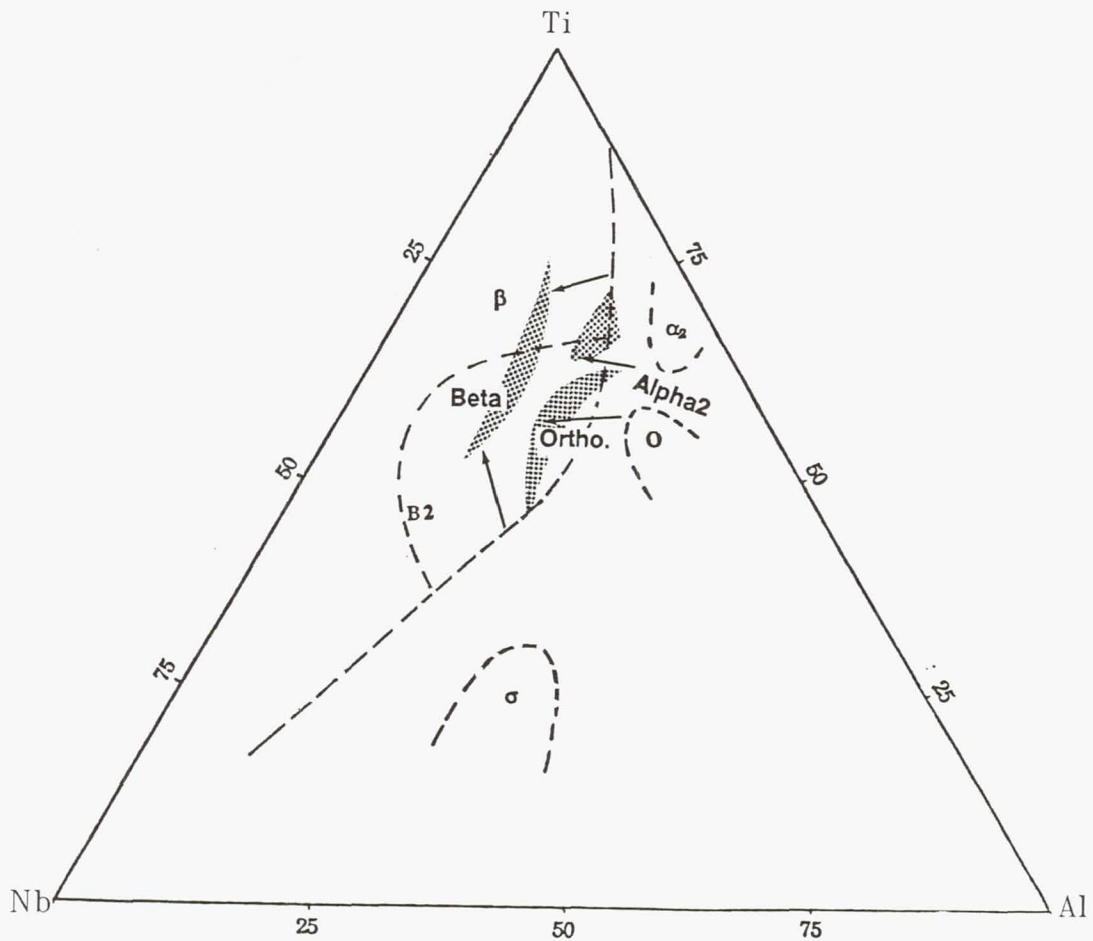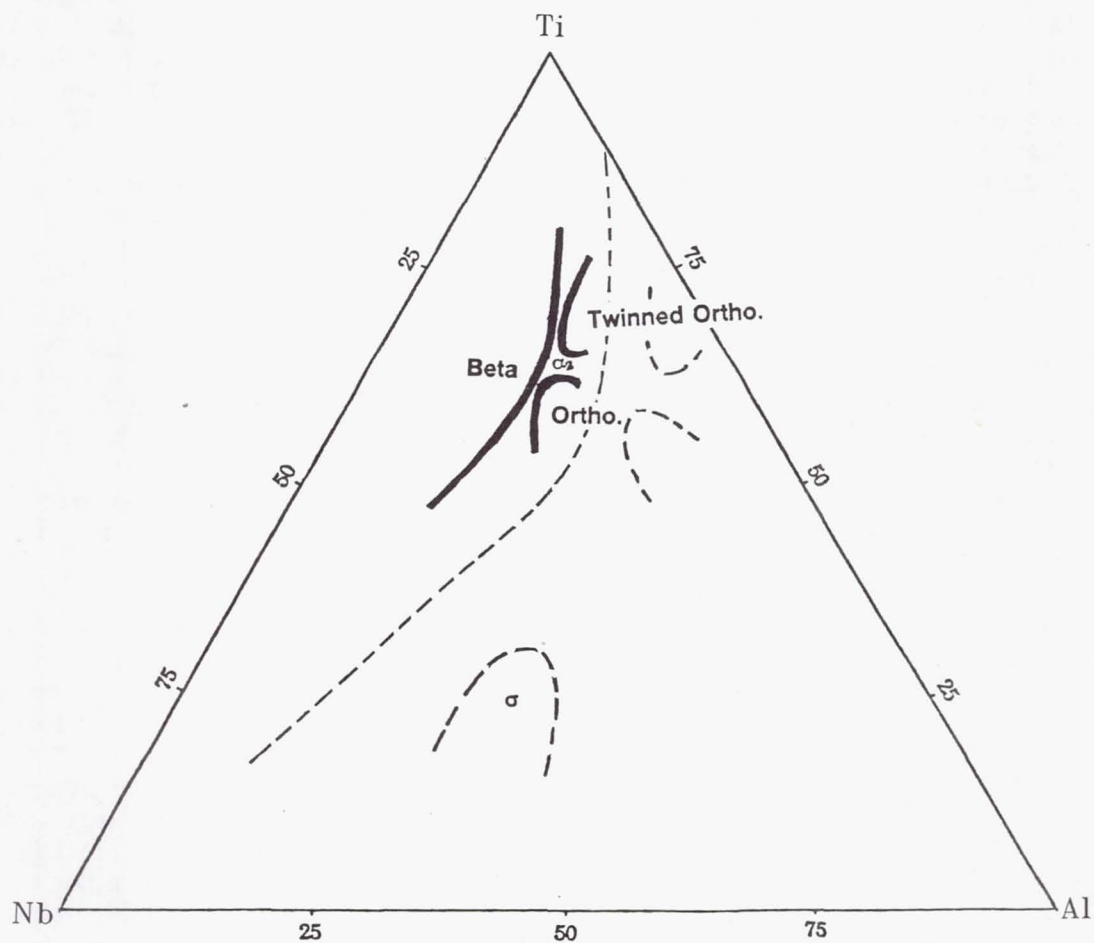
Solid line = Sputter deposited alloys
Dash line = Liquid quenched alloys

Figure 6.21.   Phase boundaries of sputter deposited alloys
resulting from 850°C/100h annealing as depicted in the ternary
Ti-Al-Nb diagram. All four different phases converge into a
small region separated only by a narrow phase field.

6c. Oxidation Characteristics

Sputter deposited nonequilibrium alloys could be useful as oxidation resistant coatings over bulk intermetallic alloys. If extended solubility alloys are identified with superior high temperature oxidation behavior [18-20], over the limiting characteristics of the Ti base alloys, sputter deposited coatings on the current commercial analogue (i.e., an improved TiAl or Ti$_3$Al alloy coating would be placed on a Ti-6Al-4V) would have the potential for extended high temperature service.

This work compares the oxidation rate and oxidation mechanism of sputter-deposited Ti-Al-Nb-Cr alloys, especially relating effects of Cr or Nb contents. Addition of Cr is currently of great interest because it would show strengthening effects as well as improvement of oxidation resistant behavior in Ti alloys. High Nb content in nonequilibrium Ti$_3$Al alloys could result in enhanced oxidation resistance for the alloy. The sputter deposited Ti$_3$Al alloy containing both Cr and Nb should provide a broad scope for understanding oxidation characteristics in the intermetallic alloys.

Seven alloys, identified in Table 6.5, were selected to compare the oxidation kinetics and relate them to the chemistry of alpha-2, orthorhombic and beta phases. Each specimen had a size of approximately 5 x 5 x 0.2 mm and weighed about 10 mg. They were obtained from the Deposit (5), gradient alloy deposit. Oxidation experiments were conducted by TGA measurements in two stages, first oxidized at 800°C and followed with a 1100°C oxidation. After the final 1100°C oxidation, characterization of oxidation path and formation of oxide/metal layers was made by electron microprobe analysis. Sections of the specimens including oxide scale, base metal and the interface were examined for oxidation products, porosity and elemental distribution.

Oxidation characteristics for this group of alloys are shown in Figure 6.22a, weight gain vs. time curves derived from the TGA measurement. During the initial oxidation stage at 800°C, overall oxidation rates were typically in the 2-8 mg/cm^2 range. These curves showed parabolic weight gain characteristics, indicating resistance to oxidation. The specimens containing high Cr content, such as -46Cr and -35Cr, were more resistant to oxidation than specimens containing high Nb content.

78

Table 6.5. Sputter deposited Ti-Al-Nb-Cr alloys subject to air oxidation studies.

Specimen Number	Composition at.%	Purpose
(5) 1-2-B7.5	Ti-14Al-50Nb-1Cr	Effects of Nb as Nb_3Al-Ti
(5) 1-2-B9.5	Ti-22Al-26Nb-1Cr	Effects of Nb in Ti_3Al
(5) 1-3-B8	Ti-11Al-44Nb-5Cr	Low Cr in Ti_3Al-Nb
(5) 1-3-B11	Ti-17Al-21Nb-11Cr	Effects of Nb and Cr
(5) 1-3-B15	Ti-17Al-5Nb-35Cr	Low Nb in Ti_3Al-Cr
(5) 1-4-B16.5	Ti-19Al-1Nb-20Cr	Primarily Cr effects
(5) 1-4-B20	Ti-14Al-1Nb-46Cr	Cr-rich beta phase

During the early second stage of oxidation at 1100°C, rapid oxidation occurred in high Nb content alloys. In this case, increase of Nb content resulted in higher oxidation rate. For alloys containing more than 20 at.% Nb, the foils were nearly completely oxidized after 500 minutes. After a maximum was reached, weight of these alloys started to drop, probably due to the volatility of niobium oxides. However, a much slower increase of the oxidation rate was found for alloys containing a high Cr content. Most significant, both -35Cr and -46Cr alloys still demonstrated parabolic weight gain characteristics.

Oxidation at both 800 and 1100°C showed similar oxidation characteristics for alloys containing high Cr content. Effects of Cr are demonstrated in a plot of maximum weight gain vs. Cr composition, Figure 6.22b. At 800°C, an increase of Cr content resulted in a decrease of oxidation rate. At 1100°C, weight gains for these alloys showed that oxidation rate initially increased with Cr content up to 20 at.% Cr, then decreased with higher Cr. In alloys containing 1 at.% Cr, increase of the Nb content from 26 to 50% resulted in an increase of the oxidation rate at both temperatures.

SEM micrographs and elemental x-ray maps obtained from polished cross-sections of thin foils after 1100°C exposure are shown in Figures 6.23 through 6.28. Microstructural and compositional analyses indicated that formation of oxide layers was strongly affected by the Cr/Nb ratio. Oxidation occurred in a homogeneous manner throughout the specimen containing a high concentration of Nb. Small additions of Cr, even 5 at.%, led to the initiation of elemental segregation. Higher Cr content, ranging from 11-46 at.%Cr, resulted in forming distinguishable multilayer oxides.

By comparison of the oxidation kinetics and microstructures, we concluded that oxidation rate normally will increase as a function of Nb content. In general, Nb addition promoted homogeneous oxidation of the foil [19]. A small amount of Cr would cause the formation of protective oxide scale and a greater amount of Cr would result in elemental segregation into oxide multilayers.

The oxidation rates observed in sputter deposited alloys are relative rates, to demonstrate effects of oxidation resistance due to various amount of Nb and Cr additives. Due to the thinness of the specimen and possible micro-porosity or microchannels in highly textured sputter deposited specimens, these oxidation rates may be higher than those which would be obtained from oxidation of thick bulk alloys.

6d. Mechanical Properties

Because of the strong interest in nonequilibrium Ti_3Al based alloy systems, new alloys based on Ti_3Al-Nb, Ti_3Al-Cr and Ti_3Al-(Nb,Cr) were further characterized for mechanical properties first at room temperature and subsequently at elevated temperatures up to 900°C. In this study, compositional gradient alloys were used to obtain preliminary behavior in terms of microhardness data as a function of alloy composition and temperature.

For materials development feasibility and screening studies, high temperature microhardness measurement is valuable, providing an efficient path to obtain mechanical properties data. Since high temperature creep mechanisms such as self-diffusion, may be identified from the hardness response, it is possible to determine the effect of creep on quasistatic indentation hardness measurements based on the following relationship derived by Atkins et.at:

$$H = A \exp (-BT) \qquad (1)$$

$$B/t = H^m \exp (-Q/RT) \qquad (2)$$

where H = hardness; A, B, and m are constants; t = loading time; Q = activation energy for creep; T = temperature; and R = gas constant.

The microhardness of as-deposited Ti_3Al-Nb, Ti_3Al-Cr and Ti_3Al(Nb,Cr) alloys were initially measured at room temperature. A series of 850°C/2h annealed alloys were then selected for high

80

temperature hardness measurements. The work was performed under a 10^{-7} torr vacuum in the test chamber of a Nikon high-temperature microhardness tester equipped with a Vickers indenter. The load range was from 100 grams to 1000 grams for times from 10 to 100 seconds. The load was applied to the approximately 0.15 mm thick cross-section of the sputter deposited alloys. Three measurements were made and their averaged values were used for the plots of microhardness vs. composition or temperature. In addition to the size of indentation, examination for crack initiation by the indentation and crack paths can yield preliminary information on the strengthening and toughness of the alloys, i.e. presence of a second phase may cause crack deflection or crack branching, contributing to fracture toughness.

The room temperature microhardness data of as-sputter deposited Ti_3Al-Nb alloys reflected the alpha2 to beta phase transition at 12-15 at.% Nb, Figure 6.29. A constant value was observed in alloys containing more than 25 at.% Nb. The high temperature microhardness data of annealed Ti_3Al-Nb alloys showed a slight increase in hardness up to 500°C and started to decrease at 600°C, Figure 6.30. An increase of Nb content, from 7.5 to 26 at.% did not produce significant changes in hardness values. The 7.5 at.% Nb alloy had the highest hardness in this group. A plot of microhardness vs. 1/T revealed the brittle to ductile transition temperature as near 636°C.

The room temperature microhardness data of as-sputter deposited Ti_3Al-Cr alloys initially showed a value of 500-600 Kg/mm^2 up to 15 at.% Cr, Figure 6.31. An increase of the hardness was associated with further increase of the Cr content. The high temperature microhardness data of the annealed alloys showed a nearly constant value up to 500°C and started to decrease at 600°C, Figure 6.32, except a high microhardness was observed for 22 at.% Cr.

The room temperature microhardness of the as-sputter deposited Ti_3Al-(Nb,Cr) alloys, Figure 6.33, exhibited a similar trend to the Ti_3Al-Nb alloys, an increasing of Nb content resulted in a decrease of hardness values. However, the high temperature microhardness values of the annealed alloys, Figure 6.34, exhibited a behavior similar to that of the Ti_3Al-Cr alloys.

In all cases, the hardness was insensitive to small composition variations. A common brittle-to-ductile transition temperature, obtained by extrapolation of the ductile and brittle regions of the hardness vs. 1/T curves, near 650°C was observed. Comparing with other alpha$_2$ alloys, such as from ALTA (cast) and RibTech (rapidly solidified), the sputter deposited alloys consistently displayed a higher microhardness up to 500°C, but the hardness rapidly decreased at temperatures greater than 600°C. At 700°C, the microhardness was still slightly higher than these reference

materials. However, rapid loss of hardness to only about 10% of the room temperature value, was observed in the 800-900°C range.

The rapid loss of microhardness at high temperatures is attributable to the lack of phase and microstructural stability in the annealed alloys. The phase and microstructural instability may have a basis in the intrinsic characteristics of the sputter deposited alloys. As-deposited alloys have an ultrafine and highly defected microstructure. This microstructure provides of a high level of available surface energy, which promotes complex phase transitions accompanied by sluggish recrystallization and grain growth during annealing. The test specimens, heat-treated at 890°C for 4 hours in vacuum before measurement, may not yet have reached the equilibrium state, as described in Section 6b. Formation of predominant beta and orthorhombic phases instead the alpha2 phase may also result in the low temperature mechanical strength.
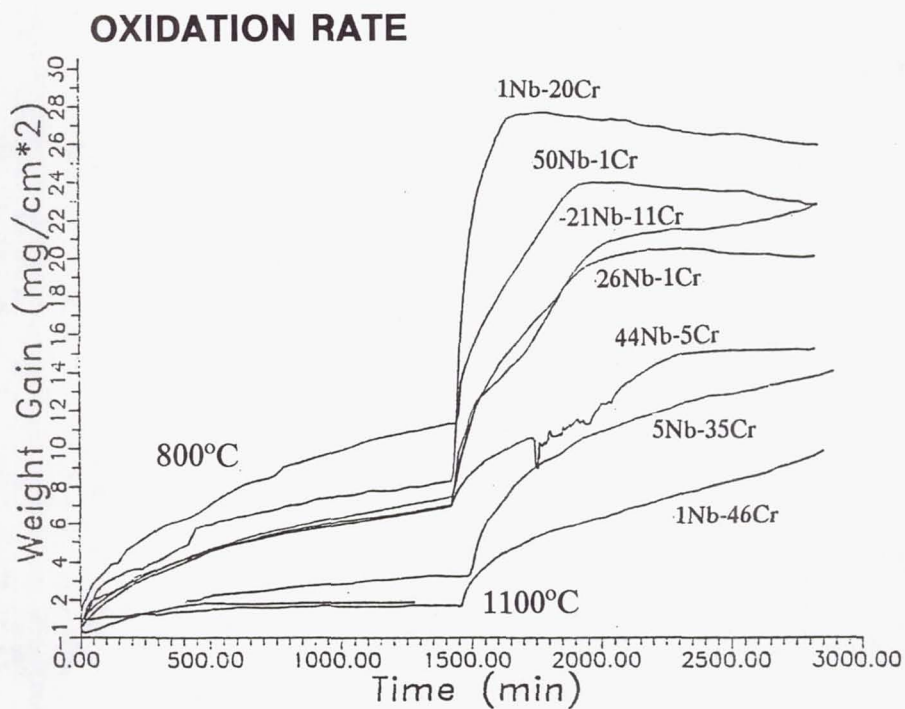
OXIDATION RATE

(a)

EFFECTS OF Cr
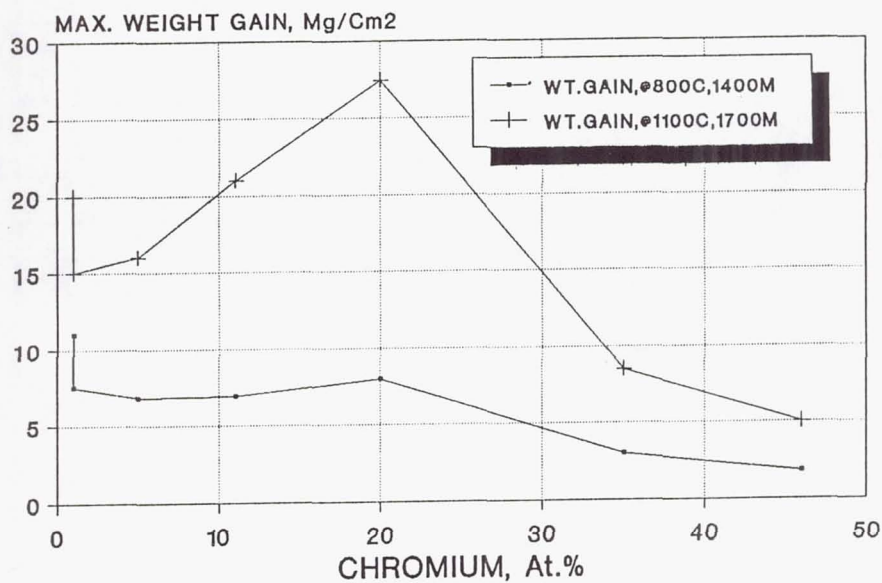
(b)

Figure 6.22.   Oxidation kinetics of Ti-Al-Nb-Cr alloys: a) as a function of oxidation temperature and time, and b) as a function of Cr content.
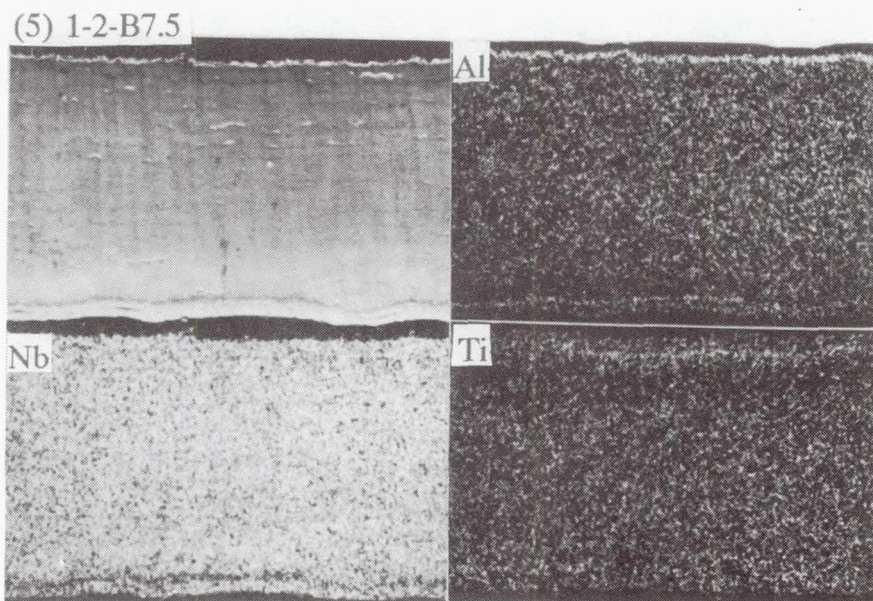
Figure 6.23. Homogeneously oxidized B7.5, 50Nb-1Cr oxidized at 1100°C. The surface has a thin Al-rich scale probably a result of early 800°C oxidation.
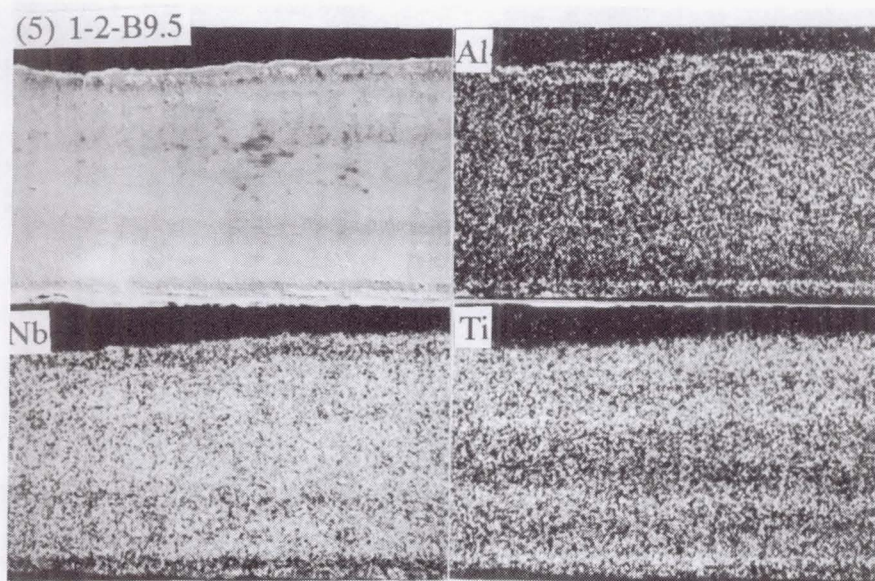
Figure 6.24. Homogeneously oxidized B9.5, 26Nb-1Cr at 1100°C showing only minor segregation of the oxides.
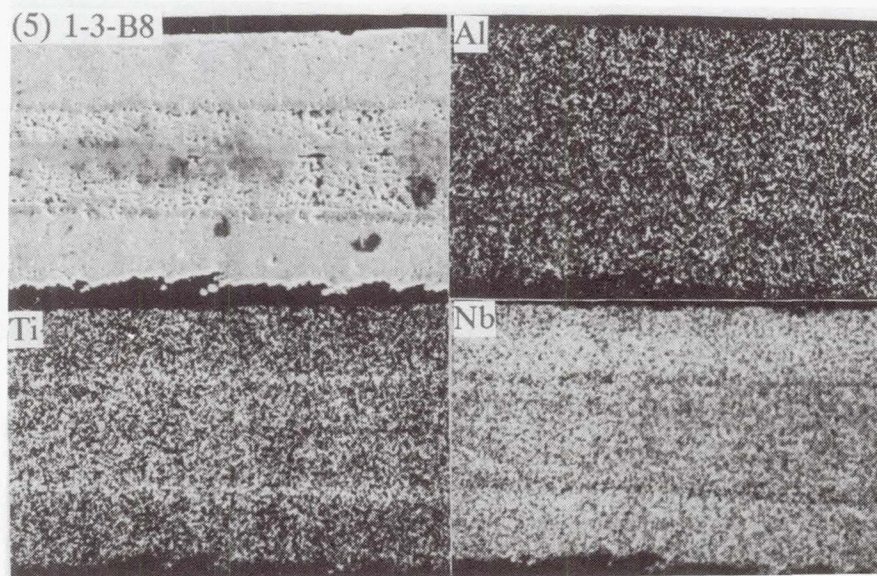
Figure 6.25. The interior of the B8, 44Nb-5Cr, foil had a black layer surrounded by a brown oxide crust. The core/crust interface is rich in Ti showing segregated oxide layers within the interior of the foil. The surface also shows a thin Al-rich scale.
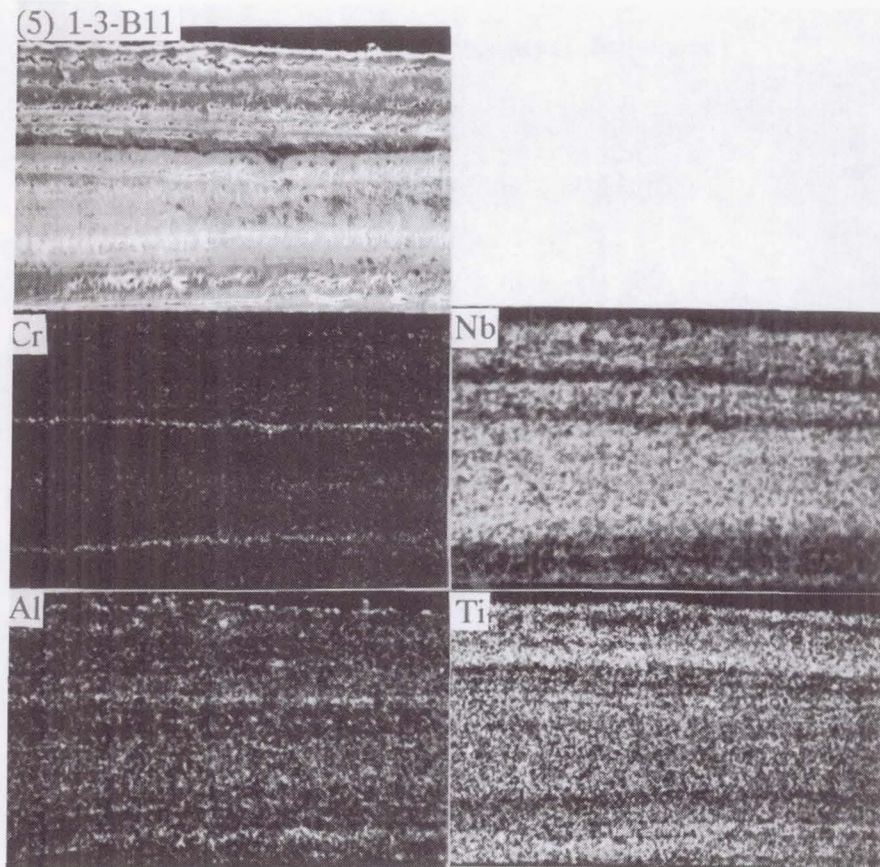
Figure 6.26. Exterior of B11, 21Nb-11Cr, foil had a multilayer oxide crust and interior had a metallic layer. The outer crust layer is rich in Ti and Nb. Inside the crust, several layers with various Nb, Ti and Cr distribution can be seen. The metallic core is protected by a Cr-rich layer.
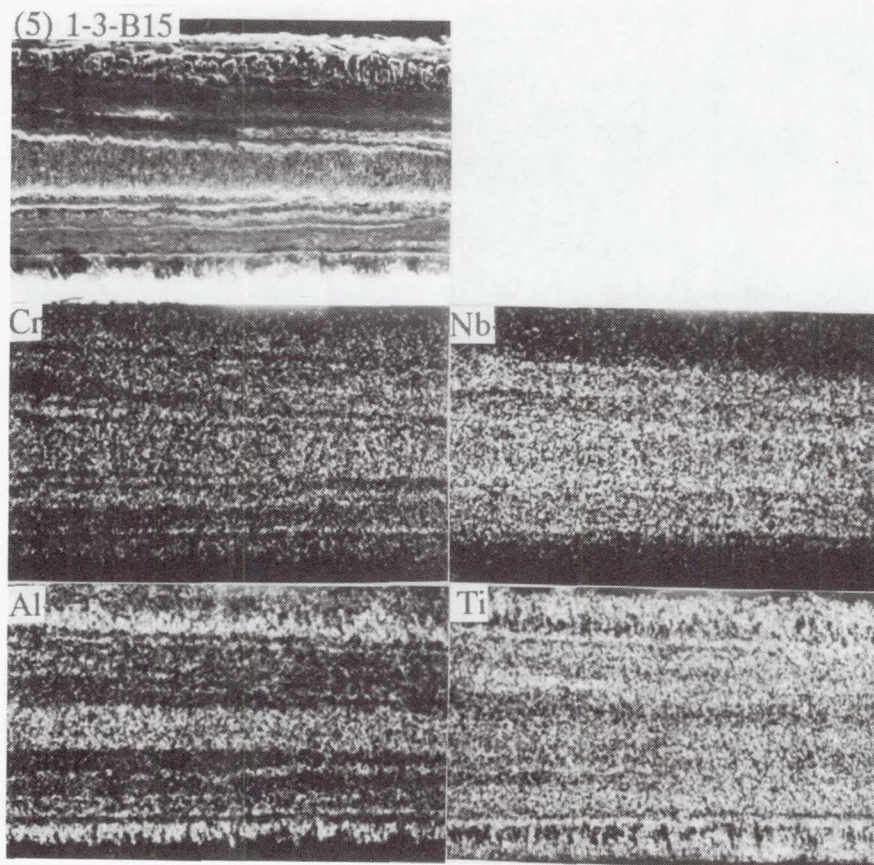
Figure 6.27. The B15, 5Nb-35Cr foil, exhibited strongly
developed oxide multilayers with an oxide exterior crust and an
interior metallic layer. The outer crust is rich in Ti followed
with a porous Al rich zone. The growth to Ti and Al oxides
normal to the foil surface has produced a scaly surface texture.

88
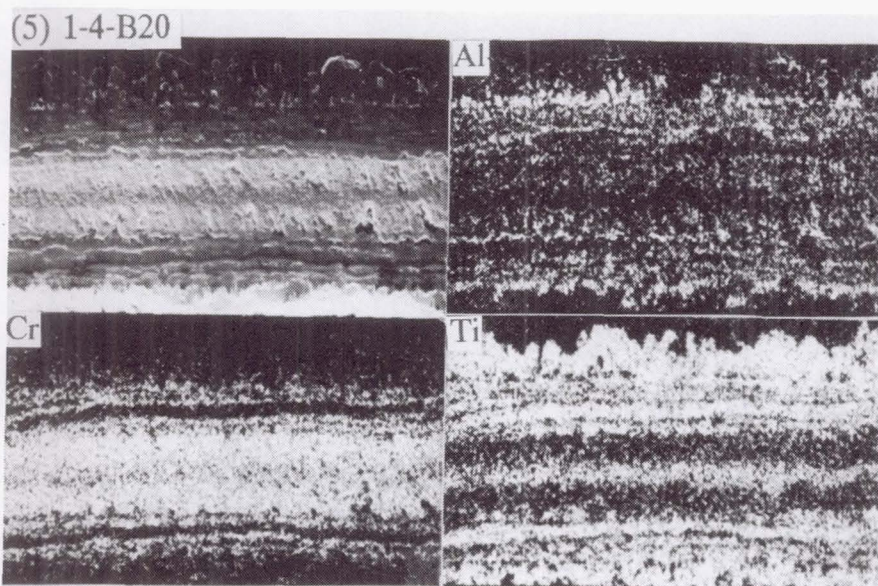
Figure 6.28. The B20, 1Nb-46Cr foil exhibited strongly segregated oxide layers and rough, scaly, foil surface consisting of a multilayer oxide exterior crust and an interior metallic layer. The outer crust is formed by Ti-oxide followed by several alternating Ti-rich and Al-rich oxide layers. The inner layer is rich in Cr and the center of the layer is rich in Ti.

MICROHARDNESS OF SPUTTER DEPOSITED
Ti3Al—Nb, (5) 1—2—A
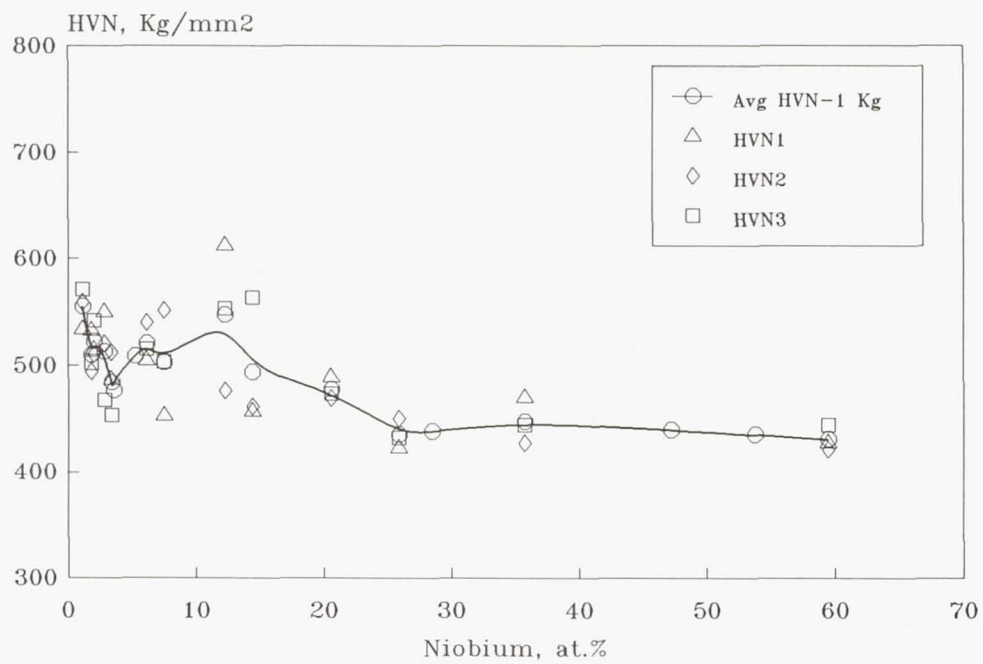
Figure 6.29. Microhardness of as-sputter deposited Ti$_3$Al-Nb
alloys.
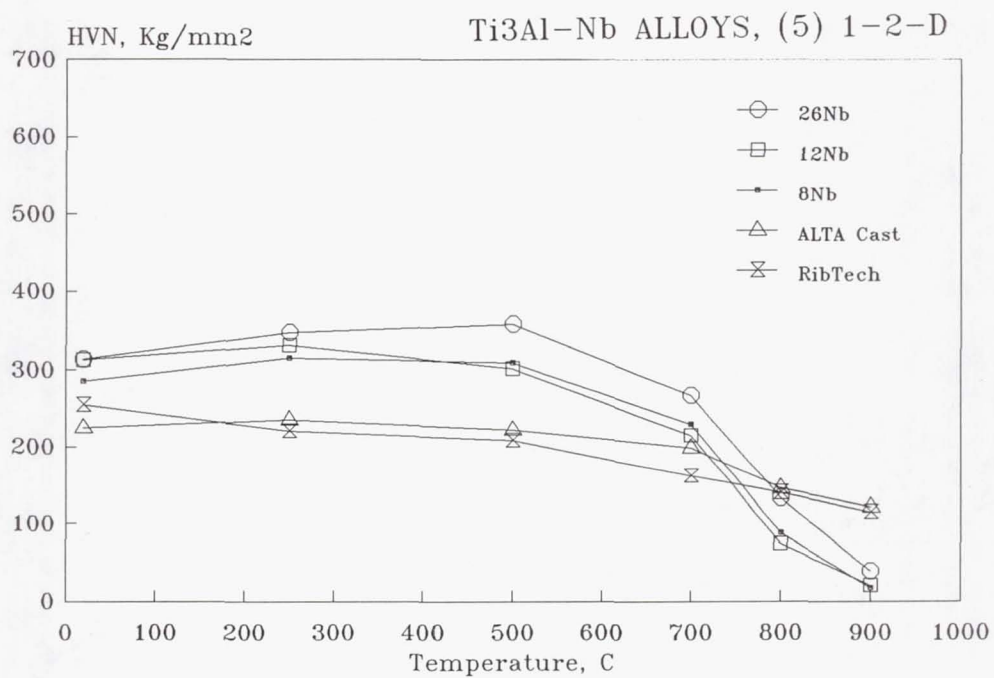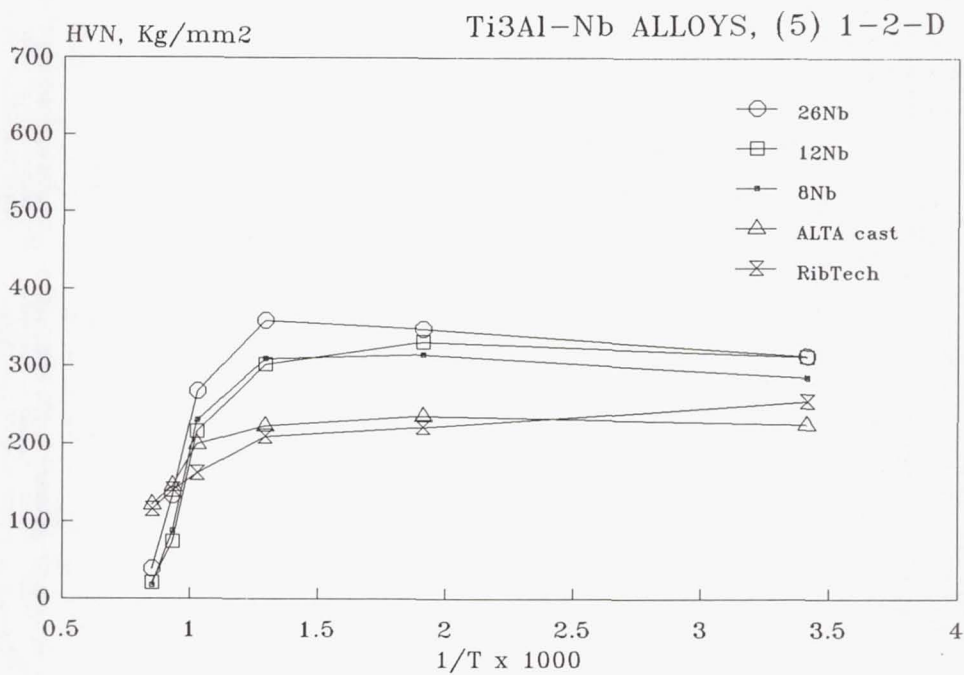
Figure 6.30. **Microhardness of sputter deposited Ti$_3$Al-Nb alloys: a) annealed alloys at different test temperature, and b) as a function of 1/T.**

MICROHARDNESS OF SPUTTER DEPOSITED
Ti3Al–Cr, (5) 1–4–A
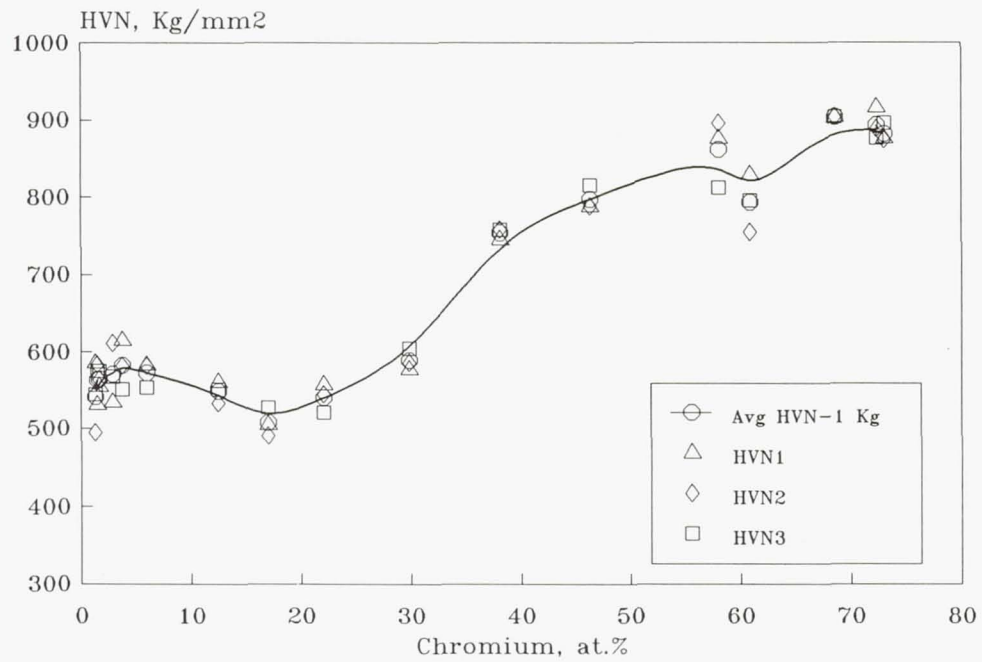
Figure 6.31. **Microhardness of as-sputter deposited Ti₃Al–Cr alloys.**
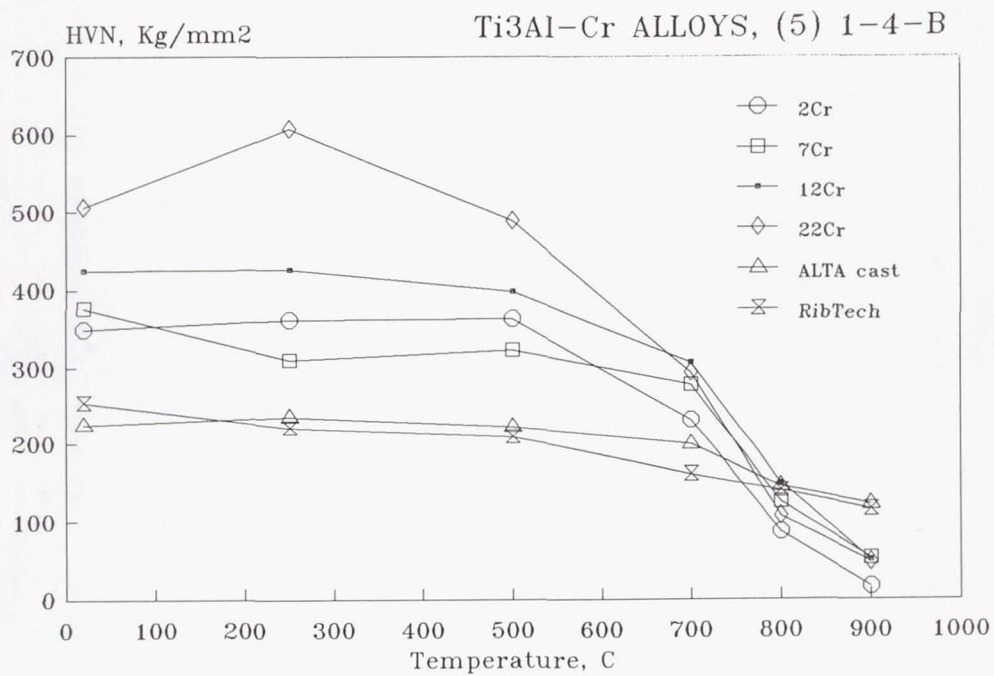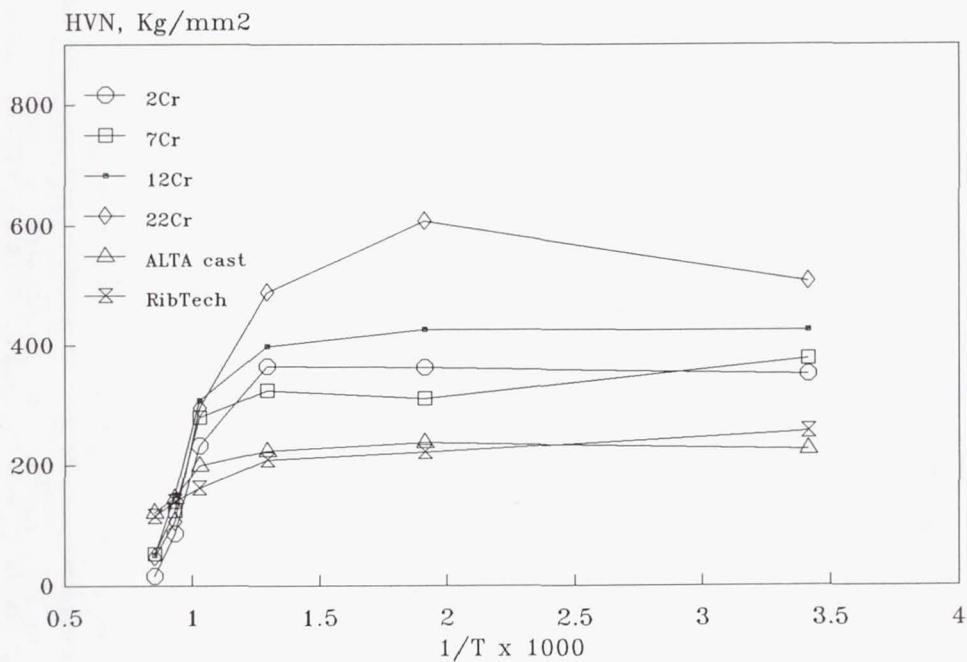
Figure 6.32. Microhardness of sputter deposited Ti$_3$Al-Cr alloys: a) annealed alloys at different test temperature, and b) as a function of 1/T.

MICROHARDNESS OF SPUTTER DEPOSITED
Ti3Al-(Nb,Cr), (5) 1-3-A
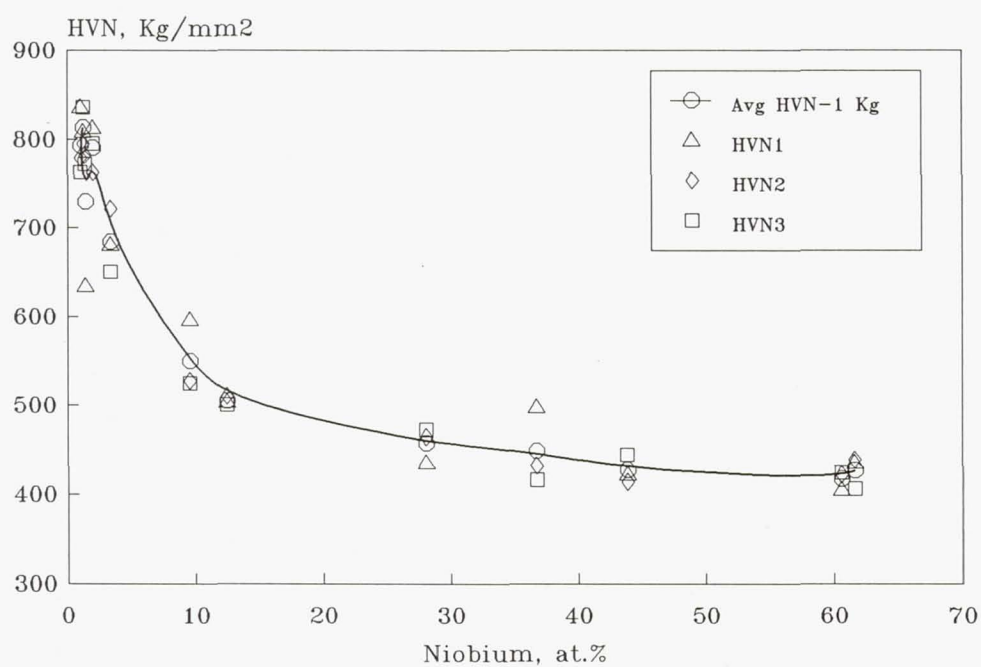
Figure 6.33.   Microhardness of as-sputter deposited Ti$_3$Al-(Nb,Cr) alloys.
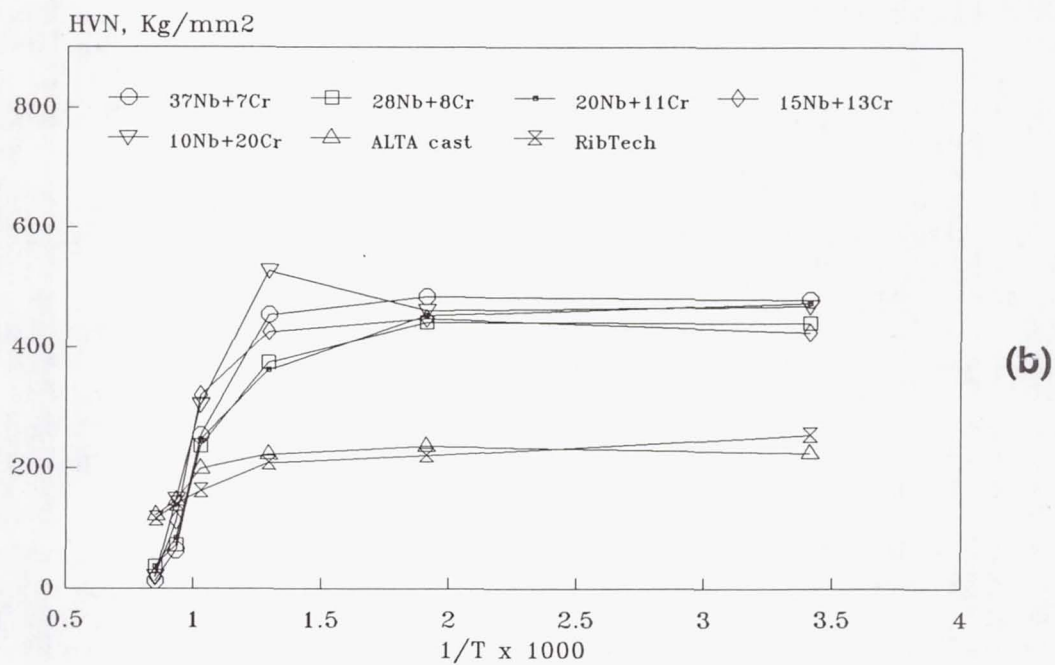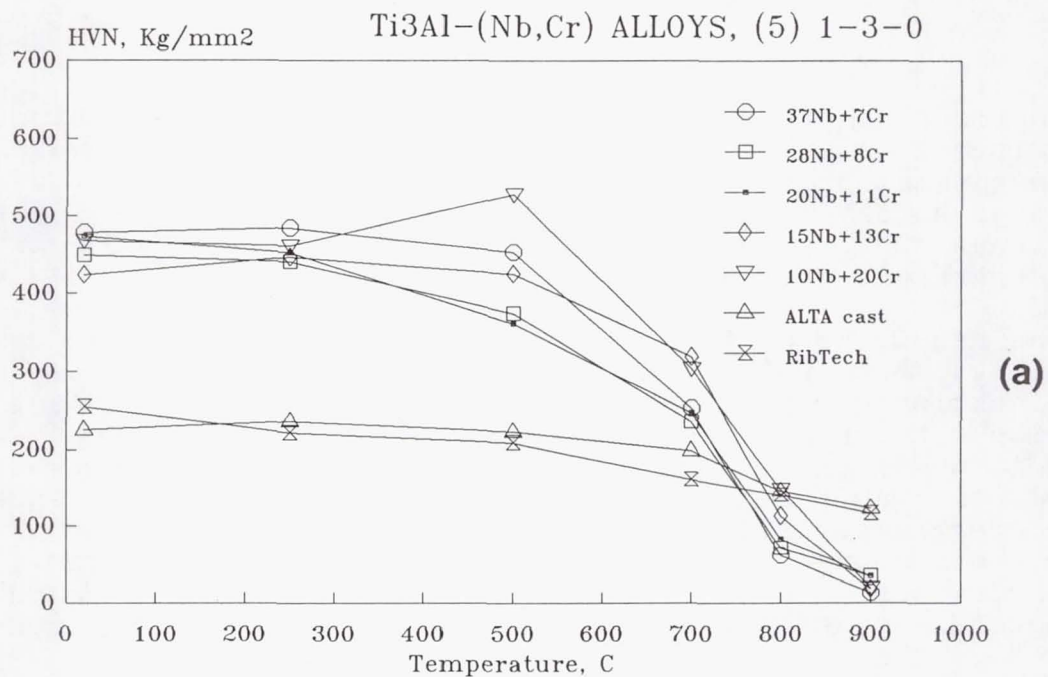
Figure 6.34. Microhardness of sputter deposited Ti_3Al-(Nb,Cr) alloys: a) annealed alloys at different test temperature, and b) as a function of 1/T.

7. FABRICATION OF HIGH QUALITY FOILS

Fabrication of high quality foils by sputter deposition was critical to ensure proper structural characterization and mechanical property evaluation for nonequilibrium alloys. A large effort was devoted to obtaining high quality foils of alpha2-Ti_3Al at an optimized alloy composition for high temperature mechanical testing.

The manufacture of thin foils based on intermetallic compound alloys, either free standing or bonded to a substrate, presents a significant processing challenge. Foil is commonly defined as wide metal strip having a thickness of 150 μm (0.006") or less. Foil produced as narrow strip is more commonly referred to as ribbon. As the thickness of foil approaches the dimension of microstructural features of the metal, the effect of microstructure irregularities becomes quite important. Large inclusions, coarse precipitates, or brittle grain boundaries can potentially span the entire thickness and may significantly reduce the net section strength of the foil. Local irregularities have a particularly strong influence on foil ductility because they serve as sources for tensile instability and result in failure at nominal section stresses below the yield point. Thus it is important to maintain alloy purity, surface quality, and a high degree of metallurgical homogeneity at all stages of foil manufacture.

Since early 1990, large size alpha2- and superalpha2- Ti_3Al foils have been successfully fabricated by rolling. Rolled foils of up to several feet wide have been commercially available from Texas Instruments (TI) [21]. Timet [22], and Teledyne Wah-Chang (WC) [23] also have demonstrated smaller size foils. Fabrication of short ribbon strips were reported by Lockheed [24] using a "pack rolling" process. These various processing methods for foil production rely on pressing in vacuum, the use of inert atmosphere chambers, or encapsulation to protect against atmospheric contamination.

Because high rate sputter deposition can produce gauge thick deposits in one-step processing, the feasibility of producing high quality foils was investigated in this research. Direct deposition of intermetallic compound alloys by a vacuum process would be attractive for high temperature alloys since the process can maintain a high degree of cleanness. Sputtering also involves a low process temperature. At present, vacuum deposition processing is not readily applied to the case of complex multicomponent alloy systems. There is difficulty associated with evaporation and condensation of a multicomponent alloy due to differences in vapor pressures. Only simple metals, such as high purity titanium, have been processed by the vacuum deposition technique. Other materials successfully deposited

include Ti-6Al-4V alloy, Zr, Hf, Ni and Cu. Sputter deposition has also been used successfully to produce metal foil from Mg and Cr.

High quality foils are defined as uniform in microstructure, low in texture, possess a high degree of purity, and exhibit a low density of defects. This type of foil is important to assess mechanical properties. Several materials and processing variables were investigated during fabrication of high quality foil by sputtering. High quality sputtering targets were prepared with pure metals and cast in vacuum by a skull casting process to reduce inhomogeneity and defects in the target materials. Formation of strong texture in sputter deposits was suppressed by using a bias voltage at the substrate. A proper selection of sputtering parameters and target materials resulted in high quality sputter deposited foils. Descriptions of processing variables, and resultant microstructure, chemistry and properties of resultant foils are given in the following sections:

7a. Sputtering target fabrication

The sputter deposition process can provide a highly clean environment for thin foil fabrication, especially in comparison to traditional alloy processing techniques involving many processing steps, such as by rolling and extrusion, and P/M processing. However, many researchers tend to use hot-pressed sputtering targets because fabrication of solid and dense high temperature intermetallic alloys into a large and flat disk of more than 3" diameter is difficult. Hot-pressed sputtering targets typically possess high oxygen content, porosity and unbonded particles. During sputtering, outgasing and loose particles could severely affect the stability of the plasma resulting in substrate overheating, flaking, wart formation and deposit inhomogeneity. Solid and dense targets containing low impurity levels are critically important to the fabrication of high quality foils. This work has resolved many problems associated with fabrication of sputtering targets for intermetallic Ti_3Al alloys.

Sputtering targets of intermetallic alloys with tailored multicomponent compositions were not available commercially. The skull casting process was used to provide solid sputtering target materials of several compositions needed for this research. Skull casting, using a nonconsumable electrode and water-cooled copper hearth enclosed in a vacuum chamber, provided a high purity cast. Skull casting was conducted at Oak Ridge National Laboratory under the direction of S.K. Sikka, first on binary Ti-Al alloys and later on multicomponent targets of Ti_3Al-Nb alloys.

Initial target fabrication work encountered numerous problems in obtaining a full 5"-diameter target material. These problems were traced to control of melt temperature, mold design and casting procedure. After several trial runs, three 1/4" thick Ti-Al target materials were cast into a special 5" x 5" size plate, Figure 7.1. The first cast, Target Alloy #1, had three visible cracks, a 3"-long crack and two smaller cracks about 1" long. Using an optimized melt temperature and better vacuum, the second (Target Alloy #2) and third (#3) casts were successfully fabricated without showing any visual cracks. X-ray radiographs revealed that the later casts were free of cracking, though they contain small voids less than 3 mm in diameter.

The cast target materials were too hard and brittle for conventional machining. Consequently, a sputtering target (Ti_3Al) was prepared by cutting a 5" diameter plate out of the cast Target Alloy #2 plate using an abrasive waterjet, and bonded to a 3/8" thick OFHC copper target holder. This target was used to fabricate the first high quality Ti-Al-Nb-Cr alloys, Deposit (6). Another cast target Ti_3Al-1Ru was prepared to demonstrate the fabrication of high quality thin foils, Deposit (7), by magnetron sputtering.

After successful casting of brittle Ti-Al alloys into 0.25" thick target materials, three highly alloyed Ti_3Al-Nb target materials, #4, #5 and #6, were fabricated in the same manner, with compositions, as shown in Table 7.1. The selection of these compositions was based on results of room temperature ductility, microstructure and phase distribution studies made on the high quality foil obtained from Deposit (6), containing a graded composition of Nb. The alloy compositions were slightly adjusted to compensate for sputtering and material characteristics. Since the sputtering yield of aluminum will be strongly affected, as much as 15%, by the bias voltage additional Al was added to compensate this expected loss. The Y addition in Target Alloy #4 was used to remove solution oxygen (2500 ppm) by forming stable Y_2O_3 dispersoids in the starting ALTA alpha2-Ti_3Al alloy used in target fabrication.

Vacuum casting of these sputtering targets into a _full_ 5" size target material was unsuccessful. The problem was associated with the combination of high melting temperature and high viscosity of molten Ti-Al-Nb alloys. After 10 casting runs, this problem was resolved by casting two half-size sections, then joining them to form a circular target.

Initial sputtering runs indicated that these targets were not bonded properly to the copper target holder by a commercial target fabricator using indium bonding agent. This problem was addressed by sputter coating the back side of the target material with a thin layer of copper, and then bonding to the copper backing plate by soldering.

98

Table 7.1. Alloy compositions selected for fabrication of single composition sputtering targets.

Target Alloy	Ti	Al	Nb	Mo	V	Y	(wt%)
#4	Bal	14	22	–	–	2	
#5	Bal	16	21	2	3	–	
#6	Bal	16	19	2	1	–	
#7	Bal	13.3	19.0	2	2.8	–	

In July 1990, a cast low oxygen content (590 ppm) alpha2-Ti_3Al ingot of 4.8" diameter was made available to this program by S. M. Tuominen of Teledyne Wah-Chang. The cast material was fabricated into a target #7, for fabrication of high quality single composition foils, deposits (11) and (12).

7b. Sputtering Process

The next step for fabrication of high quality foil was to adjust sputtering parameters for the reduction of growth textures and macroscopic voids common to sputter-deposited alloys. Both triode sputtering and magnetron sputtering were investigated.

7b.1. Triode Sputtering:

Most of the early gradient deposits fabricated during the period of 1988-89 were obtained by triode sputtering at a non-biased substrate potential, or floating potential. The floating potential was estimated in the neighborhood of -15 V referenced to ground. The resultant deposits usually developed a strongly textured microstructure as well as a low density columnar growth of microvoids throughout the thickness of the deposit. The as-deposited structures had a (0002) texture for the alpha2 phase and (110) texture for the beta phase. These textures were related to the columnar growth of the deposit, typically formed onto a room temperature substrate. The highly columnar growth resulted in microvoids such as observed at the fracture surfaces (through the thickness) and in the interior of the deposit (indicated by the presence of loosely bonded areas), Figure 7.2.

A negative bias voltage, in the range of 40-100 V, was selected to eliminate the columnar growth of the sputter deposits. The major effect of bias was equivalent to an increase of the substrate temperature via enhanced electron bombardment. A high bias voltage increases the mobility of the atoms at the surface of the substrate. In this case, alloys deposited under a high substrate bias voltage would have a lower quench rate than that without bias. Biased deposits result in larger grains and more equiaxial grain orientation than those deposited without the substrate bias.

Initial bias triode sputtering was conducted for fabrication of the gradient Ti_3Al-(Nb,Cr) alloy deposit shown in Figure 7.3. The center part of the deposit, containing Ti_3Al-(Nb,Cr) alloys, was shattered after the completion of the sputtering run, indicating a high degree of brittleness. However, the region of Ti_3Al-Nb alloys showed high quality foil characteristics, Figure 7.4. The as-deposited foil had a smooth surface appearance replicating the substrate surface topography. The foil was highly flexible and could be bent to 180° without breaking. Fractured surface examined under SEM showed mostly smooth fracture surfaces without columnar growth. Ductile fracture patterns were observed at 8-10 at.% Nb regions. X-ray diffraction showed an equiaxial grain orientation consisting of alpha2 and beta.

7d.2. Magnetron Sputtering

The feasibility of using magnetron sputtering for eliminating macroscopic defects and voids was also investigated. The resultant deposit (7) was 30 μm thick with a smooth surface appearance, as shown in Figure 7.5. Cross-section micrographs showed that the deposit had a nearly defect free microstructure. However, the fracture surface indicated the presence of some columnar growth. Since no substrate bias could be applied with the magnetron sputtering apparatus used in this study, further control of the microstructure of the resultant deposit was not possible.

7c. Single Composition High Quality Foils

A total of five sputtering runs were conducted to obtain high quality foils based on selected compositions for alpha2-Ti_3Al alloys. The purpose was to obtain sufficient thin foil materials for fabrication of high temperature mechanical testing specimens. After the purity and columnar growth problems were resolved,

concerns were focused on obtaining the desired alloy composition in the resultant foils.

Previous composition analyses indicated that bias sputtering could severely affect the Al content when compared with that of the unbiased deposit. By comparison of the sputtering rates for Ti, Al, Nb, and Cr, as shown in Figure 7.6, it was expected that Al deficiency could be as high as 3 at.% at a 100 V bias voltage. Additional Al, up to 3 at.%, was incorporated into the target alloys (Table 7.1) for compensation of the expected Al loss in preparation of the high quality foil.

The first single composition high quality foil, Deposit (8), was fabricated onto a Cu substrate using a 100 V bias based on Target Alloy #4, Figure 7.7. The deposit was nearly 7 mil thick and contained two distinct layers of foil, both had very smooth surfaces. The formation of two layers may be due to a short interruption of the sputtering process (in milliseconds) either due to plasma instability, or possibly associated with a sudden change of sputtering gas pressure. A thin foil of 180 μm thick was separated with a sharp knife edge from the underlying layer, which was bonded to the Cu substrate. Elemental analysis was made along the cross-section of this foil in order to trace the change of Al content as a function of the buildup of the foil thickness during sputtering. The results indicated that the Al content in the foil was about 19-20 at.% nearly 6-7 at.% less than the target Al content, Figure 7.8. On the other hand, Nb in the foil was between 10-11 at.% very close to the target Nb content.

Due to large Al loss in the final foils, Deposit (10) was prepared with a 60 V bias with Target Alloy #6. By using a lower bias voltage and a higher Al content target, we expected to maintain the Al content in the foil between 23-26 at.%, without degrading the high integrity of the microstructure. As shown in Figure 7.9, compared to the Al content in the sputtering target, Al loss was approximately 3 at.% in the resultant foil formed at the center of the deposit (180 μm thick). A higher loss of the Al, up to 8 at.%, was observed in the foil (130 μm thick) formed at the edge of the deposit. The 60 V bias yielded the desired Al content, near 22-28 at.% averaging 26 at.%. Apparently, Al loss is associated with both bias voltage and plasma density at various regions of the deposit. The Nb content was not affected by the bias voltage and consistently remained at 9-10 at.%.

7d. Thermal Effects and Mechanical Properties

With a large quantity of homogeneous materials available through
the single composition sputter deposited alloys, thermal effects
and mechanical properties studies were conducted based on these
thin foils. Tensile test specimens were prepared by several
steps, first by machining the deposit from the substrate by wire
EDM, and subsequently removing the remaining Al backing by
concentrated NaOH solution. The resultant thin foils are shown
in Figure 7.10. Up to 16 test specimens were EDM machined from
each foil, as shown in Figure 7.11.

Thermal annealing studies were conducted to determine the proper
treatment for these test specimens. Room temperature ductility
was compared with highly ductile alpha2-Ti_3Al foils made by Texas
Instruments and Teledyne Wah-Chang. After vacuum heat treatment
in the 850-950°C range for 0.5 to 20 hours, thick (5-7 mils)
sputter deposited foils exhibited limited ductility. Only foils
under 2 mils thick had some ductility. X-ray diffraction showed
that annealed sputter deposited foils exhibiting limited
ductility had more beta phase than exhibited in commercial
alpha2-Ti_3Al foils annealed in the same conditions.

Elemental analysis made on Deposit (10) foils indicated that Al
content could be affected by the heat treatment, Figure 7.12. A
loss of nearly 10 at.% Al from the as-deposited foil was found in
two 930°C/4h specimens. However, the loss of Al at 850°C/2h and
950°C/2h was less, approximately 5%. The loss of Al was evident
from the discoloration of the inner Ta foil surface used to wrap
the specimen during heat treatment. No Ta foil discoloration was
observed during annealing of commercial foils and sputtered foils
at 950°C. We have not identified the conditions for Al loss,
whether it was associated with a specific group of foils, or
behavior driven by phase stability as affected by annealing
temperature or time. If the observed Al loss is real, it would
indicate a high Al mobility during early stages of annealing.
This Al mobility may be driven by either the presence of
elemental Al, or the high energy state of the as-deposited alloys
consisting of ultrafine grains, disordered structure and
containing a high density of defects. A high Al mobility would
promote complex grain growth and nucleation of different phases,
such as alpha2, beta and orthorhombic phases described in Section
6c. The possible loss of Al during annealing may also explain
the continuous phase shift from 850°C/2h to 850°C/100h observed
in Ti_3Al-(Nb,Cr) alloys, in the sequence of beta, alpha2,
orthorhombic and twinned orthorhombic phases. As the Al content
is reduced below 22 at.% by heat treatment, the alpha2 phase will
be replaced by the beta and twinned orthorhombic phases.

The observation of low room temperature ductility and possible Al loss in annealed high quality foils led to questions concerning our target composition selection and oxygen content. To address these concerns, Deposits (11) and (12) were prepared based on low-oxygen content Target #7 (WC-alpha2-Ti$_3$Al), shown in Figure 7.13. The Deposit (11) foil debonded from the substrate during the final stage of sputtering. Deposit (12) resulted in high quality deposit with 23-24 at.% Al. High quality foils were fabricated at two different bias voltages, starting at 100 V for the first 1-mil thick foil and reduced to 40 V for the remaining 5-mil thick foil, Figure 7.14 The two layers of resultant foils were separated by inserting a sharp knife edge between the layers. Elemental analysis was made on as-deposited surfaces (unpolished) facing the target, Figure 7.15. Heat treatment of the Deposit (12) foil resulted in confirming previous observation of high beta phase content and low room temperature ductility. However, Al loss was not observed from the as-heated surfaces after heat treatment at 850°C. It is possible that the as-deposited surfaces may be enriched with Al diffused from the bulk. Since Deposit (12) foil was prepared at the end of this research, it was not feasible to carry studies any further. The material was archived for future studies.

Because of the lack of sufficient ductility in sputter deposited tensile testing specimens, high temperature mechanical property evaluations were made by comparison of microhardness values. Microhardness values of two ductile alpha2-Ti$_3$Al foils, rolled foil by Texas Instruments, and rapidly solidified ribbon by RibTech, were also obtained to compare with the sputter deposited foils.

Microhardness data indicated that sputter deposited foils initially had a high hardness values up to 500°C, but rapidly decreased to a very low value above 700°C, Figure 7.16. Low hardness in the 700 to 800° range must be related to the amount of beta phase and continuous phase/composition shift in sputter deposited foils. In comparison, alpha2-Ti$_3$Al alloys had lower hardness initially, but the hardness was maintained to temperatures up to 900°C. The RibTech alloy had a slightly higher hardness than that of the Texas Instruments alloy throughout this high temperature range. Microhardness values as a function of temperature are summarized in Figure 7.17.

7e. Impurity Control in Ti-Al-Nb Foils

Since the sputter deposited foils were typically less than 10 mils thick, the effects of gas impurity in the material would be a major concern. Two types of impurity could be introduced during the sputter processing, oxygen and krypton. Oxygen level in Ti-Al-Nb alloys is critical, affecting the ductility and high

temperature mechanical properties. Only recently, the oxygen level in alpha2-Ti$_3$Al alloys has been reduced to the 600 ppm range [23]. Our goal for high quality foil was to control the gas impurity levels equal to or below 1000 ppm.

7e.1. Oxygen

Oxygen levels in as-deposited alloys were previously compared qualitatively with rapidly solidified alloys by SIM and auger analyses. Quantitative determination of the oxygen level in sputtering targets, as-deposited foils and heat-treated foils were analyzed by x-ray wavelength spectroscopy in an electron microprobe, as shown in Table 7.2. Specimen surfaces were polished with 600 grit SiC paper 5 minutes before placement in the SEM vacuum chamber. Target materials were analyzed at as-fractured surfaces.

Measurements were conducted with a 15 KV beam and 15 nm beam current scanned on a 0.09 x 0.1 mm area. The diffraction crystal was scanned from 100 to 114 mm to obtain the oxygen peak. Initially, a standard reference material, Al$_2$O$_3$, was used to obtain the oxygen peak height providing a count reference of 2092 counts/second. This peak rate is equivalent to 48 wt% of oxygen. The detection limit, approximately 4 counts/s which is twice of the background of 2 counts/s, would be about:

Detection limit = 48 x (4-2)/2090 = 0.0459 wt% = 459 ppm

Compared to commercial alpha2-Ti$_3$Al alloys such as ALTA ingot, Wah-Chang low oxygen (590 ppm) alloy and RibTech ribbon, oxygen levels in our starting materials were on the low side, nearly 1000 ppm. The as-deposited foils showed slightly higher oxygen content primarily due to the surface oxides. Vacuum annealed foils including both 20 and 100 h annealing, showed lower oxygen levels than unannealed foils indicating the surface oxide layer was removed by annealing. Also freshly polished surfaces in both as-deposited and annealed foils had a lower oxygen level. Among as-deposited and heat treated foils, oxygen level above 2000 ppm was only observed on as-deposited surfaces of Deposit (9), at nearly 0.3 wt%.

The high oxygen level in Deposit (9) may be related to the high sputtering bias resulting in gas trapping in the deposit. The effect of bias voltage on oxygen level was investigated for Deposit (12) by WDS analysis. Deposit (12) was made from a low oxygen content superalpha2-Ti$_3$Al target material containing less than 700 ppm oxygen. High quality foils were fabricated at two different bias voltages, starting at 100 V for the first 1-mil

104

thick foil and reduced to 40 V for the remaining 5-mil thick foil as shown in Figure 7.14. Oxygen analysis was made on as-deposited surfaces facing the target, Figure 7.18. A low oxygen level nearly 1000 ppm was found for as-deposited surface made with a 40 V bias. An increase of oxygen level from 1000 ppm to nearly 2400 ppm was observed on the foil surfaces made with a 100 V bias voltage. Bulk oxygen levels were probably lower since the measured surfaces had been exposed to air after removal from the sputtering chamber. Increase of oxygen level observed as a function of distance from center of the deposit to the edge indicated that not only bias could enhance oxygen trapping, but the amount of oxygen could be associated with the distribution and density of the plasma.

7e.2. Krypton

Although bias sputtering can successful eliminate most of the undesired microstructures such as texture and columnar growth, a high substrate bias also could lead to trapping of the sputtering gas, such as Kr, in the deposit. The mechanical properties of the sputtered alloy could be severely affected by trapping of sputtering gas. It has been demonstrated that as much as 10 at.% Kr can be trapped in an amorphous structure such as measured in amorphous YCo_5.

Several high quality foils also were analyzed by EDS and WDS for Kr. However, the level of Kr in highly biased substrate sputtering runs was found below the detection limit of 500 ppm.

Table 7.2. Comparison of oxygen levels in starting materials and final sputter deposited foils.

Material	Form	Condition	O Count*	O Level
Standard:				
Al_2O_3	Crystal	Reference	2090	48 wt.%
Reference: Alpha2-Ti$_3$Al alloys				
RibTech	Ribbon	As-quenched	7	1607 ppm
RibTech	Ribbon	850°C/2h	4	960
ALTA	Ingot	As-received	9	2070
ALTA	Ingot	850°C/100h	6	1380
WC-700 ppm	Ingot	920°C/2h	4	960
Target alloys:				
#2 target	Cast	Fractured	6	1380 ppm
#4 target	Cast	Fractured	6	1380
#5 target	Cast	Fractured	6	1380
#6 target	Cast	Fractured	7	1607
High quality foils:				
(5)-14	Foil	As-deposited	4	960 ppm
(5)-10	Foil	850°C/100h	6	1380
(8)-100V	Foil	As-deposited	7	1607
(8)-100V	Foil	850°C/2h	5	1148
(9)-100V	Foil	As-deposited	13	2985
(10)-60V	Foil	As-deposited	5	1148
(10)-60V	Foil	850°C/2h	5	1148
(10)-60V	Foil	930°C/2h	5	1148
(10)-60V	Foil	950°C/2h	5	1148
(10)-60V	Foil	950°C/20h	6	1380
(11)-40V	Foil	As-deposited	4	960
(12)-100V	Foil	As-deposited	7	1607
(12)-40V	Foil	As-deposited	4	960

* Less the 2-3 counts of background.

CAST TITANIUM ALUMINIDE BLADE, Ti-40Al
Ti 72.7 wt.%, Al 27.3 wt.%, 372 grams

CAST TITANIUM ALUMINIDE BLADE, Ti-30Al
Ti 80.55 wt.%, Al 19.45 wt.%, 406 grams

CAST TITANIUM ALUMINIDE BLADE, Ti-30Al
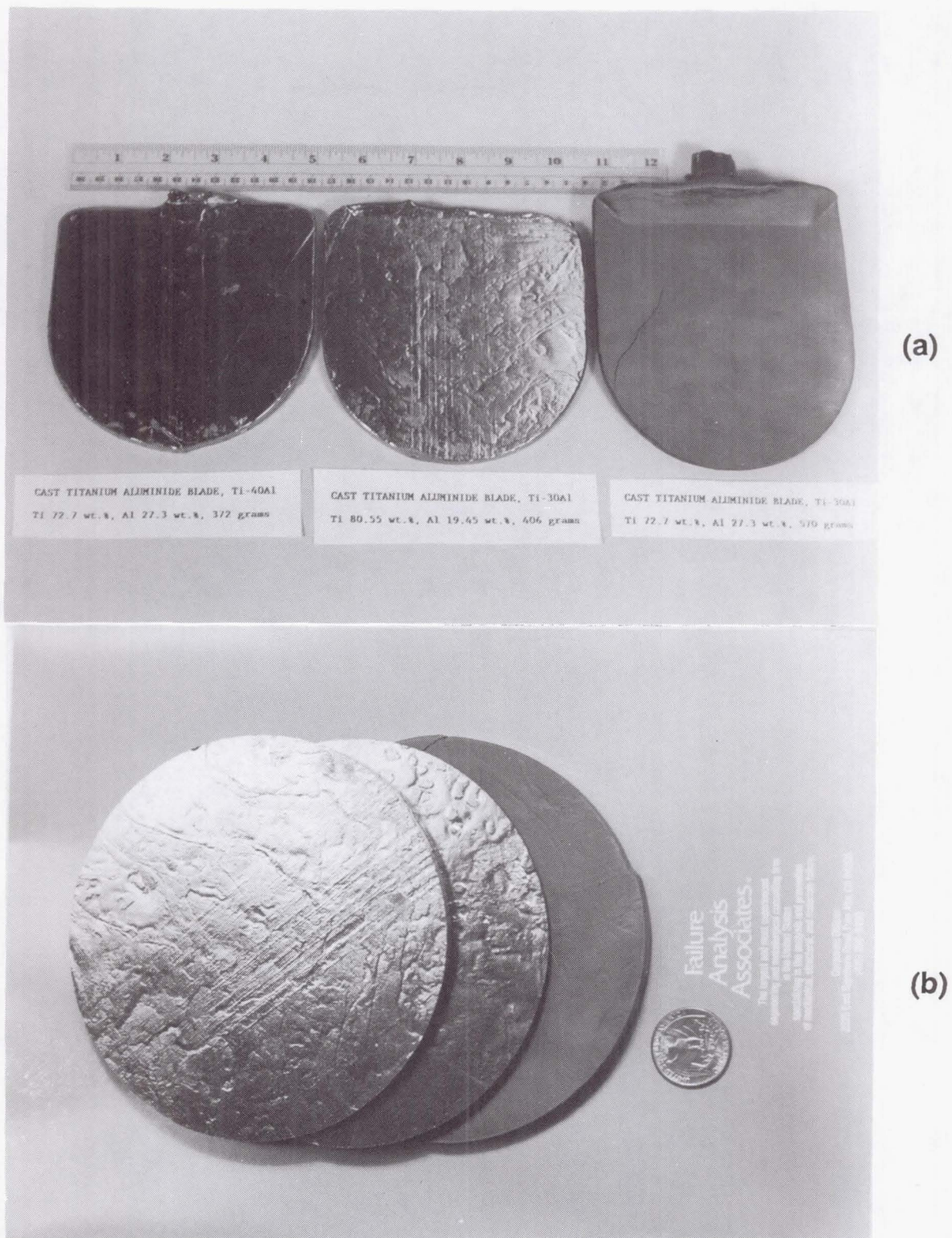Ti 72.7 wt.%, Al 27.3 wt.%, 570 grams

Figure 7.1. Thin Ti$_3$Al target alloys fabricated by skull casting, a) as-cast alloys, and b) formed into 5" diameter sputtering targets.
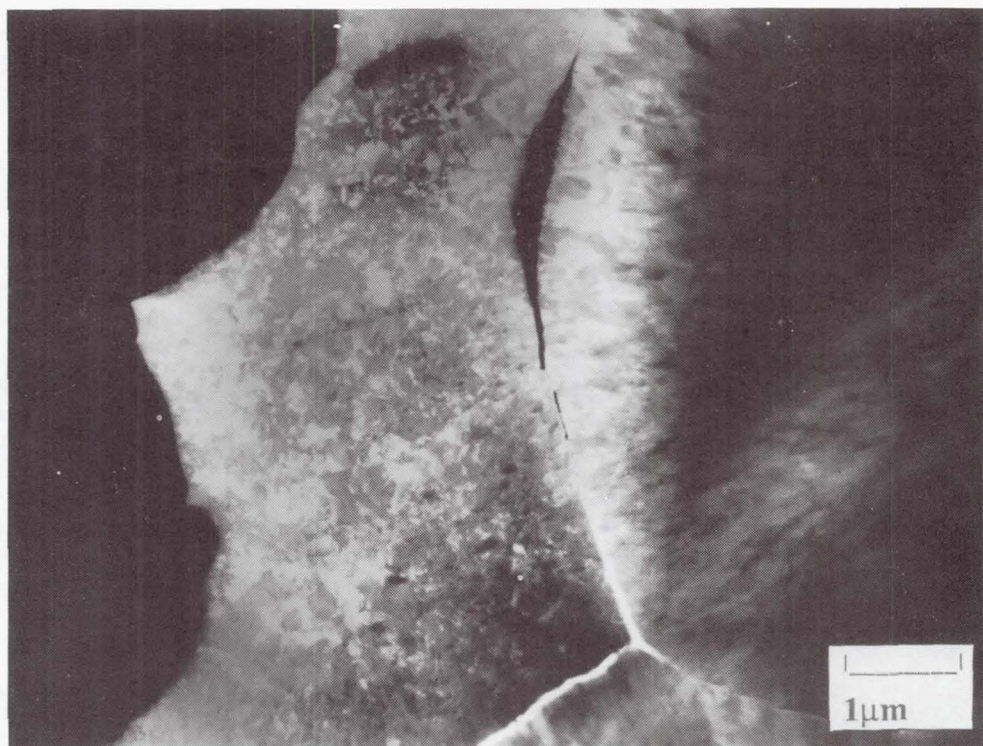
107

Figure 7.2. Typical microstructural defects associated with sputter deposited alloys, a) presence of loosely bonded areas in the interior of the deposit, and b) Highly columnar growth and microvoids,.
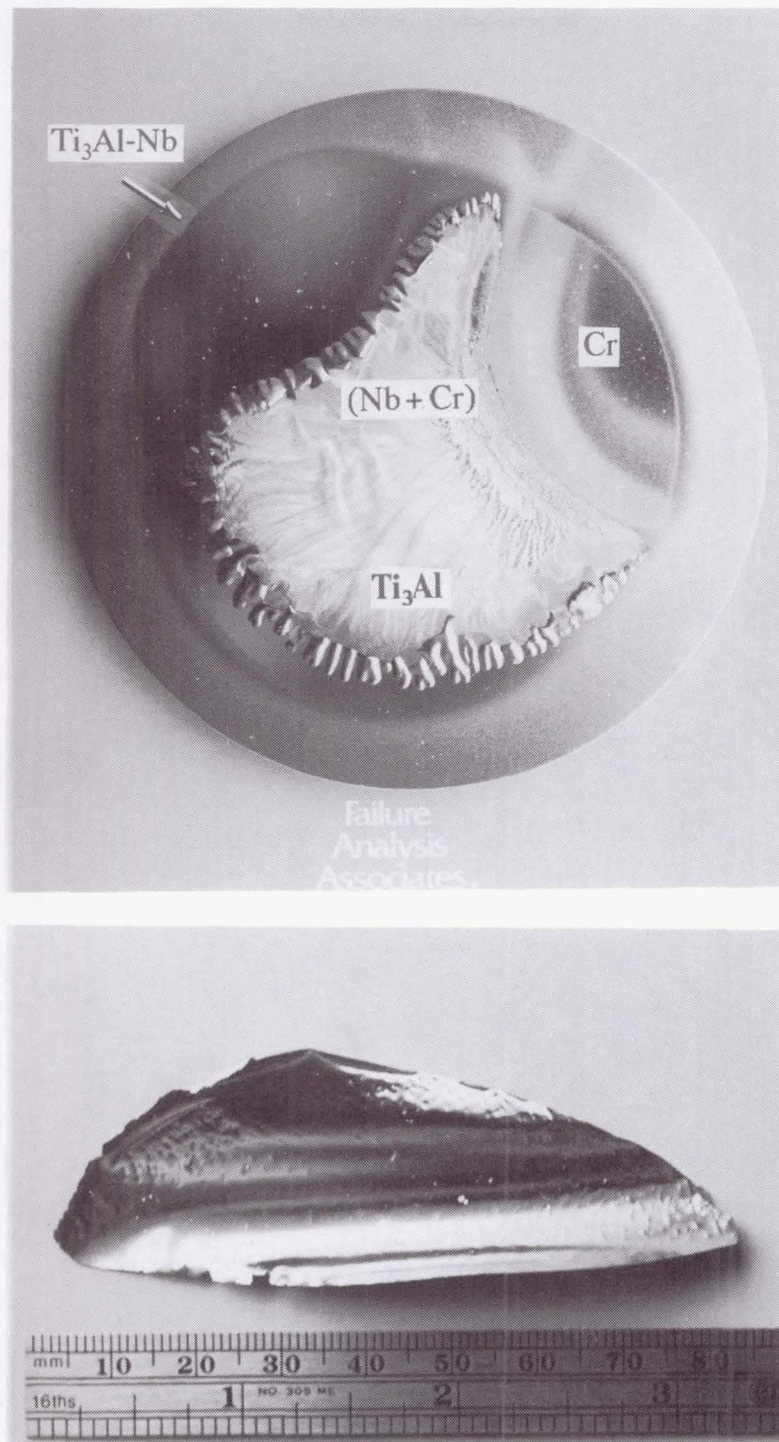
Figure 7.3. Bias triode sputtering resulting in a gradient
Ti₃Al-(Nb,Cr) alloy deposit. The center part of the deposit
containing Ti₃Al and Ti₃Al-(Nb,Cr) alloys was shattered due to a
high degree of brittleness. The region of Ti₃Al-Nb alloys
provided high quality foil.
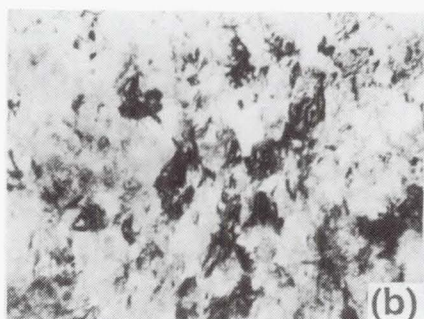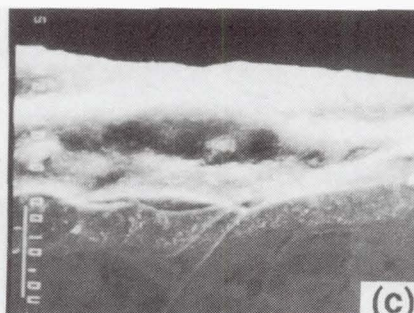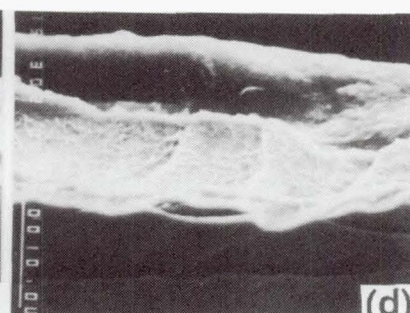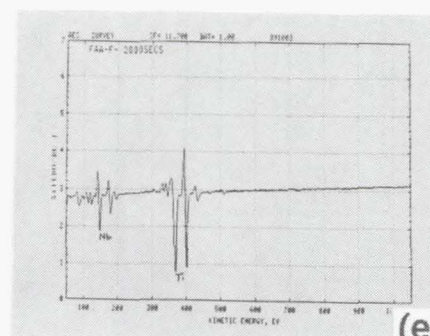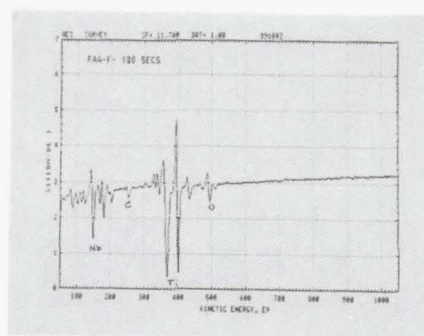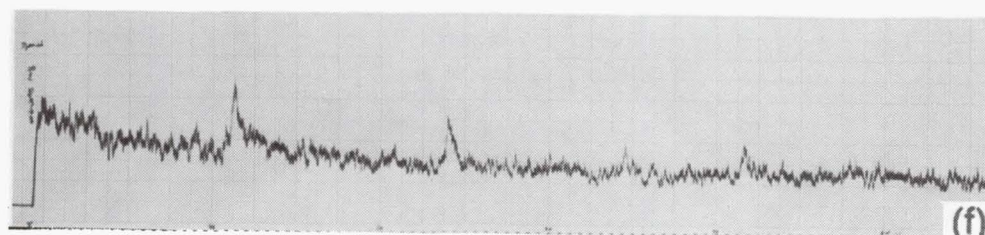
Figure 7.4. Characteristics of a high quality Ti₃Al-Nb foil showing: a) smooth surface appearance, b) fine grain, c) no columnar growth, d) region of ductile fracture, e) low oxygen level and f) equiaxial growth.
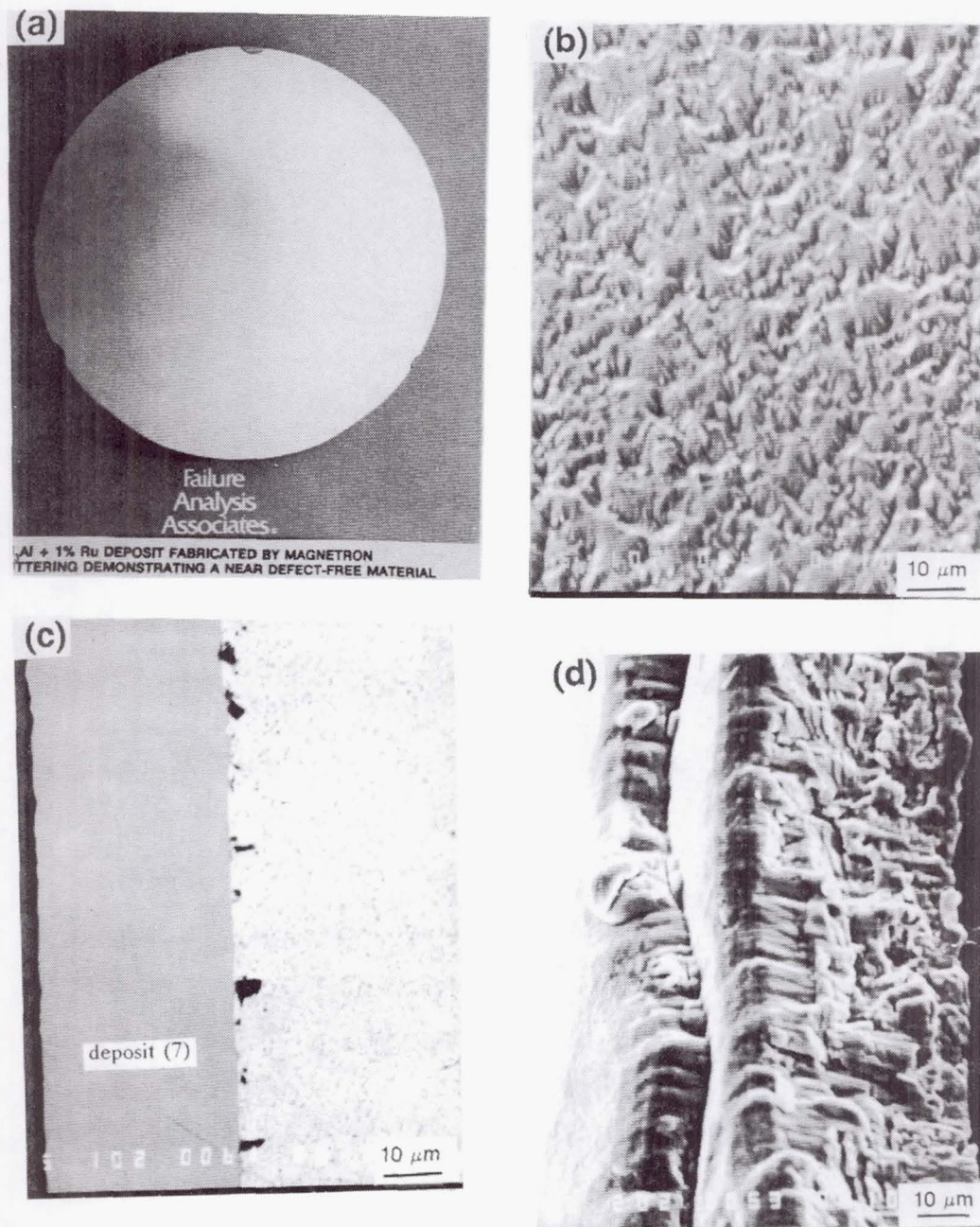
Figure 7.5.   Magnetron sputtered Ti$_3$Al-1Ru deposit showing a) the smooth surface, b) texture of the surface, c) a nearly defect free microstructure, and d) presence of some columnar growth.
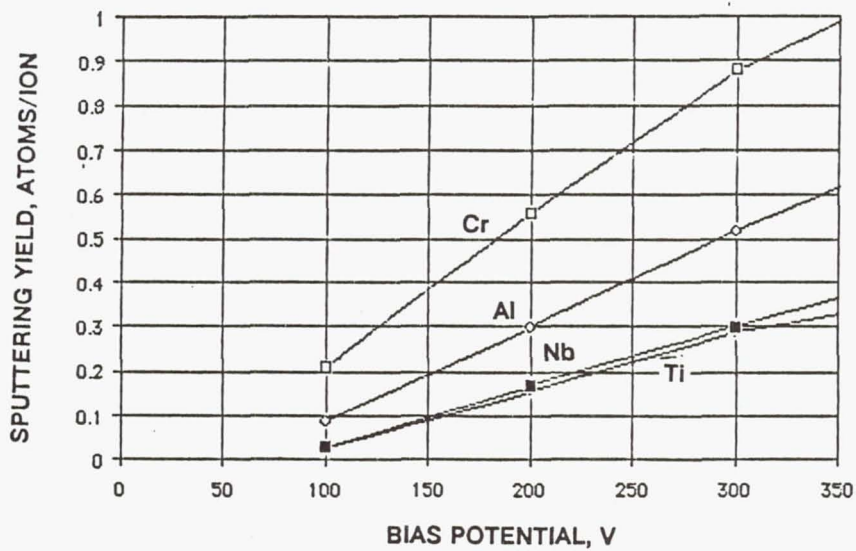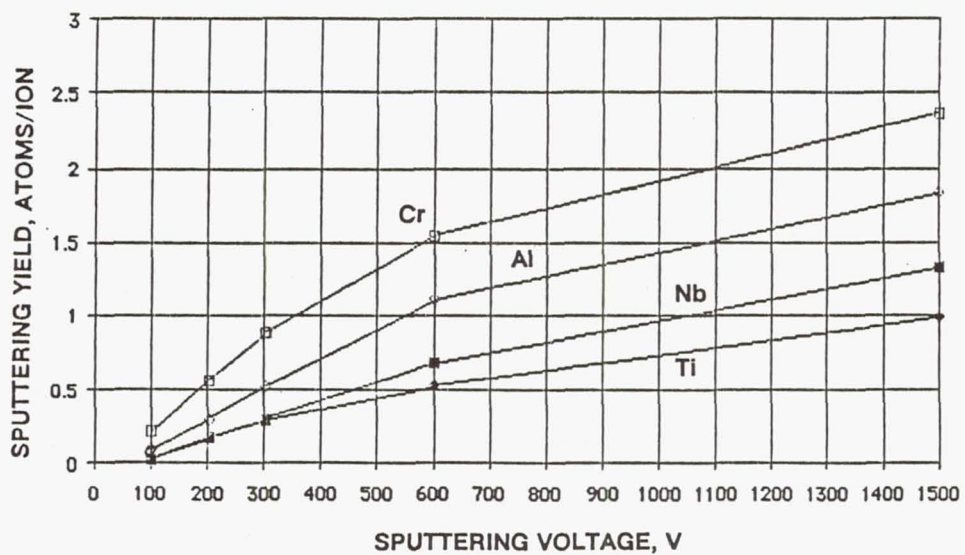
Figure 7.6. Comparison of sputtering yields of key elements as a function of sputtering voltage.
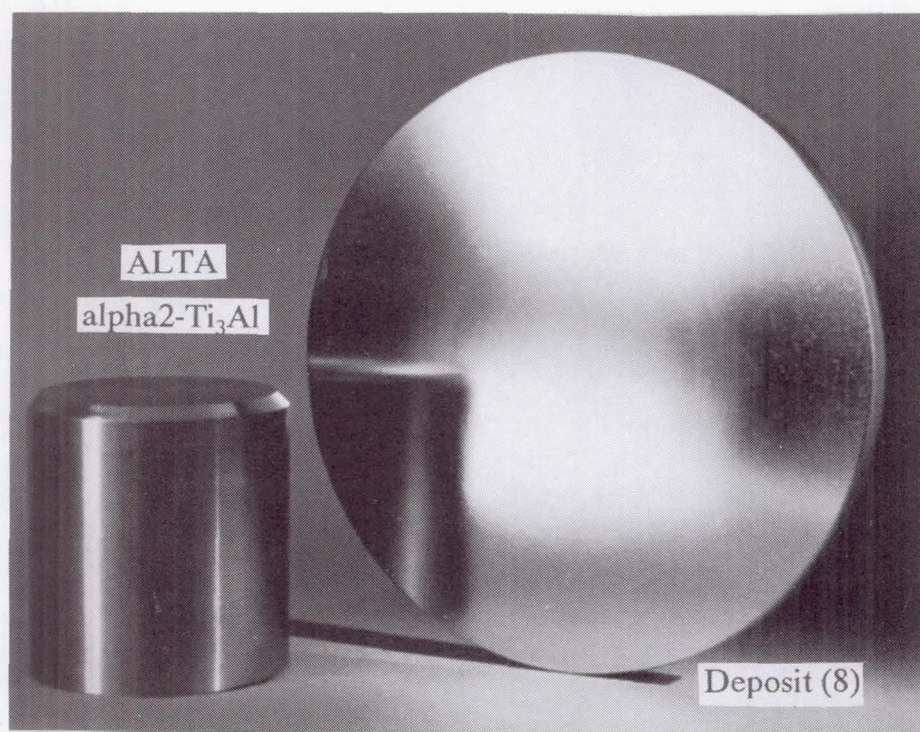
Figure 7.7. A single composition Ti$_3$Al-Nb high quality foil (8), deposited onto the Cu substrate with a -100 V bias voltage.

COMPOSITION VARIATION OF AS–DEPOSITED
Ti–Al–Nb TESTING FOIL (8)
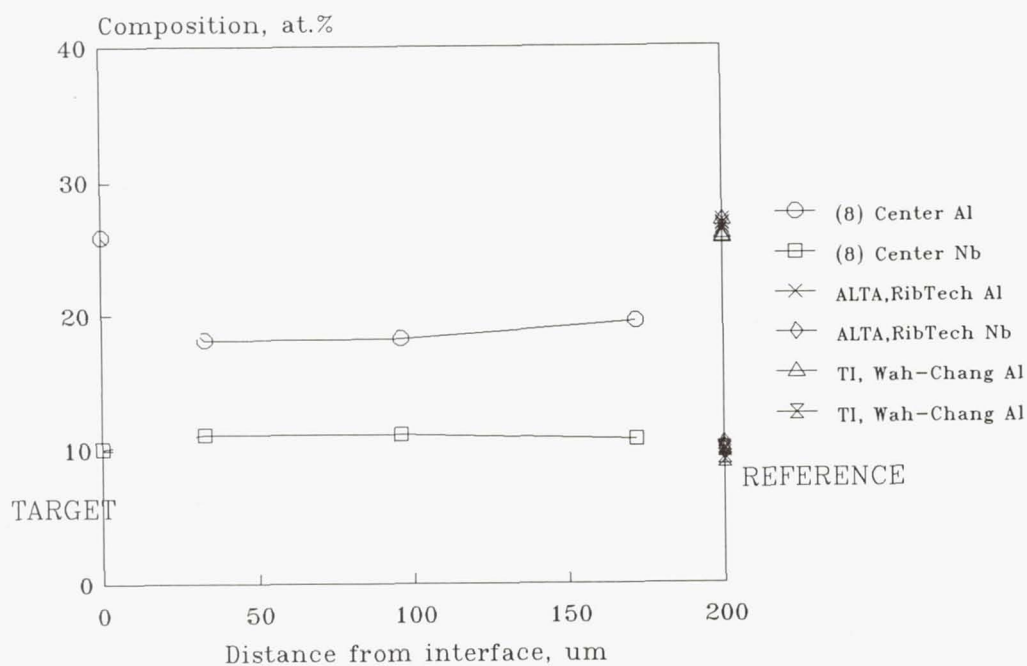
Figure 7.8. Uniform composition distribution throughout the
thickness of foil (8). Comparing with the target, the foil had a
lower Al content due to the bias sputtering process.

COMPOSITION VARIATION OF AS–DEPOSITED
Ti–Al–Nb TESTING FOIL (10)

Composition, at.%

Legend:
- ─○─ (10) CENTER Al
- ─□─ (10) CENTER Nb
- ─◇─ (10) EDGE Al
- ─△─ (10) EDGE Nb
- △ ALTA,RIBTECH Al
- ◇ ALTA,RIBTECH Nb
- △ TI, WAH–CHANG Al
- ⊠ TI, WAH–CHANG Al

TARGET   REFERENCE

Distance from interface, um
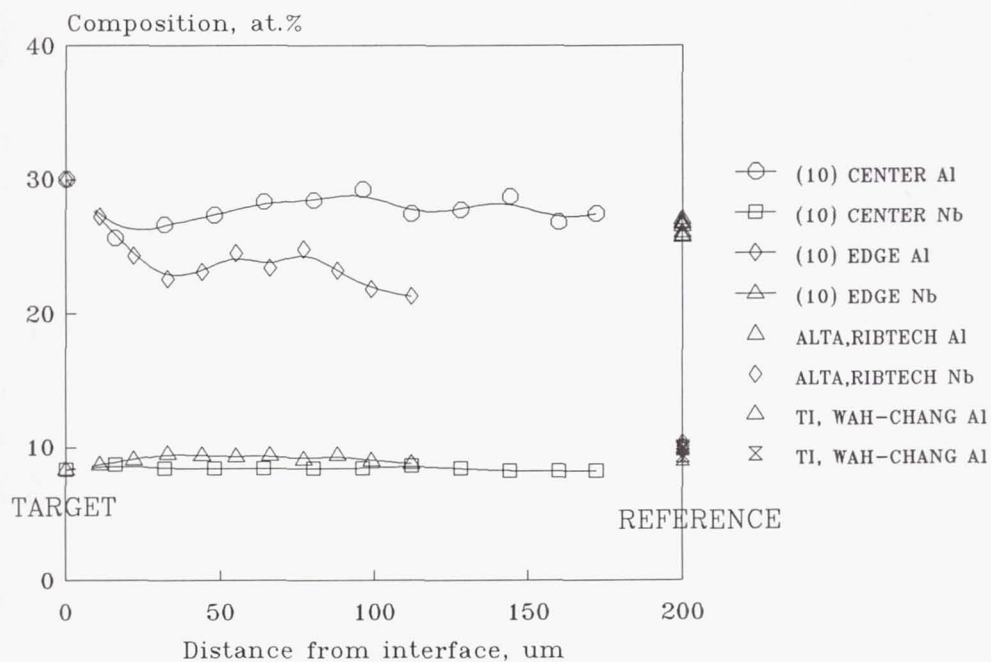
Figure 7.9. Composition distribution throughout the thickness of foil (10), showing near constant Al and Nb content at the center of the deposit. Lower Al content was observed at the edge of the deposit.

115
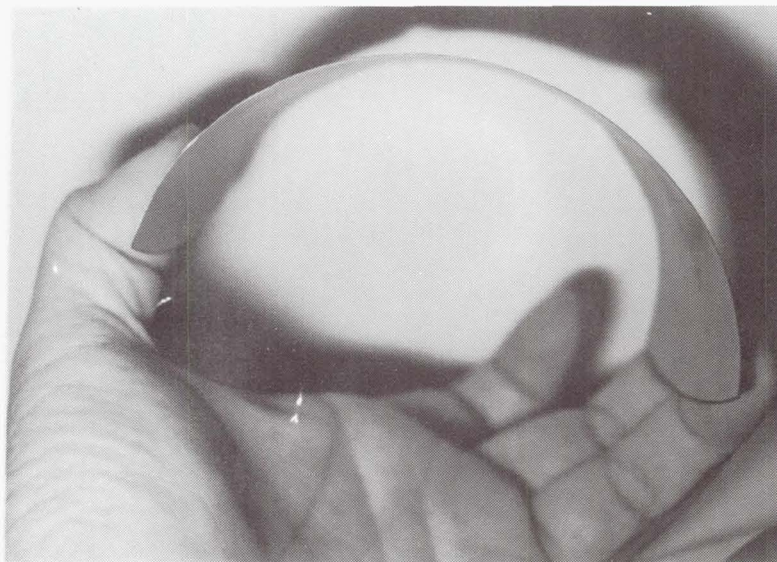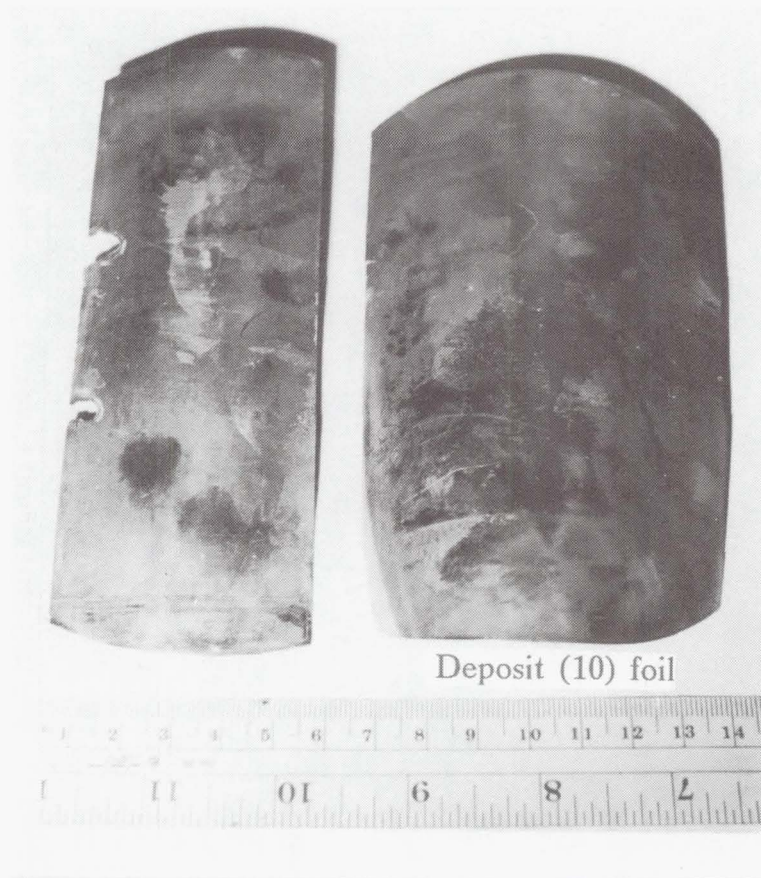
Deposit (10) foil

Figure 7.10. Foils of deposits (9) and (10) separated from the substrate showing limited flexibility.

116

Ti_3Al

0.125" ±0.0005

0.125" R TYP

0.125" +0.003 / −0.000 Ø THRU, TYP

0.500"

0.375" TYP

1.030"

1½"

EL-840820
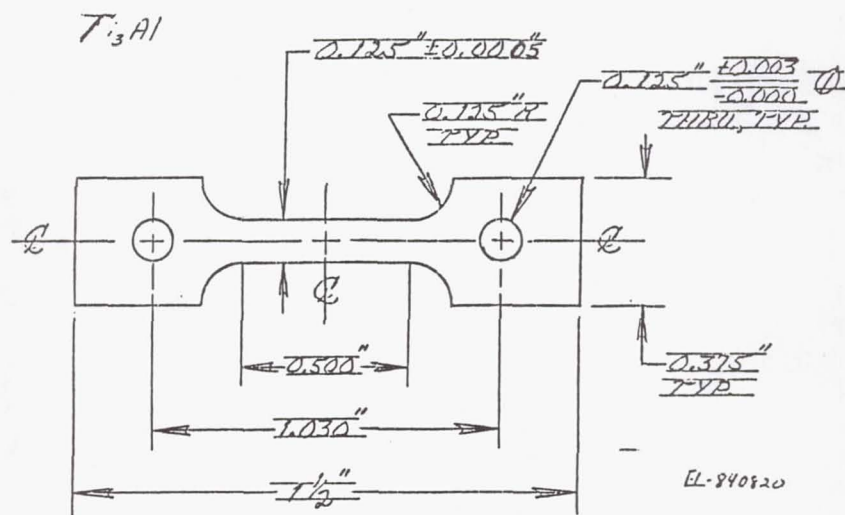
Thickness of Spec. – 0.030 mils $^{+0.001}_{-0.001}$

① All EDM surface must have 0.0005 mi. Removed by grinding
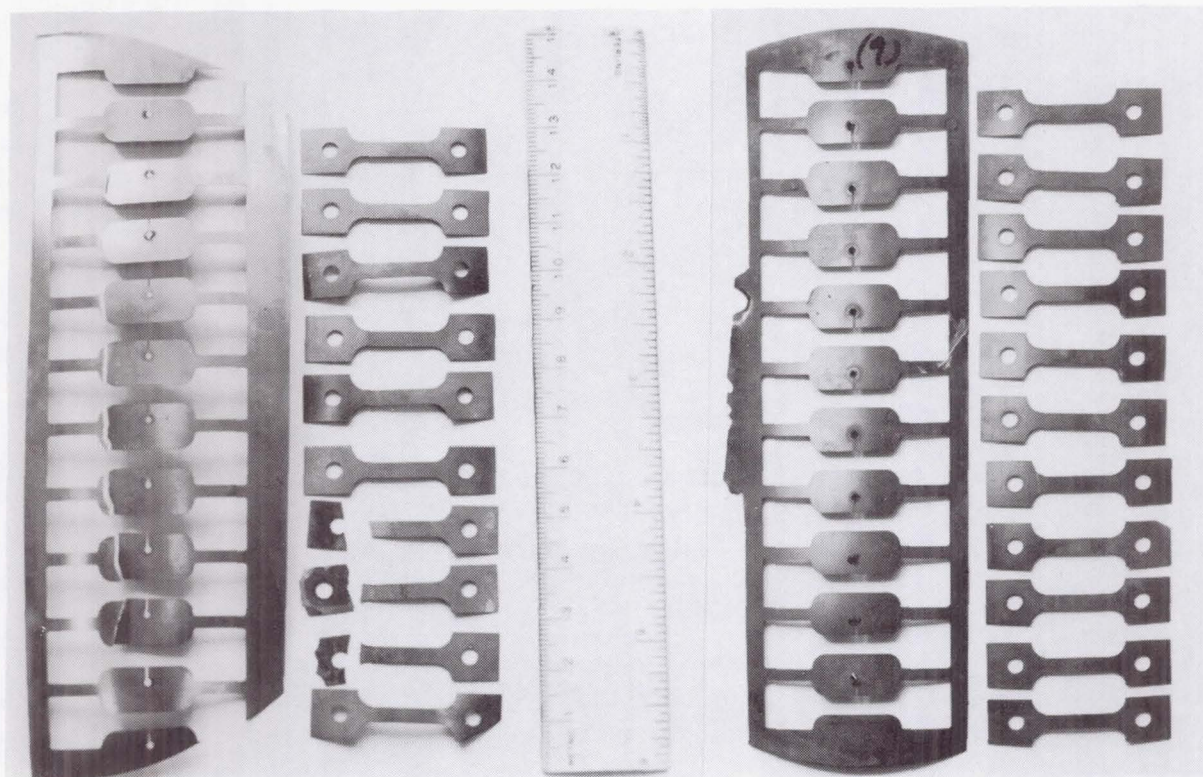
Figure 7.11. Fabrication of tensile specimens by EDM.

117

EFFECTS OF HEAT TREATMENT
Ti3Al–Nb (10)
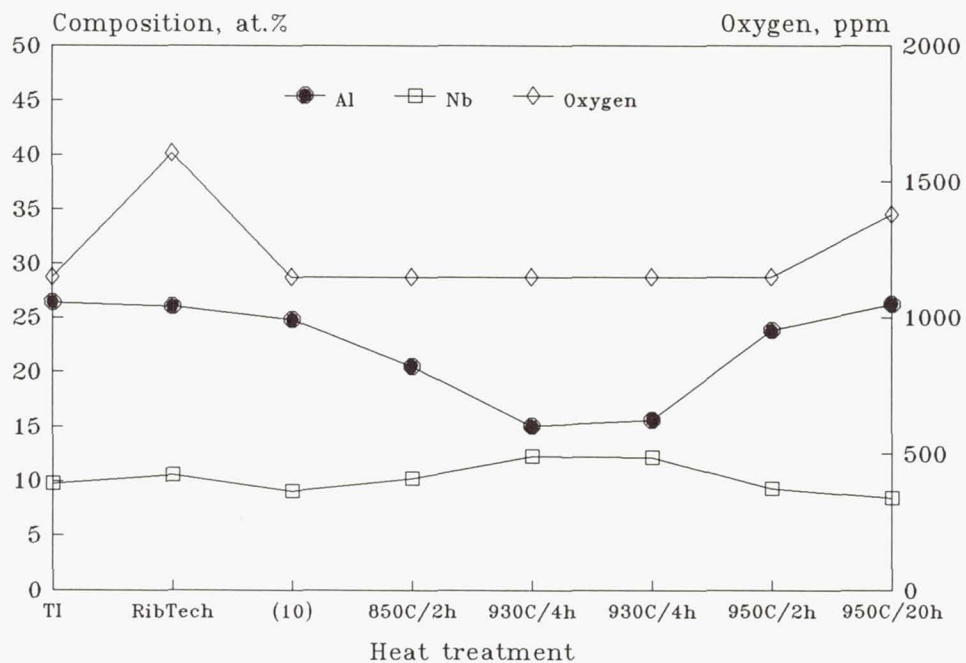
Figure 7.12. Effects of heat treatment on Nb, Al and O contents in foil (10) indicating Al loss after 930°C/4h annealing.
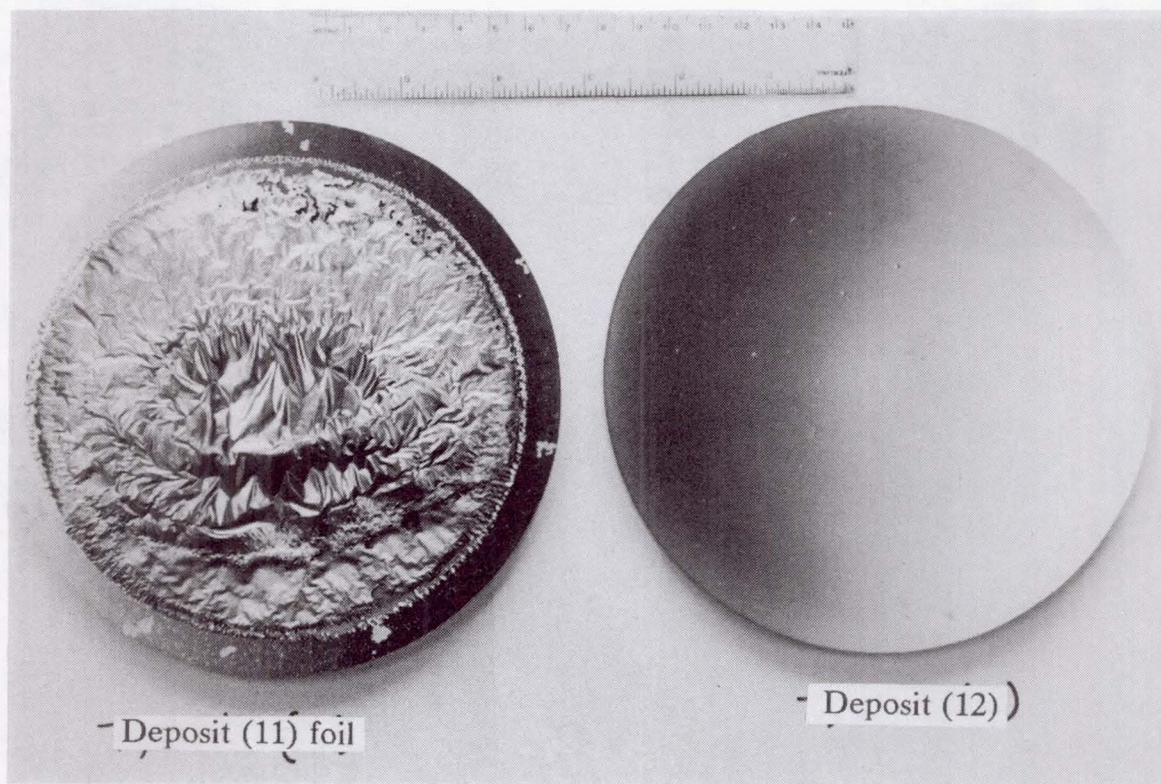
Figure 7.13. Deposits (11) and (12) obtained from a low-oxygen
content Target Alloy #7 (WC-alpha2-Ti$_3$Al). Deposit (11) foil was
debonded from the substrate during final stage of sputtering.
Deposit (12) resulting in a high quality foil.
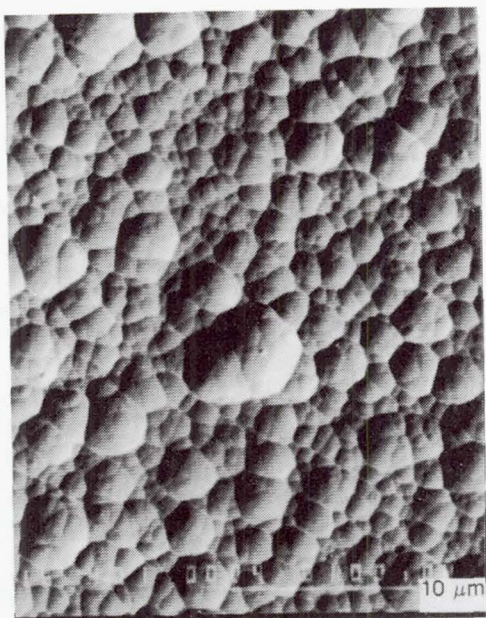
(a)
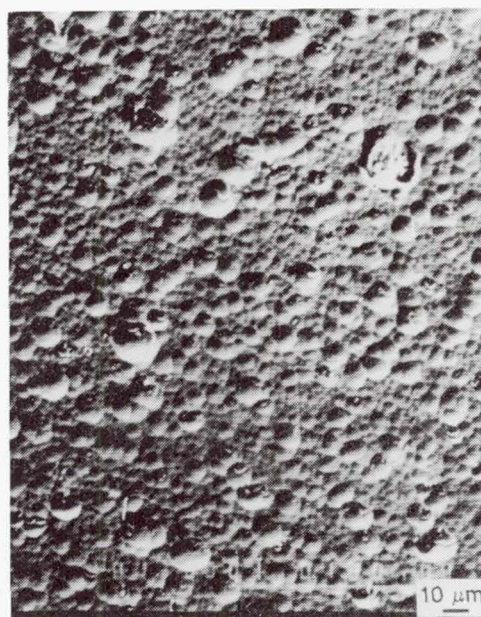
(b)
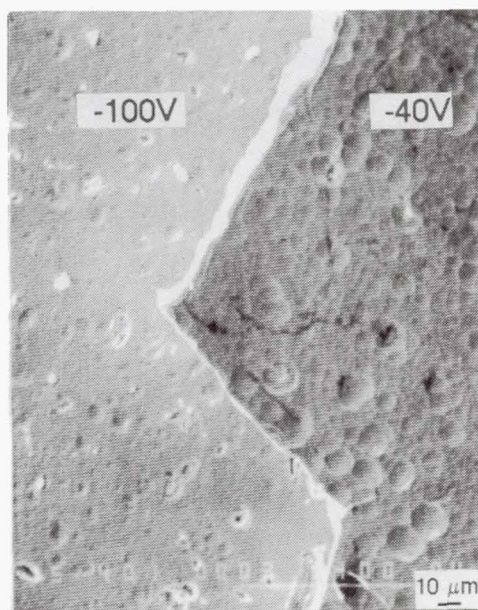
(c)

Figure 7.14.   Surface morphology of high quality foils from deposit (12) obtained from different bias voltage, a) at -40V, b) at -100V, and c) separation of foils.

COMPOSITION ANALYSIS OF SPUTTER–
DEPOSITED Ti3Al–Nb DISK (12)

Composition, at.%

WANG/NASAII
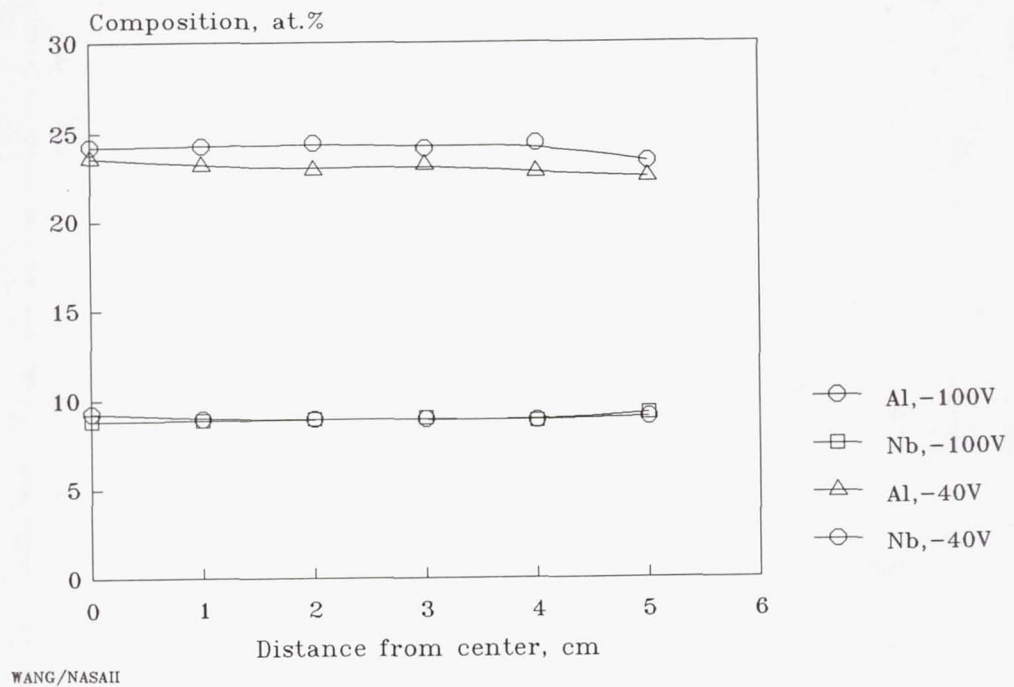
Figure 7.15. Elemental analysis of as-deposited foils from
deposit (12) as a function of distance from the center of the
deposit.

MICROHARDNESS OF SPUTTER DEPOSITED
Ti3Al–Nb ALLOYS, (8) and (10)

(a)

(b)
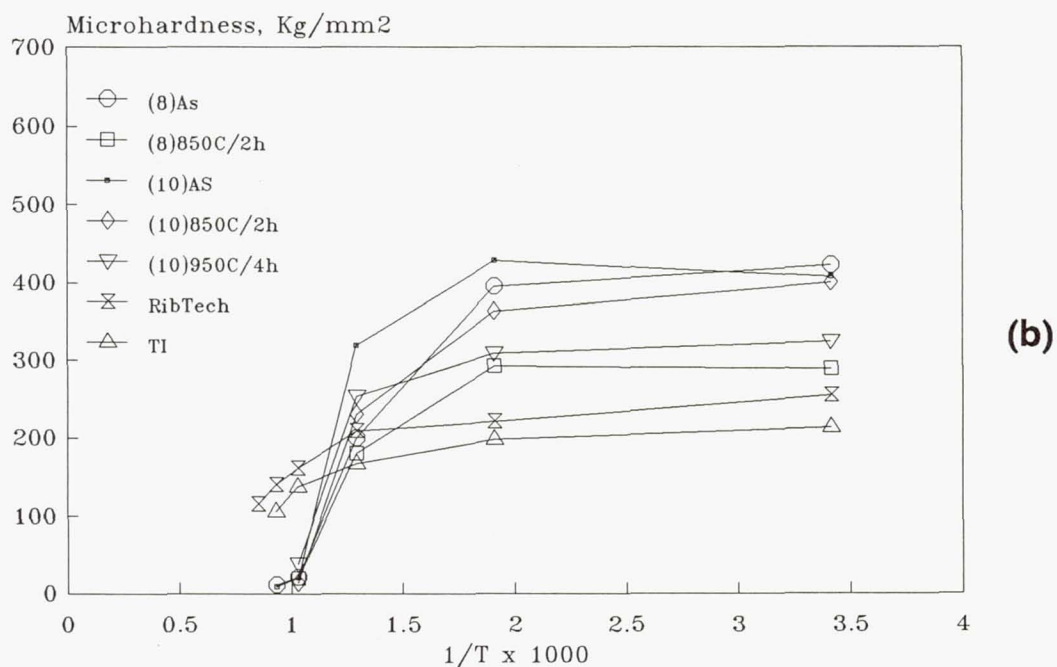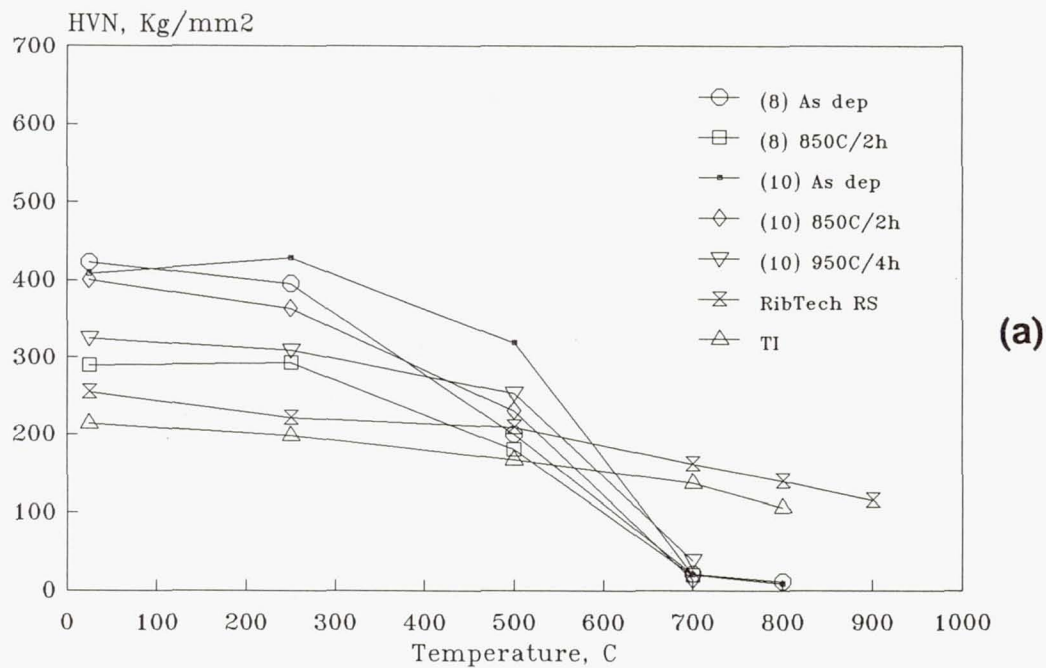
Figure 7.16. Microhardness data of foils (8) and (10) as a function of a) test temperature and b) 1/T.

MICROHARDNESS OF SPUTTER DEPOSITED
Ti3Al—Nb ALLOYS, (8) and (10)
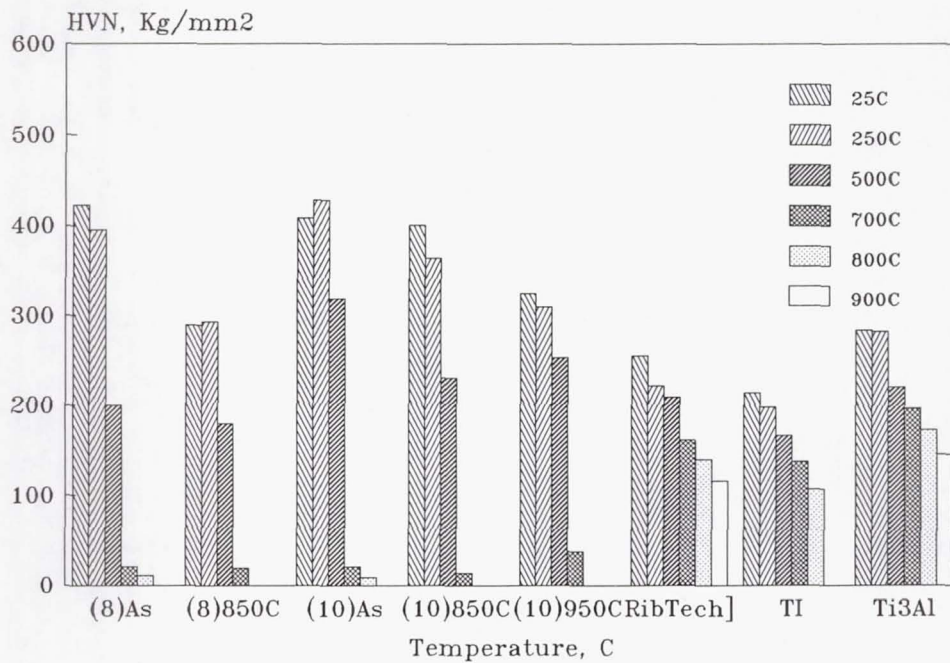
Figure 7.17.   Comparison of hardness data with different reference materials showing lower hardness values for sputter deposited foils at 700-900°C range.

OXYGEN ANALYSIS OF SPUTTER-
DEPOSITED Ti3Al—Nb DISK (12)
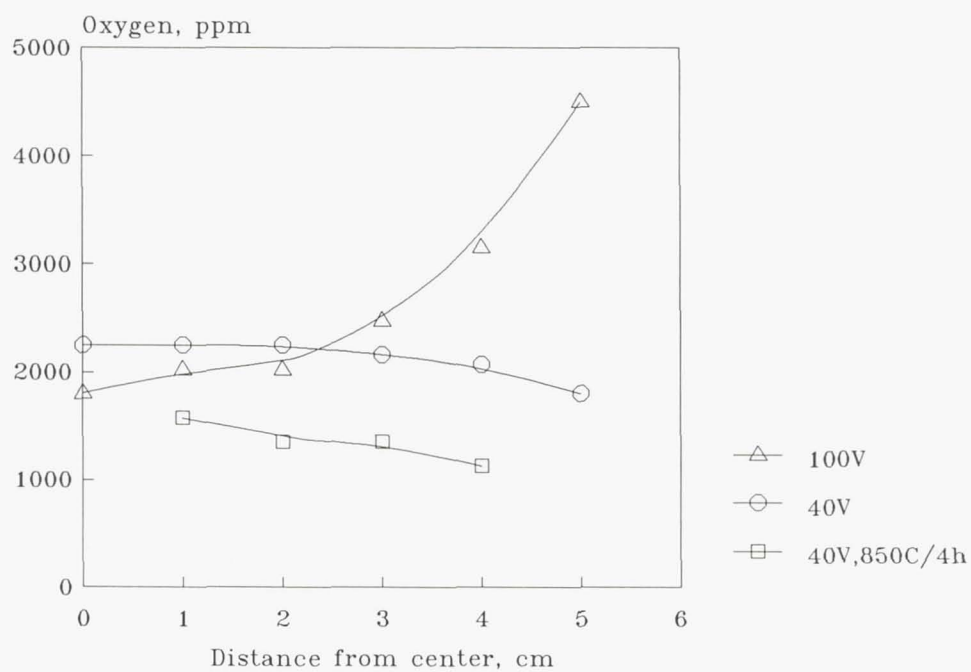
Figure 7.18.   Distribution of surface oxygen as a function of
distance from deposit center.   Analysis was conducted on foils
obtained from deposit (12) at two bias voltages.

8. MECHANICAL ALLOYING OF NONEQUILIBRIUM ALLOYS

Mechanical alloying was investigated with intention of developing a solid state alloy fabrication process to replicate the sputter deposited nonequilibrium alloys in large quantities (bulk forms). Mechanical alloying has been widely used as a commercial process for high temperature Ni base superalloys. Like high rate sputter deposition, the mechanical alloy process [25,26] has attractive features for development of nonequilibrium alloys:

1. The process can produce clean and homogeneous alloys without thickness limitations,

2. Resultant mechanical alloyed materials have been shown to resemble those of microstructurally defective sputter deposited alloys,

3. Processing parameters can be used to control the composition and microstructure.

Another important factor in selection of mechanical alloying for obtaining bulk materials was to achieve dense alloys at low consolidation temperatures, to avoid excessive dispersoid coarsening. This was particularly important for Ti alloys since, for example, rapid solidified titanium alloys containing rare earth element additives were isothermally forged at 800°C. If high degree of cleanness and high surface reactivity [27] could be obtained in the mechanical alloyed powders, a reduction of consolidation temperature could be achieved in producing full density alloys.

8a. Process variables and structures

We pursued the mechanical alloying process by forming nonequilibrium alloys from elements, such as Ni, Ti, Al, Hf, B, and C. Elementally blended alloys, especially those based on metal sponges of Ti [28], Ni and Nb are low cost. The work was to determine the processing parameters and investigate powder handling procedures in forming Ti-6Al-4V powders, Ni_3Al powders containing additives of Hf, C and B, and Ti_3Al powders containing Ru, respectively. Mechanically alloyed powders were characterized by x-ray diffraction, optical microscopy and SEM for structure, size distribution and morphology characteristics.

A total of seven mechanical alloyed powders with compositions and alloying times indicated in the Table 8.1 were investigated. Feedstock powders used in this work were argon packed 99.9 % pure, -200 to -325 mesh powders. A two-stage alloying process was used to incorporate different amounts of additives to the starting metal matrix elements. The initial powder mixtures (about 1 Kg total) were first-alloyed for 40-50 hours to form the desired alloys. Half the amount of the alloyed powder was then removed from the attritor mill. The remaining powders were further alloyed with additional additives. The work was performed initially at Illinois Institute of Technology (IIT) facilities by Dr. Philip Nash. Later, the work was conducted with our attritor mill (Union Process) and powder handling system, Figure 8.1. This system was capable of performing mechanical alloying in kilogram quantities under an inert-gas environment.

Table 8.1. Mechanical alloyed nonequilibrium alloys

Alloy System	First Stage Alloying	Time (Hrs.)	Second Stage Alloying	Time (Hrs.)
Ti_3Al-Ru	Ti 60 at.% Al 40 at.% (MA18A)	29.5	Additional 1 at.% Ru (MA18B)	19.8
$Ni_3Al-(Hf,C)$	Ni 78 at.% Al 22 at.% 0.5 at.% B 5.5 at.% Hf (MA21A)	40.9	Additional 5.5 at.% C (MA21B)	50.1
(Ti-6Al-4V)-B	Ti-6Al-4V 4 at.% B (MA22B)	40.9	Additional 3 at.% C (MA23A)	51.0
Ti-Al	Ti 60 at.% Al 40 at.% (MA8901)	40	-	-

Alloying parameters (attritor speed, medium/powder ratio and time) have been determined for both Ti- and Ni-based aluminides. Starting with the raw element powders, initial mechanical alloying produced powder particles with a characteristically

126

layered microstructure. Further milling led to an ultrafine composite with fine-grain size and amorphization by solid state reaction.

Alloyed Ti_3Al powder was not formed within the first 12 hours milling, however after a total of more than 24 hours milling an alloyed product was reached, Figure 8.2. On the other hand, initial alloying of Ni_3Al powders resulted in cold-welded agglomerates which were difficult to separate from the grinding media. Separated powders are shown in Figure 8.2. Ti-6Al-4V powders were not completely alloyed after nearly 100 h of alloying, but Ti-Al powder was adequately alloyed after 40 h milling, Figure 8.3.

X-ray diffraction patterns of the first stage alloyed materials indicated the formation of disordered intermetallic compounds after more than 24 hrs of alloying at a stirring speed of 300 RPM. Finer particle size was associated with more structural disordering, Figure 8.4a. High additive content (Hf+C) to Ni_3Al resulted in an amorphous structure similar to that obtained from sputter deposition described in Section 4, Figure 8.4b. These results indicated the feasibility of replicating the nonequilibrium alloy phases initially obtained from sputter deposition.

A few potential technical problems were identified in mechanical alloying of intermetallic alloys. The major problem was related to the sticking characteristics of the powders after intermetallic compound alloys were formed. The ductile powders were cold welded to the grinding media and container surface, preventing further homogeneous mixing. Although initially introducing a small amount of oxygen (8-14 at.%) in the argon cover gas would reduce this problem, it is not desirable to add too much oxygen in these alloys.

Another problem was the high oxygen level in the resultant powders. Selected mechanically alloyed (MA) powders were analyzed for chemical composition, including oxygen, hydrogen and nitrogen levels, as shown in Table 8.2. Although improvement of powder handling resulted in a reduction of the oxygen level in our attritor milling compared with the powders prepared at IIT, the level of contaminates in these powders was similarly high for the Ti-aluminide alloys.

Table 8.2. Elemental composition, weight %, of mechanically alloyed powders.

Element	Cast Ti-Al	MA8901	MA18B	MA21B	MA22B
Titanium	Balance	Balance	Balance	.48	Balance
Nickel	–	.059	–	Balance	2.53
Aluminum	23.5	38.2	26.3	15.3	7.10
Vanadium	–	.040	–	–	3.63
Hafnium	–	–	–	10.8	–
Boron	–	<.001	–	.023	1.06
Carbon	.043	.150	.725	.705	.079
Ruthenium	.92	–	.64	–	–
Impurities:					
Hydrogen	.0030	.094	.052	.013	.022
Oxygen	.058	1.28	1.8	1.4	.70
Nitrogen	.005	.73	3.0	.057	.42
Iron	.066	.68	.089	.065	.49
Chromium	<.001	.076	.024	.032	.11

8b. Bulk alloy fabrication

Considerable effort was expended to identify an optimized process to consolidate mechanically alloyed powders into thin ribbons for mechanical property evaluation. Several processes have been proven to be acceptable for consolidation of intermetallic compounds, such as HIPing, hot rolling and hot extrusion. In order to maximize the mechanical properties of the nonequilibrium alloys, it is desirable to form 100% dense and oxide-free grain boundaries at low temperatures. Hot vacuum rolling was determined to be a potentially viable method.

8b.1. Hot rolling

With the collaboration of the Materials Preparation Center of Ames Laboratory, Iowa State University, hot rolling experiments were conducted with MA powders. It was our intention to obtain thin ribbons. The process involved a series of steps consisting of vacuum compacting, jacketing, annealing and rolling at 800°C. The resultant product yielded fragmented materials, Figure 8.5.

Apparently conventional high temperature rolling may not be a feasible process for direct consolidation of MA powders, especially when these powders contain more than 1 wt.% oxygen.

8b.2. Hot pack rolling

Another consolidation effort was made with Dr. Jerry Wittenauer at Lockheed Missiles & Space Co on pack rolling [29,30] of MA Ti-Al powder compacts. The purpose of using pack rolling was to provide a highly clean environment for elevated temperature processing of materials to obtain 2-10 mils thick ribbons. Previous studies have utilized this identical processing method to produce foil of Ti-6Al-4V alloy [29], and Ti_3Al+Nb [30]. Although previous starting materials were all solid bulk alloys, this method was believed to be applicable to form foils directly from powder compact.

Four batches of MA powders obtained from the second stage alloying were used for pack rolling, Table 8.3. Powder was first cold pressed without binder into a preform. The powder preform was placed in a specially prepared metal frame with an applied pressure of 304 MPa. Quantities of powder were chosen such that the thickness of the compacted powder after pressing closely matched the thickness of the metal frame. It was found that the Ti-6Al-4V powder would not form an integral preform compact under the attempted consolidation process.

Metal frames containing the preform compact were combined with cover sheets and the sandwich assembly was welded at the edges, Figure 8.6. Welding was performed under 10^{-5} Torr. A release agent was used to separate the intermetallic compound being processed from the container material. In all cases, the metal frame and cover sheets were composed of high strength nickel alloy-IN 601.

Table 8.3. Pack rolling experiments for MA powders

Materials	Specimen	Powder size	Green density	Process temperature
Ti_3Al	MA18B	125 μm	2.40	1030°C
Ti-6Al-4V	MA21B	125 μm	–	–
Ni_3Al	MA22B	250 μm	4.44	990°C
Ti-Al	MA8901	125 μm	2.39	1050°C

Sandwich assemblies were heated to the processing temperature for 20 minutes. All rolling packs were reduced from an initial thickness of 13.7 mm to a final thickness of 1.0 mm, typically in 25 rolling passes. The initial rolling speed was 18 m/min and was gradually increased to 30 m/min to prevent temperature rundown at the end of the strip as the material increased in length.

The rolling experiments conducted for this study proceeded without any notable problems. The temperatures for pack rolling of these MA alloys were selected as about 50-100°C below those temperatures for conventional alloys. The protective IN-601 pack did not rupture during processing and the integrity of the welds remained sound. The attempt to produce foil, however failed. The intermetallic material was recovered as chips or flakes when the rolling packs were opened, Figure 8.6.

1. Ni$_3$Al alloy

Metallographic observations of the as-processed alloys help to explain the poor consolidation characteristics of these materials. The metallographic evidence suggests a great degree of chemical inhomogeneity in materials which were expected to be either single phase or fine-structure two-phase materials. This inhomogeneity was most evident in the Ni$_3$Al material. Shown in Figure 8.7 is a section through an as-rolled flake of the Ni$_3$Al material. In the unetched condition, discontinuous stringers of one metallic phase are seen embedded in a continuous phase. Also observed are large islands of material which appear to be inclusions rather than an integral part of the microstructure.

Shown in Figure 8.7b is the Ni$_3$Al flake after etching. The etching strikingly reveals the extent of chemical segregation in this material. It was possible that the processing temperature was too low to allow complete chemical combination between the Al and Ni. Also, nearly 100 h of mechanical alloying still did not produce complete alloying either resulting in too great of a diffusion distance for complete reaction between Ni and Al, or indicating that an excess concentration of Al was present. If phase identification reveals that an Al-rich phase is present, then the reason for formation of flakes rather than foil could be attributed to a "hot shortness" condition brought about by the presence of a liquid Al-rich phase during processing.

2. Ti$_3$Al alloy

The pack rolled Ti$_3$Al strips exhibited less chemical segregation than the Ni$_3$Al material, but the effects of segregation were equally severe. Figure 8.8a shows an etched cross section of a Ti$_3$Al flake. The highly fractured nature of this material

130

indicates the inherent brittleness of the Ti$_3$Al flake. A higher magnification of this region is shown in Figure 8.8b. The appearance of the large white feature is characteristic of incipient melting. Evidently, a liquid phase was present during processing which severely inhibited the full consolidation of this material. A continuous sheet or foil cannot be formed if a liquid phase is present during rolling deformation. The white island observed in Figure 8.8b is undoubtedly an Al-rich phase. The presence of this phase can be explained by the same hypotheses put forth for the Ni$_3$Al case: improper choice of processing temperature, insufficient amount of mechanical alloying, or improperly balanced ratio of Ti to Al.

The excessive amount of cracking observed in the microstructure points to an inherent brittleness for this mechanically alloyed Ti$_3$Al. It has previously been demonstrated that Ti$_3$Al exhibits ductile behavior at all temperatures above 700°C [31,32]. The inherent brittleness of the Ti$_3$Al processed for this study was therefore somewhat unexpected. Elemental powders of Ti and Al are coated with an oxide layer. As the powders are combined in mechanical alloying, the oxide becomes an integral part of the material. Even if mechanical alloying is carried out under inert atmosphere conditions, the initially present surface oxide on the elemental powders may result in high levels of contamination for the resultant alloy. This contamination source is unique to alloys produced by powder methods and results in interstitial oxygen and nitrogen contents above the levels normally found in vacuum cast material. Ti-based materials, particularly the intermetallics, are highly susceptible to embrittlement by interstitial impurities. Therefore, all potential sources of oxygen or nitrogen contamination must be regarded as undesirable and deleterious to the mechanical properties of the Ti-based material.

3. Ti-Al alloy

The pack rolled TiAl strips exhibited the least chemical segregation of the three alloys investigated. An example of the TiAl flake is shown in Figure 8.9a. The material was generally homogeneous although evidence of incipient melting was observed in several isolated regions. A higher magnification view of the TiAl flake is shown in Figure 8.9b. The behavior of this material during elevated temperature deformation was not unexpected. No previous investigations have demonstrated that TiAl can be extensively deformed at temperatures as low as 1050°C. The successful production of foil from this material will require elimination of Al-rich low melting point zones, greater control of interstitial impurities, and, probably, higher processing temperatures.

8b.3. Discussion

A pack rolling process which has previously been shown to be successful for the production of foil from Ti-6Al-4V alloy, Ti$_3$Al+Nb, and Be was selected as a means of consolidating MA Ti- and Ni-based aluminide alloys and processing them to a thin strip. Efforts to produce a fully consolidated strip of material were not successful for the following reasons:

1) Chemical inhomogeneity led to the presence of Al-rich low melting point phases which undoubtedly caused a "hot-shortness" condition during elevated temperature processing. The presence of a liquid phase during processing prevents compete consolidation of the powder and greatly contributed to the production of "flake" rather than "foil". This problem can be overcome by a) optimizing MA procedures to allow for more intimate mixing of the elemental powders and thus lessen the diffusion distance for reaction at elevated temperature, b) balancing the powder composition to insure that there is not an excess of Al in the powder blend, and c) adjusting the thermal processing schedule to allow for diffusion, intermetallic compound formation, and chemical homogenization to take place prior to rolling deformation.

2) Interstitial contamination has probably contributed to brittleness in the Ti-based materials. The mechanically alloyed powders may contain oxygen and nitrogen that contribute to brittleness. Oxygen was incorporated in the raw elemental powders as well as absorbed by the freshly created new surfaces during mechanical alloying. Methods for reduction of oxygen contamination in mechanically alloyed powders include vacuum degassing of raw elemental powders and performing alloying in a sealed vessel. In some cases, oxygen is necessary in MA to prevent welding of ductile particles. Thus we may have contradictory processing and end product needs.

132
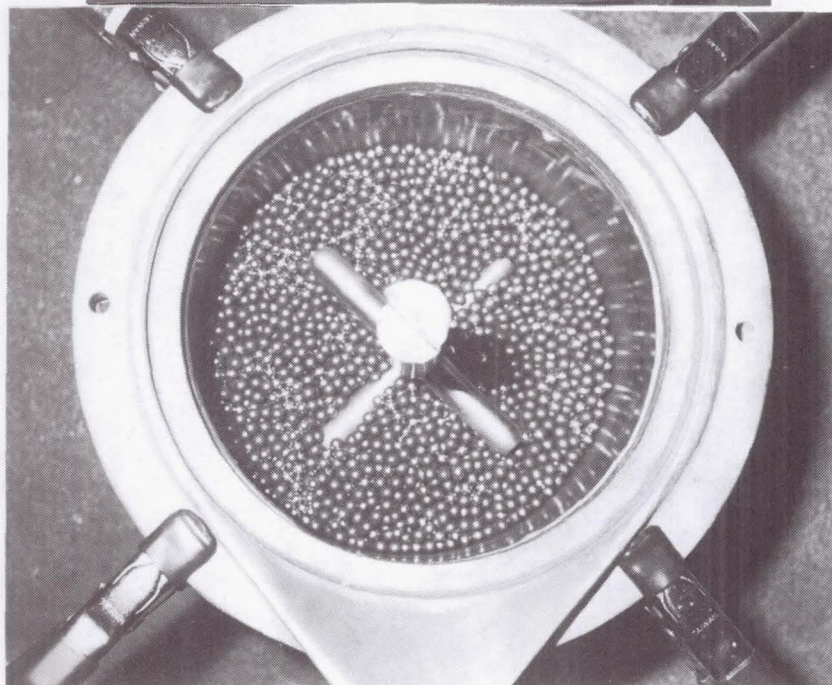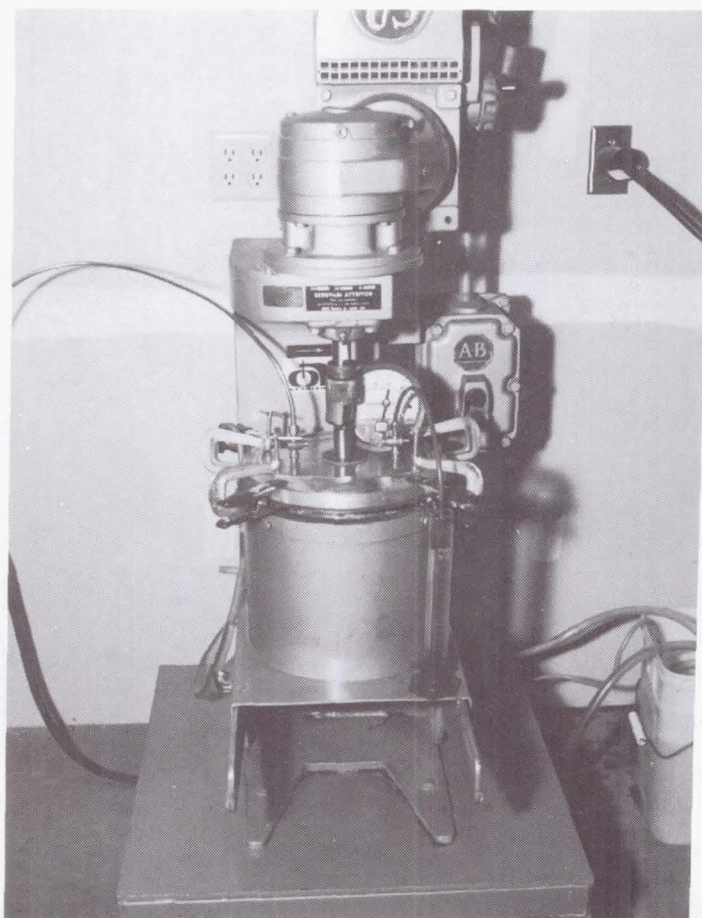
Figure 8.1. Attritor mill (Union Process) used for mechanical alloying.

MA18A 40X (A)

MA18B 40X (B)
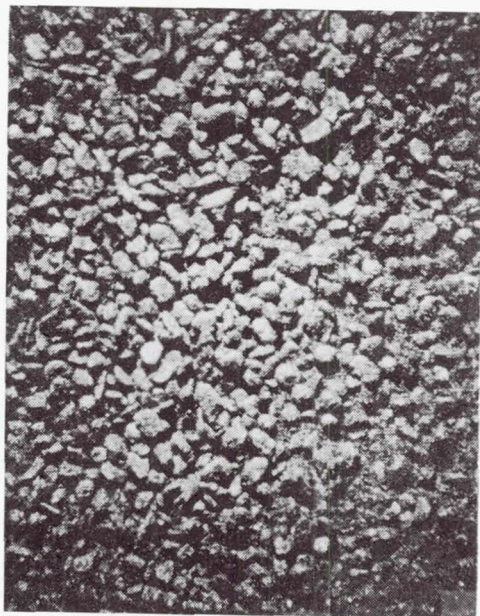
MA21A 40X (C)
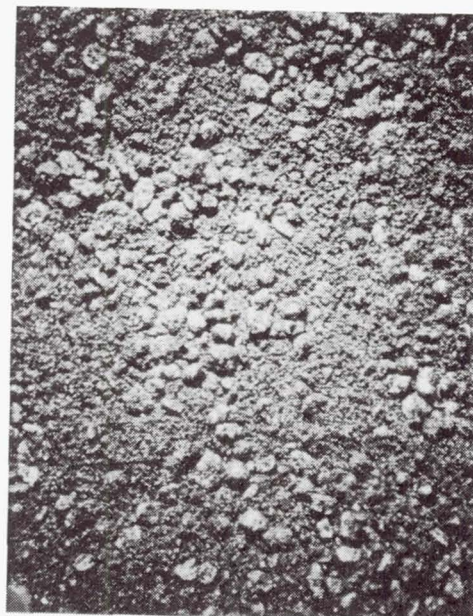
MA21B 40X (D)

Figure 8.2. Mechanically alloyed powders showing different sizing: A) MA18A, B) MA18B, C) MA21A, and D) MA21B.

134
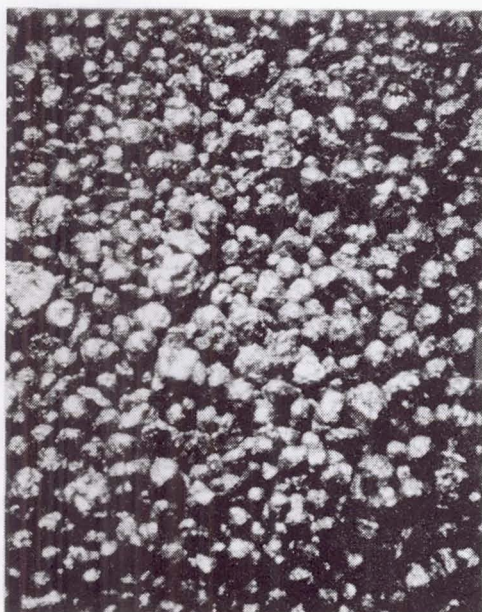
MA22B 40X (A)
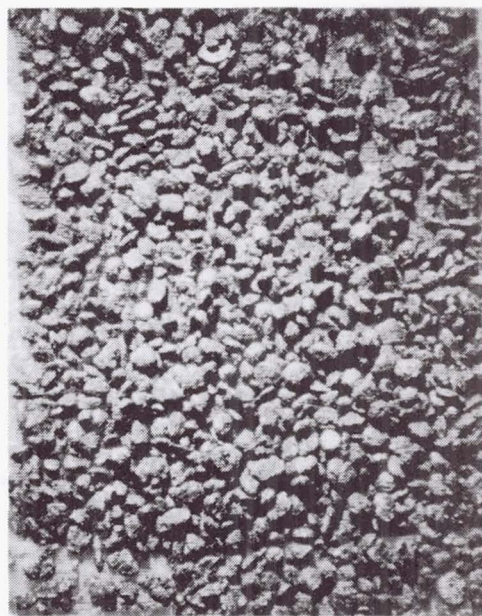
MA23A 40X (B)

MA8901 400X (C)

MA8901 400X (D)

Figure 8.3. Mechanically alloyed powders showing different sizing: A) MA22B, B) MA23A, C)MA8901 and D) MA8901 with smooth surface.

WALL COATING

(A)

1-2 MM PARTICLE

-325 MESH

Ni$_3$Al-HfC, MA21B

FINAL PRODUCT

(B)
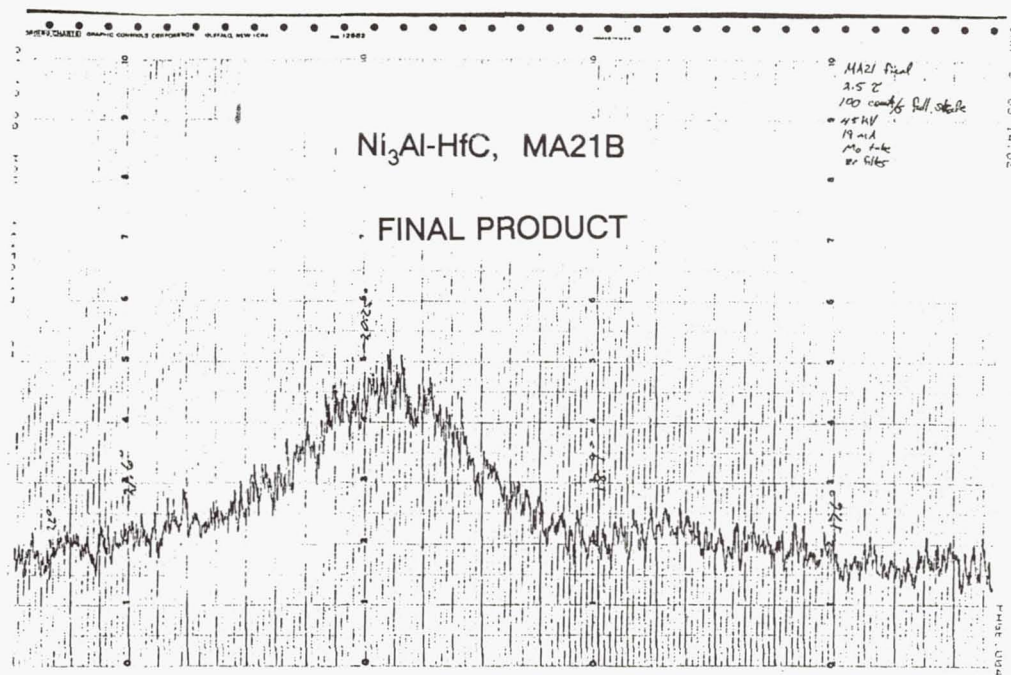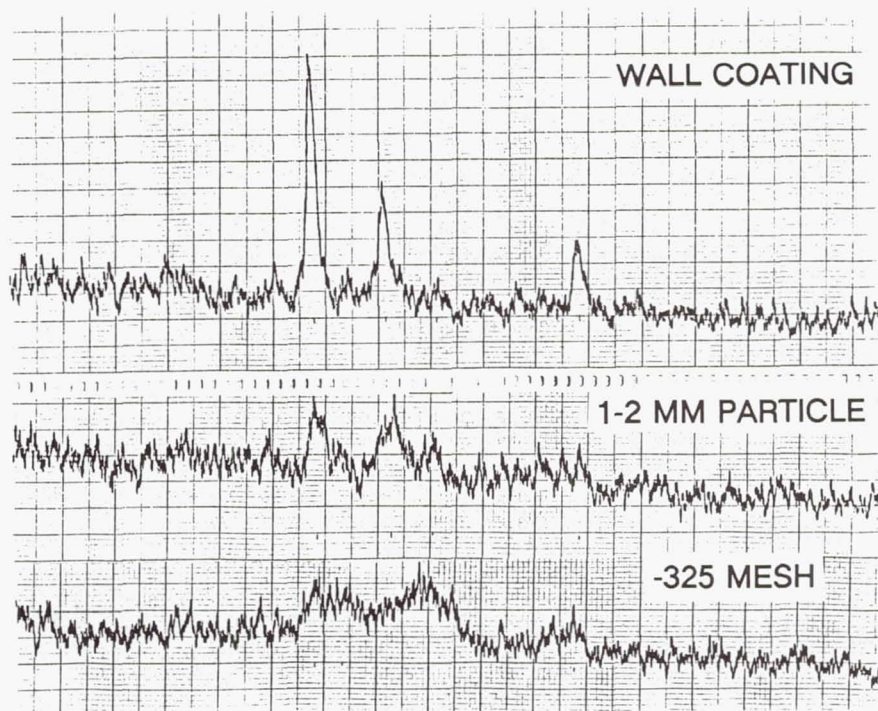
Figure 8.4. X-ray diffraction patterns showing A) an increase of line broadening as a function of particle size, and B) amorphous phase resulting in Ni$_3$Al-(Hf,C) alloys.
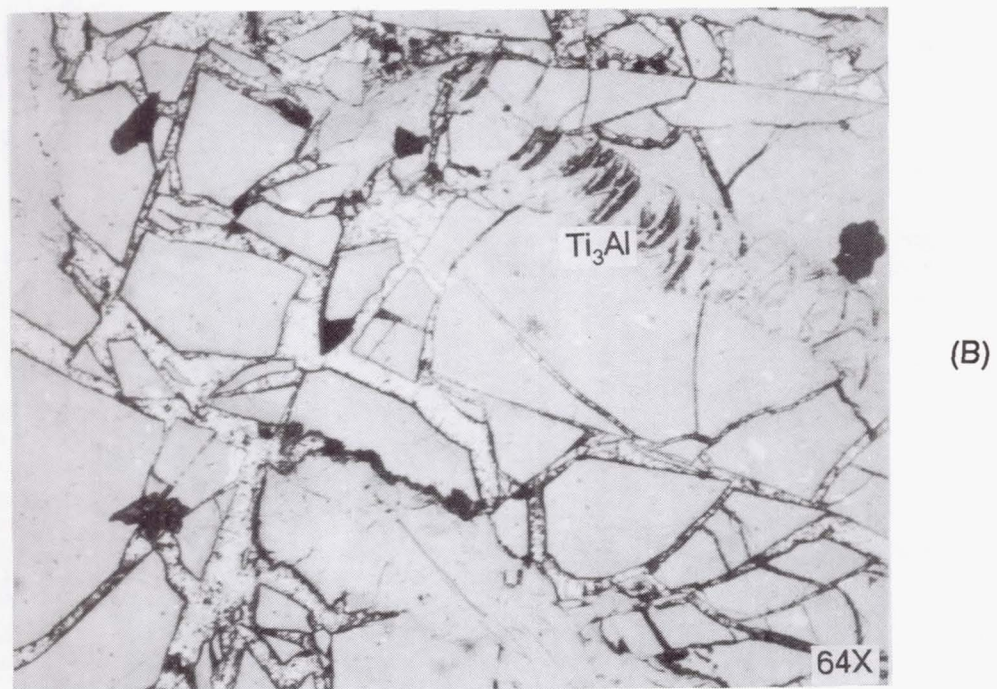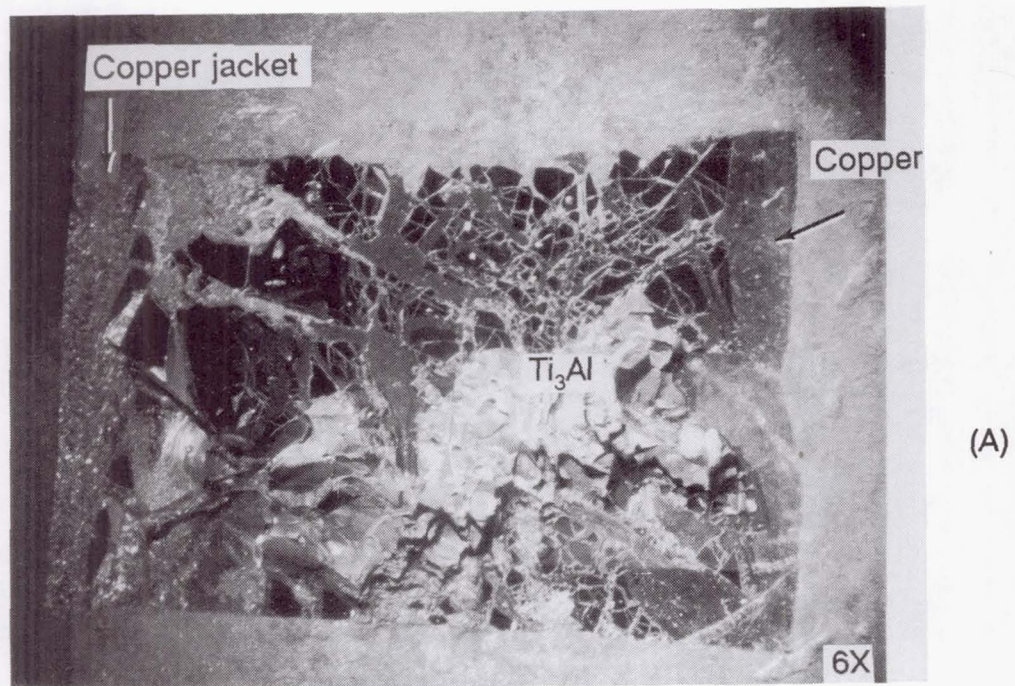
Figure 8.5. Hot rolling of MA 8901 powders resulting in
fragmented materials, A) cross section view, and B) microcracking
of the Ti₃Al phase.

137

(A)
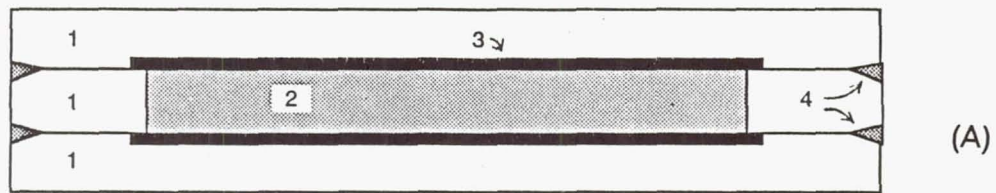
Schematic of laminated structure used to process foil for this study. Shown are: 1) Protective encapsulation layers, 2) Encapsulated reactive metal, 3) Thin layer of release agent, and 4) Welds.

1 cm

(B)
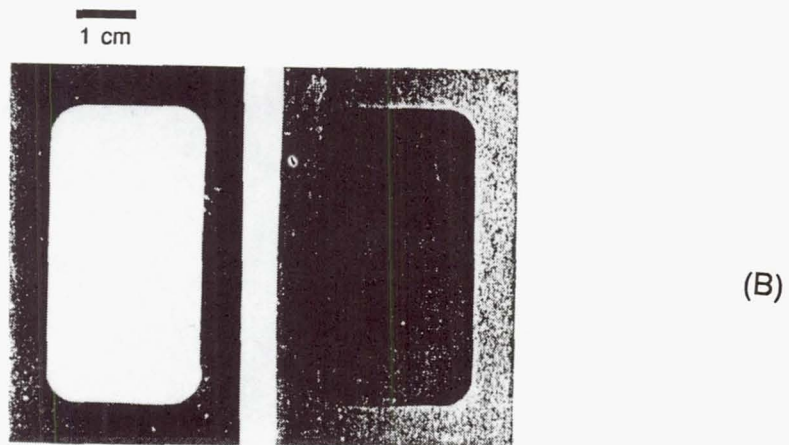
A metal frame (left) is prepared and the reactive metal is placed within the frame (right). For the case shown, metal powders were pressed into the frame using a specially constructed die. The thickness of the frame shown above is 2.5 mm. Reactive metal inserts have also been successfully prepared from solid bar stock.

(C)

| MA Material | Ti₃Al | TiAl | Ni₃Al |
| Processing Temperature | 990°C | 1030°C | 1050°C |
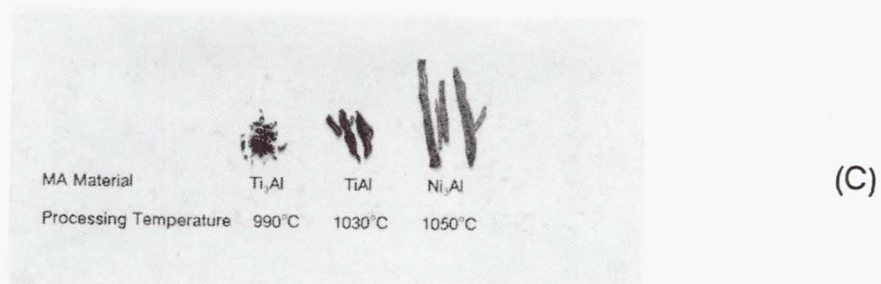
Figure 8.6. A) Schematic of laminated structure used to process foil by pack rolling, B) metal frame containing the metal powder compact was used, and C) resultant products from pack rolling.

138
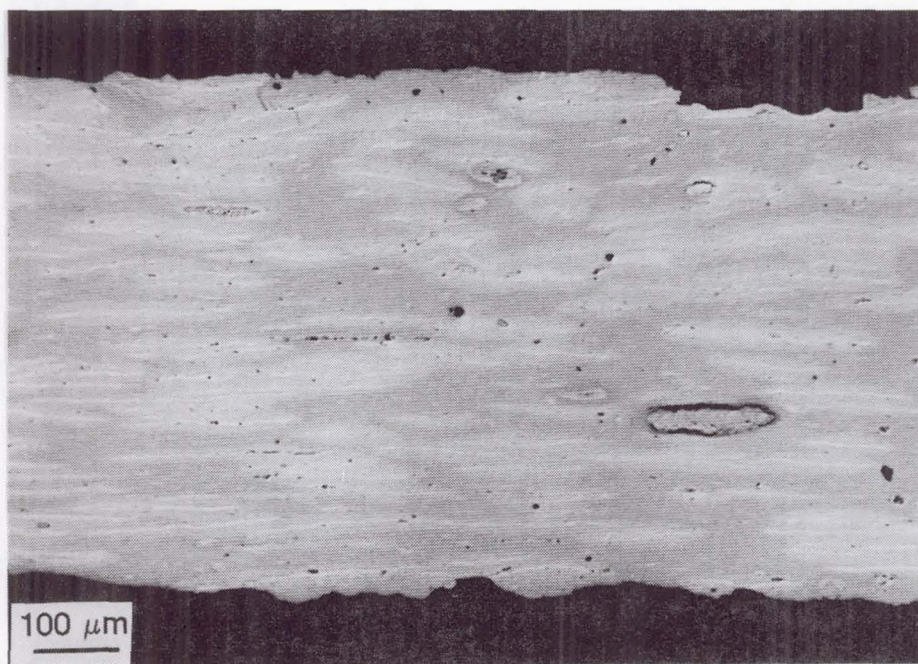
(a)
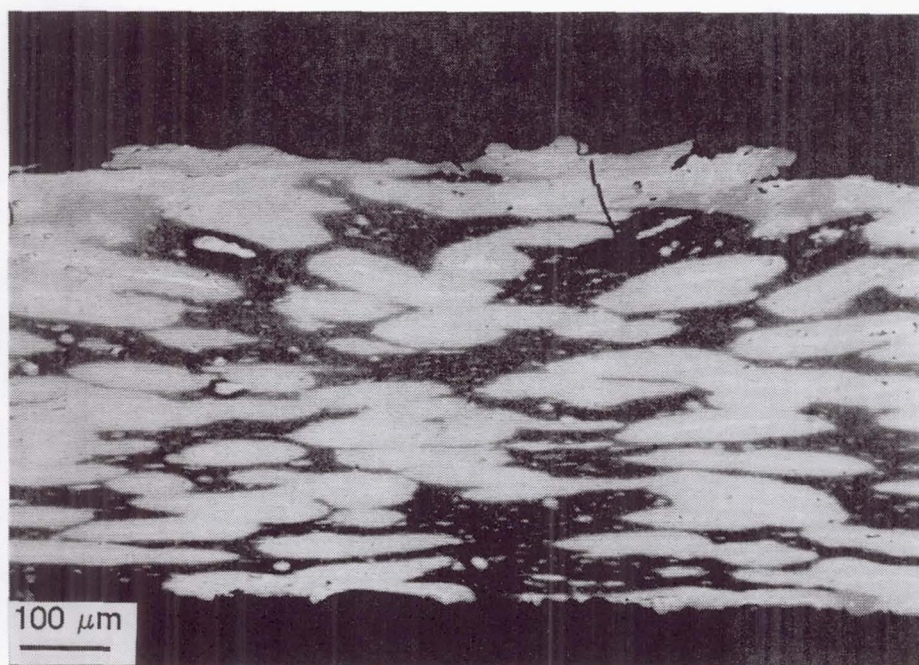
(b)

Figure 8.7. Microstructure of Ni₃Al flake showing a) unetched surface, and b) etched surface with a high degree of chemical inhomogeneity.
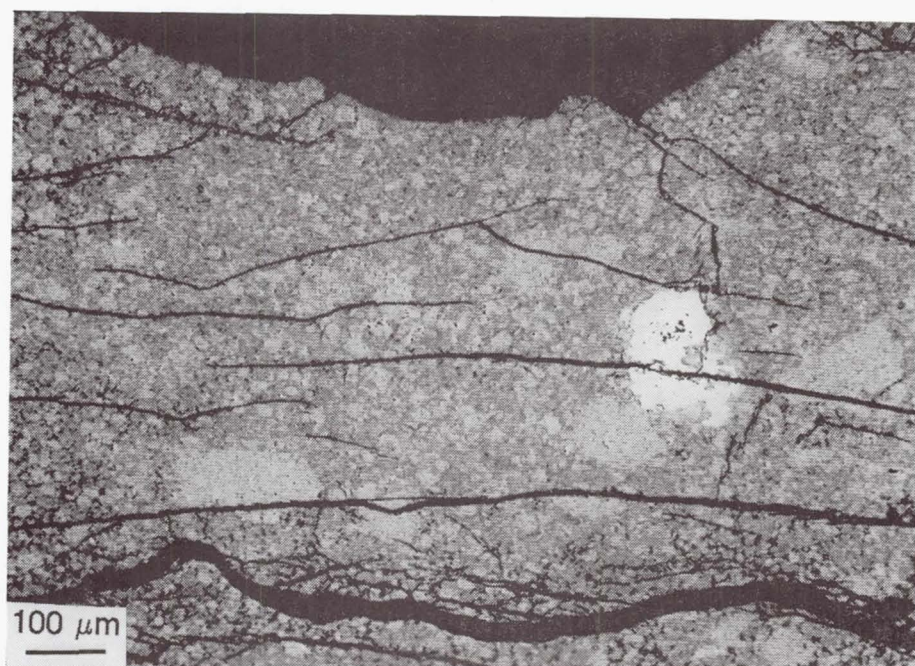
(a)
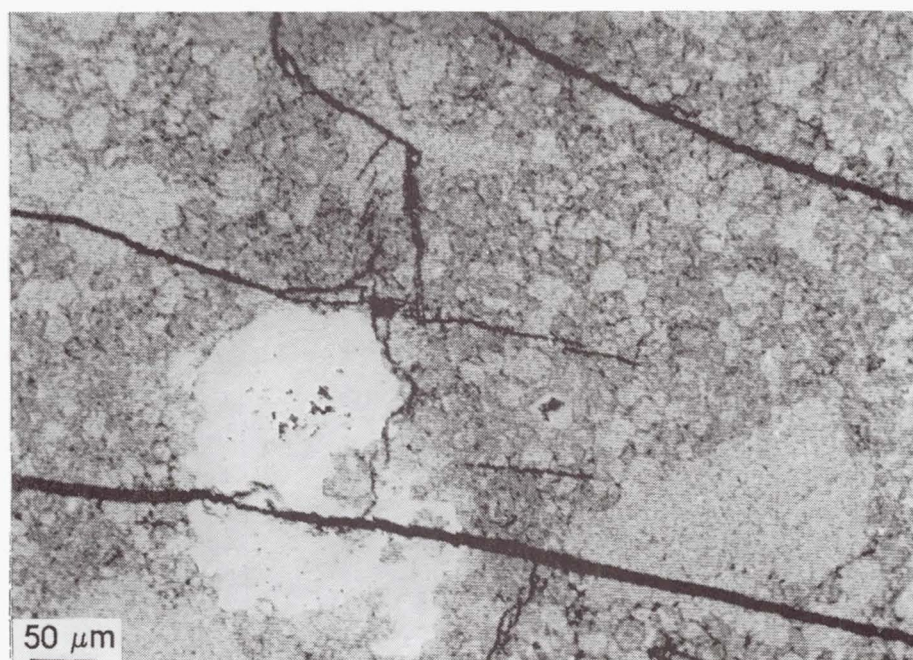
(b)

Figure 8.8.   Microstructure of Ti$_3$Al flake showing a) a high
level of cracking, and b) Al-rich incipient melting zones.

140

(a)

100 μm

(b)

50 μm
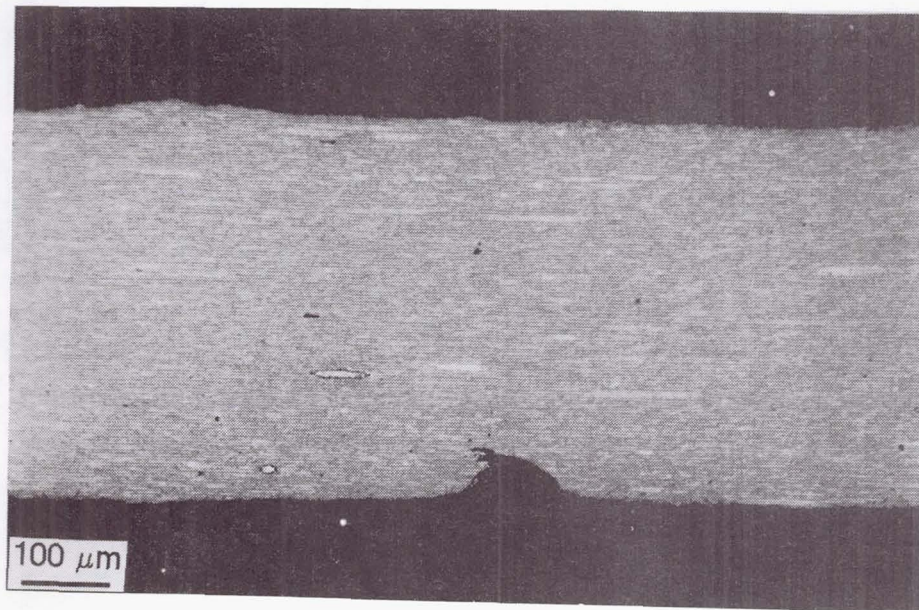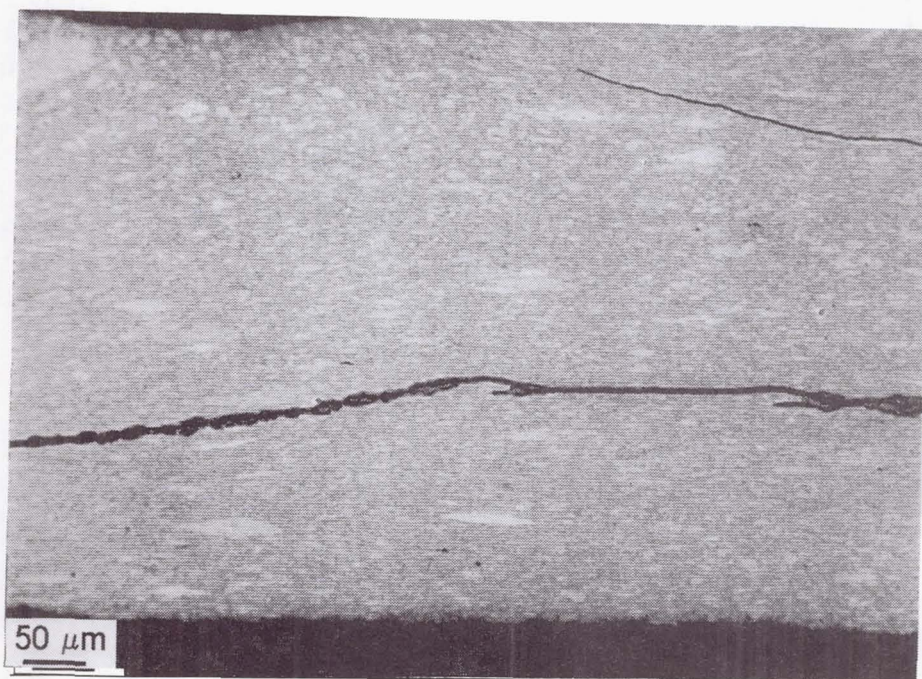
Figure 8.9. Microstructure of TiAl flake showing a) material containing a few incipient melting zones, and b) phase segregation and cracks.

141

9. SUMMARY AND CONCLUSIONS

The first part of this research provided an efficient investigation of nonequilibrium phase chemistry and microstructure of ten alloy systems. The work was derived from five 6"-diameter graded composition sputtering deposits. Ceramic additives, HfC and B, for formation of stable dispersoids in Ni_3Al and Ti-6Al-4V alloys, respectively, were investigated. Nonequilibrium Ni_3Al, Ti-6Al-4V and Ti_3Al alloys containing individual or combined metallic additives of Nb and Cr were investigated for phase stability, microstructure and potential ductility or strengthening enhancements. High temperature mechanical behavior was illustrated by microhardness obtained from room temperature to 900°C. Oxidation resistance characteristics of Ti_3Al-Nb, Ti_3Al-Cr and Ti_3Al-(Nb,Cr) alloys were studied at 900 and 1100°C. Efforts were also made to replicate the alloy phase and microstructure of sputter deposited alloys by mechanical alloying.

The second part of the research built on earlier results leading to more detailed investigation of specific promising alloys. The work focused on fabrication of high quality single composition sputter deposits based on Ti_3Al-Nb for high temperature mechanical testing. Due to complexity of the phase relationships in the Ti-Al-Nb system, a detailed investigation of microstructure, composition and thermal stability of Ti_3Al-xNb-2Cr was conducted with analytical TEM. The summary results of this research are:


9a. Phase Stability in Nonequilibrium Alloys

Fine grained disordered $L1_2$ Ni_3Al, alpha Ti-6Al-4V, and alpha2 Ti_3Al phases containing a high density of defects were obtained from sputter deposition. No new metastable and high temperature phase was observed in the as-deposited alloys.

Fine dispersoids or second phase particles were formed by addition of stable ceramic materials such as HfC and B into the Ni_3Al and Ti-6Al-4V phases, respectively. Up to 10 at.% HfC can be added to the $L1_2$ structure before an amorphous phase is formed. Annealing in the 900-1100°C range forms stable and fine HfC dispersoids. Addition of B in alpha-Ti resulted in large amounts of a TiB/Ti_2B phase in the form of thin laths.

142

Nb SOLUBILITY LIMITS IN
NONEQUILIBRIUM ALLOYS

Figure 9.1.   Comparison of extended Nb solubiliteis in nonequilibrium phases.
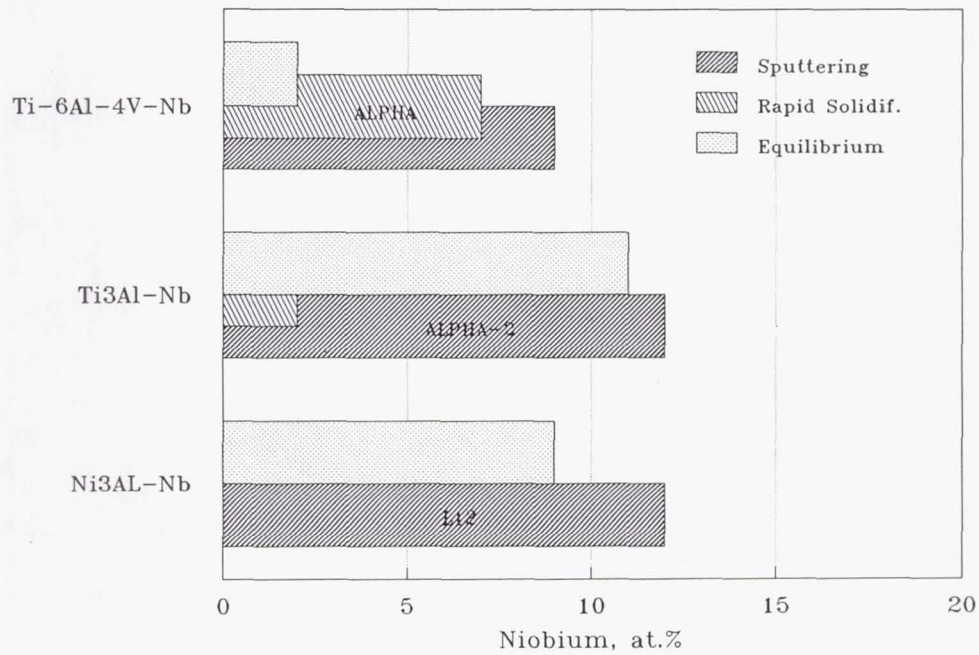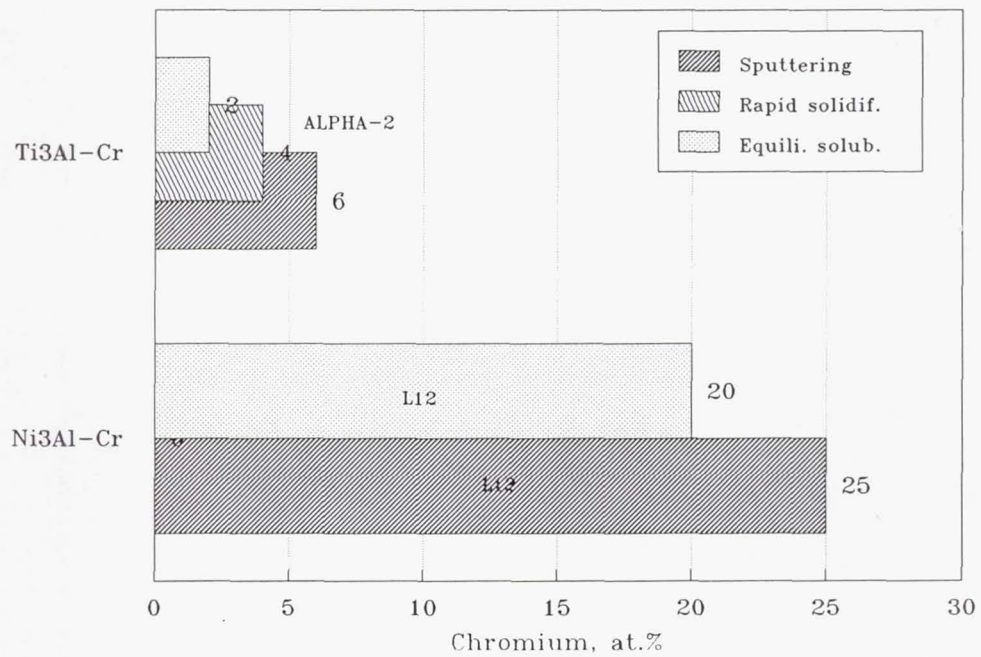
Cr SOLUBILITY LIMITS IN
Ti3Al and Ni3Al PHASES

Figure 9.2.   Comparison of extended Cr solubilities in nonequilibrium phases.

Addition of metallic elements such as Nb into the $L1_2$, alpha and alpha2 phases resulted in extended solid solutions in comparison with equilibrium and rapidly solidified alloys [33], Figure 9.1. The solubility of Nb in $L1_2$ structure was extended to 12 at.% Nb; an amorphous phase was formed with more than 15 at.% Nb. The solubility of Nb in alpha and alpha2 phases were similar 9-12 at.% Nb. Additional Nb resulted in beta phases with slightly larger grain size than the alpha phases.

Addition of metallic Cr into $L1_2$ and alpha2 phases had an opposite effect than the Nb, as shown in Figure 9.2. The solubility of Cr in the $L1_2$ structure was extended to nearly 25 at.%. A Cr-rich beta phase resulted with more than 40 at.%Cr. Solubility of Cr in alpha2 phase was extended to nearly 6 at.% Cr and a beta phase was formed between 12 and 30 at.% Cr. In the range of 30-45 at.% Cr, an amorphous phase was observed. Extended solid solubility and formation of amorphous phase affected by Nb and Cr additions may be correlated to the occurrence of several intermetallic compounds in binary Ni-Nb and Ti-Cr systems.

9b. Microstructures

All the as-deposited alloys exhibited disordered structures and very fine textured grains less than 0.1 μm in size. The microstructure contains a high density of defects. Fully annealed alloys had a well defined microstructure with grain size on the order to 0.5 to 5 μm range. Additions of HfC in Ni_3Al resulted in fine dispersoids up to 1100°C. Boron additions to Ti alloys led to segregation of TiB/Ti_2B laths. No dispersoids were observed with metal additions such as Nb and Cr.

9c. Thermal Stability

Thermal stability of Ti_3Al-Nb alloys containing 15-24 at.% Al and 8-30 at.% Nb was extensively investigated by analytical TEM. At this composition range, annealing between 800-950°C resulted in alpha2, beta, orthorhombic and twinned orthorhombic phases. Compositions for these phases were not significantly different, and differences were continuously reduced as a function of annealing time. However, formation of two different orthorhombic phases as well as resultant microstructures are strongly dependent to the heat treatment and the initial alloy composition. The observed continuous phase change may be promoted by the defect structure, high Al mobility or possible Al loss in sputter deposited alloys during annealing. Internal oxygen and stress in the thin sputter deposited foils may also play an important role in controlling the thermal stability. The sputter deposited alloys, in general, were not thermally stable in the temperature range investigated.

144

9d. Oxidation Resistance

Due to potentially improved resistant to oxidation in nonequilibrium Ti_3Al-Nb, Ti_3Al-Cr and $Ti_3Al-(Nb,Cr)$ alloys, their oxidation characteristics were studied at 900 and 1100°C. Nb addition promoted homogeneous oxidation resulting in a higher oxidation rate than alloys which contained Cr. A small amount of Cr led to the formation of protective oxide scale and elemental segregation into oxide multilayers. A greater amount of Cr resulted in better oxidation resistance. The best oxidation resistant material at 1100°C was the Ti-14Al-1Nb-46Cr alloy.

9e. High Quality Foils

Many technical difficulties associated with fabrication of alpha2-Ti_3Al-Nb foils were resolved. High quality foils of 4-10 mils thick were fabricated by using high purity cast target materials sputtered at a 40-60 V bias voltage. The resultant foils had a low oxygen content, uniform microstructure, ductile behavior, mostly equiaxial growth, and good room temperature flexibility.

9f. Mechanical Properties

The sputter deposited alloys typically exhibited a high hardness between room temperature and 600°C. At temperatures in the 700-900°C range, sputter deposited alloys exhibited a lower hardness when compared to similar liquid-quenched and thermo-mechanically processed alloys. The reduction in microhardness over 700°C may be attributable to lack of phase and microstructural stability, which may have a basis in the intrinsic characteristics of the sputter deposited alloys. As-deposited alloys have an ultrafine and highly defected microstructure. This microstructure provides a high level of available internal energy, which may promote complex phase transitions, sluggish recrystallization and grain growth during annealing. At elevated temperatures, fine and stable dispersoids seem unable to pin the grain boundary activity, as demonstrated in the $Ni_3Al-HfC$ system.

9g. Mechanical Alloying

Mechanical alloyed materials resulted in replicating the
microstructures and phases of the sputter deposited alloys.
However, laboratory mechanical alloying equipment lacked the
capability to produce kilogram quantities of homogeneous
products. Inhomogeneous products led to problems with
consolidation of these powders into ribbons, or foils.
Furthermore, small scale alloying based on laboratory equipment
and commercially available powders also resulted in a high level
of contamination with oxygen and possibly other gases. Lack of
powder cleanness and homogeneity prevented powder consolidation
and fabrication of high quality bulk materials.

9h. Recommendations

The results of this research point to areas of additional work
useful for the development of strengthening mechanisms for high
temperature structural alloys:

1. Ni_3Al based alloys: Additions of HfC to Ni_3Al has resulted
in a highly stable HfC dispersoids in the Ni_3Al matrix. However,
HfC alone was not completely effective in reducing grain boundary
movement at temperatures above 700°C. Combination of dispersoids
and a second phase (with B or Nb) may promote creep resistance in
Ni_3Al alloys.

2. Ti-6Al-4V: Combination of Nb and B additions may also
promote improved high temperature mechanical properties in Ti
alloys. Alloys of Ti-6Al-4V-Nb-B with 4-9 at.% Nb and 2-5 at.% B
should be investigated. These materials could yield high
temperature strength in the 600-700°C range.

3. Ti_3Al: Further studies should address the phase stability
mechanisms for different orthorhombic phases. The role of Al on
complex phase relationships should be studied as a function of Al
content and annealing conditions. Comparison of short time
annealing at a high temperature (1h at 1000°C) with long time
annealing at a low temperature (100 h at 800°C) should determine
whether Al loss is associated with free Al in the deposit. This
understanding could then lead to the development of alloy
chemistry for the suppression of excess beta and orthorhombic
phases. One approach would be to assess effects of increasing
the Al content and reducing the Nb content in the alloy. Ti-Al-
Nb alloys with 25-28 at.% Al and 7-10 at.% Nb should be studied
initially. A two-step heat treatment, 1000°C followed by 850°C,
is recommended to remove the defect structures and stabilize the
final phase distribution in the alloy. The effects of bias and
substrate temperature for high quality foil fabrication should be

146

investigated further. Tensile testing should be performed only with promising materials previously screened by microhardness measurements.

This research has identified unique microstructures and properties of nonequilibrium structural alloys formed by sputter deposition. These materials have a ultrafine grain size with highly defected microstructure. With intermetallic alloys based on a wide range of "phase compound" characteristics, containing multiple phases in a wide solid solution range, the degree of nonequilibrium behavior contributes to difficulties for controlling the microstructure, phase distribution and composition in the final product by heat treatment. However, these structural and microstructural characteristics offer opportunities to explore other high temperature structural materials based on simple line compound behavior, such as the beryllides and silicides. The capability of obtaining extended solid solubility and fine grain size by sputter deposition should lead to high toughness without the loss of mechanical strength.

10. REFERENCES

1. T.W. Barbee Jr., W.H. Holmes, D.L. Keith, M.K. Tyzyna and G. Ilonca, Thin Solid Films, 45, 591 (1977).

2. H.F. Rizzo, T.B. Massalski and E.D. McClanahan, Met. Trans. 19A, 5 (1988).

3. Wu, Y.P., J.M. Sanchez, and J.K. Tien, "Microsegregation to Antiphase Boundaries in Monolithic Gamma-prime Phase with Ternary Additions", Mat. Res. Soc. Symp. Proc. vol. 133, p. 119, (1988)

4. Ackland, G.L., and V. Vitek, "Effect of Ordering Energy on Grain Boundary Structure in $L1_2$ Alloys", Mat. Res. Soc. Symp. Proc. vol. 133, p 105, (1988)

5. Kaufman, M.J.,"Phase Relations in the Ti_3Al-Nb System", AFWAL-TR-88-4113, Final Report, July 1988.

6. Kaufman, M.J., T. F. Broderick, C.H. Ward, J.K. Kim, R.G. Rowe, and F.H. Froes, "Phase Relationships in the Ti_3Al+Nb System", Proceedings of the 6th World Conf on Titanium, Cannes, France, June 1988, P. Lacombe, R. Tricot and G. Beranger, eds., (Societe Francaise de Metallurgie, Les Editions de Physique, Les Ulis, France, 1989) p. 985.

7. Wang, R., "Thermal Stability Data of Amorphous Binary Alloys", Bull. of Alloy Phase Diagrams, 2, 269 (1981).

8. McCullough, C., J.J. Valencia, H. Mateos, C.G. Levi, and R. Mehrabian, Scripta Metall., 22, 1131-36 (1988).

9. Ogden, H.R., D.J. Maykuth, W.L. Finlay, and R.I. Jaffee, Trans. AIME, 195, 1150-55 (1951).

10. Valencia, J.J., C. McCullogh, C.G. Levi, and R. Mehrabian, Scripta Metall., 21, 1341-46 (1987).

11. Ence, E., and H. Margolin: Trans. AIME, 221, 151-57 (1967).

12. Banerjee D., A.K. Gogia, T.K. Nandi, and V.A. Joshi, "A new Ordered Orthorhombic Phase in a Ti_3Al-Nb Alloy", Acta Metallurgica, 36, [4], 871 (1988).

13. Strychor R., and J.C. Williams, and W. A. Soffa, Met. Trans A., 19A, 225-232 (1988).

14. Weykamp, H.T., Master Thesis, University of Washington (1989).

15. Kestner-Weykamp, H.T., C.H. Ward, T.F. Broderick and M.J. Kaufman," Microstructures and Phase Relationships in the Ti_3Al+Nb System", Scripta Met. 23, 1697-1702 (1989).

16. Brown, A.R.G., D. Clark, J. Eastabrook, and J.S. Jepson, Nature, 201, 914-915 (1964).

17. Muraleedharan, K., S.V. Nagender Naidu and D. Banerjee, "Orthorhombic Distortions of the alpha2 phase in Ti_3Al-Nb Alloys: Artifacts and Facts", Scripta Met. 24, 27-32 (1990).

18. Perkins, R.A. and K.T. Chiang, "Formation of Alumina on Niobium and Titanium Alloys", in Oxidation of High Temperature Intermetallics, eds T. Grobstein and J. Doychak, The Minerals, Metals & Materials Society, 157-170 (1989).

19. Wiedemann K.E., S.N. Sankaran, R.K. Clark and T.A. Wallace, "Static and Dynamic Oxidation of Ti-14Al-21Nb", in Oxidation of High Temperature Intermetallics, eds T. Grobstein and J. Doychak, The Minerals, Metals & Materials Society, 195-206 (1989).

20. Welsch G. and A.I. Kahveci,"Oxidation Behavior of Titanium Aluminide Alloys", in Oxidation of High Temperature Intermetallics, eds T. Grobstein and J. Doychak, The Minerals, Metals & Materials Society, 207-218 (1989).

21. Jha, S.C., J.A. Forster, A.K. Pandey, R.G. Delagi," Microstructures and Mechanical Properties of Sheets and Foils of Ti_3Al Based Alloys", Presented at the Conference of Advanced Aerospace Materials/Processes, Long Beach, California, May 1990.

22. Bania, P.J., "Production of Alpha2 and Gamma Titanium Aluminide Mill Products", Presented at the Conference of Advanced Aerospace Materials/Processes, Long Beach, California, May 1990.

23. Tuominen, S.M.,"Extra Low Oxygen Content of Super Alpha-2", Presented at the Conference of Advanced Aerospace Materials/Processes, Long Beach, California, May 1990.

24. Bassi, C., J.A. Peters and J. Wittenauer, "Processing Titanium Aluminide Foils", J of Metals, 41, 18-20 (1989).

25. Benjamin J. S. Sci. Amer. "Mechanical Alloying," 234, 40 (1976).

26. Koch, C. C., O. B. Cavin, C. G. McKamey, and J.O. Scarbrough, Appl. Phys. Lett. 43, 1017 (1983).

27. Politis C. and W. L. Johnson, J. Appl. Phys. Lett. 48, 124 (1986).

28. Starrett, H. S., and N. R. Ontko, "Mechanical Properties of Elementally Blended Ti-6Al-4V," Final Report, AD-A176640, AFWAL-TR-86-4119, (1986).

29. Wittenauer, J and B. Walser,"Processing and Properties of Titanium Foils," Mat. Sci. Eng, A123, 45-52 (1990).

30. Wittenauer, J., C. Bassi, and B. Walser,"Hot Deformation Characteristics of Nb-modified Ti_3Al," Scripta Met, 23, 1381-86 (1989).

31. Lipsitt, H. D. Shechtman, and R.E. Schafrik,"The Deformation and Fracture of Ti_3Al at Elevated Temperatures", Metall. Trans. A, 11, 1369-1375 (1980).

32. Sastry, S.M.L., and H.A. Lipsitt,"Ordering Transformation and Mechanical Properties of Ti_3Al and Ti_3Al-Nb Alloys", Metall. Trans. A8, 1543-1552 (1977).

33. Whang, S.H., and C.S. Chi, "Formation of Metastable Phases in Rapidly Quenched Binary Ti Alloys", Mat. Res. Soc. Symp. Proc. 58, 353-358 (1986).

NASA National Aeronautics and Space Administration	Report Documentation Page		
1. Report No. NASA CR-4353	**2. Government Accession No.**	**3. Recipient's Catalog No.**	

4. Title and Subtitle

Nonequilibrium Phase Chemistry in High Temperature Structural Alloys

5. Report Date

March 1991

6. Performing Organization Code

7. Author(s)

R. Wang

8. Performing Organization Report No.

10. Work Unit No.

324-02-00

9. Performing Organization Name and Address

Failure Analysis Associates, Inc.
8411 154th Ave NE, Redmond, WA 98052

11. Contract or Grant No.

NAS1-18693

13. Type of Report and Period Covered

Contractor Report
June 1988 – November 1990

12. Sponsoring Agency Name and Address

NASA Langley Research Center
Hampton, VA 23665-5225

14. Sponsoring Agency Code

15. Supplementary Notes

Langley Technical Monitor: Ronald K. Clark
Final Report

16. Abstract

This research identified, characterized and produced Ti and Ni aluminides of nonequilibrium microstructures and in thin gauge thickness for potential high temperature applications. The work demonstrated a high rate sputter deposition technique for rapid surveillance of the microstructures and nonequilibrium phase chemistry. Alloys with specific compositions were synthesized with extended solid solutions, stable dispersoids and specific phase boundaries associated with different heat treatments. Phase stability and mechanical behavior of these nonequilibrium alloys were investigated and compared.

17. Key Words (Suggested by Author(s))

Titanium aluminides
Nickel aluminides
Sputter deposition
Alloy chemistry

18. Distribution Statement

Unclassified-Unlimited
Subject category 26

19. Security Classif. (of this report)	**20. Security Classif. (of this page)**	**21. No. of pages**	**22. Price**
Unclassified	Unclassified	164	A08

NASA FORM 1626 OCT 86

NASA-Langley, 1991